

УДК 517

Публікуються результати експериментальних та теоретичних досліджень у галузях фізичної електроніки, фізики плазми, фізики поверхні твердого тіла, емісійної електроніки, криогенної та мікроелектроніки, нанофізики та наноелектроніки, високотемпературної надпровідності, квантової радіофізики, функціональної електроніки, твердотільної електроніки, мобільного зв'язку, медичної радіофізики, методів отримання діагностичної інформації та її комп'ютерної обробки.

Для науковців, викладачів вищої школи, студентів.

Experimental and theoretical contributions are published in the following fields: physical electronics, plasma physics, solid-state surface physics, emission electronics, cryogenic electronics, microelectronics, nanophysics and nanoelectronics, high-temperature superconductive electronics, solid-state electronics, functional electronics, microwave electronics, quantum electronics, mobile communication, medical radiophysics, methods of receipt and computer processing of diagnosis information

Designed for researches, university teachers, students.

РЕДАКЦІЙНА КОЛЕГІЯ	І. О. Анісімов, д-р фіз.-мат. наук, проф. (відп. ред.); Г. А. Мелков, д-р фіз.-мат. наук, проф. (заст. відп. ред.); В. А. Львов, д-р фіз.-мат. наук, проф. (наук. ред.); Т. В. Родіонова, канд. фіз.-мат. наук, ст. наук. співроб. (відп. секр.); Ю. В. Бойко, канд. фіз.-мат. наук, доц.; А. М. Веклич, д-р фіз.-мат. наук, проф.; В. І. Висоцький, д-р фіз.-мат. наук, проф.; В. І. Григорук, д-р фіз.-мат. наук, проф., І. В. Зависляк, д-р фіз.-мат. наук, проф.; Б. О. Іванов, д-р фіз.-мат. наук, проф.; В. І. Кисленко, канд. фіз.-мат. наук, доц.; В. Ф. Коваленко, д-р фіз.-мат. наук, проф.; І. П. Коваль, канд. фіз.-мат. наук, доц.; М. В. Кононов, канд. фіз.-мат. наук, доц.; В. Г. Литовченко, д-р фіз.-мат. наук, проф.; Є. В. Мартиш, д-р фіз.-мат. наук, проф.; С. Д. Погорілий, д-р техн. наук, проф.; С. М. Савенков, д-р фіз.-мат. наук, доц.; В. А. Скришевський, д-р фіз.-мат. наук, проф.; V. Bartlova (Milada Bartlová), Ph. D., (Brno University of Technology, Czech Republic); N. Kukhtarev (Nickolai Kukhtarev), Research Professor, (Alabama A&M University, USA)
Адреса редколегії	03127, м. Київ-127, просп. акад. Глушкова, 4 Г, факультет радіофізики, електроніки та комп'ютерних систем. ☎ (38044) 526 05 60
Затверджено	Вченою радою радіофізичного факультету 14.10.13 (протокол № 3)
Атестовано	Вищою атестаційною комісією України. Постанова Президії ВАК України № 1-05/1 від 10.02.2010 р.
Зареєстровано	Міністерством юстиції України. Свідоцтво про державну реєстрацію КВ № 15797-4269Р від 02.10.2009 р.
Засновник та видавець	Київський національний університет імені Тараса Шевченка, ВПЦ "Київський університет" Свідоцтво внесено до Державного реєстру ДК № 1103 від 31.10.02
Адреса видавця	01601, Київ-601, б-р Т.Шевченка, 14, кімн. 43 ☎ (38044) 239 31 72, 239 32 22; факс 239 31 28

ЗМІСТ

Ананьїна О., Северина О. Адсорбція водню на поверхні алмазу C(111): квантово-хімічне моделювання	8
Андрусенко В., Бех І., Новак С. Аналогова обчислювальна машина (АОМ) для моделювання нейронних мереж (задачі апроксимації математичних функцій).....	10
Бабіч Д., Кузькова Н., Попенко О., Якунов А. Вимірювання температури в системі опромінюваної електромагнітними хвилями міліметрового діапазону з використанням температурозалежних флуоресцентних органічних барвників	13
Бондар Б., Кметюк Я. Радіаційна безпека при роботі та технічному обслуговуванні 11-Мев медичного циклотрону.....	16
Гайдар В., Радченко С., Судаков О. Видалення артефактів електроокулограми та електроміограми з ЕЕГ сигналу	19
Гайдар О., Тришин В., Сваричевська О., Павленко І., Гайдар В. Оцінка впливу на довкілля експлуатації центра позитронно-емісійної томографії.....	21
Глушков А., Говорун Д. Повне сімейство н-зв'язаних гомоасоціатів 1-метилцитозину: квантово-механічне дослідження	24
Горбаченко В., Череди І., Врублевський С., Крученко Ж., Лук'янець О. Розробка та експериментальна апробація системи реєстрації харчового рефлексу щурів	31
Горячко А., Мельник П., Сидоров Р., Попова О., Находкін М. Новітня система нано-позиціонування для скануючої зондової мікроскопії.....	33
Денбновецький С., Мельник І., Тугай С. Аналітичні співвідношення для розрахунку енергетичної ефективності тріодних газорозрядних електронних гармат	37
Заболотний М., Довбешко Г., Соляник Г., Кондацький Ю., Естрела-Льопис В., Куліш М., Дмитренко О., Момот А., Полуян Н., Буско Т. Основні проблеми модифікації протиракових препаратів	42
Зависляк І., Попов М., Мовчан М. Пристрої міліметрового діапазону на основі пасивних феритових резонаторів	44
Зайцев С., Кисельов Н., Розенбуш В., Величко Ф., Колесніков С. Поляриметрія галілесвих супутників Юпітера біля опозиції у 2012–2014 роках	49
Зеленюк М., Сусли А., Гуйван Г., Сливка О., Кедюлич В. Вплив зовнішнього електричного поля та одновісного тиску на діелектричні властивості кристалів TGS+Cu ²⁺	51
Іщенко О., Шкавро А., Брайман О., Нечепуренко Д. Люмінесцентні властивості органічних барвників у полімерах PEPK і PVE	53
Карлаш А. Fтіг та фл спектроскопія порошкоподібного аерогелю кремнезему ar-SiOx	55
Короновський В., Вакула Ю. Візуалізація магнітоелектричних проявів у епітаксійних структурах ФГ/ГГГ	59
Куліш М., Дмитренко О., Мельник О., Малий Є., Пінковська М., Тартачник В., Шлапацька В. Оцінка дозового розподілу в області пенумбри з використанням світлодіодних структур	61
Лавренко К., Коломієць І., Савенков С., Оберемок Є., Клімов О. Еволюція стану поляризації в поздовжньо неоднорідному середовищі з лінійним двопронезаломленням	64
Лавренко М., Коломієць І., Савенков С., Оберемок Є. Порівняння розв'язків оберненої задачі поляриметрії при послідовній та одночасній дії механізмів анізотропії середовищ з еліптичним двопронезаломленням.....	67

ЗМІСТ

Левитський С. Чи можна виявити будь-які сліди сигналу до його початку?	70
Мартиш Є., Яценко В. Автономне стикування з некооперованими космічними об'єктами	72
Мачулянський О., Бабич Б. Енергозберігаючі нанокompозитні покриття на основі міді	74
Мельник О., Козаревич В., Собченко А. Синтез програмованих наноелектронних пристроїв	78
Мірошниченко С., Мотоліга О., Невгасимий А., Сенчуров С. Теоретична оцінка товщини реконструйованого зрізу при цифровому томосинтезі	82
Находкін М., Куліш М., Литвин П., Родіонова Т., Сутягіна А. Спеціальні стики границь зерен у нанокремнієвих плівках з рівноосьовою та волокнистою структурою	83
Оберемок Є. Структура матриці Мюллера середовищ з ортогональними поляризаціями власних хвиль	86
Шиян І., Чуйко Г., Павленко А. Цифрова обробка медичних зображень засобами СКМ Maple	90
Яковенко В., Ковальчук О., Сорокин Ю., Пугач В., Охріменко О., Презадо Й., Мартінез-Ровіра І., Ілюхіна А. Металеві мікро-детектори для візуалізації та моніторингу профілю пучка в радіаційній терапії	93
Іванісік А., Ісаєнко О., Коротков П., Понежа Г. Фазова само модуляція лазерного імпульсу в шаруватих самофокуруючих середовищах	95
Костровій П., Маркович Б., Чорноморець Ю., Токарчук Р., Токарчук М. Статистична теорія електродифузійних процесів інтеркаляції іонів в системі "електроліт-електрод"	98

СОДЕРЖАНИЕ

Ананьина О., Северина Е. Адсорбция водорода на поверхности алмаза C(111): квантово-химическое моделирование	8
Андрусенко В., Бех И., Новак С. Аналоговая вычислительная машина (АВМ) для моделирования нейронных сетей (задачи аппроксимации математических функций).....	10
Бабич Д., Кузькова Н., Попенко А., Якунов А. Измерения температуры в системе облучаемой электромагнитными волнами миллиметрового диапазона с использованием температурозависимых флуоресцентных органических красителей	13
Бондар Б., Кметюк Я. Радиационная безопасность при работе и техническом обслуживании 11-Мев медицинского циклотрона	16
Гайдар В., Радченко С., Судаков О. Выделение артефактов электроокулограммы и электромиограммы с ЭЭГ сигнала	19
Гайдар А., Тришин В., Сваричевская Е., Павленко И., Гайдар В. Оценка воздействия на окружающую среду эксплуатации центра позитронно-эмиссионной томографии	21
Глушков А., Говорун Д. Полное семейство Н-связанных гомоассоциатов 1-метилцитозина: квантово-механическое исследование	24
Горбаченко В., Черета И., Врублевский С., Крученко Ж., Лукьянец Е. Разработка и экспериментальная апробация системы регистрации пищевого рефлекса крыс.....	31
Горячко А., Мельник П., Сидоров Р., Попова О., Находкин Н. Новая система нано-позиционирования для сканирующей зондовой микроскопии	33
Денбновецкий С., Мельник И., Тугай С. Аналитические соотношения для расчета энергетической эффективности триодных газоразрядных электронных пушек.....	37
Заболотный М., Довбешко Г., Соляник Г., Кондацкий Ю., Естрела-Льопис В., Кулиш М., Дмитренко О., Момот А., Полуян Н., Буско Т. Основные проблемы модификации противораковых препаратов.....	42
Зависляк І., Попов М., Мовчан Н. Приборы миллиметрового диапазона на основе пассивных ферритовых резонаторов	44
Зайцев С., Киселев Н., Розенбуш В., Величко Ф., Колесников С. Поляриметрия галилеевых спутников Юпитера вблизи оппозиции в 2012–2014 годах.....	49
Зеленюк М, Сусла А., Гуйван А., Сливка А, Кедюлич В. Влияние внешнего электрического поля и одноосного давления на диэлектрические свойства кристаллов TGS+Cu ²⁺	51
Ищенко А., Шкавро А., Брайман А., Нечепуренко Д. Люминесцентные свойства органических красителей в полимерах РЕРК и РВЕ.....	53
Карлаш А. Ftir и фл спектроскопия порошкообразного аэрогеля кремнезема ar-SiOx.....	55
Короновский В., Вакула Ю. Визуализация магнитоэлектрических проявлений в эпитаксиальных структурах ФГ/ГГГ	59
Кулиш Н., Дмитренко О., Мельник О., Малый Е., Пинковская М., Тартачник В., Шлапацька В. Оценка дозового распределения в области пенумбры с использованием светодиодных структур	61
Лавренко К., Коломиец И., Савенков С., Оберемок Е., Климов А. Эволюция состояния поляризации в продольно неоднородной среде с линейным двулучепреломлением	64
Лавренко М., Коломиец И., Савенков С., Оберемок Е. Сравнение решений обратной задачи поляриметрии при последовательном и одновременном действии механизмов анизотропии сред с эллиптическим двулучепреломлением	67
Левитский С. Можно ли обнаружить какие-либо следы сигнала до его начала?	70

СОДЕРЖАНИЕ

Мартыш Е., Яценко В. Автономная стыковка с некооперированными космическими объектами.....	72
Мачулянский А., Бабыч Б. Энергосберегающие нанокompозитные покрытия на основе меди	74
Мельник А., Козаревич В., Собченко А. Синтез программируемых нанoeлектронных устройств	78
Мірошниченко С., Мотолыга А., Невгасимый А., Сенчуров С. Теоретическая оценка толщины реконструированного среза при цифровом томосинтезе.....	82
Находкин Н., Кулиш Н., Литвин П., Родионова Т., Сутягина А. Специальные стыки границ зерен в нанокремниевых пленках с равноосной и волокнистой структурой.....	83
Оберемок Е. Структура матрицы Мюллера сред с ортогональными поляризациями собственных волн.....	86
Шиян И., Чуйко Г., Павленко А. Цифровая обработка медицинских изображений методами СКМ Maple	90
Яковенко В., Ковальчук А., Сорокин Ю., Пугач В., Охрименко А., Презадо Й., Мартинез-Ровира И., Илюхина А. Металлические микро-детекторы для визуализации и мониторинга профиля пучка в радиационной терапии.....	93
Иванисик А., Исаенко А., Коротков П., Понежа Г. Фазовая самомодуляция лазерного импульса в слоистых самофокусирующих средах	95
Костробий П., Маркович Б., Черноморец Ю., Токарчук Р., Токарчук М. Статистическая теория электродиффузионных процессов интеркаляции ионов в системе "электродит-электрод"	98

CONTENTS

Ananina O., Severina E. Hydrogen adsorption on the diamond C(111) surface: quantum-chemical simulation	8
Andrusenko V., Bekh I., Novak S. Simulation of neural networks by the analog calculating machine (ACM) (in the task of approximation of mathematical functions).....	10
Babich D, Kuzkova N., Popenko O., Yakunov A. Temperature measurement in microwave-irradiated systems using a temperature-dependent fluorescent dye.....	13
Bondar B., Kmetyuk Ya. Radiation safety aspects during 11-Mev medical cyclotron operation and maintenance	16
Gaidar V., Radchenko S., Sudakov O. Removal EMG and EOG artifacts from EEG signal.....	19
Gaidar O., Tryshyn V., Svarichevska O. Pavlenko I., Gaidar V. Environmental impact assessment of operation of positron emission tomography center	21
Glushenkov A., Hovorun D. Complete family of H-bonded 1-methylcytosine homoassociates: quantum-mechanical investigation	24
Gorbachenko V., Chereda I., Vrublevsky S., Kruchenko J., Lukyanetz O. Development and testing of the experimental system for registration of food reflex in rats.....	31
Goriachko A., Melnik P., Sydorov R., Popova O., Nakhodkin M. A novel nanopositioning system for scanning probe microscopy	33
Denbnovetskiy S., Melnyk I., Tuhai S. Analytical relations for calculation the energetic efficiency of triode glow discharge electron guns	37
Zabolotnyy M., Dovbeshko G., Solyanyk G., Kondratsky Y., Estrela-Lyopis V., Kulysh M., Dmytrenko O., Poluyan N., Busko T. Main problems of anticancer drugs' modification.....	42
Zavislyak I., Popov M., Movchan M. Passive ferrite resonator-based millimeter wave band components.....	44
Zaitsev S., Kiselev N., Rosenbush V., Velichko F., Kolesnikov N. Polarimetry of galilean satellites of jupiter near opposition in 2012–2014	49
Zelenyuk M., Susla A., Guyvan H., Slivka A., Kedyulich V. The influence of an external electric field and uniaxial pressure on the dielectric properties of TGS+Cu ²⁺ crystals.....	51
Ischenko O, Shkavro A., Braiman O., Nechepurenko D. Luminescent properties of organic dyes in polymers PEPK and PVE	53
Karlash A. PI and ftir spectroscopy of powdered silica aerogel ar-SIOX.....	55
Koronovskyy V., Vakyla Y. Visualization of magneto-electric displays in FG/GGG epitaxial structures	59
Kulish M., Dmytrenko O., Melnyk O., Malyy E., Pinkovska M., Tartachnyk V., Shlapatska V. Evaluation of dose distribution in penumbra area by using lidht emitting structures	61
Lavrenko K., Kolomiets I., Savenkov S., Oberemok Ye., Klimov A. The evolution of polarization state in longitudinally inhomogeneous medium with linear birefringence	64
Lavrenko M., Kolomiets I., Savenkov S., Oberemok Ye. Relation between the anisotropy parameters of multiplicative and homogeneous model for medium with elliptical birefringence	67
Levitsky S. On the possibility to detect any traces of signal before it's beginning.....	70

CONTENTS

Martysh E., Yatsenko V. Autonomous rendez-vous with uncooperative space objects	72
Machulansky A., Babych B. Selective energy-saving metal-dielectric nanocomposite coatings based on copper	74
Melnyk O., Kozarevych V., Sobchenko A. Synthesis of nanoelectronic devices with programmable structures	78
Miroshnichenko S., Motolyga O., Nevgasimii A., Senchurov S. Theoretical estimation of the reconstructed slice thickness in digital tomsynthesis	82
Nakhodkin N., Kulish N., Lytvyn P., Rodionova T., Sutyagina A. Special joints of grain boundaries in nanosilicon films with equiaxed and fibrous structures	83
Oberemok Ye. The Mueller matrix structure of media with orthogonal eigenpolarizations	86
Shyian I., Chuiko G., Pavlenko A. Digital processing of medical image with maple	90
Iakovenko V., Kovalchuk A., Sorokin I., Pugatch V., Okrimenko O., Prezado Y., Martinez-Rovira I., Iliukhina A. Metal micro-detectors for imaging and beam profile monitoring in radiation therapy	93
Ivanisik A., Isaienko O., Korotkov P., Ponezha G. Self-phase modulation of laser pulse in stratified self-focusing medium	95
Kostrobij P., Markovych B., Chernomorets Yu., Tokarchuk R., Tokarchuk M. Statistical theory of electro-diffusion processes of ions intercalation in "electrolyte – electrode" system	98

HYDROGEN ADSORPTION ON THE DIAMOND C(111) SURFACE: QUANTUM-CHEMICAL SIMULATION

The interaction of atomic hydrogen with the C(111) surface is the subject of the present work. Two configurations of the surface have been studied – C(111)-1x1:H and C(111)-2x1:H. The hydrogen adsorption on the diamond surface C(111) have been studied with the help of semi-empirical method of quantum-chemical modeling MNDO (MOPAC) and ab-initio Hartree-Fock method (PC GAMESS).

Keywords: diamond C(111) surface, hydrogen adsorption, cluster, computer simulation, MNDO (Modified Neglect of Differential Overlap), ab-initio method.

Introduction. Interest from both a fundamental and an applicative perspective has stimulated much research in diamonds interfaces and adsorption of different atoms and radicals on diamond surfaces. In particular, considerable attention has been directed at the study of the hydrogen adsorption on C surfaces. Hydrogen terminated diamond surfaces exhibit unique properties: negative electron affinity and high p-type surface conductivity under appropriate conditions [2]. Also the interaction of atomic hydrogen with the C(111) surface have been studied due to their importance in the CVD process [8]. H atoms not only can preferentially etch away graphite component and assure the smoothness of diamond surfaces, they can also terminate the surface C atoms to maintain the sp^3 hybridization so that graphite formation can be prevented [9]. Consequently, the interaction between H and diamond surfaces becomes an important issue for both diamond technology and surface science study [3, 4].

Mitsuda et al. [5] studied the effects of addition atomic hydrogen to the reconstructed C(111)-2x1 surface from both LEED and second harmonic generation (SHG) techniques. They discovered that the transition $(2x1) \rightarrow (1x1)$ to occur at approximately 5% of the saturation hydrogen coverage. Chin et al. [1] confirmed this result and found that C-H stretch mode for the begins to transforms $(2x1)$ to $(1x1)$ structure was slightly up-shifted in energy as compared to the fully hydrogenated C(111)-1x1:H surface. It means, that this surface structure is some different that the fully relaxed or fully hydrogenated surface. That a small fraction of a monolayer of chemisorbed hydrogen has implications for impurity stabilized surface diamond structures.

Many theoretical and experimental works have been performed in the reaction of H with diamond surfaces by using various methods. But for today the interaction of H atoms with surfaces C(111) is the unknown mechanism of the $(2x1)$ to $(1x1)$ transformation induced by hydrogen adsorption on a diamond surface, along with the structure of an intermediate metastable surface reconstruction that appears in the initial stages of hydrogen absorption on the $(2x1)$ structure.

Results and discussion. Investigations of diamond surfaces C(111) were performed on the diamond nanoclusters C123H79, which used as a models for C(111)-2x1:H and C(111)-1x1:H surface simulation (fig. 1). The broken bonds of the carbon atoms at the edge of the clusters (i.e., the bonds leading into the bulk of the diamond crystal) were saturated with hydrogen atoms (the univalent pseudoatoms model). In our calculations, all carbon atoms were freely optimized, and the hydrogen atoms (the so called hydrogen bowl) were fixed.

The calculations were performed using the semiempirical quantum-chemical techniques contained in the MOPAC software package and the Hartree-Fock (ab initio) methods of the PC GAMESS package. The Hartree-Fock method was used as a basis for solving the Roothaan

equations. In determining the optimized geometry of the system corresponding to the minimum energy, the method of Davidson-Fletcher-Powell was applied. In the system stationary points, the gradients on the atoms did not exceed 3 kcal/Å. We calculated the energy of the clusters, the atomic bond orders, the population of atomic orbitals and the molecular, localized orbitals.

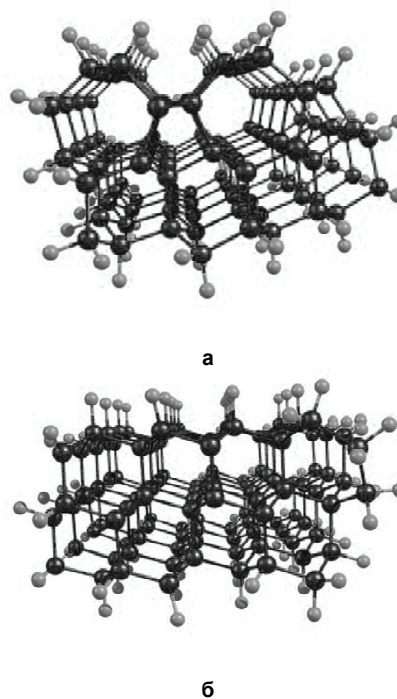


Fig. 1. Clusters, modeling the hydrogen terminated C(111) surfaces:
a) the Pandey-chain reconstructed C(111)-2x1:H surface,
b) the "ideal" structure C(111)-1x1:H

These clusters reproduce reconstructed diamond C(111)-2x1 surface with the chain reconstruction as proposed by Pandey [6] and the ideal C(111)-1x1 surface respectively. We constructed cluster to model ideal C(111)-1x1 the following way: all of the carbon atoms in these clusters are positioned at the diamond lattice sites, i.e., at distances of 1.54 Å from one to another. The angle between the C-C bonds amounts to 109.47°. Then, from the "ideal" structure C(111) was obtained the cluster with the reconstructed geometry 2x1.

The most probable reconstruction of the C(111) surface (occurring at higher temperatures) is the 2x1 – π - bonded Pandey chain structure. The exposed C atoms form upper and lower zig-zag chains that run in parallel across the surface. Surface structure composed of a topmost layer of carbon chains with mostly sp^2 character and a next layer of carbon chains with mostly sp^3 character. We find that this

structure C(111)-2x1 is highly asymmetric: on the first layer a relatively strong buckling $\Delta z=0.17 \text{ \AA}$ is present [7]. The atoms belonging to the top chains is undimerized.

Search for the stable configurations of a monohydride form for the diamond surface (111) leads to two forms differing in geometry and electronic state: C(111)-2x1:H and C(111)-1x1:H. In case of C(111)-2x1:H the total cluster energy is by 15.12 eV higher than in case of C(111)-1x1:H. The unreconstructed C(111)-1x1:H surface was found to be lower in energy than the Pandey-chain reconstructed C(111)-2x1:H surface by 0.84 eV per surface C atom.

The analysis of molecular orbital compositions were carried out. Properties of the possible of two forms of hydrogen terminated surfaces on a diamond C(111) surface with different geometry, electronic properties and energy of formation is presented in the table 1.

Table 1

Geometric, electronic and energy parameters of the C132H79 diamond surface C(111) cluster (Fig1. a-b)

cluster	C-C, Å	C-H, Å	q (Csuf), e
C(111)-2x1:H	1.55	1.086	1 layer: -0.054 ± -0.056 2 layer: +0.008 ± +0.016
C(111)-1x1:H	1.55	1.086	1 layer: -0.044 ± -0.049 2 layer: +0.016 ± +0.02
cluster	q (H), e	Ea, eV	Eb, eV
C(111)-2x1:H	+0.044 ± +0.055	1 position- 0.2 2 position- 0.45	1 position- 3.4 2 position- 3.1
C(111)-1x1:H	+0.041 ± +0.042	0.16	3.7

Ea (eV) – the activation energy of the hydrogen atoms adsorption on the clean surface C(111);

Eb (eV) – the binding energy of the hydrogen atoms on the clean surface C(111).

Hydrogen saturation of dangling bonds on the surface C(111)-1x1 and C(111)-2x1 of carbon atoms leads to a redistribution of the surface charge: the charge on the hydrogen atoms is +0.4e±+0.5e and the charge on the carbon atoms is -0.4e±-0.5e (on the clean C(111)-2x1 surface $q(\text{C}) = -0.01 \pm -0.02e$, on the clean C(111)-1x1 surface $q(\text{C}) = -0.02 \pm -0.03e$).

Hydrogenated diamond (111)-1x1:H has an "ideal" structure, with the surface carbon atoms very near their bulk-terminated positions. The nearest-neighbor C-C distance is 1.55 Å. Each surface carbon is bonded to a single hydrogen atom, and the C-H bond vector is perpendicular to the surface plane. The main difference between the clean and monohydrogenated C(111)-2x1 structures is in the bond length along the chains, which is 1.46 Å and 1.56 Å respectively. Increasing the length of the bond between the carbon atoms in the chains on the monohydride surface leads respectively to a decrease of the distance between the rows of chains – 3.33 Å (was 4.37 Å). In both cases, there is a formation of the covalent carbon-hydrogen bonds, which have a length of 1.086 Å.

To simulate the hydrogen adsorption processes, the reaction coordinate calculation was used. The hydrogen atom is located at a distance of 6 Å from the surface and the gradual approach of the H atom to the surface of the cluster in the process of calculating the reaction coordinate.

On clean ideal surface diamond C(111) we are not found preferential adsorption centers. The activation energy of adsorption H on any atom of surface C(111)-1x1 is equals $E_a=0.16 \text{ eV}$, the binding energy C-H is $E_b=3.7 \text{ eV}$. Because the chain of the surface C(111)-1x2 have a slope, on the reconstructed surface adsorption mostly will

take place at the higher atoms (1 position): $E_a=0.2 \text{ eV}$, $E_b=3.4 \text{ eV}$ (fig.2).

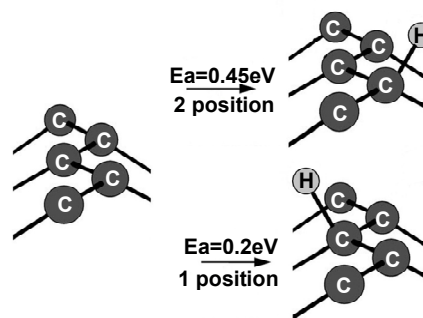


Fig. 2. The results of hydrogen adsorption on the clean diamond C(111)-2x1 surface

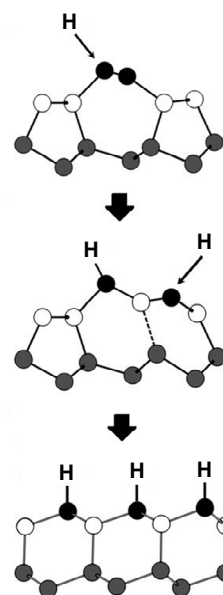


Fig. 3. The hypothetical mechanism transformation process from C(111)-2x1 to C(111)-1x1:H

Black color shows atoms of the first layer, white – the second layer, gray – the third layer.

Conclusion. Hydrogenation of the surface leads to formation two configurations: a metastable (2x1) configuration with Pandey chains and a stable (1x1) configuration that is very close to bulk-terminated geometry. For both configurations bond length C-C is about equal to the interatomic distance in the bulk. Hydrogen terminates the surface C atoms to maintain the sp^3 hybridization. We find that the most probable monohydride form for the surface diamond (111) is C(111)-1x1:H. So, in the case of the hydrogen termination of the diamond (111) surface, the surface dangling bonds stabilizes without any noticeable relaxation of the carbon atoms, in contrast to the C(100) surface.

We proposed the mechanism of the (2x1) to (1x1) surface transformation induced by hydrogen adsorption on a diamond surface (fig. 3). Most probably adsorption of the hydrogen atoms on the reconstructed surface of diamond with (111)-2x1 will occur selectively, mainly in the upper atoms of the surface chains.

REFERENCE:

1. Chin R. P. Vibrational spectra of hydrogen on diamond C(111)-(1x1) / R. P. Chin, J. Y. Huang, Y. R. Shen et al. // Phys. Rev. B, 1992. – Vol. 45, № 3. – P. 1552–1524.

2. Garrido J. A. pH sensors based on hydrogenated diamond surfaces / J. A. Garrido, A. Härtl, S. Kuch et al. // Appl. Phys. Lett., 2005. – № 86. – P. 073504(1)–073504(3).

3. Nichols B. M. Photochemical functionalization of hydrogen-terminated diamond surfaces: a structural and mechanistic study / B. M. Nichols, J. E. Butler, J. N. Russell and R. J. Hamers // J. Phys. Chem., 2005. – Vol. 109, № 44. – P. 20938–20947.

4. Marsili M. Tight-binding calculations of quasiparticle wave functions for C(111)2x1 / M. Marsili, O. Pulci, F. Bechstedt and R. D. Sole // Phys. Rev. B., 2005. – Vol. 72. – P. 115415(1)–115415(5).

5. Mitsuda Y. Interactions of deuterium and hydrocarbon species with the diamond C(111) surface. / Y. Mitsuda, T. Yamada, T. J. Chuang et al. // Surf. Sci. – Vol. 257, Iss. 1–3. – P. L633–L641.

6. Pandey K. C. New pi-Bonded Chain Model for Si(111)-2x1 Surface / K. C. Pandey // Phys. Rev. Lett., 1981. – Vol. 47, № 26. – P. 1913–1917.

7. Severina E. Diamond C(111) surface reconstruction / E. Severina // Sci. Lett. of Acad. Soc. of Michal Baludansky, 2014. – Vol. 2, № 1. – P. 122–125.

8. Su C. Hydrogen chemisorption and thermal desorption on the diamond C(111) surface / C. Su and K.-J. Song, Y. L. Wang, et al. // J. Chem. Phys., 1997. – Vol. 107, № 18. – P. 7543–7558.

9. Zhigilei L. V. Intermediate metastable structure of the C(111)/(1x1)H-C(111)/(2x1) surface phase transition / L. V. Zhigilei, D. Srivastava and B. J. Garrison // Phys. Rev. B., 1997. – Vol. 55. – № 3. – P. 1838–1843.

Submitted on 22.10.14

Ананьїна О., канд. фіз.-мат. наук,

Северина О., асп., каф. фізики напівпровідників, Фізичний факультет
Запорізький національний університет

АДСОРБЦІЯ ВОДНЮ НА ПОВЕРХНІ АЛМАЗУ C(111): КВАНТОВО-ХІМІЧНЕ МОДЕЛЮВАННЯ

Процеси взаємодії атомарного водню з поверхнею C(111) є об'єктом даного дослідження. Було розглянуто дві конфігурації поверхні – C(111)-1x1:H and C(111)-2x1:H. Вивчення адсорбції водню на поверхні алмазу C(111) здійснювалось за допомогою напівемпіричного методу квантово-хімічного моделювання MNDO (MOPAC) і ab-initio методу Хартри-Фока (PC GAMESS).

Ключові слова: поверхня алмазу C(111), адсорбція водню, кластер, квантово-хімічне моделювання, МНДП (модифіковане нехтування диференціальним перекриттям), ab-initio.

Ананьїна О., канд. физ.-мат. наук,

Северина Е., асп., каф. физики полупроводников, Физический факультет
Запорожский национальный университет

АДСОРБЦІЯ ВОДОРОДА НА ПОВЕРХНОСТІ АЛМАЗА C(111): КВАНТОВО-ХІМІЧЕСЬКЕ МОДЕЛЮВАННЯ

Процеси взаємодії атомарного водню з поверхнею C(111) є об'єктом даного дослідження. Було розглянуто дві конфігурації поверхні – C(111)-1x1:H and C(111)-2x1:H. Вивчення адсорбції водню на поверхні алмазу C(111) здійснювалось за допомогою напівемпіричного методу квантово-хімічного моделювання MNDO (MOPAC) і ab-initio методу Хартри-Фока (PC GAMESS).

Ключевые слова: поверхность алмаза C(111), адсорбция водорода, кластер, квантово-химическое моделирование, МПДП (модифицированное пренебрежение дифференциальным перекрытием), ab-initio.

UDC 621; 621.371.39; 621.382.21.3; 321.387

V. Andrusenko, stud.,
I. Bekh, PhD, S. Novak, stud.
Faculty of radiophysics, electronics and computer systems,
Taras Shevchenko National University of Kyiv

SIMULATION OF NEURAL NETWORKS BY THE ANALOG CALCULATING MACHINE (ACM) (IN THE TASK OF APPROXIMATION OF MATHEMATICAL FUNCTIONS)

By means of environment of design NI Multisim realized and investigated ACM which is modeling Rumelhart's perceptron that is presently most investigational. Using ACM was obtained approximated mathematical function $\sin(x)$. Analysis of approximation showed that ACM meets implemented to the task and meet the stated accuracy of the simulation function.

Keywords: neural network, Rumelhart's perceptron, approximation of function, analog calculating machine.

Introduction. For a long time people tried to explain, as functions their own thinking. Neurobiologists and neuroanatomists attained considerable progress in the study of cerebration. Prospecting a structure and functions of the nervous system of human, they much understood in the "wiring" of brain, but small learned about his functioning. In the process of researches it turned out, that a brain had stunning complexity: billion of neurons, each of that is connected with hundreds or thousands others, form the system that far exceeds our brave dreams about super computers. A concept "artificial neural network" was first entered in 40's years of last century [6]. On logical level an artificial neural network designs activity of the nervous system of human and animals. The formal neurons united in network can decide tasks that traditionally behave to the area of "human activity" (for example recognition of patterns and even making decision on the basis of incomplete information). Especially interesting is ability of neural networks to study and memorize information that reminds human's intellection. Therefore in early works of research of neural networks a term "artificial intelligence" was often used.

Short time ago interest to artificial neural networks quickly grew. They took up specialists on such distant areas, as a technical constructing [8], physiology [7] and psychology [1]. This interest is clear: an artificial neural network, essentially, is the model of the natural nervous system, that is why creation and study of such networks allows to know much about functioning of the natural systems. Other important property of neural network is reliability [3]: even if a few elements will work wrong or break ranks, however, a network will be able to give out correct results, but with less exactness.

Some types of neural networks have the ability to generate an abstract image on the basis of a few input signals [5]. For example, it is possible to teach a network, giving the sequence of the twisted images of letter of "A". After studies a network will be able to generate the letter of "A" without distortions, namely the network can generate it that she never given.

Neural networks can execute the enormous amount of various tasks most widespread from that is: nonlinear approximation of multidimensional functions, prognostication of development of processes that depend on many the

variables in time, classification of input images, recognition of images, search of associations, clench of data and other.

In this work one of these tasks is examined – approximation of multidimensional mathematical functions. This task is very interesting from the point of view of analysis of experimental data and search of decisions, that it is impossible, or very difficult to find analytical methods

Tools of analysis and physical model. A biological neuron consists of body of cage, dendrites, and long axon. Dendrites is input fibres of neuron, they get information from other neurons. The receipt of signal on a dendrite excites or inhibits a neuron proportionally to amplitude of signal. Every dendrite influences on a cage with different force, in the process of studies this force changes constantly. The amount of dendrites can be varied in very wide limits - from units to a few hundreds. In totality all dendrites set the state of neuron that is passed through the axon to the next neurons.

These properties were fixed in basis of mathematical model of neuron. A mathematical neuron is an adder, the unique exit of that is determined through his inputs and matrix of weighting coefficients as follows: $y = f(u)$, where

$$u = \sum_{i=1}^n w_i \cdot x_i + w_0 \cdot x_0$$

Here x_i and w_i - accordingly signals on the inputs of neuron and weighting coefficients of entrance, the function of u is called the state of neuron, and $f(u)$ – a transmission (activating) function. Inputs signals can be discrete and analog. The additional entrance of x_0 and corresponding to it weicher coefficient of w_0 are used for creation of change. Type of activating function of neuron of $y = f(u)$, as be shown below, can be arbitrary (but integrated with the square) and elected in accordance with certain technical requirements, or certain task [2].

A network consists of arbitrary amount of layers of neurons. The neurons of every layer combine with neurons previous and next layers, following on principle that each with each (Fig. 1). The youngest layer is named sensory, or entrance, internal layers are called hidden, or associative, last – the outlet or effective. An amount of neurons in every layer can be arbitrary, and elected in accordance with a task.

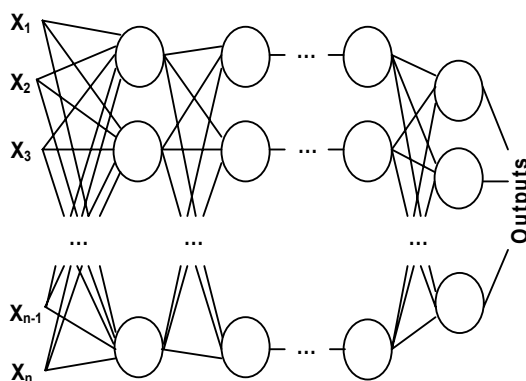


Fig. 1. Internal connections in the neural network

Mathematical neurons can unite by different way, forming the neural networks of different architecture. As a rule, neurons collect in separate layers, where all neurons are equal in rights and layers combine among ourselves, forming a neural network.

The multi-layered network of direct distribution is used in our work – multi-layered Rumelhart's perceptron, which is the most researched and has an easy learning algorithm [4].

Work of select network is described thereby. Inputs data come on the first (entrance) layer. For every neuron of

entrance layer the sum of products of signal on entrances (sinaps) and corresponding weight coefficients. Outputs signals of neurons of the first layer calculated according to an activating function.

The inputs signals of neurons of the first layer are used as entrance signals for a next layer, the status of neurons calculate at a next layer. This operation is repeating while the last layer is not attained. Signals of neurons in output layer are outputs signals. This operation can be described by expression:

$$f(x) = F \left(\underbrace{\sum_{i_N} w_{i_N j_N} \dots \sum_{i_2} w_{i_2 j_2}}_{\text{шар}_2} \cdot \underbrace{F \left(\sum_{i_1} w_{i_1 j_1} - \theta_{j_1} \right)}_{\text{шар}_1} - \theta_{j_2} \dots \theta_{j_N} \right)$$

For today simulation of neural networks is conducted mainly on digital computing machines. It has plenty of advantages: emergency universality, big exactness (and thus predictability of algorithm), stability and many other. But per all these advantages would to pay a very small speed and productivity.

On the other hand modern operational amplifiers can work with frequency a few gigahertz. Maximal frequency of calculation of function by an operational amplifier is in several times less, than his marginal frequency. If to increase the amount of connections of model neuron, say, in two times, productivity of digital model will decrease approximately in the same number of times, and the productivity of analog model will not almost change (although a scheme considerably will become complicated). In addition a price per processor is far more than on the analog scheme of the near productivity.

Thus development of analog machines for modeling of neural networks is a perspective task.

From the successfully selected analog model of neuron very much depends successful implementation it in the real scheme of ACM for modeling of neural network. The technical requirement for the analog model of neuron is ranges of input and output voltages and exactness of approximation. The range of output voltages of analog model of neuron is choosing within the limits of $\pm 15B$. Necessary exactness of accordance of analog model of neuron to the mathematical model must be anymore than desirable exactness of approximation, namely a nearly 0.01%. From the latter follows, that an analog neuron must have mechanisms of exact correction of error.

Going out from the architecture of neural network that was selected by us, ACM for her modeling must consist of multipliers, adder and nonlinear element.

Important part of ACM is a nonlinear element. At the time of creation of the real scheme it is necessary to take into account some reasonings:

a) the transmission function of nonlinear element must squeeze, namely at presence a large argument she must become a line. It follows out from the real limitation of range of output voltages of operational amplifier on the base of whose created nonlinear element. In other time, behavior of function at large arguments will become unforeseeable;

б) a transmission function of nonlinear element must be symmetric relatively to beginning of coordinates (odd). Otherwise it will not be succeeded to use all dynamic range of operational amplifier and scheme will become very sensitive to zero drift of operational amplifier;

в) it is desirable, that a transmission function of nonlinear element was the easy, and her derivative was

easily expressed through the value of function, that will considerably simplify the algorithm of studies.

These criteria befit for a hyperbolic tangent. Analog computation of hyperbolic tangent is implemented simply enough, about that testifies curve on Fig. 2.

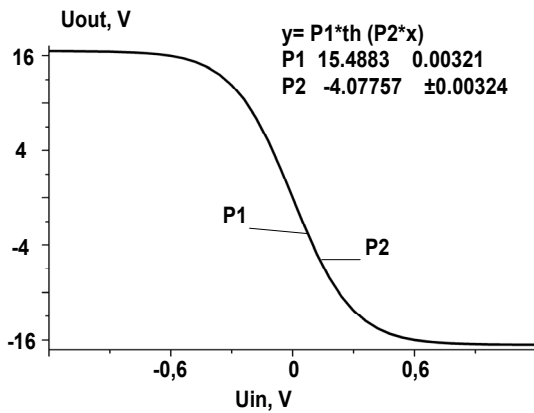


Fig. 2. Graphic of function of hyperbolic tangent, got as a result of analog calculation

A multiplier must have large exactness, maximum frequency and possibility of work with a bipolar signal. And temperature drift of parameters must be enough small. Parabolic multipliers (on quadrants) are satisfying these requirements.

Principle of work of such multipliers is based on a mathematical operation:

$$X \cdot Y = \frac{(X+Y)^2 - (X-Y)^2}{4},$$

what is executed by means of diode functional converters that work in the mode of piecewise-linear approximation. Creation of similar multiplier on the base of operational amplifiers, technically enough not simple task. Therefore, for realization of ACM was selected the prepared multiplier in integral implementation AD734AN.

Any analog scheme has certain admittance of parameters and AD734AN of no exception. Therefore, to assert possibility of creation of the real analog neural network it is necessary to have the opportunity to eliminate the errors caused by variation of parameters of elements. To compensate errors, enough to give the proper tension with an opposite sign on the corresponding entrances of microcircuit of multiplier. The change of result of approximation advantageously compensated in the scheme of adder, at once for all multipliers.

In the process of studies ACM was turned out, that the parameters of analog model of separate neuron were taken into account only in the process of studies. It means that a necessity to create artificial neurons with exact selection of parameters is not. Mainly, that parameters of neuron were measured with high exactness. From a neuron require only the independence of parameters from surrounding terms. It gives large advantage by comparison to others schemes of analog computing devices.

The software environment of NI Multisim was selected for the modeling of work of separate blocks and whole ACM.

Results and discussions. Demonstration of possibilities of the created analog machine for modeling of Rumelhart's perceptron was performed by approximating mathematical functions $\sin(x)$. For this purpose took the schedule of the specified functions in a Taylor series:

$$\sin(x) = x - \frac{x^3}{3!} + \frac{x^5}{5!} - \frac{x^7}{7!} + \dots + (-1)^n \frac{x^{2n+1}}{(2n+1)!}.$$

In an order to minimize the scheme of ACM, it is needed to define the amount of members of Taylor series that will provide necessary exactness of approximation. This parameter is determined by means of relative error.

Comparative analysis of graphics of function of $\sin(x)$ the obtained analytically and by means of Taylor series (Fig. 3) showed that for providing of the set exactness of approximation is enough to tear off a series on 4 elements.

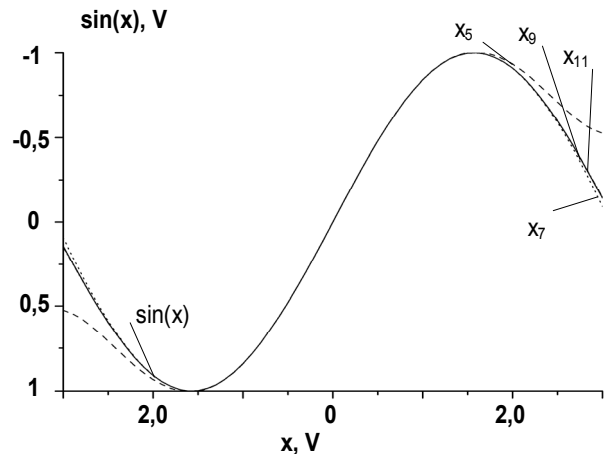


Fig. 3. Graphic of function of $\sin(x)$, got analytically and by means of Taylor series

As a result a polynomial for approximation will have a kind:

$$\sin(x) = x - \frac{x^3}{3!} + \frac{x^5}{5!} - \frac{x^7}{7!}.$$

Graphics of function of $\sin(x)$, that obtained analytically and by means of created ACM is brought around to Fig. 4. The analysis of the obtained results shows that the error of approximation of function of $\sin(x)$ is 0.07% that satisfies the task in this work.

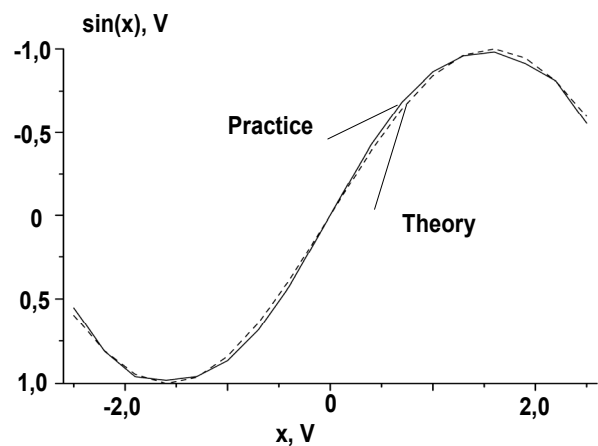


Fig. 4. Graphic of function of $\sin(x)$, got analytically and by means of created ACM

Conclusions. 1. ACM for modeling of neural network can be successfully used for a decision the tasks of approximation of continuous functions. There are no theoretical limits on complication of task that an artificial neural network can execute.

2. By comparison to the ordinary methods of approximation of ACM for modeling of neural network have a row of advantages:

- it is universality: they consist of identical elements, united by a simple law (every neuron of previous layer with each following);

▪ it is an universal algorithm of studies, that does not depend on the type of function that is approximated, amount of arguments and results of function;

▪ they consist with the adders collected on analog an component, that is increasing a fast-acting and exactness of implementation of operations;

▪ they give the wide field for the choice of parameters component (neurons).

3. ACM for modeling of neural network can be easily created on a modern element base.

REFERENCE:

1. Goldberg J. A. Computational physiology of the neural networks of the primate globus pallidus: function and dysfunction / J. A. Goldberg, H. Bergman // *Neuroscience*, 15 December 2011. – Vol. 198. – P. 171–192.

2. Gorban A. N. Generalized approximation theorem and computational capabilities of neural networks / A. N. Gorban // *Siberian Journal of Computational Mathematics*, 1998.

3. Hosni A. E. Reliability analysis of structures using neural network method / A. E. Hosni, E. Mesbahi, Y. Pu // *Probabilistic Engineering Mechanics*, January 2006. – Vol. 21, Iss. 1. – P. 44–53.

4. Многослойный перцептрон Румельхарта [Электронный ресурс]. – Режим доступа: http://ru.wikipedia.org/wiki/Многослойный_перцептрон_Румельхарта. Дата звернення: 25.03.2014.

5. Kusetogullari Huseyin. Meta-heuristic algorithms for optimized network flow wavelet-based image coding / Huseyin Kusetogullari, S. L. Mark, Kole Burak, L. H. Evor // *Applied Soft Computing*, January 2014. – Vol. 14, Part C. – P. 536–553.

6. McCulloch W. Logical Calculus of the Ideas Imminent in Nervous Activity / W. McCulloch, W. A. Pitts // *Bulletin of Mathematical Biophysics* 5, 1943. – № 33. – P. 115.

7. Rafiq M.Y. Neural network design for engineering applications / M. Y. Rafiq, G. Bugmann, D. J. Easterbrook // *Computers & Structures*, July 2001. – Vol. 79, Iss. 17. – P. 1541–1552.

8. Sarat Kumar Das. 10 – Artificial Neural Networks in Geotechnical Engineering: Modeling and Application Issues / Sarat Kumar Das // *Metaheuristics in Water, Geotechnical and Transport Engineering*, 2013. – P. 231–270.

Submitted on 11.06.14

Андрусенко В., студ., Бех І., канд. .физ.-мат. наук, доц., Новак С., студ. каф. радіотехніки та радіоелектронних систем, факультет радіофізики, електроніки та комп'ютерних систем, Київський національний університет імені Тараса Шевченка

АНАЛОГОВА ОБЧИСЛЮВАЛЬНА МАШИНА (АОМ) ДЛЯ МОДЕЛЮВАННЯ НЕЙРОННИХ МЕРЕЖ (ЗАДАЧІ АПРОКСИМАЦІЇ МАТЕМАТИЧНИХ ФУНКЦІЙ)

За допомогою середовища моделювання NI Multisim реалізовано і досліджено аналогову обчислювальну машину, що моделює перцептрон Румельхарта, що на теперішній час є найбільш дослідженим. За допомогою отриманої АОМ було апроксимовано математичну функцію $\sin(x)$. Аналіз результатів апроксимації показав, що реалізована АОМ задовольняє поставлені задачі і відповідає встановленій точності моделювання функції.

Ключові слова: нейронна мережа, перцептрон Румельхарта, апроксимація функції, аналогова обчислювальна машина.

Андрусенко В., студ., Бех І., канд. физ.-мат. наук, доц., Новак С., студ. каф. радиотехники и радиоэлектронных систем, факультет радиофизики, электроники та компьютерных систем, Киевский национальный университет имени Тараса Шевченко

АНАЛОГОВАЯ ВЫЧИСЛИТЕЛЬНАЯ МАШИНА (АВМ) ДЛЯ МОДЕЛИРОВАНИЯ НЕЙРОННЫХ СЕТЕЙ (ЗАДАЧИ АПРОКСИМАЦИИ МАТЕМАТИЧЕСКИХ ФУНКЦИЙ)

С помощью среды моделирования NI Multisim реализовано и исследовано аналоговую вычислительную машину, моделирующую перцептрон Румельхарта, который, в настоящее время, является наиболее исследованным. С помощью полученной АВМ была апроксимирована математическая функция $\sin(x)$. Анализ результатов аппроксимации показал, что реализованная АВМ удовлетворяет поставленной задаче и соответствует установленной точности моделирования функции.

Ключевые слова: нейронная сеть, перцептрон Румельхарта, аппроксимация функции, аналоговая вычислительная машина.

UDC 535.3

D. Babich, stud., N. Kuzkova, post grad. stud., O. Popenko, stud., A. Yakunov, Ph.D.

Taras Shevchenko National University of Kyiv, Physics Department

TEMPERATURE MEASUREMENT IN MICROWAVE-IRRADIATED SYSTEMS USING A TEMPERATURE-DEPENDENT FLUORESCENT DYE

Temperature sensitivity of the fluorescence intensity of the organic dyes solutions used for non-contact measurement of the electromagnetic millimeter wave absorption in water. By using two different dyes with opposite temperature effects, it was defined local temperature increase in the capillary that is placed inside a rectangular waveguide in which millimeter waves propagate. The application of this non-contact temperature sensing is a simple and novel method to detect temperature change in small biological objects.

Keywords: millimeter waves, non-contact temperature sensing, fluorescence, organic dyes, water, biomedical applications

Introduction Biological effects of electromagnetic millimeter waves were observed in many experiments on various biological objects, starting from the bacteria to the whole human body as well as model systems in general [1]. Repeatedly noted that the nature of the microwaves on biological objects is different from the conventional thermal effect of electromagnetic waves of the other bands, and the physical nature of this phenomenon is still unclear.

One of the main problems, which complicates the construction of an adequate physical model, is the uncertainty of "non-thermal effect" definition, and the fact that in different experiments the power of millimeter waves, which have biological effects, differ by orders of magnitude [1]. For a correct measurement of absorbed radiation power and detecting possible heating as a result of

irradiation, it is necessary to use special sensors, which can react to the absorption of millimeter waves in systems, close by their parameters to biological tissues.

It is considered that the use of low power (with output power up to 20 MW) millimeter waves generators does not result to significant heating of the irradiated matter. Calculations [4] provide an increase of temperature to 1°C for different patterns of exposure, which should not cause essential biological effects. However, direct measurement of the temperature change in the area of irradiation is a challenging technical problem. High-sensitivity temperature sensors (thermocouples, thermistors, etc.) making perturbations in the investigated samples, affect the local temperature and heat transfer characteristics in a given place. Although less accurate,

© Babich D., Kuzkova N., Popenko O., Yakunov A., 2014

optical methods are more convenient for registration of temperature changes in small volumes [3].

The water in the millimeter wave range is characterized by a considerable absorption of electromagnetic waves. In particular, at a frequency of 50 GHz, corresponding to wavelengths in vacuum of 6 mm, the absorption coefficient is equal to 5.1 mm⁻¹ [4]. Accordingly, the spatial temperature distribution in the irradiated samples containing water is very inhomogeneous. Electromagnetic millimeter waves heat the substances containing water in a thin surface layer with high temperature gradient, the numerical value of which can be estimated only by indirect methods. Therefore, existing methods for irradiation of biological objects are imperfect and metrological control tools are not reliable.

To determine temperature changes in water caused by the millimeter wave absorption we used an optical non-contact method, which is based on the existence of the fluorescence intensity dependence of temperature of organic dyes. It was measured the local temperature rise in the capillary, placed inside a rectangular waveguide, in which millimeter waves propagate. We have chosen two dyes with opposite temperature effects: Rhodamine 6G (R6G) and Rhodamine C (RC).

Methodology and experimental measurements

Calibration of the fluorescence intensity of organic dyes aqueous solutions on temperature were carried out by means of diffraction spectrometer. Semiconductor laser emission with 406 nm wavelength and 60 mW output power was used as an excitation source. The samples were prepared from standard distilled water for medical purpose. The concentration of dyes (~ 0.4 g/liter) was chosen from the condition of maximum temperature sensitivity and temperature coefficients of approximate equality [3].

It was used a straight-through scheme for illumination and viewing [2]. The glass cuvette (3 mm pass length) with the dye solution was placed inside a large glass rectangular cell with water, which served as a water bath. Water temperature was maintained to within 0.2°.

The fluorescence spectra were measured at temperatures from 20 °C to 40 °C, over each 5 °C (Fig.1). The intensity of fluorescence was normalized by the initial value, corresponded to the temperature of 20 °C (Fig.2).

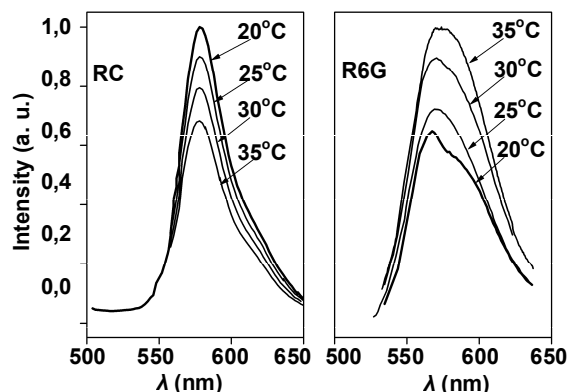


Fig.1. Fluorescence spectrum of Rhodamine 6G (R6G) and Rhodamine C (RC) at 5 °C intervals from 20 to 35 °C

Established, that in most cases, the temperature rise is making destructive contribution to the fluorescence yield [3]. With the growth of temperature, increases the frequency and energy of molecules collisions in solution as well as the amplitude of internal molecular vibrations, leading to an increase in non-radiative relaxation of the excited levels, and thus fluorescence quenching. Along with the temperature quenching of the dye solution are

possible mechanisms that increase the overall yield of fluorescence with increasing temperature [3]. In particular, some organic molecules in aqueous solution tend to form associated complexes: dimers, trimers, etc., where fluorescence quantum yield is much lower than in the individual molecules. At sufficiently high concentrations, the fluorescence spectrum is formed as a superposition of the spectra of individual molecules and their associates. Some associates divided into separate molecules with increasing temperature that is accompanied by a relative increase in fluorescence intensity.

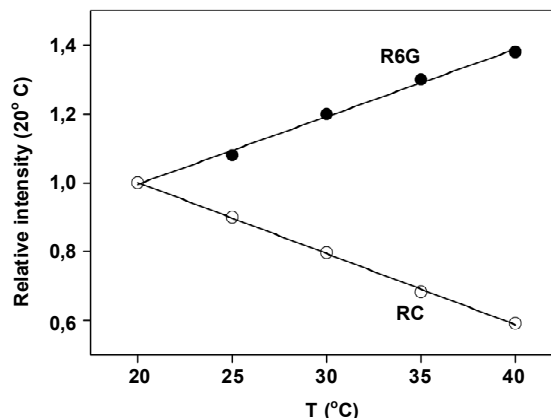


Fig.2. Temperature dependence of the relative fluorescence intensity of R6G and RC

Fig. 2 shows that the fluorescence temperature dependence of the RC solution corresponding to the first scenario, R6G – to the second, and in the range 20 ÷ 40°C intensities approximated by a linear function: $I(T)/I(20^{\circ}\text{C}) = a + bT$, where b – temperature sensitivity coefficient. For given concentrations of solutions this parameter is equal $b_{R6G} = 0.019^{\circ}\text{C}^{-1}$ and $b_{RC} = -0.021^{\circ}\text{C}^{-1}$.

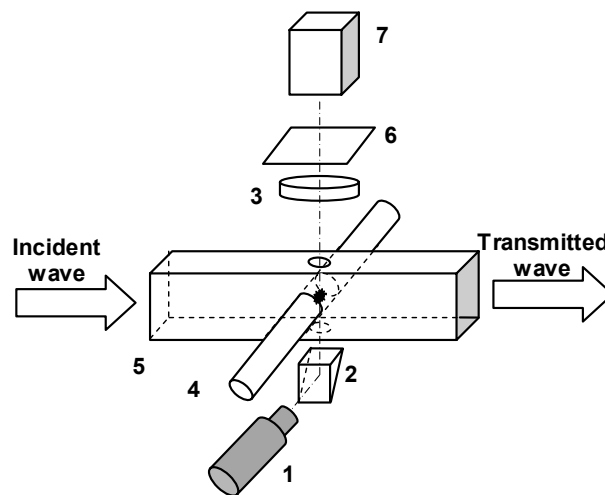


Fig.3. The measuring module is composed of laser (1), prism (2), focusing lens (3), glass capillary with a dye solution (4), waveguide (5), orange filter (6) and photo-detector (7)

Millimeter wave radiation from high frequency signal generator through polarizing attenuator was applied to the measuring module. Attenuator is included to prevent reflected power from damaging the amplifier. The measuring module (Fig. 3) consists of the segment of rectangular waveguide with a cross section 7.2 x 3.4 mm,

inside which through the middle was inserted a glass capillary with an inner diameter of 0.5 mm. Focused laser beam excites fluorescence in filled capillary of dye solution.

For capillary with water in a rectangular waveguide area of maximum absorption of the electromagnetic millimeter wave corresponding to antinodes of electrical components and is concentrated in the central part of $\Delta x \sim 1$ mm [2]. Fluorescence signal from the central section was removed through a round hole made in the middle of the narrow waveguide wall opposite the capillary. The light stream focused by lens and passed through an orange filter to a photo-detector.

By using a thermal detector, the incident and transmitted radiation power was measured. The difference was equal to the power, absorbed in the sample. Previously in the range of 40–50 GHz was measured frequency dependence of the capillary absorption of water. At a frequency of 47.5 GHz it was observed a pronounced resonance maximum, typical for rectangular waveguide with dielectric cylinder of small diameter [2].

Further experiments were carried out at the frequency of resonance. Power absorbed into the capillary with a solution governed by polarization attenuator with attenuation coefficients 0, 1, 2, 3, 4 dB, which corresponded to an absolute absorbed power value of 20 mW, 15.8 mW, 12.5 mW, 10 mW, 7.9 mW respectively.

Duration of registration signal $T \approx 40$ s was chosen from the condition significantly exceeded time of establishing of thermal equilibrium: $T \gg \tau$. Constant of relaxation was assessed by the expression $\tau \sim (\Delta x)^2 / D$, where D – coefficient of thermal conductivity of water, and for a given irradiation scheme was of the order of a few seconds.

Results and Analysis Fig. 4 shows the dynamics of R6G and PC fluorescence dyes for switched on and off microwave radiation with different capacities. The absorption of microwaves leads to fluorescence increasing for R6G solution and fluorescence quenching for RC. The gradual decrease in fluorescence intensity caused by photodestruction of organic dye molecules. By switching off temporarily laser emission, the initial level of fluorescence almost restored.

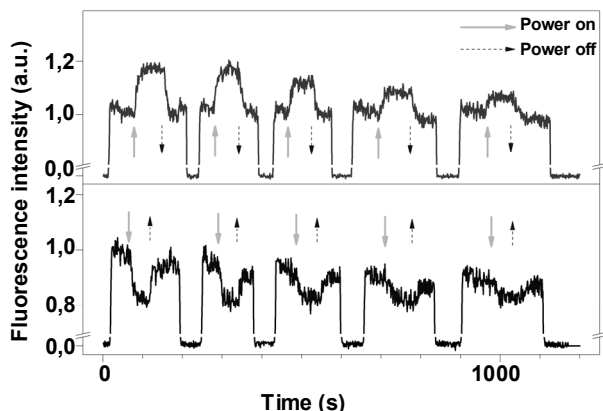


Fig. 4. Dynamics of the change in fluorescence intensity when millimeter wave radiation is turned on and turned off.

The voltage is switched off and the fluorescence returns to the base line before a different voltage is applied to the microheater. The two curves illustrate the repeatability of the fluorescence to achieve the same level for a given temperature

The dependence of the relative change in fluorescence intensity $|I - I_{20}| / I$ of the absorbed power in the capillary obtained from the experimental data (Fig. 5). In the first approximation it can be approximated by linear functions:

$$y = 0.15 - 0.023x \text{ for R6G; } y = 0.14 - 0.024x \text{ for RC}$$

Thus taking into account the calibration dependence (Fig. 2), it corresponds to a local temperature increase in the capillary absorbed at maximum power 20 mW: $\Delta T_1 = (7.7 \pm 0.4)^\circ\text{C}$ for R6G and $\Delta T_2 = (7.4 \pm 0.4)^\circ\text{C}$ for RC.

It could be seen that even a low-power microwave source, under certain conditions, cause significant heating of the sample, which can lead to significant biological effects. It should be noted that the special conditions of the experiment (placing the sample inside the waveguide, radiation at the resonant frequency) determine the maximum possible temperature response.

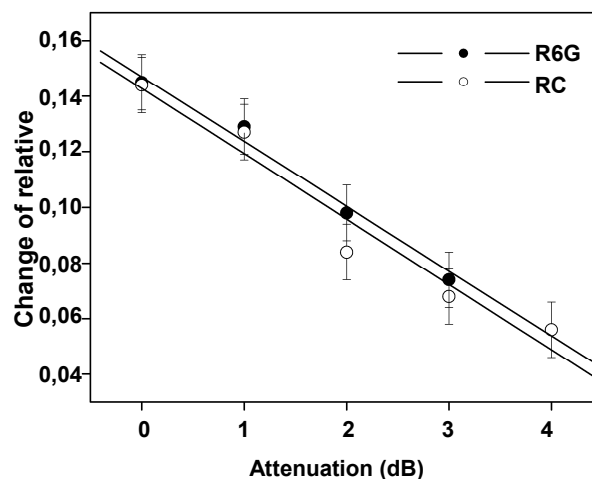


Fig. 5. Change of relative fluorescence intensity of the relaxation factor of attenuator

In most biophysical experiments with millimeter wave irradiation conditions of the samples, although not as severe, but carried out in the near zone of the waveguide. In the vicinity of the irradiated object there are standing waves that form parasitic resonances. The appearance of the local area temperature increase of a few degrees can cause thermal biological effects at low levels of total radiation power.

It is assumed [3,4] that with millimeter wave irradiation of dyes solutions possible additional non-thermal effect of millimeter waves on the spectral properties of solutions that is due to the change in the structure of water. During irradiation, pseudopolymer hydrogen bonding network undergoes deformation, rearrangement, and perhaps destruction. Restructuring of water under millimeter wave field causes structural changes in the molecular associates and promotes their decay.

In our study, we obtained the same value of the effective temperature for solutions with different scenarios of temperature behavior. This indicates on the absence of non-thermal effect of millimeter waves on water, at least in the conditions of sample irradiation inside the resonator at the resonant frequency.

Moreover, to the same conclusion leads comparison of dependency in Fig. 4. The equality of slope coefficients approximating lines indicates on the fact that probable non-thermal effect of millimeter waves on water under the given conditions can be neglected.

Conclusions. Optical non-contact method, which is based on the existence of the fluorescence intensity temperature dependence of the organic dyes used to determine changes in water temperature in the millimeter wave absorption.

Using two dyes with opposite effects, it was measured temperature heating an aqueous solution in the capillary, placed inside a rectangular waveguide.

Using even low-power sources of millimeter waves, the local increase in temperature of the sample can be several degrees. At the same time, the results indicate the absence of non-thermal effect of millimeter waves on the water.

The application of non-contact temperature sensing based on the temperature sensitivity of fluorescent dyes is a simple and novel method to detect temperature change in biological objects irradiated by millimeter waves.

REFERENCE:

1. Belyaev I. Nonthermal biological effects of microwaves: current knowledge, further perspective, and urgent needs / I. Belyaev // *Electromagnetic Biology and Medicine*, 2005. – Vol. 24. – P. 375–403.
2. Belyakov E.V. High-Q resonance in a waveguide with a highly absorbing dielectric / E.V. Belyakov // *Electronic Engineering. Ser.1., Microwave Electronics*, 1987. – Vol. 401, № 7. – P. 51–53.
3. Domnina N.A. Influence of microwave radiation on the association processes of rhodamine 6G molecules in aqueous solutions / N.A. Domnina,

A.F. Korolev, A.V. Potapov // *Journal of Applied Spectroscopy*, 2005. – Vol. 72, № 1. – P. 33–36.

4. Kiselev V.F. Influence of weak magnetic fields and UHF radiation on certain dielectric and optical properties of water and aqueous solutions / V.F. Kiselev, A.M. Saletskii, L.P. Semikhina // *Theoretical and Experimental Chemistry*, 1988. – Vol. 24, № 3. – P. 319–323.

5. Lou J. Fluorescence-based thermometry: principles and applications / J. Lou, M. Finegan, P. Mohsen // *Reviews in Analytical Chemistry*, 1991. – Vol. 18, № 4. – P. 235–284.

6. Parket C.A. Fluorescence Spectrometry / C.A. Parket, W.T. Rees // *A Review – Analyst*, 1962. – Vol. 87. – P. 83–111.

7. Robert K. Adair biophysical limitson athermal effects of RF and microwave radiation / K. Robert // *Bioelectromagnetics*, 2003. – Vol. 24. – P. 39–48.

8. Viznyuk S. A. The effect of temperature combustion luminescence in water solution of rhodamine 6G / S. A. Viznyuk, P. P. Pashinin // *JETP Letters*, 1988. – Vol. 47, № 4. – P. 190–193.

Submitted on 06.10.14

Бабіч Д., студ., Кузькова Н., асп., Попенко О., студ., Якунов А., канд. фіз.-мат. наук,
кафедра оптики, фізичний факультет
Київський національний університет імені Тараса Шевченка

ВИМІРЮВАННЯ ТЕМПЕРАТУРИ В СИТЕМІ ОПРОМІНЮВАНІЙ ЕЛЕКТРОМАГНІТНИМИ ХВИЛЯМИ МІЛІМЕТРОВОГО ДІАПАЗОНУ З ВИКОРИСТАННЯМ ТЕМПЕРАТУРОЗАЛЕЖНИХ ФЛУОРЕСЦЕНТНИХ ОРГАНІЧНИХ БАРВНИКІВ

Температурну чутливість флуоресценції розчинів органічних барвників використано для безконтактного вимірювання поглинання електромагнітних хвиль міліметрового діапазону у воді. За допомогою двох барвників з протилежними температурними ефектами визначено локальне підвищення температури в капілярі, розміщеному в середині прямокутного хвилеводу.

Застосування безконтактного температурного датчика є новим, простим методом визначення зміни температури малих біологічних об'єктів.

Ключові слова: міліметрові хвилі, безконтактне вимірювання температури, флуоресценція, органічні барвники, вода, біомедичне застосування.

Бабич Д., студ., Кузькова Н., асп., Попенко А., студ., Якунов А., канд. физ.-мат. наук,
кафедра оптики, физический факультет
Киевский национальный университет имени Тараса Шевченко

ИЗМЕРЕНИЯ ТЕМПЕРАТУРЫ В СИСТЕМЕ ОБЛУЧАЕМОЙ ЭЛЕКТРОМАГНИТНЫМИ ВОЛНАМИ МИЛЛИМЕТРОВОГО ДИАПАЗОНА С ИСПОЛЬЗОВАНИЕМ ТЕМПЕРАТУРОЗАВИСИМЫХ ФЛУОРЕСЦЕНТНЫХ ОРГАНИЧЕСКИХ КРАСИТЕЛЕЙ

Температурная чувствительность флуоресценции растворов органических красителей использована для бесконтактного измерения поглощения электромагнитных волн миллиметрового диапазона в воде. С помощью двух красителей с противоположными температурными эффектами определено локальное повышение температуры в капилляре, размещенном внутри прямоугольного волновода.

Применение бесконтактного температурного датчика является новым, простым методом определения изменения температуры малых биологических объектов.

Ключевые слова: миллиметровые волны, бесконтактное измерение температуры, флуоресценция, органические красители, вода, биомедицинское применение

UDC 539.1.03; 621.039.76

B. Bondar, Engineer-physicist, Clinical Hospital "Feofaniya",
Nuclear physics department, Taras Shevchenko National university of Kyiv
I. Mikhnytsky, Engineer-physicist, Ya. Kmetiyuk,
Head of All-Ukrainian center for radiosurgery, Clinical Hospital "Feofaniya"

RADIATION SAFETY ASPECTS DURING 11-MEV MEDICAL CYCLOTRON OPERATION AND MAINTENANCE

The paper brings up the question of radiation safety aspects dealing with exploitation of cyclotron Eclipse RD (Siemens), that is used for positron-emission tomography with fluorodeoxyglucose (^{18}F -FDG). The main sources of radiation exposure and the efficiency of a cyclotron shielding were analyzed. The dose rates were measured from the activated details and wastes and the effective dose to personnel, performing operation and technical support of a cyclotron was estimated with the help of electronic personnel dosimeters EPD Mk2+ and thermoluminescence dosimeters TLD Harshaw 100.

Keywords: positron-emission tomography, fluorodeoxyglucose, cyclotron, radiation safety, effective dose.

Introduction. Positron-emission tomography (PET) plays a crucial role in cancer diagnostics and can give information about the location of neoplasm and metastases, the intensity of metabolism and allows to estimate the efficiency of performed treatment [4]. PET requires radioactive tracers, and in this connection the low energy cyclotrons (up to 20 MeV) have found widespread applications in nuclear medicine for tracer production technologies [2]. The most commonly used PET radioisotopes (^{11}C , ^{13}N , ^{15}O , ^{18}F) can be produced through the proton induced reactions, such as (p,n) and (p,a). It is obvious, that the usage of cyclotrons leads to

radiation exposure, caused by prompt radiation, produced tracer and induced activity. Moreover, in most cases cyclotron maintenance requires handling of radioactive components and wastes. Therefore special attention should be paid to the radiation safety aspects, providing additional shielding and dose control for personnel, who perform cyclotron operation and technical support. Besides, the analysis of the dose values enables to make a conclusion about the achieved radiation safety conditions and implementation of new safe measures, directed at a minimization of radiation exposure to personnel according to the ALARA principle.

© Bondar B., Mikhnytsky I., Kmetiyuk Ya., 2014

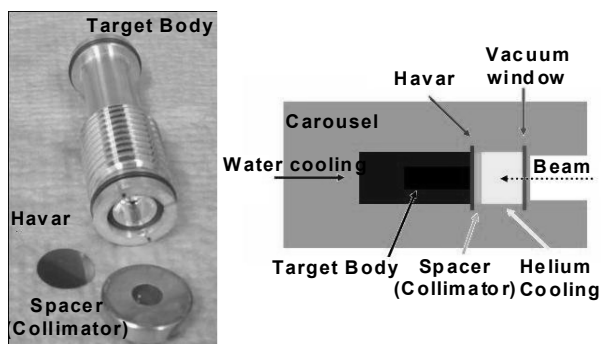
F-18 production. PET-Cyclotrons produce different isotopes through the proton induced reactions, shown in table 1. For the different isotopes different types of targets are used (gas and liquid), and they have special properties, that ensures effective tracer yield in a harsh irradiation conditions.

Table 1

PET tracers, produced by medical cyclotrons

Product	Target Type	Half-life, min	Reaction
^{18}F	Liquid	110	$^{18}\text{O}(p,n)^{18}\text{F}$
^{11}C	Gas	20	$^{14}\text{N}(p,\alpha)^{11}\text{C}$
^{15}N	Liquid	10	$^{16}\text{O}(p,\alpha)^{15}\text{N}$
^{15}O	Gas	2	$^{15}\text{N}(p,n)^{15}\text{O}$

In All-Ukrainian center for radiosurgery of the Clinical Hospital "Feofaniya" the fluorodeoxyglucose (FDG) production technology was successfully implemented using self-shielded Siemens cyclotron Eclipse RD [1]. The self-shielding consists of concrete, borated polyethylene and lead, ensuring good radiation protection from neutrons and gamma rays. For ^{18}F production the enriched water with ^{18}O 98% enrichment and 1.2 ml volume is loaded to a target and due to $^{18}\text{O}(p,n)^{18}\text{F}$ nuclear reaction isotope ^{18}F is produced. For this production technology the liquid target is used, shown in fig.1a. It consists of silver target body, collimator and target window, made of Havar alloy [5], which is pressure and temperature resistant (melting point for Havar is 1753 K). During bombardment the target body and Havar window are cooled by water and helium systems respectively (fig. 1b. demonstrates target working conditions during irradiation). The beam extraction is performed through the 25 μm aluminum vacuum window, behind which a target is installed.

Fig. 1. ^{18}O liquid target:

a) construction b) irradiation conditions

The tracer yield decreases with time, which is caused by target deterioration during irradiation. Therefore the target and its components must be cleaned and replaced periodically. Fig. 2 demonstrates the ^{18}F tracer yield depending on a target usage. These data were obtained after 150 production runs without target rinse, and it should be noted that with assumption of 4 working days/week and 1 hour/day production, the target lifetime of 1950 μAh will be reached after 3 months.

Radiation exposure and dose rate measurements.

Cyclotron exploitation is accompanied by several sources of radiation, that cause additional exposure to personnel: prompt gamma rays and neutrons, produced tracer and induced activity of a cyclotron components. The prompt radiation exists only during irradiation and the greater part of it is absorbed by the cyclotron self-shielding. The dose rate on shielding surface during irradiation is 15 $\mu\text{Sv/h}$ for neutrons and 75 $\mu\text{Sv/h}$ for gamma rays respectively. The working place is located in the control room, where dose rate does not exceed 0.3 $\mu\text{Sv/h}$.

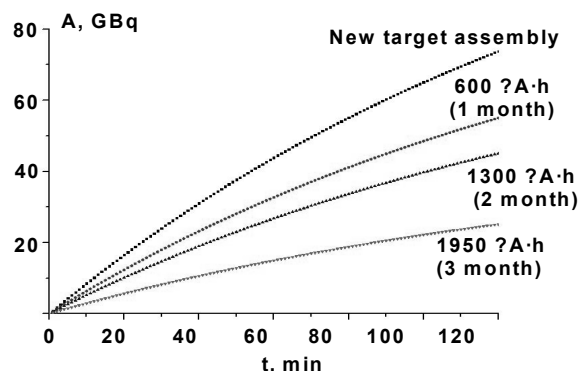


Fig. 2. Tracer yield dependence on a target usage

Table 2

Dose rates from vacuum window, target and its components

Element	Usage, mA·h	Time after last bombardment, hours	Dose rate at 0.1m mSv/h
Target body	5210	60	0.14
Collimator (spacer)	5210	60	0.05
Havar foil	1950	60	5.42
Vacuum window	3540	60	2.52

After bombardment and tracer delivery to the lab, the relics of produced tracer and induced activity become as the main sources of radiation. The shielding fully absorbs this radiation, but when the shield is open the dose rate near the target module can be very high (>15 mSv/h), and hence for technical maintenance it is necessary to wait at least for a one day for short-lived radionuclide decay.

The dose rates from different target components, measured after 60 hours from last bombardment are shown in table 2. The highest dose rate was measured from Havar window (about 5 mSv/h). Apart from the Havar foil long-lived isotopes are also induced in other target components and vacuum window, where dose rate can be up to 2.5 mSv/h. The technical maintenance of a cyclotron is performed by engineer-physicist and taking into account these dose rates, the effective dose to engineer is mostly caused by the actions, to be done in a close proximity to the target module (these works include target replacement, extractor replacement, ion source maintenance, vacuum window replacement and other). Regardless of type of work, almost all of them include 3 steps, mixed with exposure: there are demounting and installation, transportation and handling of radioactive parts of a cyclotron. Each of these steps must be executed using different types of shielding, such as lead screen, lead containers and fume hood with lead shielding and leadglass window for wastes handling. Activated details handling must be done very carefully using tweezers and after usage they should be enclosed in a special storage for farther decay.

Effective doses and data analysis. The yearly effective dose to engineer depends on the number of works, that should be done during a year. Since the irradiated target is the most activated detail, its maintenance forms the bigger part of dose. The average target lifetime appeared to be 1950 μAh (3months), so there are minimum 4 target replacement actions per year, excluding periodic target leakages and blowing of vacuum window. Table 3 shows the type and number of technical works, that were done in 2013 and corresponding effective doses to engineer, measured with the help of EPD MK2+ and TLD Harshaw 100 dosimeters. There were 6 target

rebuilt, 1 extractor and cathodes replacement and 2 vacuum window replacements.

Table 3

Doses to engineer-physicist for different types of actions (10.01.13–26.12.13; 150 productions)

Type of work	Dose/action, μSv and number of actions (EPD Mk2+ measurements)	Effective dose, mSv/year (TLD measurements)
Target rebuild	0.152 (6)	-
Extractor replacement	0.075 (1)	-
Cathodes of ion source replacement	0.063 (1)	-
Vacuum window replacement	0.078 (2)	-
SUM	1.206	1.06 0.85 [3]

For the works, presented in table 3, the sum effective dose for EPD measurements is 1.206 mSv/year, and almost 80% of it goes from the target rebuild actions. For TLD measurements dose value is slightly lower: our results give 1.06 mSv, and in the Department of Nuclear Medicine of All India Institute of Medical Sciences, where the same cyclotron with the same parameters is used, the effective dose to engineer is 0.85 mSv/year [3]. Summarizing these data it is clear that all doses are considerably lower than dose limits, adopted by International Commission of Radiological Protection (ICRP) [6] and the average dose is about 1 mSv/year, which is comparable with the average background dose per year.

Conclusions. The radiation safety aspects during cyclotron exploitation were considered and the main sources of radiation exposure were analyzed. The dose rate measurements were performed and the effective dose

to engineer, occupied with tracer production and technical maintenance was determined using EPD Mk2+ and TLD Harshaw 100 dosimeters.

One of the ways to get higher radiation doses is the increment of production runs, which leads to faster target degradation and therefore to bigger number of works. Since April, 2014, Hospital has started tracer productions not only for own, but also for external needs, and now production intensity increased twice. In these conditions the effective dose is expected to be 2.4 mSv/year, and even in this case the effective dose is sufficiently low and does not exceed 15% of dose limits, adopted by ICRP. So, it can be concluded, that providing good shielding and organization of work, the usage of low energy cyclotrons can be absolutely safe and secure.

REFERENCES.

1. F-18 production for PET imaging / B. M. Bondar, M. V. Kostianyj, I. B. Mikhnytsky, Ya. V. Kmetyuk // Proceedings of 2-d International Workshop "Medical physics – the current status, problems, the ways of development. Innovation technologies", 27-28 september, Kyiv 2012.
2. Paans M. J. Compact cyclotrons for the production of tracers and radiopharmaceuticals / M. J. Paans // NUKLEONIKA, 2003 – Vol. 48 – P. 169–172.
3. Pant G.S. Initial experience with an 11-MeV self-shielded medical cyclotron on operation and radiation safety / G. S. Pant, S. Senthambichelvan // Journal of Medical Physics, 2007 – Vol. 32, № 3. – P. 118–123.
4. Semeniv I. P. Introduction experience and first results of positron-emission tomography application in All-Ukrainian radiosurgery center / I. P. Semeniv, Ya. V. Kmetyuk, O. I. Moskalets et al. // Radiation therapy and diagnostics, 2013 – Vol. 2/3 – P. 88–92.
5. www.goodfellow.com/E/Havar-High-Strength-Non-Magnetic-Alloy.htm. [Електронний ресурс].
6. International Commission on Radiological Protection (ICRP), Publication 103: The 2007 Recommendations of ICRP – 2007.

Submitted on 06.10.14

Бондар Б., інженер-радіофізик, клінічна лікарня "Феофанія";
каф. ядерної фізики, фізичний факультет, Київський національний університет імені Тараса Шевченка
Міхницький І., інженер-радіофізик,
Кметюк Я., керівник Всеукраїнського центру радіохірургії
Клінічна лікарня "Феофанія"

РАДІАЦІЙНА БЕЗПЕКА ПРИ РОБОТІ ТА ТЕХНІЧНОМУ ОБСЛУГОВУВАННІ 11-МЕВ МЕДИЧНОГО ЦИКЛОТРОНУ

В роботі висвітлюються основні питання радіаційної безпеки при експлуатації циклотрону Eclipse RD (Siemens), що використовується для позитронно-емісійної томографії з фтордезоксиглюкозою (ФДГ). Проаналізовано основні джерела іонізуючого випромінювання та ефективність власного захисту циклотрону. Проведені вимірювання потужностей доз від активованих деталей та радіоактивних відходів, оцінено ефективні дози персоналу з використанням електронних індивідуальних дозиметрів EPD Mk2+ та термолюмінесцентних дозиметрів Harshaw 100.

Ключові слова: позитронно-емісійна томографія, фтордезоксиглюкоза, циклотрон, радіаційна безпека, ефективна доза.

Бондар Б., инженер-радиофизик, клиническая больница "Феофанія";
каф. ядерной физики, физический факультет, Киевский национальный университет имени Тараса Шевченко
Михницкий И., инженер-радиофизик,
Кметюк Я., руководитель Всеукраинского центра радиохирургии,
Клиническая больница "Феофанія"

РАДИАЦИОННАЯ БЕЗОПАСНОСТЬ ПРИ РАБОТЕ И ТЕХНИЧЕСКОМ ОБСЛУЖИВАНИИ 11-МЕВ МЕДИЦИНСКОГО ЦИКЛОТРОНА

В работе приведены вопросы радиационной безопасности при эксплуатации циклотрона Eclipse RD (Siemens), который используется для позитронно-эмиссионной томографии с фтордезоксиглюкозой (ФДГ). Проанализированы основные источники излучения и эффективность собственной защиты циклотрона. Проведены измерения мощностей доз от активированных деталей и радиоактивных отходов, а так же сделана оценка эффективных доз персонала с использованием электронных индивидуальных дозиметров EPD Mk2+ и термолюминесцентных дозиметров Harshaw 100.

Ключевые слова: позитронно-эмиссионная томография, фтордезоксиглюкоза, циклотрон, радиационная безопасность, эффективная доза.

UDC 577.3

V. Gaidar, post grad. stud.,
S. Radchenko, Ph.D., O. Sudakov, Ph.D.
Department Medical radiophysics, Faculty of Radiophysics, electronics and computer systems,
Taras Shevchenko National University of Kyiv

REMOVAL EMG AND EOG ARTIFACTS FROM EEG SIGNAL

One of the main problems in electroencephalography analysis is artifacts: electromyogram (EMG) and electro-oculogram (EOG). Considered removal methods are based on blind source separation techniques (BSS) with the Second Order Blind Identification (SOBI). We applied the modified SOBI algorithm with asymptotically optimal weights (WASOBI).

Keywords: electroencephalogram, electromyogram, electro-oculogram, blind source separation techniques.

Introduction. Electroencephalography (EEG) is a common method of research of the brain [7]. EEG non-invasive and safe method of direct mapping of functional activity of the central nervous system that allows us to monitor those signals in real time. EEG is based on getting the bioelectric potentials from the surface of the scalp. We get signals due to the electrical interaction of a large number of neurons (which include action potentials, the electrical synaptic transmission of information and other). So we can say that the signal at each electrode is based on the summation of elementary processes, actually occurring at the level of individual neurons. Electroencephalograph used in clinical practice for the detection of various pathologies and malfunction of the brain function, and it is save method for learning about brain functionality. If we could create the database with data, which would contain a large number of electroencephalographic researches, so in the future it would allowed to us analyzing various pathologies for a large data set and picking up some statistics to create a classifier.

However electroencephalogram is very sensitive to different artifacts. Among them the most distorted the real data are: motor artifacts (also called miogramm (EMG) [2], that caused by muscle reduction) and oculogramm artifacts (EOG) arising from motion of eyes and blinking. The systematic approach of recognition, source identification and elimination of artifact is an important process to reduce the chance of misinterpretation of the EEG and limit the potential for adverse clinical consequences.

Therefore, without the prior automatic processing data and removal of artifacts does not make sense to do some analysis, because, the signal will be distorted by EOG and EMG artifacts. That is why in this work we focus on solving the problem of the artifacts removal.

When we talk about EEG data taken from specific electrodes, we must consider that this signal is weighted linear mixture of underlying cortical source signal [1, 4]. The weights of each recorded mixture are determined by the distance of cortical sources domains from the electrodes pair, the electrical properties of underlined tissues etc. The method of Blind Source Separation (BSS) [5] allows separate a set of sources from a set of mixed signals without the aid of information about signals or mixing process. BSS technique is able to separate EEG signal into spatial components and then identify the artifacts components by using the proper criterion. After that we can remove artifact components and reconstruct the signal free of artifacts. BSS relies on the assumption that the signals are not correlated and statistically independent from each other. The main idea of the method can be represented as follow [5, p. 164]: $g(t) = As(t) + n(t)$. The data from i electrode $g_i(t)$ can be obtained by mixing a large number of independent sources $s_j(t)$, where mixing can be expressed in $[n \times m]$ matrix A called the mixing matrix, here n - number of electrodes, m - number of sources (the assumption $n = m$) and $n(t)$ - white noise. Thus can find signals solving the inverse problem of finding unmixing matrix $[m \times n] - W$:

$s(t) = Wg(t)$. For these purposes, we used algorithm SOBI [9] and reformulating the problem as a weighted least-squares (WLS) problem [10]. Thus, we achieve two main goals: minimizing the mean square error (MSE) of the estimated matrix A ; second, rather than estimate A from M vectors we estimate A from a small number of estimated correlation matrices. The true correlation matrices have the structure [9] $R_x[\tau] = AR_s[\tau]A^T \quad \forall \tau$ where due to the spatial independence of the sources, their correlation matrices $R_s[\tau] = \text{diag}[\lambda_{\tau}^{(1)}, \lambda_{\tau}^{(2)} \dots]$ are diagonal matrices.

After obtained matrix A we can identify columns of A corresponding to EOG and EMG sources by using the criteria that marks as artifacts the components with smaller fractal dimension [6]. Conceptually, components with low fractal dimensions are those who are composed of few low-frequency components. This is often the case of ocular activity and therefore this is a suitable criterion for detecting ocular (EOG) components.

Now that we have defined a set of independent signals $s_j(t)$ we can remove by equate to null some of the weight coefficients mixing matrix. We talk about the weights because on different electrodes these independent signals will be represented in different ways.

But for remove signals that corresponding to the artifacts, we need to have some criteria [3]. So going directly to the removal of artifacts we can define a general algorithm:

1. Background EEG decomposed into a set of spatial components.
 2. Provision artifact components using the appropriate automatic criteria.
 3. EEG reconstructed, but without the selected artifacts.
- We can write the obtained from j -electrode signal:

$$x_j(t) = \sum_{i \in EEG} a_{ji} s_i(t) + \sum_{i \in EOG} a_{ji} s_i(t) \quad X(t) = A_{EEG} s_{EEG} + A_{EOG} s_{EOG}$$

where $x_{EEG}(t) = A_{EEG} s_{EEG}$ and $x_{EOG}(t) = A_{EOG} s_{EOG}$.

Experimental. In our case we had a real EEG signal that was collected from 21 scalp electrodes placed according to the international 10–20 System at the Department of Medical Radiophysics, Electronics and Computer Systems.

EEG records the potential between two electrodes. Electrodes are placed on the skin of head, so that the multi-channel system covers all major parts of the brain.

Two types of EEG montages are used: monopolar and bipolar [8]. The monopolar montage is when the "input 1" amplifier is supplied from the electrode potential, which stands on the brain, and to "input 2" – from the electrode which is removed from the brain.

Electrode located above the brain, often called active electrode. The removed from the brain tissue electrode, called the reference: As the reference electrode often used electrodes that placed on the left (A1) or right (A2) earlobe. The active electrode is connected to "input 1", the reference electrode connected to the "input 2".

Since EEG recorded the potential between two electrodes, the position of a point on the curve will display changes under each of the pair of electrodes.

Electrode location under active electrode generates an alternating of brain potential. In reference electrode located far from the brain, there is a constant potential that does not affect on the record. However, the region of the head between the active and reference electrodes forming part of an electrical circuit "power object".

If the "input 1" and "input 2" electrodes both are active we talk about bipolar montage. In this case EEG recording monitor equally changes in potentials under each of the pair of electrodes, and recorded curve a potential difference reflects each electrode.

In our case we use the bipolar montage and experimental conditions provided the opportunity for display EOG and EMG signals on the obtained data (Fig. 1).

Movement during the recording of an EEG may product artifact through both the electrical fields generated by muscle and through a movement effects on the electrode contacts and their leads. It is the most common and significant source of noise in EEG. EMG activity almost always obscures the concurrent EEG because of its higher amplitude and frequency.

In our case we can see the EMG artifact in the right circle and the EOG in the top circle. With bipolar montage, positive and negative phase reversals of EOG are seen at the frontal electrodes, because they placed near the eyes. Observe that original EEG frame contains few blinks and well defined EMG signal (designated in the right and left circles respectively). As we can see the WASOBI algorithm using with fractal dimension criteria gives desirable result of remove EOG and EMG data from EEG data and wherein applied method do not distort real EEG signal.

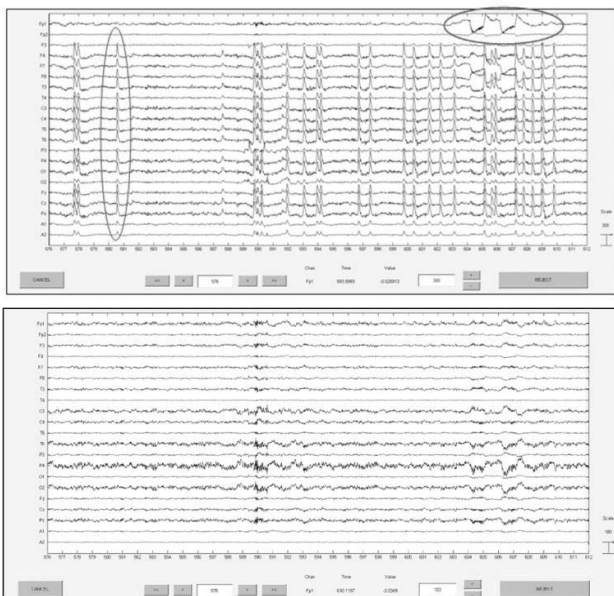


Fig. 1 Original EEG (the top frame) and corrected frames respectively

In order to make sure that, after using this method of artifacts remove, our data, that did not consist artifacts has not changed significantly we used Kolmogorov – Smirnov test. We have chosen the range between 104.5–107.5 seconds, which doesn't consist the artifacts before we using the WASOBI method (Fig. 2).

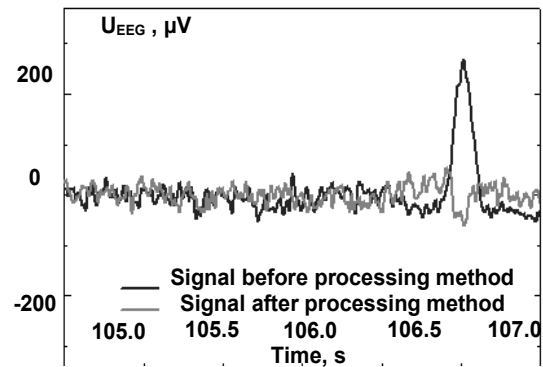


Fig. 2. EEG signal before (blue) and after EMG removal (red)

As the result, the function of the probability that a signal obtained specific amplitude range was built (Fig. 3).

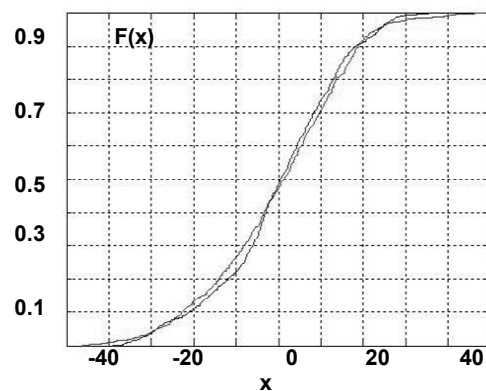


Fig. 3. Cumulative distribution function

Obtained value of the parameter p : $p = 0.18$ enables us to say that the method can be used for processing EEG data. The suggested algorithm of remove artifacts of oculogram and miogram provides low distortion of signal that does not contained artifacts, which was confirmed by the Kolmogorov-Smirnov test. Thus, in further it provides an opportunity to create expert systems for classification and analysis of EEG signals.

REFERENCE:

1. *Dominic L.* Introduction to Independent Component Analysis: InfoMax and FastICA algorithms / L. Dominic, C. Sylvain, G. Dominique // *Tutorials in Quantitative Methods for Psychology*, 2010. – Vol. 6. – P. 31–38.
2. *Fetz E. E.* Operant conditioning of specific patterns of neural and muscular activity / E. E. Fetz, D. V. Finocchio // *Science*, 1971. – Vol. 174, № 4007. – P. 431–435.
3. *Jung T. P.* Removing electroencephalographic artifacts from blind source separation / T. P. Jung, S. Makeig, C. Humphries, T.V. Lee // *Psychophysiology*, 2000. – Vol. 37. – P. 163–178.
4. *Jutten C.* Blind separation of sources An adaptive algorithm based on neuromimetic architecture / C. Jutten, J. Hererault // *Signal Processing*. – 1991. – Vol. 24. – P. 1–10.
5. *Removing electroencephalographic artifacts by blind source separation* / T.-P. Jung, S. Makeig, C. Humphries et al. // *Psychophysiology*, 2000. – Vol. 37. – P. 163–178.
6. *Removing noise and artifacts from EEG using Adaptive noise cancelator and Blind* / Nguyen T. K. Cuong, Vo Q. Ha, Nguyen T. M. Huong et al. // *Proceedings of the 3rd International Conference on the Development of BME in Vietnam*, 2010.
7. *Saeid S.* EEG signal processing / S. Saeid, J. A. Chambers // *Cardiff University, UK: John Wiley&Sons*, 2007 – 267 p.
8. *Tichavsky P.* A fast approximate joint diagonalization algorithm using a criterion with a block diagonal weight matrix / P. Tichavsky, A. Yeredor, J. Nielsen // In: *Submitted to ICASSP*, 2008.
9. *Yeredor A.* Blind separation of Gaussian sources via second-order statistics with asymptotically optimal weighting / A. Yeredor // *IEEE Signal Processing Letters*, 2000. – Vol. 7. – P. 197–200.
10. *Tatum W.O.* Handbook of EEG interpretation / W.O. Tatum, A. M. Husain, S. R. Benbadis // *Florida : Demos Medical Publishing*, 2007. – 300 p.

Гайдар В. О., Радченко С. П., Судаков О. О.
кафедра медичної радіофізики, факультет радіофізики, електроніки та комп'ютерних систем
Київський національний університет імені Тараса Шевченка

ВИДАЛЕННЯ АРТЕФАКТІВ ЕЛЕКТРООКУЛОГРАМИ ТА ЕЛЕКТРОМІОГРАМИ З ЕЕГ СИГНАЛУ

Однією з основних проблем при аналізі електроенцефалограм є артефакти: електроміограми (ЕМГ) і електроокулограми (ЕОГ). Були розглянуті методи видалення основані на методі сліпого розділення джерел (BSS) із використанням статистики другого порядку (SOBI). Ми застосували модифікований алгоритм SOBI з підбором асимптотично оптимальних вагових коефіцієнтів (WASOBI).

Ключові слова: електроенцефалограма, електроміограма, електроокулограма, метод сліпого розділення компонент.

Гайдар В. О., Радченко С. П., Судаков О. О.
кафедра медицинской радиофизики, факультет радиофизики, электроники и компьютерных систем,
Киевский национальный университет имени Тараса Шевченко

ВЫДЕЛЕНИЕ АРТЕФАКТОВ ЭЛЕКТРООКУЛОГРАММЫ И ЭЛЕКТРОМИОГРАММЫ С ЭЭГ СИГНАЛА

Главной проблемой при анализе электроэнцефалограмм есть артефакты, которые сильно искажают ЭЭГ сигнал. Наибольшее проявляются: артефакты электромиограммы (ЭМГ) и электроокулограммы (ЭОГ). Были рассмотрены методы выделения и дальнейшего изъятия этих сигналов с выходных электроэнцефалограмм. Нами был применен метод "слепого разделения компонент" (BSS) с использованием статистики второго порядка. Мы применили модифицированный метод SOBI с подбором асимптотических коэффициентов (WASOBI).

Ключевые слова: электроэнцефалограмма, электромиограмма, электроокулограмма, метод слепого разделения.

UDC 539.12.04:614.876

O. Gaidar, Ph.D, V. Tryshyn, Ph.D,
O. Svarichevska, Ph.D, I. Pavlenko, Ph.D,
Institute for Nuclear Research National Academy of Sciences of Ukraine
V. Gaidar, post grad. stud.,
Taras Shevchenko National University of Kyiv

ENVIRONMENTAL IMPACT ASSESSMENT OF OPERATION OF POSITRON EMISSION TOMOGRAPHY CENTER

Impact assessment for centre of positron emission tomography has been carried out. It has been shown that risks, that arise due to the radiation impact factor, are acceptable. The adequacy of protective measures to ensure radiation safety of personnel, population and environment is analysed.

Keywords: fluorodeoxyglucose, medical cyclotron, radionuclides, source term, radioactive waste.

Introduction. The oncology illnesses are placed second in the mortality structure of the population after the heart-vessel system. The early diagnose is the very important moment in treatment of these illnesses what is explained the importance of creation of modern centre nets in the Ukraine for the positron-emission tomography (PET).

Today radiopharmaceuticals (RPhP), which include short-half-life radionuclides ^{11}C , ^{13}N , ^{15}O , ^{18}F , are generally recognized. The short period of life of these radionuclides demands location of cyclotron (for their production) and laboratories of radiopharmaceutical synthesis (RPhP) in close proximity to diagnostics centers, which often are located in dense population districts of the large towns. This requires the careful approaches to create reliable systems of engineering barriers to prevent unreasonable release of radioactive substances to the environment and to protect from irradiation personnel and population.

The modern center for early diagnostic of cancer by positron emission tomography (PET-center) will be built in Donetsk, where for manufacturing of fluorodeoxyglucose (FDH), based on short-lived radionuclides ^{18}F , the medical cyclotron MINITrace of GE Medical systems company is used.

Production is based on the irradiation of the target (with water, enriched by isotope ^{18}O) by protons, accelerated to the energy of 9.6 MeV. The produced radionuclide ^{18}F further is used for the synthesis of FDH radiopharmaceutical, its dosage and transfer to the block of radio diagnostic department of PET-center.

PET center has several blocks, first is the cyclotron unit, block of radiopharmaceutical synthesis and block of radio diagnostic studies.

The block of cyclotron unit includes: cyclotron tank, utility room of cyclotron, the cyclotron control room, sanitary gateway in the output of the cyclotron block.

The block of radiopharmaceutical synthesis includes: laboratory of synthesis, clean changing rooms; laboratory

of quality, passageway to transmit radiopharmaceutical to the diagnostic department of PET-center, sanitary gateway at the output of the block.

Also available support facilities, technical service corridor for the hot cells of laboratory of synthesis and interim storage of radioactive waste, emergency shower at the exit from the technical corridor to the corridor; space for calculations, documentation and personnel office room, and others.

Block of radio diagnostic studies is on the 2-nd floor and provides the facilities for receiving and preparation of radiopharmaceuticals based on ^{18}F , procedural for introduction of radiopharmaceuticals to patients; waiting rooms for patients after introduction of radiopharmaceuticals with a bathroom connected with the system of special sewage as well as procedural and console of PET/KT system.

During the operating the PET Center main factor of negative impact on the environment is the radiation one, namely:

- pollution of the surface layer of air in the surrounding PET-center territory by radioactive airborne emissions;
- formation and accumulation of solid radioactive waste (RW);
- formation of radioactive liquid radioactive waste (radioactive runoff).

In normal mode, the PET-center radioactive substances will be localized by system of protective barriers (containers, protective screens, elements of process equipment) that prevent their direct contact with the environment.

For this purpose we have developed the system of stationary biological barriers and appropriate calculations have been made. In this calculations as base was selected the request of non-exceeding of acceptable levels of design dose, which provide non-exceeding of the established limits of effective dose of irradiation for different categories of people: the staff category A and B, and

population [1]. Also in accordance with the requirements of paragraph 9.1.4 OSPU 2005 [2], biological shielding calculations were carried out with taking into account the safety factor equal to 2.

Emission of radioactive substances and the impact of PET-center on the environment and population on surrounding territory are possible due to emissions and discharges.

To reduce the environmental impacts during the operation of the PET center a number of special measures has been implemented.

Measures to protect air quality.

- Radioactive substances in gaseous state are collected in the vicinity of the cyclotron target node and time delay are proved to prevent their immediate release in to ventilation system in the case of possible leakage from the target;

- Cleaning from dust of air that is fed into the hopper of the cyclotron, with the aim to reduce the generation of radioactive aerosols in the room;

- Guarantee the maximum possible sealing of open radiation sources during operation, transport and storage operations;

- Carrying out work with radioactive substances of open type in the boxes, laboratory modules, and fume hoods with local ventilation and cleaning filters;

- The appropriate organization of special ventilation system and schemes of air overflows to prevent the direct flow of radioactive substances into the environment;

- Organization of special ventilation systems to adequate pressure distribution and air flow in the block of cyclotron, laboratories of syntheses, laboratory of quality control, technology corridor and buffer zone;

- Installation of automatic control and display pressure alarm and valve overlap for exhaust ventilation in case of accidental release of radioactive substances into the air of technological premises;

- Cleaning of ventilation air-out through the HEPA filters (with purification efficiency of at least 99.9%) and activated carbon at the outlet of exhaust systems and organization of continuously monitoring of the activity of airborne emissions from the manufacturing unit of PET-center.

Measures to protect the aquatic environment

To protect the water environment in the operation of the PET center will be used special sewerage system, consisting of four central decanter tanks, where radioactive wastewater will be accumulated.

The automatic control of filling of decanter tanks is used. After filling the tank drains automatically addressing to another tank, and filled tank is sludged overnight, after which, if the level of residual activity is less than control level, the content will be dumped to sanitary sewer.

To control of accumulated in tanks activity, they will be equipped with detectors of ionizing radiation dose rate and sampling devices.

Solutions, which will arise during routine operations with the parts of the cyclotron and decontamination of laboratory equipment, contaminated transport containers, etc., are considered as liquid radioactive waste (LRW) and be poured upon to special containers. These tanks will be located in a special shielded cabinet with ventilation in the premises of the temporary storage of radioactive waste.

Measures to minimize radioactive waste.

Radioactively contaminated materials of the PET/CT system, testing block in gamma camera, laboratories of synthesis and quality control, cyclotron block will be transferred to the appropriated premises of temporary storage for radioactive waste to store in special containers until the desired level of decay will be achieved. After that these they can be removed with the household waste.

Operating portable generators will be returned for recycling to the plant-manufacturer. Radioactive waste to be disposed will be transferred to a specialized company that has a license. To prevent uncontrolled radioactive waste, an alarm system and a blocking system will be used to lock the door to premises of temporary storage for radioactive waste.

The prediction of the formation of radioactive waste during decommissioning of PET-CT centre has been performed. So highest activity will be accumulated in the following structural elements:

- Accelerating chamber and the magnet yoke.
- Tantalum collimator.
- Foil made of titanium and HAVAR to remove the proton beam.

- Target holder with silver.

- Plastic protector of target.

- Concrete of integrated cyclotron radiation protection.

- Stainless steel designs of cyclotron and auxiliaries.

To reduce the amount of radioactive waste that will be disposed of, it is recommended to carry out decommission of the center in several stages, one of which is a conservation of facility for at least 1 year. As estimated, the largest by volume ($m \approx 35 \text{ t}$, $V \approx 10 \text{ m}^3$) of radioactive material at decommission of the cyclotron MINITrace will be the concrete, which is the part of integrated protection which activity after a relatively long exposure (within 1 year) is mainly determined by the content of long-lived gamma emitters ^{152}Eu and ^{60}Co and "pure" beta-emitting radionuclides ^3H , ^{39}Ar and ^{45}Sa .

To control the influence of the operation of PET Center, we have developed a system of radiological control, one element of which is the radiation monitoring of radionuclide activity in the emissions and discharges that flow into the environment.

Results.

We have evaluated the environmental impact of exploitation of PET-center during normal operation and emergency situations.

To evaluate environmental impact of operation of PET center on air and water the Ukrainian norms and methodology, the IAEA recommendations, and advanced specialized software (HotSpot, FRAMES, MCNP, MicroShield) were used.

According to forecasts, in normal operation the maximum daily discharge of ^{18}F from ventilation pipe of bloc for fluorodeoxyglucose manufacturing (BFM) does not exceed $1,85 \cdot 10^7 \text{ Bq}$. Thus the annual effective radiation dose of the population will not exceed $8,2 \cdot 10^{-8} \text{ Sv}$, which is almost 500 times less than the quota of limit dose of 40 mSv per year, which is set [1] for reference nuclear radiation facility.

Maximum activity of the radionuclide ^{18}F in wastewater (end of second shift normal operation) in decanter of BFM will be $\sim 10^8 \text{ Bq}$ in the sump and in the block of radio diagnostic tests (BRT) - $1,87 \cdot 10^9 \text{ Bq}$. After their retention interval (for at least 24 hours before being discharged to the sanitary sewer) concentration of ^{18}F radionuclide will be lower than the calculated value for allowable concentration in drinking water for category B ($\text{DK}_B^{\text{ingest}}$).

As a result of consideration of possible emergency situations during the operation of PET-center, which can lead to increasing of radiation impact on the environment, staff and population, the conservative and most likely scenarios were selected and evaluations of their impact were made, namely:

1. Design basis accidents in the block of cyclotron:

- Failure of the locking system startup accelerator, causing the cyclotron began working with open shielding door;

▪ Depressurization target or transport channel that leads to the release of all worked out activity of ^{18}F ($9,25 \cdot 10^{10}$ Bq per cycle).

2. Design basis accidents in the block of FDH production:

- Loss of external power supply;
- Emergency release of the produced ^{18}F activity to internal volume of synthesis/dosage modules or to the laboratory of FDH production due to violation of manufacturing process;
- Emergency release of the produced ^{18}F activity to the corridor due to a fire, caused by internal in-doings;
- Violation of the system of special ventilation (no filtering emissions through human error, violation of the integrity of the duct as a result of mechanical damage).

3. Design basis accidents in the block of radio diagnostic department:

- Spill a single dose of FDH in the room of reception and training FDH or procedural for intravenous introduction of FDH to patients;
- Loss of sources of ionizing radiation (closed or open);
- Carried out estimations shown that greatest possible impact on the environment is at design basis accident, associated with the release of ^{18}F to air environment due to failure of filtration in special ventilation system.

To exclude the possibility of such situation it is developed multiple levels of cleaning in particular HEPA filter (with an efficiency of more than 99.9%) and activated carbon filters, as well as continuous monitoring of release volume activity through the ventilation pipe and alarm in the case of excess of control levels of emissions. However, for the conservative estimation one more failure was considered – failure of monitoring system (within one month) and, as result, during this time contaminated air was released from the system of special ventilation without purification.

As magnitude of the total emissions from the block of FDH production (per cycle during normal operation of equipment) we conservative accept 1% of the worked out activity. Thus, the daily total emissions will be $\sim 2 \cdot 10^9$ Bq of ^{18}F .

It was also assumed that during the month the wind direction does not change, but the distribution of values of wind speed and categories of atmospheric stability were selected basing on regional conditions of the object disposition. To enhance the conservatism estimation it was assumed that during entire month the precipitation with intensity of 1 mm/h are observed.

Obtained results of estimations show that in the case of noted design basis accident maximum total effective dose to the persons from population is not exceeded $1,2 \cdot 10^{-5}$ Sv (at a distance of 10 m from the building), that does not exceed the level of acceptable risk.

Also the following beyond design basis accidents were considered:

1. Accidents caused by an earthquake or a sudden shift as:

Variant 1. Simultaneously, the destruction of the duct and release of contaminated air to the environment at a height of 3 m (ground-level release).

Variant 2. The integrity of the duct is remained, however, the filtration chamber is damaged and at a height of 16 m the unfiltered air is released.

2. Accidents caused by external anthropogenic impact (fire and destruction of the protective barriers due to the fall of the aircraft);

3. Car accident with a fire during a transportation of worked out production.

Obtained results indicate that even in the most challenging case of beyond design basis accidents (earthquake, variant 1) total effective dose to members of the population, which is located at a distance of 150 m from

the emission source, not to exceed $5 \cdot 10^{-5}$ Sv. According to Table D.7.1 [1], this value is much less than the lowest limit for any countermeasures.

When analyzing the impact of failures on the PET-center in the aquatic environment the design base accidents, associated with flooding surface and groundwater, technical flooding and emergency discharges of radioactive substances or radioactive effluents have been considered.

Emergency discharges of radioactive substances into the environment directly are prevented by protective barriers and organizational measures, implemented in the PET-center.

In case of accidental discharge of all worked out activity of radionuclide ^{18}F ($9,25 \cdot 10^{10}$ Bq/per cycle) to the tank sump after 24-hour exposure its total activity decreased to about 10^7 Bq, and the specific activity - to ~ 5 MBq/m³, that is well below $DK_{\text{B}}^{\text{ingest}}$ for ^{18}F . Waste water with the noted concentration of ^{18}F can be discounted to the sanitary sewer.

To prevent accidents when operating PET center the emergency plans and instructions for radiation safety in emergency situations will be developed, conducted training with using the hardware (sensors with sound and light alarm, emergency alarm system, blocking the entrance to the premises, physical protection, etc.) and organizational measures will be carried out.

All locations with elevated levels of radiation hazard will be marked with appropriate warning signs.

There will be an organized system alerts staff in controlled areas on the first and second floors.

In case of power failure of cyclotron the security system, modules of synthesis and dosing provides automatic (without operator intervention) transfer of means in a safe condition which guarantees the preservation of the integrity of engineered barriers and prevent the release of radioactive substances in the environment, above.

The room and corridors will be equipped with autonomous emergency lighting and markings pointing toward exits (including emergency) in case of disconnection from the centralized energy supply system.

The diesel generator with an eight-hour supply of fuel is provided to prevent accidents due to disconnection of the object.

It is also provided the automatic monitoring and display of pressure (pressure difference) and backup ventilation system in block of FDH production. In the case of failure of prescribed limits of working pressure values, a alarm signal will be generated by which staff should activate the duplicate ventilation system or alarm system and stop operations at facility.

To prevent accidents involving emergency release of produced activity in the internal volume of the unit safety cameras of PD manufacturing, even in case of failure of standard filters and system of lock of chamber the project provides additional filters (HEPA-filters and activated carbon) of exhaust ventilation systems installed in the outlet exhaust system.

To prevent infiltration of groundwater into basements of PET Center it is provided that the floors and exterior walls are made of reinforced concrete with modern materials for extra waterproofing and back-filling clay around the perimeter of the exterior walls of the building. Moreover basement near decanter tanks will be equipped with alarm triggering, which operation will stop the operation of the facility till elimination of emergency.

To prevent the release of radioactive substances into the environment as a result of man-made flooding, after carelessness of staff, accident in water system in the public network sanitary sewer, the project envisages the following measures:

▪ The use of pedal taps or faucets automatic water supply in areas where we are working with radioactive substances;

▪ Drainage system drains to special sewerage from the rooms of premises and second zones;

▪ Alarm of overflow of decanter tanks of special sewerage;

▪ Floor and basement walls made of reinforced concrete.

To prevent accidents due to loss of ionizing radiation sources (IRS), the project envisages a system of lock and alarm facilities, which are stored the IRS, that will prevent the unauthorized access to IRS.

Also, PET-center is planned to organize security system, which should ensure the physical protection of the object (prevent accidental penetration of the public or third party personnel to the controlled area).

Conclusions Thus, basing on the results of environmental impact assessment of PET-center operation during normal mode and under emergency situations, it can be concluded that the risks arising from radiation influence on the environment and the population are within acceptable limit. At the same time the influence of construction of state-of-the-art medical center on the social environment will be positive.

REFERENCE:

1. Normy radiatsiinoi bezpeky Ukrainy (NRBU-97).DGN 6.6.1.–6.5.001.98.
2. Osnovni sanitarni pravyla zabezpechennia radiatsiinoi bezpeky Ukrainy (OSPU–2005).DSP 6.177-2005-09-02

Submitted on 07.11.14

Гайдар О., канд. фіз.-мат. наук, Тришин В., канд. фіз.-мат. наук,
Сваричевська О., канд. біол. наук, Павленко І., канд. біол. наук, Інститут ядерних досліджень НАН України
Гайдар В., асп., Київський національний університет імені Тараса Шевченка

ОЦІНКА ВПЛИВУ НА ДОВКІЛЛЯ ЕКСПЛУАТАЦІЇ ЦЕНТРА ПОЗИТРОННО-ЕМІСІЙНОЇ ТОМОГРАФІЇ

Проведено аналіз впливу експлуатації центру позитронно-емісійної томографії на навколишнє природне середовище за рахунок радіаційних факторів. Показано, що в умовах нормального режиму експлуатації, а також при проектних і запроектованих аваріях ризику, обумовлені цим впливом, знаходяться в межах прийнятних. Проаналізовано достатність захисних заходів для забезпечення радіаційної безпеки персоналу, населення і довкілля.

Ключові слова: фтордеоксиглюкоза, медичний циклотрон, радіонукліди, радіоактивні газо-аерозольні викиди, радіоактивні відходи

Гайдар А., канд. фіз.-мат. наук,
Тришин В., канд. фіз.-мат. наук, Сваричевская Е., канд. биол. наук,
Павленко И., канд. биол. наук, Институт ядерных исследований НАН Украины
Гайдар В., асп., Киевский национальный университет имени Тараса Шевченко

ОЦЕНКА ВОЗДЕЙСТВИЯ НА ОКРУЖАЮЩУЮ СРЕДУ ЭКСПЛУАТАЦИИ ЦЕНТРА ПОЗИТРОННО-ЭМИССИОННОЙ ТОМОГРАФИИ

Проведен анализ воздействия эксплуатации центра позитронно-эмиссионной томографии на окружающую среду за счет радиационных факторов. Показано, что в условиях нормального режима эксплуатации, а также при проектных и запроектованных авариях риски, обусловленные этим воздействием, находятся в пределах приемлемых. Проанализировано достаточность защитных мер для обеспечения радиационной безопасности персонала, населения и окружающей среды.

Ключевые слова: фтордеоксиглюкоза, медицинский циклотрон, радионуклиды, радиоактивные газо-аерозольные выбросы, радиоактивные отходы.

UDC 577.332

A. Glushenkov, post. grad. stud., D. Hovorun, Doc. Sci,
Department Molecular biotechnology and bioinformatics, Institute of High Technologies,
Taras Shevchenko National University of Kyiv

COMPLETE FAMILY OF H-BONDED 1-METHYLCYTOSINE HOMOASSOCIATES: QUANTUM-MECHANICAL INVESTIGATION

On the MP2/6-311++G(2df,pd)//B3LYP/6-311++G(d,p) theory level in vacuum for the first time was shown that stabilized by specific intermolecular contacts complete family of $m^1\text{Cyt}\cdot m^1\text{Cyt}$ homoassociates counts 37 structures in diapason of 0–34,42 kcal/mol relative Gibbs energies. Centrally symmetric homoassociate corresponds to global minima which is stabilized by pair of antiparallel H-bonds N4H...N1 and has enthalpy of formation practically the same as in mass-spectrometry experiment (L.F. Sukhodub et al., 1976). Detail analysis of intermolecular H-bonds, especially weak CH...O/N, physico-chemical properties has been performed. Briefly discussed application of results in spontaneous point mutations of DNA theory.

Keywords: nucleic base, nucleic bases pair, complete family, hydrogen bond, cytosine, methyl-, methyl group.

Introduction. Nucleic bases (NB) play major role in coding genetic information, RNA spatial structure, engineering synthetic DNA. It's generally known that DNA strands hold complementary NB pairs of Gua·Cyt and Ade·Thy [23]. The complimentary principle is key factor supplying the transmission of genetic information in heredity line. Point changes of NB – mutations are possible through creation of incorrect pairs by rare NB tautomeric forms [24] which in turn leads to transformation of canonical NB pairs into non-canonical and errors during biosynthesis of DNA. RNA spatial structure in many respects is defined by intermolecular H-bonds between NB. Special emphasis in literature gives attention to non-canonical NB pairs in RNA [10–12, 20]. At the same time synthetic DNA can be designed to have non-canonical NB pairs. Every mentioned aspect demands knowledge about geometrical and physico-

chemical properties of isolated NB as well as of their H-bonded associates.

Object and methods. The goal of this paper is to obtain geometrical and physico-chemical properties of all possible 1-methylcytosine ($m^1\text{Cyt}$) homoassociates which involve all of it's seven possible tautomeric forms. Input structures automatically generated by original algorithm. Geometrical and electronic structure of molecules and complexes as well as their wavefunctions were obtained using density functional theory on B3LYP/6-311++G(d,p) theory level in vacuum. All optimized structures has been checked on stability by absence of imaginary frequencies in their spectra. Electronic energies of NB interaction and NB Gibbs free energies were obtained on MP2/6-311++G(2df,pd)//B3LYP/6-311++G(d,p) theory level. Quantum-mechanical calculations were done in Gaussian 03 for Win32 application [9].

Intermolecular H-bond identification were done by QTAIM method [2]. For identification of CH...O/N H-bonds NBO-analysis [5] and Grunenberg constant [14,15] methods were additionally used. Grunenberg constants calculations were done in Compliance 3.0.2 application [8]. Classical H-bond energies were calculated by logansen method [4,19]. Non-canonical CH...O/N H-bond energies and van-der-Waals contacts were calculated by Espinosa-Mollins-Lecomte method (EML) [18].

Results and discussion.

Fundamental physico-chemical properties of $m^1\text{Cyt}\cdot m^1\text{Cyt}$ homoassociates. Results are presented in table 1. Atomic numbering based on standard scheme [3]. Belonging to the same plane as molecule methyl group hydrogen atom has index 1. Complete family of H-bonded

homoassociates $m^1\text{Cyt}\cdot m^1\text{Cyt}$ contains 37 structures. These structures consists of NB pairs in common tautomeric form as well as rare tautomeric forms. Most energetically favorable conformer **1** has centrosymmetrical structure, stabilized by two antiparallel H-bonds on $m^1\text{Cyt}$ Watson-Crick binding site (naming convention by [21]) and has zero dipole moment. Ten homoassociates $m^1\text{Cyt}\cdot m^1\text{Cyt}$ has planesymmetrical structure (3 of them are centrosymmetrical); other 27 are significantly non-planar.

Conformer **1**'s population in standard conditions is 99,97% and conformers **2, 3** has total population of ~0,03%.

It was established that homoassociates $m^1\text{Cyt}\cdot m^1\text{Cyt}$ are stabilized by bond types: NH...N; NH...O; OH...N; OH...O; CH...N; CH...O. Classic H-bond energies lie in diapason 0,39÷2,80 kcal/mol (table 1).

Table 1a

Fundamental physicochemical properties of $m^1\text{Cyt}\cdot m^1\text{Cyt}$ homoassociates

Complex	ΔG° , kcal/mol	μ , D	H-bond/vdW contact AH...B /A...B	ρ , a.u.	$\Delta\rho$, a.u.	100 ϵ	E_{HB} , kcal/mol
1	0.00	0.00	N4H1...N3	0.032	0.088	0.08	6.39
			N4H1...N3	0.032	0.088	0.08	6.39
2	5.31	6.54	N3H...N3	0.028	0.080	0.07	5.90
			N4H...O2	0.016	0.054	0.02	3.11
			N4H1...O2	0.031	0.031	0.05	5.42
3	5.49	4.79	N3...C2	0.007	0.024	139.4	1.22
			N4H1...N3	0.020	0.063	0.05	4.20
			C1H...O2	0.002	0.009	0.41	0.39
4	6.47	2.99	C1H...N3	0.014	0.041	0.05	2.19
			N4H1...O2	0.027	0.105	0.06	4.67
5	6.64	13.38	N4H2...O2	0.025	0.088	0.06	4.16
6	7.48	14.93	C5H...N3	0.006	0.017	0.05	0.96
			N4H2...O2	0.024	0.089	0.04	4.06
7	7.54	10.60	N4H2...N3	0.022	0.068	0.02	4.71
			N4H1...N4	0.014	0.044	0.12	2.63
8	7.81	13.28	N4H2...N3	0.019	0.060	0.08	3.67
			C5H...O2	0.009	0.030	0.04	1.69
9	7.85	10.64	C6H...O2	0.012	0.037	0.03	2.14
			C1H1...O2	0.006	0.019	0.23	1.15
10	8.01	1.00	N1...O2	0.004	0.017	170.5	0.92
			C1H...O2	0.008	0.025	0.13	1.44
			O2...N1	0.005	0.018	232.2	1.02
			C1H...O2	0.006	0.022	0.38	1.24
			C1H...N3	0.006	0.018	0.70	0.99
11	8.16	5.54	N3...C5	0.005	0.014	109.4	0.72
			N4H1...N4	0.011	0.033	0.04	2.22
			C1H...O2	0.007	0.022	0.20	1.28
12	8.82	12.25	C6H...O2	0.013	0.042	0.04	2.35
			C1H1...O2	0.007	0.021	0.22	1.28
13	8.83	3.99	N3H...N3	0.029	0.080	5.81	6.76
			N4H1...N4	0.033	0.088	5.46	6.75
			O2...O2	0.002	0.002	4.74	0.34
14	8.97	13.90	C6H...O2	0.014	0.045	0.03	2.50
			C1H1...O2	0.008	0.025	0.20	1.43

Table 1a (Continue)

Complex	ΔG^0 , kcal/mol	μ , D	H-bond/vdW contact AH...B /A...B	ρ , a.u.	$\Delta\rho$, a.u.	100 ϵ	E_{HB} , kcal/mol
15	9.52	12.69	C6H...O2	0.015	0.052	0.04	2.80
			C1H1...N3	0.006	0.016	0.02	0.89
16	9.75	0.41	N3H...O2	0.027	0.100	3.38	5.22
			N3H...N4	0.037	0.092	5.44	7.48
17	10.16	6.31	N4H...N3	0.019	0.060	0.05	2.45
			N3H...O2	0.023	0.082	0.05	3.77
18	10.30	4.86	C5H...N3	0.017	0.052	0.07	1.96
			N4H1...N4	0.028	0.080	0.08	5.91
19	10.37	5.28	C1H...O2	0.013	0.045	0.07	2.41
			C1H...O2	0.013	0.044	0.07	2.36
20	10.63	3.89	N4H1...O2	0.028	0.101	0.04	4.85
			N3H...N3	0.027	0.077	0.06	6.13
			O2...N4	0.002	0.007	20.11	0.28
21	10.95	10.81	C5H...N3	0.010	0.030	0.09	1.58
			N4H2...N4	0.011	0.031	0.06	1.15
22	11.21	0.97	C1H...O2	0.013	0.043	0.07	2.34
			C1H...O2	0.013	0.043	0.07	2.32
23	11.48	4.05	C1H...O2	0.012	0.040	0.07	2.16
			C1H...O2	0.012	0.045	0.04	2.34
24	11.96	6.81	N4H2...N4	0.014	0.041	0.05	2.23
25	12.68	0.00	N3H...O2	0.026	0.097	0.03	4.70
			N3H...O2	0.026	0.097	0.03	4.70
26	16.62	1.30	N4H1...N3	0.038	0.098	0.07	6.98
			O2H...N3	0.058	0.093	0.06	10.72
27	17.70	4.89	O2H...N3	0.057	0.096	0.05	10.34
			N4H1...N3	0.035	0.090	0.07	6.90
28	21.55	3.42	C1H...N3	0.011	0.034	0.11	1.87
			O2H...O2	0.050	0.143	0.05	8.54
29	22.05	2.81	C1H...N3	0.010	0.026	0.05	1.49
			O2H...O2	0.047	0.146	0.05	7.77
30	22.54	6.82	N3H...N3	0.033	0.084	0.06	7.15
			N4H...N4	0.015	0.045	0.05	2.41
			O2H...O2	0.048	0.142	0.03	7.69
31	23.22	0.96	N3...N3	0.012	0.038	9.80	2.18
			O2H...O2	0.045	0.127	0.04	8.62
			N4H1...N4	0.027	0.076	0.08	6.78
32	23.53	4.34	N3H...N3	0.034	0.087	0.06	7.12
			O2H...N4	0.078	0.084	0.05	12.59
			N4...O2	0.002	0.008	8.96	0.39
33	28.30	4.17	N3H...N3	0.025	0.077	5.88	5.90
			N4...N4	0.002	0.006	9.11	0.29
			O2H...O2	0.050	0.128	1.53	8.33
34	29.70	12.35	C1H...O2	0.008	0.027	0.39	1.55
			C1H...O2	0.010	0.035	0.19	1.89
			O2H...O2	0.041	0.140	0.04	6.79
35	30.72	15.03	O2H...O2	0.039	0.126	0.05	6.87
			C1H...O2	0.011	0.038	0.23	2.10

Table 1a (End)

Complex	ΔG^0 , kcal/mol	μ , D	H-bond/vdW contact AH...B / A...B	ρ , a.u.	$\Delta\rho$, a.u.	100 ϵ	E_{HB} , kcal/mol
36	31.68	0.06	O2H...N3	0.081	0.073	0.05	13.10
			O2H...N3	0.081	0.074	0.05	13.06
37	34.42	13.38	O2H...O2	0.039	0.125	0.05	6.80
			C1H...O2	0.010	0.037	0.24	2.00

Table 1b

Fundamental physicochemical properties of m¹Cyt-m¹Cyt homoassociates

Complex	H-bond/vdW contact AH...B / A...B	d_{AB} , Å	d_{HB} , Å	Δd_{AH} , Å	$\angle AHB$, deg
1	N4H1...N3	2.946	1.917	0.023	175.7
	N4H1...N3	2.946	1.917	0.023	175.7
2	N3H...N3	3.005	1.977	0.020	174.6
	N4H...O2	3.187	2.164	0.004	177.8
	N4H1...O2	2.864	1.840	0.017	176.6
3	N3...C2	3.202	-	-	-
	N4H1...N3	3.096	2.110	0.012	161.8
	C1H...O2	3.794	3.289	0.000	109.5
4	C1H...N3	3.427	2.349	0.000	168.9
	N4H1...O2	2.888	1.867	0.014	176.3
5	N4H2...O2	2.970	1.953	0.011	179.8
6	C5H...N3	3.762	2.746	0.000	156.5
	N4H2...O2	2.967	1.952	0.011	176.0
7	N4H2...N3	3.032	2.109	0.015	149.5
	N4H1...N4	3.190	2.298	0.006	146.1
8	N4H2...N3	3.152	2.149	0.009	169.4
	C5H...O2	3.456	2.440	0.000	156.0
9	C6H...O2	3.372	2.345	0.000	157.3
	C1H1...O2	3.675	2.689	-0.002	150.4
10	N1...O2	3.360	-	-	-
	C1H...O2	3.403	2.599	0.000	129.9
	O2...N1	3.317	-	-	-
	C1H...O2	3.476	2.685	0.000	129.0
	C1H...N3	3.794	2.751	0.000	160.0
11	N3...C5	3.568	-	-	-
	N4H1...N4	3.416	2.408	0.005	172.7
	C1H...O2	3.368	2.659	0.000	122.2
12	C6H...O2	3.352	2.294	0.001	164.5
	C1H1...O2	3.637	2.621	-0.001	155.0
13	N3H...N3	2.977	1.946	0.025	173.0
	N4H1...N4	2.927	1.898	0.025	174.0
	O2...O2	3.701	-	-	-
14	C6H...O2	3.316	2.264	0.001	162.8
	C1H1...O2	3.552	2.527	-0.001	156.4
15	C6H...O2	3.277	2.201	0.001	171.0
	C1H1...N3	3.875	2.791	0.000	172.8
16	N3H...O2	2.902	1.879	0.017	172.5
	N3H...N4	2.883	1.846	0.030	172.5

Table 1b (Continue)

Complex	H-bond/vdW contact AH...B /A...B	d_{AB} , Å	d_{HB} , Å	Δd_{AH} , Å	$\angle AHB$, deg
17	N4H...N3	3.185	2.170	0.002	171.7
	N3H...O2	3.001	1.978	0.014	176.4
18	C5H...N3	3.310	2.242	0.005	167.7
	N4H1...N4	3.008	1.981	0.020	176.4
19	C1H...O2	3.323	2.260	0.000	164.2
	C1H...O2	3.332	2.271	0.000	163.6
20	N4H1...O2	2.903	1.887	0.014	172.7
	N3H...N3	3.010	1.988	0.022	169.3
	O2...N4	3.862	-	-	-
21	C5H...N3	3.529	2.477	0.001	163.9
	N4H2...N4	3.437	2.429	0.002	178.3
22	C1H...O2	3.352	2.267	0.000	172.3
	C1H...O2	3.357	2.271	0.000	172.3
23	C1H...O2	3.340	2.311	-0.002	156.9
	C1H...O2	3.350	2.262	0.000	175.1
24	N4H2...N4	3.288	2.325	0.004	159.0
25	N3H...O2	2.913	1.903	0.014	167.2
	N3H...O2	2.913	1.904	0.014	167.2
26	N4H1...N3	2.868	1.843	0.027	170.1
	O2H...N3	2.689	1.667	0.057	175.3
27	O2H...N3	2.686	1.671	0.052	173.3
	N4H1...N3	2.923	1.894	0.026	173.0
28	C1H...N3	3.313	2.469	-0.002	133.4
	O2H...O2	2.630	1.627	0.036	177.5
29	C1H...N3	3.517	2.558	-0.001	146.3
	O2H...O2	2.637	1.640	0.029	176.2
30	N3H...N3	2.950	1.918	0.028	171.0
	N4H...N4	3.312	2.289	0.002	178.3
	O2H...O2	2.647	1.658	0.028	171.3
31	N3...N3	2.972	-	-	-
	O2H...O2	2.674	1.687	0.038	166.0
	N4H1...N4	3.019	1.988	0.027	173.2
32	N3H...N3	2.920	1.903	0.029	164.8
	O2H...N4	2.594	1.547	0.081	175.8
	N4...O2	3.733	-	-	-
33	N3H...N3	2.998	2.001	0.021	161.4
	N4...N4	3.948	-	-	-
	O2H...O2	2.631	1.631	0.034	175.2
34	C1H...O2	3.359	2.565	-0.002	129.0
	C1H...O2	3.308	2.421	-0.005	137.4
	O2H...O2	2.680	1.705	0.023	168.9
35	O2H...O2	2.720	1.746	0.024	168.5
	C1H...O2	3.278	2.379	-0.006	138.7
36	O2H...N3	2.591	1.534	0.089	179.2
	O2H...N3	2.594	1.537	0.089	179.5

Table 1b (End)

Complex	H-bond/vdW contact AH...B /A...B	d_{AB} , Å	d_{HB} , Å	Δd_{AH} , Å	$\angle AHB$, deg
37	O2H...O2	2.723	1.750	0.024	168.1
	C1H...O2	3.294	2.396	-0.006	138.7

*Note: ΔG^0 - relative Gibbs free energy (T=298,15K; P=1atm); μ — dipole moment; AH...B/A...B — atoms forming H-bond and/or van-der-Waals contact; ρ — electron density at BCP, $\Delta\rho$ — laplacian of electron density at the BCP, ε — ellipticity at the BCP; E_{HB} — H-bond energy; distances d_{AB} , d_{HB} and angle $\angle AHB$ between H-bond atoms; elongation Δd_{AH} of H-bonded AH group

Identification of weak CH...O/N H-bonds. Weak CH...O and CH...N bonds attract special interest in literature. One of the problems discussed are their physicochemical properties and classification. It was established [17] that in such conditions that type of specific contacts is true H-bond. Our interest has been attracted to this H-bonds because 20 out of 37 conformers in complete conformational family of $m^1\text{Cyt}\cdot m^1\text{Cyt}$ homoassociates are stabilized through CH...O/N H-bonds. In 16 conformers m-group in position 1 takes part in CH...O/N H-bonds as proton donor. As we can see from table 1 QTAIM method identifies all specific CH...O/N contacts as H-bond. Although for their robust identification as a true H-bonds we additionally used NBO-analysis [5] and Grunenber constants methods [14,15].

Quantum-mechanical calculations' results of stabilization energies $E^{(2)}$ and Grunenber constants for these H-bonds are presented in table 2. As we can see all values $E^{(2)} > 0$ which means charge transfer from atom-acceptor lone pair to C-H antibond. Also all Grunenber constants are positive which means stabilization (pull not push) nature of specific CH...O/N contacts. No charge transfer in complex 3 means borderline case of transformation H-bond into van-der-Waals contact and can be useful for future investigations of lower bounds for electron density and it's laplacian in corresponding H-bond critical point. Obviously, that by using QTAIM theory only,

it's hard if not possible at all to tell the difference between AH...B H-bond and A...B van-der-Waals contact. It's seen from table 1 that for van-der-Waals contacts electron density values belong to 0.002-0.012 a.u. diapason and laplacian of electron density values belong to 0.006-0.038 a.u. diapason. At the same time for weak H-bonds electron density values belong to 0.006-0.019 a.u. and laplacian of electron density values belong to 0.009-0.052 a.u. Comparability of values in both cases shows us the necessity of QTAIM usage in pair with NBO-analysis for identification and investigation of weak H-bonds nature. Although this fact doesn't diminish the value of QTAIM analysis as most generic and relatively cheap method for modeling electronic clouds.

We'll add that for CH...O/N contacts we found linear relation of H-bond energy E_{HB} from electron density in bond critical point ρ . Relations for data in table 1 are $E_{HB}^{CH...O} = 175.121 \cdot \rho + 0.107$ and $E_{HB}^{CH...N} = 163.684 \cdot \rho - 0.044$ with RMSD values of 0.0003 kcal/mol and 0.0043 kcal/mol respectively. Data extrapolation on base of these relations to minimal electron density value of $\rho = 0,002$ a.u. gives adequate minimal H-bond energy values of $E_{HB}^{CH...O}(\text{min}) = 0,46\text{kcal/mol}$ and

$$E_{HB}^{CH...N}(\text{min}) = 0,28\text{kcal/mol}.$$

Table 2

Stabilization energies $E^{(2)}$ and linear Grunenber constant Cstr values for intermolecular CH...O/N H-bonds in $m^1\text{Cyt}\cdot m^1\text{Cyt}$ homoassociates (calculations on B3LYP/6-311++G(d,p) theory level)

Complex	AH...B	$E^{(2)}$, kcal/mol	Cstr, Å/mdyn
3	C1H...O2	0.00	210.862
4	C1H...N3	3.32	11.904
6	C5H...N3	0.96	56.735
8	C5H...O2	1.79	35.720
9	C6H...O2	2.36	29.497
	C1H1...O2	0.37	66.103
10	C1H...O2	0.16	55.063
	C1H...O2	0.08	81.740
	C1H...N3	0.21	58.270
11	C1H...O2	0.06	233.045
12	C6H...O2	3.03	20.523
	C1H1...O2	0.42	71.288
14	C6H...O2	3.30	16.476
	C1H1...O2	0.60	42.019
15	C6H...O2	4.41	9.990
	C1H1...N3	0.89	49.176
18	C5H...N3	5.53	8.214
19	C1H...O2	1.66	14.329
	C1H...O2	1.62	15.430

Table 2 (End)

Complex	AH...B	E ⁽²⁾ , kcal/mol	Cstr, Å/mdyn
21	C5H...N3	1.46	18.925
22	C1H...O2	1.41	14.395
	C1H...O2	1.35	14.539
23	C1H...O2	1.12	25.317
	C1H...O2	2.49	13.805
28	C1H...N3	0.90	17.845
29	C1H...N3	1.08	56.163
34	C1H...O2	0.51	30.099
	C1H...O2	0.75	24.909
35	C1H...O2	0.72	21.020
37	C1H...O2	0.71	21.897

Interpretation of classic mass-spectrometry experiment. In [1, 6, 7] is described mass-spectrometry experiment with registration of associating biomolecules in vacuum. In this experiment reaction $m^1\text{Cyt} + m^1\text{Cyt} \leftrightarrow m^1\text{Cyt}\cdot m^1\text{Cyt}$ has been registered and it's reported standard enthalpy of formation has value of $\Delta H = 73,3 \text{ kJ/mol}$ for $T=383\text{K}$. Basing our hypothesis on population value of most energetically favorable homoassociate 1, we calculated for it standard enthalpy of formation with account of so-called BSSE correction. We report theoretical value of $\Delta H = 72,09 \text{ kJ/mol}$ which coincides with experimental value with precision of 1.65%. This tells us that experimental value of standard enthalpy of formation corresponds to most energetically favorable complex 1 (table 1, pic. 1). By the way, exceptional coincidence of theoretical and experimental data which were obtained through extrapolation on zero field technique points on legitimacy of the last.

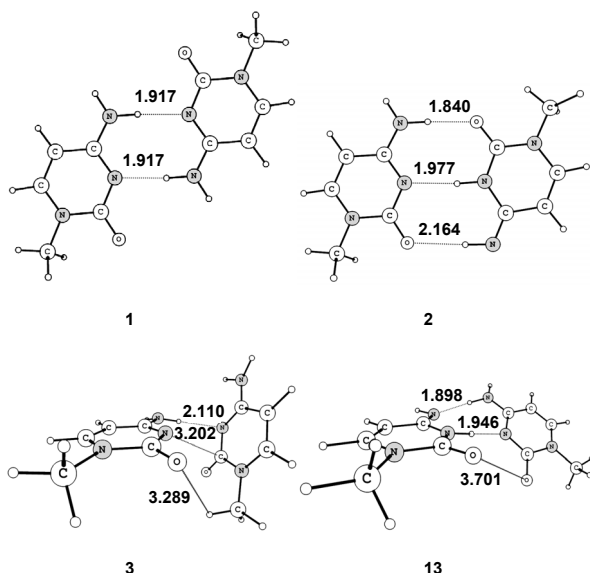


Fig. 1. Chosen $m^1\text{Cyt}\cdot m^1\text{Cyt}$ homoassociates (see also tables 1 and 2).

Intermolecular H-bonds and van-der-Waals contacts are depicted by dotted lines. Their distances H...B and A...B are shown in Å.

Spontaneous point mutations theory. Obtained data is also useful in spontaneous point mutations theory which is today far from it's complete and non-contradiction state. Such in paper [16] propeller-like homoassociate is postulated. It's so-called short Watson-Crick pair of

Cyt·Cyt* which is stabilized by two H-bonds N3 H...N3, N4 H4-1...N4 and van-der-Waals contact O2...O2 and is transversion. Our data shows that this same complex is homoassociate 13 ($\Delta G^0=8,83 \text{ kcal/mol}$) and is most energetically favorable among all other homoassociates with syn-oriented glycosidic bonds N1-C1m. This fact strongly evidences against all other possible alternatives and pair of Cyt·Cyt* is responsible for spontaneous point mutations of this type during DNA biosynthesis.

Conclusions. First to obtain complete family of $m^1\text{Cyt}\cdot m^1\text{Cyt}$ homoassociates for standard conditions. Complete family contains 37 structures with relative Gibbs free energies in $0\div 34,42 \text{ kcal/mol}$. Homoassociates are stabilized through classic (NH...N; NH...O; OH...N; OH...O) and weak (CH...N; CH...O) H-bonds as well as van-der-Waals contacts. It's shown that sugar-replacing methyl group is proton donor in H-bonds and influences Gibbs distribution for homoassociates. We show that QTAIM theory should be used in concert with NBO-analysis while investigating specific intermolecular contacts. Linear relation between CH...O/N H-bond energy EHB and electron density in bond critical point ρ . First to interpret theoretically result of classical mass-spectrometry experiment (L.F. Sukhodub et al., 1976). Showed theoretically that homoassociate $m^1\text{Cyt}\cdot m^1\text{Cyt}^*$ is responsible for spontaneous point mutations during DNA biosynthesis.

REFERENCE:

1. Biomolecules interactions. New experimental approaches and methods (in russian) / B. I. Verkin, I. K. Janson, L. F. Sukhodub et al. // K.: Naukova dumka, 1985. – P.164.
2. Bader R. F. W. Atoms in molecules – A quantum theory. / R.F.W. Bader // NY: Oxford University Press Inc., 1995. – P. 532.
3. Saenger W. Principles of nucleic acid structure / W. Saenger // NY: Springer-Verlag, 1984. – P. 556.
4. logansen A. V. Infrared spectroscopy and spectral hydrogen bond determination (in russian) / A.V. logansen / Hydrogen bond / under ed. Sokolova N.D. // M.: Khimia, 1981. – P. 112–155.
5. Weinhold F. Discovering Chemistry With Natural Bond Orbitals / F. Weinhold, C.R. Landis // New Jersey: John Wiley & Sons, Inc., 2012. – P. 350.
6. Sukhodub L.F. Mass-spectrometry study of nucleic bases interactions in vacuum (in russian) / L. F. Sukhodub, I. K. Janson // Stud. Biophys, 1976. – V.59. – P. 209–220.
7. Janson I.K. Stability row of nucleic bases pairs (in Russian) / I.K. Janson, L.F. Sukhodub // Dokl. AN SSSR, 1975. – № 223. – P. 1010-1013.
8. Compliance 2.0.3. [Електронний ресурс] – Режим доступу: <http://www.oc.tu-bs.de/Grunenberg/compliance.html>.
9. Frisch J.M. Gaussian 03, Revision E.01 / M. J. Frisch, G. W. Trucks, H. B. Schlegel et al. // Inc., Wallingford, CT. 2009. – V. 200.
10. Molecular Mechanics Investigation of an Adenine-Adenine Non-Canonical Pair Conformational Change / K. P. Van Nostrand, S. D. Kennedy, D. H. Turner, D. H. Mathews // J. Chem. Theory Comput, 2011. – V. 11. – P. 3779–3792.
11. Non-Watson-Crick Base Pairing in RNA. Quantum Chemical Analysis of the cis Watson-Crick/Sugar Edge Base Pair Family / J. E. Sponer, N. Spackova, P. Kulhanek, et al. // J. Phys. Chem. A, 2005. – V. 109. – P. 2292–2301.

12. *Principles of RNA Base Pairing: Structures and Energies of the Trans Watson-Crick/Sugar Edge Base Pairs* / J.E. Spomer, N. Spackova, J. Leszczynski, J. Spomer // *J. Phys.Chem. B.*, 2005. – V. 109. – P. 11399–11410.

13. *Boys S.F.* Calculation of Small Molecular Interactions by Differences of Separate Total Energies – Some Procedures with Reduced Errors / S.F. Boys, F. Bernardi // *Mol. Phys.*, 1970. – V.19. – P.553.

14. *Brandhorst K.* Efficient computation of compliance matrices in redundant internal coordinates from Cartesian Hessians for nonstationary points / K. Brandhorst, J. Grunenberg // *J. Chem. Phys.*, 2010. – V. 132. – P.184101.

15. *Brandhorst K.* How strong is it? The interpretation of force and compliance constants as bond strength descriptors. / K. Brandhorst, J. Grunenberg // *Chem. Soc. Rev.*, 2008. – V. 37. – P. 1558–1567.

16. *Brovarets' O.O.* Atomistic nature of the DPT tautomerisation of the biologically important C-C* DNA base mispair containing amino and imino tautomers of the cytosine: A QM and QAIM approach / O.O. Brovarets', D.M. Hovorun // *Phys. Chem. Chem. Phys.*, 2013. DOI: 10.1039/C3CP52644E

17. *Brovarets' O.O.* Intermolecular CH...O/N H-bonds in the biologically important pairs of natural nucleobases: a thorough quantum-mechanical study / O. O. Brovarets', Y. P. Yurenko, D.M. Hovorun // *Journal of Biomolecular Structure and Dynamics*, 2013. – <http://dx.doi.org/10.1080/07391102.2013.799439>

18. *Espinosa E.* Hydrogen bond strengths revealed by topological analyses of experimentally observed electron densities / E. Espinosa, E. Molins, E. Lecomte // *Chem. Phys. Letters.*, 1998. – Vol. 285. – P. 170–173.

19. *logansen A.V.* Direct proportionality of the hydrogen bonding energy and the intensification of the stretching (XH) vibration in infrared spectra / A.V. logansen // *Spectrochimica Acta Part A.*, 1999. – Vol. 55. – P. 1585–1612.

20. *Lemieux S.* RNA canonical and non-canonical base pairing types: a recognition method and complete repertoire / S. Lemieux, F. Major // *Nucleic Acids Research*, 2002. – V. 30. – P. 4250–4263.

21. *Leontis N.B.* Nomenclature proposal. Geometric nomenclature and classification of RNA base pairs. / N.B. Leontis, E. Westhof // *RNA*, 2001. – V. 7. – P. 499–512.

22. *Simon S.* How does basis set superposition error change the potential surfaces for hydrogen bonded dimers? / S. Simon, M. Duran, J. J. Dannenberg // *J. Chem. Phys.*, 1996. – V. 105. – P. 11024–31.

23. *Watson J.D.* Molecular Structure of Nucleic Acids: A Structure for Deoxyribose Nucleic Acid / J.D. Watson, F.H.C. Crick // *Nature*, 1953. – V. 171. – P. 737–738.

24. *Watson J.D.* Genetical Implications of the Structure of DNA / J.D. Watson, F.H.C. Crick // *Nature*, 1953. – V. 171. – P. 964–967.

Submitted on 14.02.14

Глушенков А., асп., Говорун Д., д-р біол. наук,
каф. біотехнології та біоінформатики, Інститут високих технологій
Київський національний університет імені Тараса Шевченка

ПОВНЕ СІМЕЙСТВО Н-ЗВ'ЯЗАНИХ ГОМОАСОЦІАТІВ 1-МЕТИЛЦИТОЗИНУ: КВАНТОВО-МЕХАНІЧНЕ ДОСЛІДЖЕННЯ

На рівні квантово-механічної теорії MP2/6-311++G(2df,pd)/B3LYP/6-311++G(d,p) в вакуумному наближенні вперше показано, що повне сімейство гомоасоціатів $m^1\text{Cyt}\cdot m^1\text{Cyt}$, стабілізованих специфічними міжмолекулярними контактами за нормальних умов, нараховує 37 структур в діапазоні відносних енергій Гіббса $0\text{--}34,42$ ккал/моль. Глобальному мінімуму енергії відповідає центросиметричний гомоасоціат, стабілізований парю антипаралельних Н-зв'язків N4H...N1: ентальпія його утворення практично співпадає із результатами мас-спектрометричного експерименту (Л.Ф. Суходуба та ін., 1976). Детально проаналізовано основні фізико-хімічні властивості міжмолекулярних, особливо слабких CH...O/N, Н-зв'язків. Коротко обговорюється застосування отриманих результатів в теорії спонтанних точкових мутацій ДНК.

Ключові слова: нуклеїнова основа, пара нуклеїнових основ, повне сімейство, водневий зв'язок, цитозин, метил-, метильна група.

Глушенков А., асп., Говорун Д., д-р біол. наук,
каф. біотехнології та біоінформатики, Інститут високих технологій
Київський національний університет імені Тараса Шевченка

ПОЛНОЕ СЕМЕЙСТВО Н-СВЯЗАННЫХ ГОМОАССОЦИАТОВ 1-МЕТИЛЦИТОЗИНА: КВАНТОВО-МЕХАНИЧЕСКОЕ ИССЛЕДОВАНИЕ

На уровне квантово-механической теории MP2/6-311++G(2df,pd)/B3LYP/6-311++G(d,p) в вакуумном приближении впервые показано, что полное семейство гомоассоциатов $m^1\text{Cyt}\cdot m^1\text{Cyt}$, стабилизируемых специфическими межмолекулярными контактами при нормальных условиях, насчитывает 37 структур в диапазоне относительных энергий Гиббса $0\text{--}34,42$ ккал/моль. Глобальному минимуму энергии соответствует центросимметричный гомоассоциат, стабилизирующийся парю антипаралельных Н-связей N4H...N1: энтальпия его образования практически совпадает с результатами масс-спектрометрического эксперимента (Л.Ф. Суходуба и др., 1976). Детально проанализированы основные физико-химические свойства межмолекулярных, особенно слабых CH...O/N, Н-связей. Кратко обсуждается применение полученных результатов в теории спонтанных точечных мутаций ДНК.

Ключевые слова: основание нуклеиновой кислоты, пара нуклеиновых оснований, полное семейство, водородная связь, цитозин, метил-, метильная группа.

UDC 57.042:57.024:615.21:612.821.5

V. Gorbachenko, stud., I. Chereda, stud.,
Department of Medical Radiophysics, Faculty of Radio Physics,
Electronics and Computer Systems, Taras Shevchenko National University of Kyiv
S. Vrublevsky, Lead. Engin., J. Kruchenko, Ph.D., E. Lukyanetz, Dr.Sci, Prof.
O. O. Bogomoletz Institute of Physiology, NAS of Ukraine

DEVELOPMENT AND TESTING OF THE EXPERIMENTAL SYSTEM FOR REGISTRATION OF FOOD REFLEX IN RATS

Automated system for registration of behavioural feeding response in rats designed and developed. The system includes the specialized hardware and software. The testing of the system is conducted.

Keywords: cognitive abilities, food reflex, rat, photoelectric registration.

Introduction. According to the World Health Organization, currently about 450 million people worldwide suffer from mental and neurological disorders, the most widespread are cognitive impairment. Among those it should be mentioned the diseases such as ischemia, Alzheimer's disease, Parkinson's disease, neuropathy and others [2]. However, the molecular mechanisms involved in the abnormal neurogenesis of various nervous diseases are not yet fully understood. In this connection, it is relevant to study the mechanisms of nervous diseases that are the basis of integrative brain function in the implementation of complex behaviors in normal and most common

neurodegenerative pathologies. For recording of the changes in the functioning of the brain and cognitive abilities the study of complex behaviors in animals are used. The aim of given work was to create a registration system of food behavioral responses of rats for the automatic recording of the time characteristics of a conditioned reflex movements and manipulations of rat. Comparing the characteristics for control animals and animal model (with induced disease of the nervous system) makes it possible to evaluate objectively the disruption of the brain function during pathologies and to assess the cognitive abilities of experimental animals. This system

© Gorbachenko V., Chereda I., Vrublevsky S., Kruchenko J., Lukyanetz E., 2014

allows to test new pharmacological agents and drugs for their ability to prevent the development of severe pathologies of the brain.

Experimental results and discussion. To perform the required tasks we used the methods of electronic circuit design, software development, programming of the microcontroller and the method a conditioned food reflex in rats.

We developed the system for estimation of cognitive properties of experimental rats called the feeder. It is shown on the figure below, Fig. 1. Feeder consists of the following areas: the area of electronics and power supply; zone of the stepper motor; zone of plates with cells for food; the area of a chamber with a hole for food, in which a rat is located. The general block diagram of the developed experimental setup is presented on Fig. 1.

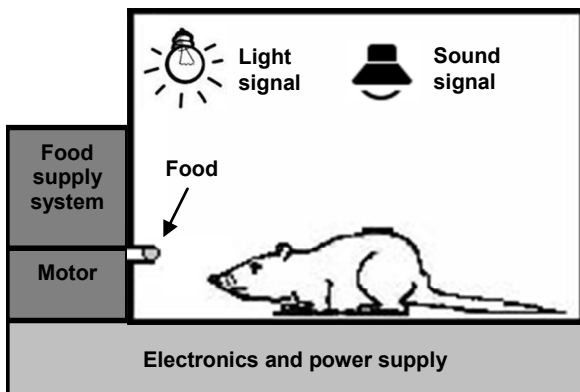


Fig. 1. The general block diagram of the experimental setup

Area of electronics and power supply consists of two power supplies (5V DC, 2A and 24V DC, 2A); the controller for the stepper motor; control board with microcontroller ATMEGA8A, firm ATMEL for operation of food feeder, audio and light stimuli, and Infrared (IR) sensors, Fig. 2. IR sensors, sound and light sources were used for stimulation and registration of rat behavior.

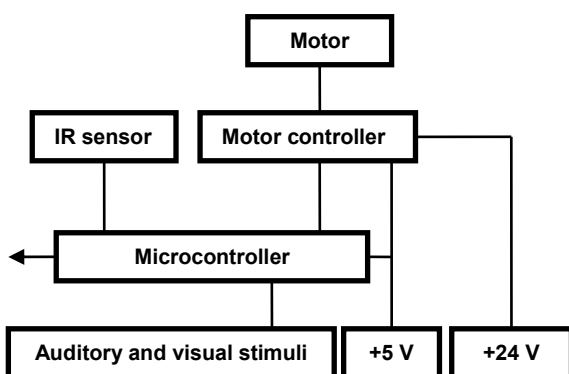


Fig. 2. The general block diagram of the area of electronics

The concept of system operation is the following: after presenting the audio or light signal, the rat with produced a food conditioned reflex, has approached the feeding hole and tried to get the food ball by mouth or paw [1]. The events in the feeding hole are registered by the photocell. Schematic representation of the block diagram of the electronic area is shown on Fig. 3.

On the scheme there are presented the audio or visual stimulus that triggers registration (Fig. 3 A); the latent period (time for a new movement of searching in the feeder

(Fig. 3 B); the intersection of a ray of light (photocell registration) number of intersections – search movements and time spent on obtaining food are pointed by dashes (Fig. 3 C); the motor activity of rat in interpulse period (MI) (6–80 sec), moving around the chamber, and the number of search movements (Fig. 3 D).

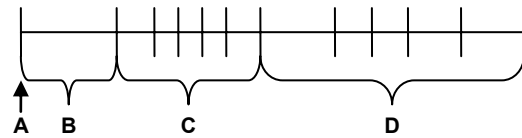


Fig. 3. Schematic representation of the course of the experiment

Figure 4 shows the photoelectric recording process of getting the food by rat. To register the events the following parameters were used (Fig. 4): *r* – obtaining of food ball from empty feeder; feeder charged with food ball; *r + p* – getting from charged feeder; arrows point the charging feeder with food and obtaining of food ball by animal; *RD* – summary duration of food getting; *TRr* – summary interval between attempts of food getting; *RN* – number of attempts required for obtaining the ball; *RT* – the time between the first attempt and the final disposal of the ball; *IRI*– interval between attempts.

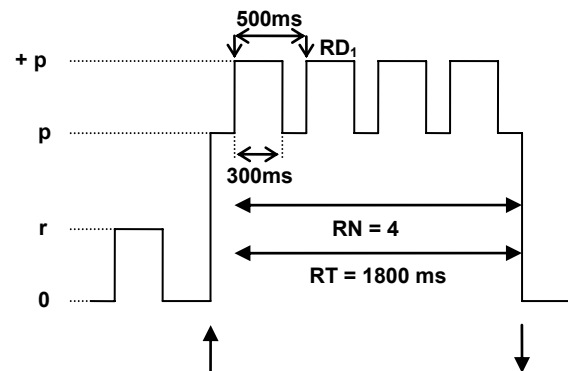


Fig. 4. Photoelectric registration of obtaining food

The software for the microcontroller is written with using the environment IDE AVRStudio 4. This software supports the work of feeder, namely controls positioning feeder and registration of events, such as the presence or absence of food, the presence or absence of legs in the hole for food, "RESET" position of feeder, closed shutter position of feeder, feed ready position. Serial data transfer to the computer is implemented in the software. Acceptance of data from the computer occurs through the interrupts.

Computer software written by the environment of Borland C++ Builder 6. The exchange of data through the serial port is implemented with a WINAPI. The software is called "KORMUSE" and consists of five Units, each of which performs its functions. Unit 1 – is the main program form. It is the main menu, the indicators, parameters, experiment control and log of the data exchange between MCU and PC via the serial port are presented. Unit 2 - the window setting serial port. It is possible to set the number of the serial port and communication speed. Unit 3 – the window with experimental data, log events. In this window all the events registered with system are recorded. Unit 4 – the protocols of the experiment setup. In this window, different experiment settings, time delays and control of a sound and light stimulus can be set. Unit 5 – experimental

data statistics. In this window, statistical processing of experimental data are performed.

Developed system was tested on animals. As testing animals, the male Wistar rats aged 5 months were used. In these rats previously the conditioned food reflex was worked out. Studies of the dynamics of conditioned-reflex activity of rats in the experimental chamber were fulfilled using the developed Feeder system. The obtained numeric results are presented in Tab. 1. The designations of measured parameters correspond to those on Fig. 4. As can be seen from the Tab. 1 we measured parameters *RD*, *TRr*, *RN*, *RT* and *MI*. The data shows that rat took out the food in the average of two attempts (*RN*), the time of getting out of food was quite long and was about 1600 ms (*RD*). Also important to note the high activity of rat that tried to get the food at a time when the feeder was closed. The average number of such attempts was 14 (*MI*).

Table 1

Numerical characteristics
of the conditioned reflex of the rat

Parameter / attempt	RD, ms	TRr, ms	RN	RT, ms	MI
1	1750	0	1	1750	11
2	2016	0	1	2016	29
3	1969	251	5	2220	10
4	875	0	1	875	10
5	1489	327	2	1816	11
mean	1619	116	2	1735	14
± SE	± 208	± 72	± 1,7	± 230	± 4

The data from the Tab. 1 were graphically presented in Fig. 5.

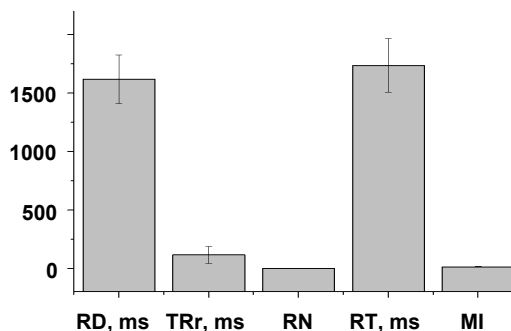


Fig. 5. Graphical representation of results

Conclusions. It was developed the automated registration system for registration of food behaviors of rats, analogues of which did not exist.

Testing of the system has shown its efficiency and effectiveness in the use of automated quantitative assessment of behavioral responses of rats.

The numerical parameters estimating the food conditioned reflex in rats were obtained with using the developed system.

REFERENCE:

1. Bures J. Techniques and basic experiments for the study of brain and behavior / J. Bures, O. Bureshova, D. P. Houston // Vysshaya Shkola, Moscow, 1991, – P. 216–220. (in Russian).
2. Kostyk P.G. Calcium ions in brain function – from physiology to pathology / P. G. Kostyk, E. P. Kostyuk, E. A. Lukyanetz // Kyiv: Naukova Dumka, 2005, – P. 99–152. (in Ukrainian).

Submitted on 09.10.14

Горбаченко В., студ., Черета І., студ.,
каф. медичної радіофізики, факультет радіофізики, електроніки та комп'ютерних систем,
Київський національний університет імені Тараса Шевченка
Врублевський С., пров. інж., Крученко Ж., канд. біол. наук, Лук'янець О., д-р біол. наук, проф.,
Інститут фізіології ім. О.О. Богомольця НАН України

РОЗРОБКА ТА ЕКСПЕРИМЕНТАЛЬНА АПРОБАЦІЯ СИСТЕМИ РЕЄСТРАЦІЇ ХАРЧОВОГО РЕФЛЕКСУ ЩУРІВ

Розроблено та створено автоматизовану систему для реєстрації поведінкової харчової реакції щурів. Система включає спеціалізоване обладнання та програмне забезпечення. Проведена апробація системи.

Ключові слова: когнітивні здібності, харчовий рефлекс, щур, фотоелектрична реєстрація.

Горбаченко В., студ., Черета І., студ., каф. медицинской радиопизики, факультет радиопизики, электроники и компьютерных систем,
Киевский национальный университет имени Тараса Шевченка
Врублевский С., вед. инж., Крученко Ж., канд. биол. наук, Лукьянец Е., д-р биол. наук, проф.,
Институт физиологии им. А. А. Богомольца НАН Украины

РАЗРАБОТКА И ЭКСПЕРИМЕНТАЛЬНАЯ АПРОБАЦИЯ СИСТЕМЫ РЕГИСТРАЦИИ ПИЩЕВОГО РЕФЛЕКСА КРЫС

Разработана и создана автоматизированная система для регистрации поведенческой пищевой реакции крыс. Система включает специализированное оборудование и программное обеспечение. Проведена апробация системы.

Ключевые слова: крыса, когнитивные способности, пищевой рефлекс, фотоэлектрическая регистрация

UDC 53; 547.136.13; 576.535; 577.037

A. Goriachko, Ph.D., P. Melnik, Ph.D., R. Sydorov, stud.,
O. Popova, stud., M. Nakhodkin, Dr.Sc., Acad. of NAS
Department Nanophysics and Nanoelectronics,
Faculty of Radiophysics, electronics and computer systems,
Taras Shevchenko National University of Kyiv

A NOVEL NANOPositionING SYSTEM FOR SCANNING PROBE MICROSCOPY

We describe a new original design of the nano-positioning device to be used in scanning probe microscopy applications. It consists of four piezoelectric elements producing linear displacements, which are mechanically combined to obtain fully independent positioning capability along three orthogonal axes. The new device is ultra-compact, ultra-high vacuum compatible, and does not require any expensive parts to produce it. We report the results of preliminary testing of the scanning tunnelling microscope equipped with the novel nano-positioning system, which was used to obtain images of the graphite (0001) surface in ambient environment and the Ge(111) surface in ultra-high vacuum conditions.

Keywords: scanning probe microscopy, piezoelectric effect, nano-positioning, ultra-high vacuum

© Goriachko A., Melnik P., Sydorov R., Popova O., Nakhodkin M., 2014

Introduction. Investigating matter at nano-scale is becoming ever more important in modern scientific endeavor. The nanostructures on solid surfaces can be researched in great detail by a group of techniques usually referred to as scanning probe microscopy (SPM). Among them are the scanning tunneling microscopy (STM) and the atomic force microscopy (AFM), which can routinely achieve atomic resolution on various solid surfaces.

All SPM techniques rely on the so-called "scanning" procedure, being essentially a controlled movement of a very sharp tip in a very close proximity to the surface of investigated sample. In order to obtain an image, one has to be able to move (scan) the tip independently in any orthogonal direction with a precision of ~0.01 nm. The easiest way to achieve this is to utilize an inverse piezoelectric effect, therefore, most SPMs are equipped with piezoelectric scanners. In Fig. 1, we summarize the previous known designs of piezoelectric scanners most often used in practical SPMs. They allow to move the probe tip relative to the investigated sample with the above mentioned precision, while a typical travel range is equal to several micrometers.

Historically, the first type of scanner was a tripod combination of three linear piezoelectric drives (Fig. 1a). These drives are attached to each other within the holder of the SPM probe tip, while their other sides are fixed to orthogonal reference planes. The simplest drive consists of a slab of some piezoelectric material with two of its opposing sides being covered by metal electrodes, to which a voltage can be applied. In this way, each individual drive can be independently elongated or contracted, thus moving the probe tip along the corresponding orthogonal axis. The linear drives are cheap and readily available, making the tripod scanner an easy option in SPM design. However, the tripod is problematic in terms of spatial limitations in ultra-high vacuum (UHV) microscopes, the latter being severely constrained by the inner diameter of the vacuum chamber flange.

The tube scanner (Fig. 1b) is by far the most often used type of scanner in modern SPMs. It consists of the piezoelectric material of the tubular shape, with inner and outer metallic electrodes, one end of the tube being fixed to the reference plane. The inner electrode is continuous, but there are four separate outer electrodes, each covering one fourth of the tube's outer perimeter. Normally, the inner electrode is grounded, so applying independent voltages to outer electrodes, one causes independent contraction or elongation of the tube's quarters. Inequivalent deformation of different quarters leads to bending of the entire tube. The direction of bending relative to the tube's axis is determined by voltage differences on the pairs of opposite outer electrodes. The magnitude of bending is negligible on the scale of tubes' dimensions, which is why such bending is equivalent to linear movement of the tube's free end in the plane perpendicular to the tube's axis.

This provides for the probe tip movement along two orthogonal axes (normally X, Y within the surface plane of the sample). Simultaneously, changing the average voltage on all four outer electrodes, leads to scanner's tube contraction or elongation as a whole, being equivalent to the movement of the tube's free end (where the probe tip is attached to) along the symmetry axis (normally Z axis perpendicular to the sample's surface).

Similar to the tube scanner in terms of the operation principle is the cross scanner (Fig. 1c). Instead of a tube, the piezoelectric material is shaped as a cross, which is extruded along the Z axis. One end of the scanner is firmly attached to the reference plane, while the other end (where the probe tip sits) is free to move according to actual deformations of the cross' four bars: X1, X2, Y1 and Y2.

The latter can be addressed individually by applying voltages to their corresponding electrodes. Low magnitude bending of this scanner relative to its symmetry axis is equivalent to the movement of its free end within the plane, which is perpendicular to the axis (XY plane). Contraction or elongation of the scanner as a whole shifts its free end along the Z axis. In a nutshell, it is possible to set the XYZ coordinates of the scanner's free end in an arbitrary manner (within the maximum travel range) by setting the voltages on the X1, X2, Y1 and Y2 bars according to a specific algorithm.

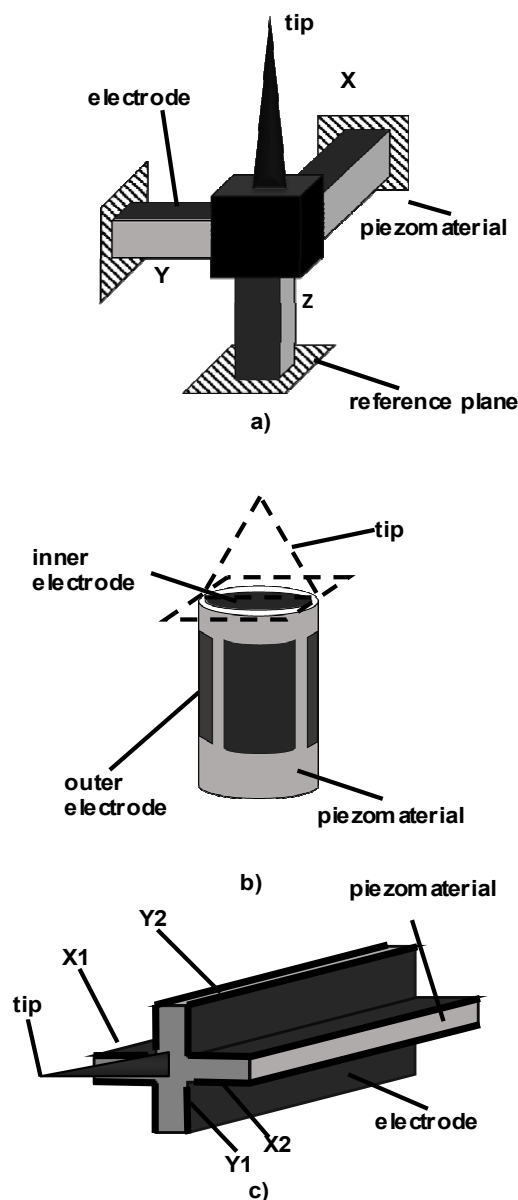


Fig. 1. Previously existing types of nano-positioning systems (scanners) for scanning probe microscopy:
a) tripod; b) tube ; c) cross

The tube and cross scanners are rather compact, thus being favorable for use in the UHV compatible SPMs. However, their production involves a sophisticated machining of the piezoelectric material, resulting in expensive devices. The major goal of the present work, was creation and testing of the new type of scanner, which would combine the compact shape of the cross scanner, but will be built as a combination of inexpensive linear piezoelectric drives.

Basic principles of the new nano-positioning system. The pivotal idea of the new nano-positioning device is to achieve a full three-dimensional positioning capability by combination of tilting with elongations or contractions. A proposed device (Fig. 2a) consists of the central cross-bar and the bridge (both made of stainless steel, aluminum, etc.) and four linear piezoelectric drives (similar to the ones used in the tripod scanner). A pair of two opposite drives has their lower ends glued to the reference plane, while their upper ends support the shoulders of the cross-bar. In its own turn, the lower part of the freely suspended cross-bar serves to support another orthogonal pair of linear drives. The latter are joined by the bridge above the cross-bar.

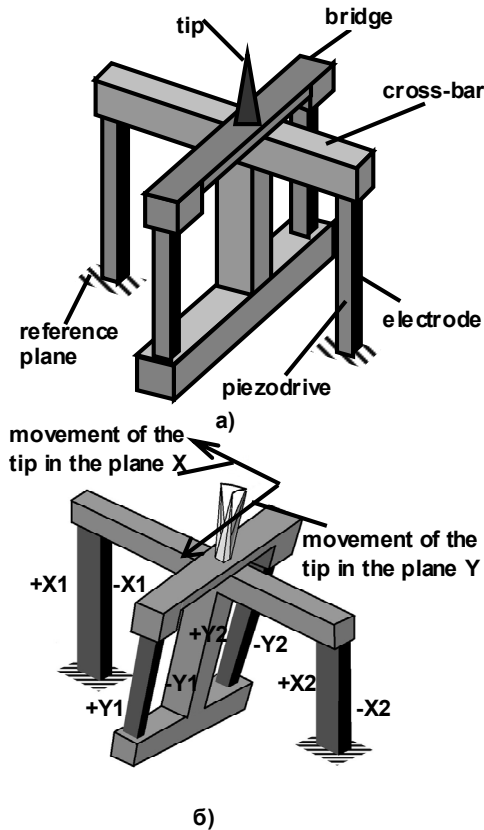


Fig. 2. The new proposed cross-bar type of scanner for nano-positioning in scanning probe microscopy:

- a) general scheme of the scanner with the probe tip;
- b) translation of tilting in different directions into linear movements of the tip within the XY plane of the sample's surface

The operation principle of the cross-bar scanner is depicted in Fig. 2b. If X drives are contracted/elongated to a different extent, the cross-bar becomes tilted together with another pair of drives and the bridge, which supports the SPM tip. As the magnitude of tilting is infinitesimal, it is equivalent to moving the tip along the X axis. If the Y drives are contracted/elongated to a different extent, only the bridge will be tilted, but in direction orthogonal to that described above. This is equivalent to the tip being moved along the Y axis. Finally, the tip's position along the Z axis is determined by the sum of average lengths of both pairs of piezoelectric drives.

In the following we describe the electrical addressing scheme of the piezodrives in the cross-bar scanner, which allows to set all three orthogonal coordinates of the tip independently (Fig. 3). The positive electrodes of all four piezodrives are connected together and biased by the UZ voltage source. The negative electrodes are biased separately by their respective voltage sources: UX1, UX2,

UY1 and UY2. At any given value of UZ, the difference between UX1 and UX2 (or UY1 and UY2) will determine the X (or Y) coordinate of the tip. Also, changing the UZ at any given set of values UX1, UX2, UY1 and UY2 will change the Z coordinate of the probe tip.

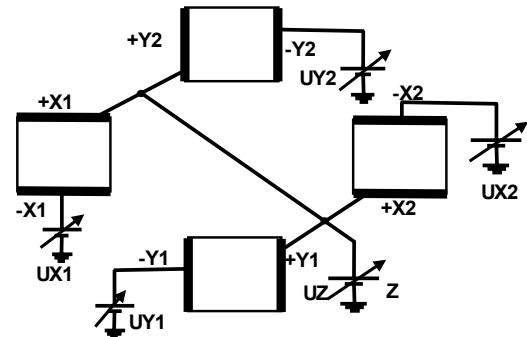


Fig. 3. Electrical addressing scheme of individual piezoelectric drives within the cross-bar scanner

The UX1 and UX2, or UY1 and UY2 are pairs of complementary voltages: if UX1 (UY1) is increased, then UX2 (UY2) is decreased correspondingly. This introduces unequal lengths within the X (Y) pair of piezoelectric drives and thus, tilting of the cross-bar and the bridge. In the limit of infinitesimal tilt, there is a linear dependence of X and Y coordinates on UX1, UX2, UY1 and UY2 voltages (Fig. 4). Due to the complementarity of the UX1 and UX2, or UY1 and UY2 voltages, their average remains constant. This leads to linear dependence of the tip's Z coordinate on the UZ voltage (Fig. 4). To avoid depolarization of the piezoelectric material, the minimum possible value of UZ must be higher than the maximum possible value of UX1, UX2, UY1 and UY2.

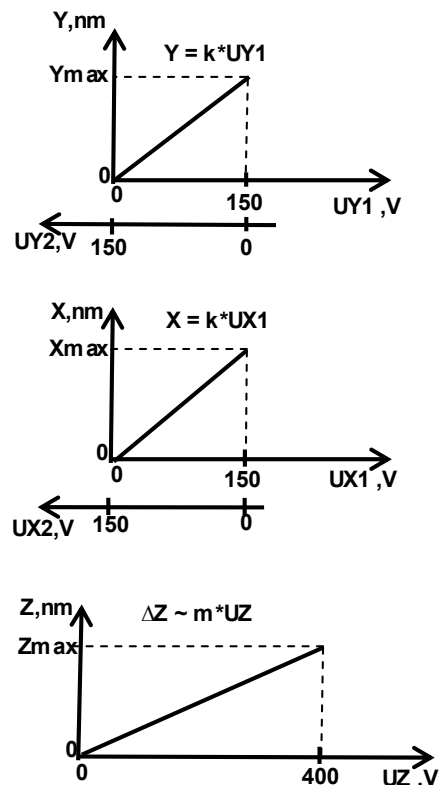
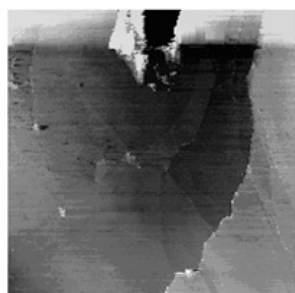


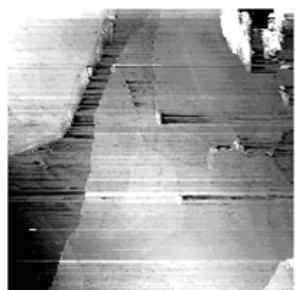
Fig. 4. Dependencies of X, Y and Z coordinates of the tip on the voltages supplied to the cross-bar scanner

Experimental. We have used simple home-made linear drives consisting of a PZT-type piezoelectric material (size: 14 mm x 1mm x 1mm) with two opposite sides covered by silver electrodes. They were glued to the cross-bar and the bridge by means of two-component UHV-compatible epoxy. This assembly was used as a scanner of a home-built STM mounted on the 6" conflate-type flange of the UHV chamber with the base pressure of 3×10^{-10} mbar. The UX1, UX2, UY1, UY2 and UZ voltages were supplied by the STM control unit, the maximum values of UX1, UX2, UY1 and UY2 being equal to 150 V, while the maximum value of UZ was equal to 400 V.

The scanner was tested for operation at 300 K in the ambient and UHV environments. The probe tip was hand-cut from the wire composed of 80% Pt and 20% Ir. Two samples were investigated: highly oriented pyro lithic graphite (HOPG) and p-type Ga-doped Ge(111). The fresh (0001) natural cleavage surface of HOPG was obtained by simple detachment procedure using the scotch tape. The Ge(111) wafer was cleaned in-situ by 500 eV Ar⁺ ion bombardment and annealing at 900K.



a)



b)

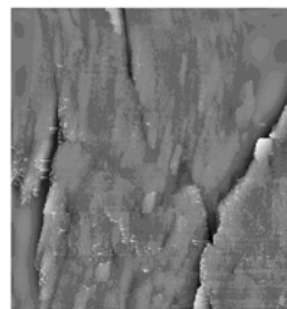


c)

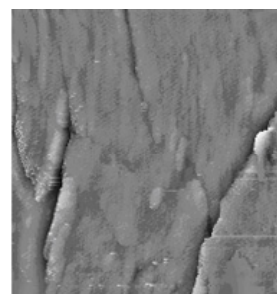
Fig. 5. a-c: Consecutive STM images of the HOPG(0001) surface.

The 1.5 μm x 1.5 μm imaged area is shifted from a) through c) due to thermal drift. Sample bias voltage U = 50 mV, tunneling current 5 nA.

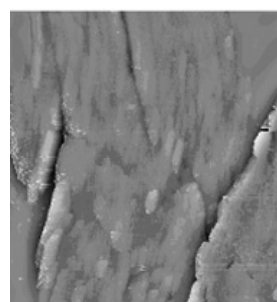
The problem of rapid thermal drift is substantially reduced when the STM is operated in UHV, which improves the thermal isolation from the ambient environment. This is demonstrated by three consecutive images of the Ge(111) surface in Fig. 6a, 6b and 6c (image size 1.5 μm x 1.5 μm), with no substantial shifts of the imaged area. A smaller area (100 nm x 100 nm) on the same sample shows three atomically flat terraces separated by two single atomic steps (Fig. 7). Although atomic-size objects are plentiful on every terrace, no long range order is observed, indicating that the topmost layer of germanium sample is amorphous.



a)



b)



c)

Fig. 6. a-c: Consecutive STM images of the Ge(111) surface. The image size is 1.5 μm x 1.5 μm, sample bias voltage U = 2.5 V, tunneling current I = 0.5 nA. No thermal drift is noticeable from a) through c).

Conclusions. In this work we have successfully designed and constructed a new type of the nano-positioning device (scanner) for applications in scanning probe microscopy. Its functioning was tested in the scanning tunneling microscope both in ambient and UHV environments. The obtained images of HOPG(0001) and Ge(111) show atomically flat terraces and single atomic steps.

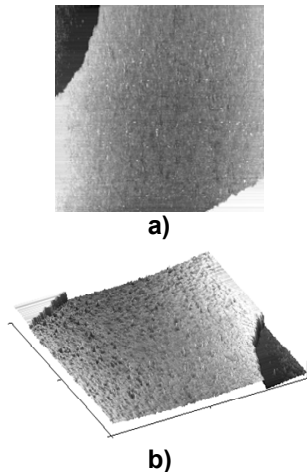


Fig. 7. STM images of the Ge(111) surface.

The image size is 100 nm x 100 nm, sample bias voltage $U = 2.5$ V, tunnelling current $I = 0.5$ nA. a) grey-scale representation of the surface topography: brighter areas are closer to the viewer; b) 3D reconstruction of the surface topography.

Горячко А., канд. фіз.-мат. наук, Мельник П., канд. фіз.-мат. наук, Сидоров Р., студ., Попова О., студ., Находкін М., д-р фіз.-мат. наук, проф. акад. НАНУ каф. нанозфізики та наноелектроніки, факультет радіофізики, електроніки та комп'ютерних систем Київський національний університет імені Тараса Шевченка

НОВІТНЯ СИСТЕМА НАНОПОЗИЦІОНУВАННЯ ДЛЯ СКАНУЮЧОЇ ЗОНДОВОЇ МІКРОСКОПІЇ

Описано новий оригінальний пристрій нанопозиціонування для застосування у скануючій зондовій мікроскопії. Пристрій складається з чотирьох п'єзо-електричних приводів лінійного переміщення, що механічно комбінуються в переміщення зонду скануючого мікроскопу уздовж трьох ортогональних осей у просторі. Така система є надкомпактною, сумісною із надвисоковакуумним обладнанням та не містить компонентів високої вартості. Попереднє тестування проводилося в скануючому тунельному мікроскопі на поверхнях графіту (0001), у повітряному середовищі та германію (111), у надвисоковакуумному середовищі.

Ключові слова: скануюча зондова мікроскопія, п'єзоелектричний ефект, нано-позиціонування, надвисокий вакуум.

Горячко А., канд. физ.-мат. наук, Мельник П., канд. физ.-мат. наук, Сидоров Р., студ., Попова О., студ., Находкин Н., д-р физ.-мат. наук, проф. акад. НАНУ каф. нанозфізики и наноелектроніки, факультет радиофизики, электроники и компьютерных систем Киевский национальный университет имени Тараса Шевченко

НОВАЯ СИСТЕМА НАНОПОЗИЦИОНИРОВАНИЯ ДЛЯ СКАНИРУЮЩЕЙ ЗОНДОВОЙ МИКРОСКОПИИ

Описывается новое оригинальное устройство нанопозиционирования для применения в сканирующей зондовой микроскопии. Устройство состоит из четырех пьезоэлектрических приводов линейного перемещения, которые механически комбинируются в перемещение зонда сканирующего микроскопа вдоль трех ортогональных осей в пространстве. Такая система является сверхкомпактной, совместимой со сверхвысоковакуумным оборудованием и не содержит компонентов высокой стоимости. Предварительное тестирование проводилось в сканирующем туннельном микроскопе на поверхностях графита (0001), в воздушной среде и германия (111), в условиях сверхвысокого вакуума.

Ключевые слова: сканирующая зондовая микроскопия, пьезоэлектрический эффект, нано-позиционирование, сверхвысокий вакуум.

UDC 537.525:621.325

S. Denbnovetskiy, Dr. of Tech. Sc.,
I. Melnyk, Dr. of Tech. Sc., S. Tuhai, Ph.D.
Electronic Devices Department, Electronic Faculty,
National Technical University of Ukraine "KPI", Kyiv

ANALYTICAL RELATIONS FOR CALCULATION THE ENERGETIC EFFICIENCY OF TRIODE GLOW DISCHARGE ELECTRON GUNS

Dependences of energetic efficiency of triode high-voltage glow discharge electron guns from acceleration voltage, operation pressure and from voltage on additional electrode have been obtained and presented in the article. Obtained mathematical model is formed by analytical solving of algebraic equations, which is a result of consideration of equations of ions balance in anode plasma and equation of discharge self-consistency. Obtained simulation results are shown, that the energetic efficiency of triode glow discharge electron guns is lead in range 80–90%, therefore such type of electron guns can be successfully used in the modern electron-beam technologies.

Keywords: electron guns, electron-beam technologies, high voltage glow discharge, anode plasma, triode electrode system

Introduction. Glow discharge electron guns (GDEG) are widely used in industry for providing different technological operations, such as: effective, high-rate and high-quality welding in the soft vacuum; refusing of refractory materials; deposition of high-quality ceramics films and coatings in the

soft vacuum; high-rate annealing of items in the soft vacuum [1, 2, 5, 6, 12–15]. Great interest to development and applying in industry of high voltage glow discharge (HVGD) electron guns is caused by many important advantages, which are difference such type of guns from the traditional

guns with heated cathodes. Among these advantages most important are follows.

1. GDEG operated in the medium of soft vacuum, range of 1–10 Pa, with acceleration voltage range of 5–30 kV [1, 2, 12, 13]. Therefore, low cost, simple evacuated systems are suitable for providing the operation of GDEG. Usually level of vacuum is defined by the requirement of realised technological process.

2. GDEG can successfully operate in the medium of different gases, including active and noble ones, dependence on the requirement of technological process [2, 5, 6 12].

3. Relative simplicity of guns' construction and low cost of technological equipment [2, 5, 6, 12].

4. Simplicity of realising control of discharge current, and, as a result, of beam current, by changing the pressure of operation gas in the gun's volume. This control method is simply realised by changing the gas flux in the gun's volume with its uninterrupted pumping [2, 4].

Therefore, elaboration of HVGD electron guns and its applying in industry is the very actual scientific and technical problem for future development of modern electron-beam technologies [2, 6].

Problems and its' discussion. However, well-known gas-dynamic method of gun current control is very slow, usually time constant of current regulation is range of from hundreds millisecond to few second. Such slow regulation is explained by the low speed of gas-dynamic processes [4]. Such high value of time regulation constant is not suitable for modern electron-beam technologies [2, 5, 6, 13–15]. Therefore, many years ago was considered the possibility of fast electric control of HVGD current in more complicated triode electrodes systems by applying relatively small potential to the additional electrode [3]. Provided experimental investigations show, that for electrical control of the discharge current time regulation constant is much smaller, range of tens or hundreds microsecond. Therefore, using of triode GDEG in the modern electron beam technologies is really very promising [6, 14].

However, investigation of complex physical processes in the triode HVGD electrodes systems was provided only in last years and has been considered in papers [7, 9–11]. This advance caused by development of mathematical methods in computer-aided design (CAD) software, such as MatLab and other, which are allow today solving the complex physical problems, such as simulation of discharge systems with located plasma region and with interacted fluxes of charged particles. In the published papers the ion concentration in anode plasma is estimated by solving the algebraic equations of ions balance with taking into account the equation of discharge self-consistency. Firstly was found very important analytical relation for position of plasma boundary relative to the cathode [10]. When position of plasma boundary, and, certainly, plasma volume, is known, was obtained the correspondent simple relations for ion concentration [7, 9, 11], for current of main discharge and for current of additional discharge [9, 11].

Provided theoretical investigations allows to estimate the beam current of triode GDEG and its' energetic efficiency, and, finally, possibilities of its' applying in the modern electron-beam technologies. Complex methodology of estimation of triode GDEG parameters and characteristics was described in paper [7]. The aim of this article is considering of energetic efficiency of triode HVGD electrodes systems for different values of acceleration voltages and pressure of operation gas.

Analyzed physical processes in high-voltage glow discharge. For solving the task of analyzing the anode plasma parameters and for finding the energy distribution

in HVGD solving of equation system for ions' balance in the discharge gap with taking into account the condition of discharge self-consistency is necessary [8]. Therefore, writing and analyzing the equation of ion balance in the anode plasma in the first step of simulation is needed. It is well-known fact from HVGD theory, that anode plasma formed as a result of gas ionization by the several groups of electrons, including fast beam electrons and slow electrons, reflected from the anode [12]. In triode electrodes systems gas ionization in additional, non-self-maintaining discharge, also must be taking into account [10]. Among another discharge processes interaction of particles fluxes with themselves and with the electrodes surfaces are also very important and must be analysed [8, 10]. Anode plasma in the physical models of HVGD electrodes systems is usually considered as the source of ions and as transparent to electrons moving electrode with the fixed potential [1, 8, 10]. Among the fluxes interaction processes, the gas ionising by fast and slow electrons and the resonance recharging of accelerated ions' on the molecules of residual gas are very important [1, 7]. Among the processes, taking place at the electrodes surfaces, grate role play the emission of electrons from the cathode surface as a result of its' bombarding by the accelerated ions. Although emission of slow electrons from the anode surface as a results of its radiation by the flux of fast electrons must be also taking into account [1, 7–12].

Structure of investigated HVGD electrodes systems and its parameters. Therefore analyzing of necessary physical processes is very complex, for simplifying the theoretical estimations one-dimensional auxiliary triode HVGD system is considered [7, 9–12]. This is a system with plane cathode, cylindrical anode and with the ring-like additional electrode for lighting of low-voltage, non-self-maintained discharge. As must be pointed out, that different geometry of electrodes is also possible, but in any case for lighting of additional discharge the condition of hollow-cathode geometry must be fulfilled. For example, the system with the negative cylindrical hollow additional electrode was presented in the paper [3]. Anode plasma, as have been pointed out, considered as the moving virtual electrode with the fixed potential [1, 7–12]. Basic structure scheme of simulated HVGD electrodes system is presented at Fig. 1 [7, 9–11].

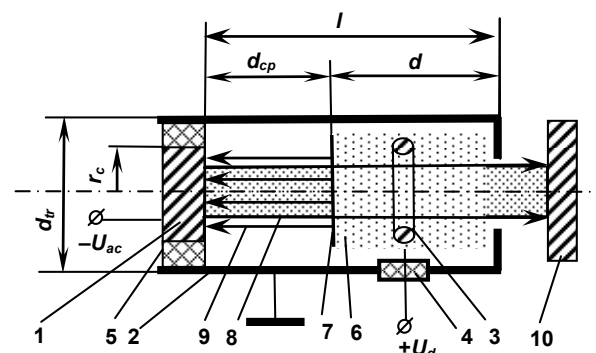


Fig. 1. Scheme of simulated HVGD triode electrodes system.

1 – cathode; 2 – HVGD anode; 3 – electrode for lighting of additional discharge; 4 – low-voltage insulator; 5 – high-voltage insulator; 6 – anode plasma; 7 – anode plasma boundary; 8 – electron beam; 9 – ion flux; 10 – treated item.

As have been pointed out, considered system contains three main electrodes: HVGD cathode 1, HVGD anode 2, which also can be considered as a cathode of additional discharge, and ring-like electrode 3 for lighting of additional

discharge. Negative acceleration voltage U_{ac} , which value for real electron guns usual lead in the range from 5 kV to 40 kV, applied to the cathode. Value of positive potential on the additional electrode U_d is significantly smaller, range of from tens to few hundreds V. Main internal parameter of considered HVGD system is the residual pressure in the discharge gap p_{a0} , which, taking into account the additional gas ionization in discharge, is usually in range 0.1 – 10 Pa [7, 9–13]. The low-voltage insulator 4 and high-voltage insulator 5 are established between electrodes for providing the conditions of dielectric strength. Anode plasma 6 is appeared as a result of gas ionization, and plasma boundary 7 in mathematical models is considered as ions' source and as additional virtual electrode with the fixed potential [1, 2, 7–12]. Electron beam 8 is formed as a result of electrons' emission from the surface of cathode 1, which bombarding by the ions flux 9. Finally, beam electrons are collected on the treated item 10.

Main geometric parameters of simulated HVGD electrodes system are also pointed out in Fig. 1. There are: longitudinal length of discharge gap l , its transversal diameter d_{tr} , longitudinal length of anode plasma d_p , distance from cathode to plasma boundary d_{cp} , as well as the cathode radius r_c . All these parameters will be used later for forming complex mathematical model of triode HVGD gap.

Basic equations of mathematical model of triode high-voltage glow discharge gap. For finding the currents of main and additional discharges information about the value of ions concentration in anode plasma and about its volume is necessary. It is clear from Fig. 1, that plasma volume in considered system is defined by transversal diameter of discharge gap d_{tr} and by the longitudinal plasma length d_p .

For defining of ions concentration in anode plasma and its longitudinal length consideration of ionization and diffusion processes in plasma volume is necessary [10, 12]. Therefore, the main equations of forming mathematical model are following.

1. Equation for balance of ions in anode plasma.
 2. Equation for describing the discharge self-maintaining and self-consistency.
 3. Equations for describing the elementary processes of fluxes of charged particles interactions with themselves.
 4. Equations for describing the elementary processes of fluxes of charged particles interaction with electrodes surfaces.
- During forming this equations system the main considered physical processes are follows.
1. Gas ionization by the fast beam electrons [7, 10].
 2. Gas ionization by the slow electrons, reflected from the anode surface [7, 10].
 3. Gas ionization in the additional discharge [7, 9, 10].
 4. Diffusion of ions from anode plasma in direction to HVGD anode [7, 9, 10].
 5. Resonance recharge of ions on the molecules of the residual gas [7, 10–13].
 6. Emission of electrons in the cathode surface, caused by its bombarding by accelerated ions [10, 12].

All this processes have been described complexly in the pervious section of this paper and must be included to forming mathematical model of discharge gap. It must be pointed out, that in pervious section only the main energetic and geometry parameters of formed mathematical model have been considered. Really described beyond physical processes are very complex and depended from many internal parameters of simulated

system, which defined by using electrodes materials and operation gas [7, 10, 12]. All these necessary model parameters will be considered and defined below.

For presented at Fig. 1 triode HVGD electrode system the equation of ions balance in the discharge gap can be written in the following form:

$$z_f + z_s + z_{dis} = z_{dif}, \quad (1)$$

with z_f – efficiency of gas ionization by fast electrons, z_s – efficiency of gas ionization by slow electrons, z_{dis} – efficiency of gas ionization in the additional discharge, z_{dif} – efficiency of leaving the ions from anode plasma as a result of diffusion process [7, 10, 12]. Relations for efficiency of gas ionization z_f , z_s , z_{dis} and of diffusion process z_{dif} can be written in the following form [7, 10]:

$$z_f = \frac{j_{ec} d_p p_{a0} A_i U_c^{-a_i}}{e} \left(1 + \eta (1 - f (1 - d_p p_{a0} Q_{ep0})) \right) \eta_i^a k_e, \quad (2)$$

$$z_s = \frac{d_p p_{a0} n_e}{4} \sqrt{\frac{8kT_e}{\pi m_e}} \frac{1}{Q_0}, \quad Q_0 = N_0 \alpha_i \left(U_i + \frac{2kT_e}{e} \right) e^{-\frac{eU_i}{kT_e}}, \quad (3)$$

$$z_{dis} = \frac{4\pi^3 e^4 n_i \mu_{i0} \gamma_a d_i U_d \ln \left(1.5 - \sqrt{\frac{kT_e (eU_d + kT_e)^3}{\pi p_{a0}}} \right)}{9kT_e d_p (eU_d + kT_e)}, \quad (4)$$

$$z_{dif} = \frac{\pi^2 n_i \mu_0 kT_e}{d_p p_{a0} e}. \quad (5)$$

where j_{ec} – density of electron current at the cathode surface, T_e – temperature of slow electrons in anode plasma, η_i and η_U – coefficients of electrons reflection from the anode by the current and by the voltage correspondently, f – transparent coefficient for anode plasma, Q_0 – cross-section of ions scattering at the residual gas molecules, k_e – coefficient of electrons' trajectories longitude, n_e – concentration of free electrons in anode plasma, U_i – potential of gas ionization, N_0 – Loschmidt constant, k – Boltzmann constant, A_i , a_i , q – empirical constants for defined operation gas and electrodes material, μ_0 – mobility of ions' in anode plasma, γ_a – secondary ion-electron emission coefficient from anode surface [2, 5–8]. The equation, described the self-consistent conditions of HVGD lighting, can be written in such form [7, 9, 10, 12]:

$$n_i = \frac{j_{ec} \sqrt{\frac{kT_e}{2m_e}}}{e (A_i U_{ac}^{-a_i} + 1)}, \quad (6)$$

where n_i – ions concentration in anode plasma, e and m_e – electron's charge and mass correspondently.

Equations system (1–6) is full, closed and self-maintained, and it can be solved relative to parameter d_p . With known plasma longitude size d_p ion concentration n_i also can be simply defined from equations (1–6).

Defining the size of anode plasma. With taking into account relations (2–5), equation of ions balance in anode plasma can be written in the form:

$$\frac{\pi^2 \mu_0 (kT_e + eU_d)}{(p_{a0} d_p)^2} \left(1 + \frac{\gamma d_{tr}}{\lambda} \right) - 3(kT_e + eU_d) \times$$

$$\times N_0 q \sqrt{\frac{e(kT_e + eU_d)}{2\pi m_e}} e^{-\frac{U_i}{kT_e + U_d}} = \quad (7)$$

$$= A_i U_{ac}^{-a_i} (A_i U_{ac}^{-a_i} + 1) \sqrt{\frac{kT_e}{2\pi m_e}} (1 + \eta(1 - f(1 - d_p \rho_{a0} Q_{ep0}))) \eta^{a_i} k_e.$$

Equation (7) is the cubic equation relatively to parameter d_p , therefore it can be solved analytically by using famous Cordano relations. Corresponded solution is [10]:

$$R_1 = A_i U_{ac}^{-a_i} (A_i U_{ac}^{-a_i} + 1) \sqrt{\frac{kT_e + eU_d}{2\pi m_e}}, R_2 = f \eta \eta^{a_i} k_e,$$

$$R_3 = 3(kT_e + eU_d) N_0 q \sqrt{\frac{kT_e + eU_d}{2\pi m_e}} e^{-\frac{U_i}{kT_e + U_d}},$$

$$R_4 = \mu_0 (kT_e + eU_d) \left(\frac{\pi}{\rho_{a0}}\right)^2 \left(1 + \frac{\gamma d_{tr}}{\lambda_e}\right), \quad (8)$$

$$R_5 = R_1 R_2 \rho_{a0} Q_{ep0}, C_{eq} = -\frac{R_1 + R_3 + R_1 R_2}{R_5}, D_{eq} = \frac{R_4}{R_5},$$

$$p = -\frac{C_{eq}^2}{3}, q = \frac{2C_{eq}^3}{27} + D_{eq}, D = \left(\frac{p}{3}\right)^3 + \left(\frac{q}{2}\right)^2,$$

$$u = \sqrt[3]{-\frac{q}{2} + \sqrt{D}}, v = \sqrt[3]{-\frac{q}{2} - \sqrt{D}}, y = u + v,$$

$$\lambda_e = \frac{2.25 kT_e (eU_d + kT_e)^2}{\pi e^4 \rho_{a0} \ln \left(1.5 - \sqrt{\frac{kT_e (eU_d + kT_e)^3}{\pi \rho_{a0}}}\right)},$$

$$d_p = y - \frac{C_y}{3}, \quad d_{cp} = l - d_p,$$

where λ_e – free path of electrons in anode plasma, $R_1, R_2, R_3, R_4, R_5, p, q, u, v$ and y – additional variables, C_{eq} and D_{eq} – coefficient of solved cubic equation, obtained form (7), D_{eq} – discriminate of this equation.

Equations (8) are writing for obtaining two geometry parameters of simulated electrodes system, which are strongly interconnected, namely: longitudinal size of anode plasma d_p and distance from cathode to plasma boundary d_{cp} (see Fig. 1). Such approach in this case is very important, because volume of anode plasma and ion concentration defined by its longitudinal length, but cathode-plasma distance also used in HVGD theory for defining processes in the discharge gap and electron-optical properties of elaborated electron gun [7, 8, 10, 12].

Clear, that plasma boundary position relatively to the cathode surface d_{cp} is depended from acceleration voltage U_{ac} , voltage of additional discharge U_d and from residual pressure in the discharge gap p_{a0} . But also all coefficients of proposed model depended from using electrodes materials and operation gas, therefore defining the conditions of HVGD lighting is necessary. In this work calculation with using equation system (8) was provided for aluminium cathode and cooper anode, the nitrogen was considered as operation gas. Such conditions of HVGD lighting are often used in industrial electron guns and they are very suitable for many technological processes. In conformity with this physical conditions such values of coefficients were choose: $U_i = 18$ V; $T_e = 800$ K; $\eta = 0.7$; $a_i = 0.343$; $q = 1.452$;

$$\eta_U = 0.95; \quad \gamma = 4.6; \quad f = 0.99; \quad \mu_0 = 1.27 \cdot 10^{-4} \frac{m^2}{V \cdot s};$$

$A_i = 3.8 \cdot 10^{-6}$; $\bar{Q}_0 = 5.3 \cdot 10^{-19} m^{-2}$ Considered range of operation pressure was $p_{a0} = 0.1 - 1$ Pa, range of acceleration voltage $U_{ac} = 5 - 30$ kV, and range of the voltage of additional discharge is $U_d = 30 - 100$ V. At the same time the geometrical dimensions of simulated discharge gap was: $l = 0.07$ m, $d_{tr} = 0.035$ m and $r_c = 0.025$ m [10]. The results for another geometry sizes also have been obtained and analysed [7].

Dependences of plasma boundary position from the acceleration voltage, voltage of additional discharge and from the residual pressure in the discharge gap are presented in Fig. 2. These dependences are very important, its' allows to make necessary conclusions about the singularity of operation of GDEG.

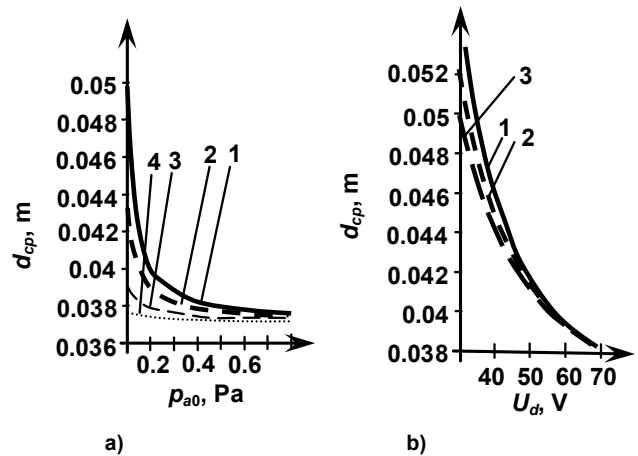


Fig. 2. Dependences of cathode-plasma distance from residual pressure in the discharge gap (a) and from the voltage on additional electrode (b):

a – $U_{ac} = 10$ kV; 1 – $U_d = 30$ V, 2 – $U_d = 50$ V, 3 – $U_d = 80$ V, 4 – $U_d = 100$ V; b – $p_{a0} = 0.5$ Pa; 1 – $U_{ac} = 30$ kV, 2 – $U_{ac} = 15$ kV; 3 – $U_{ac} = 5$ kV

First conclusion is, that cathode-plasma distance d_{cp} is decreasing with increasing the residual pressure in discharge gap p_{a0} and with increasing the voltage of additional discharge U_d . These conditions are corresponded to increasing of plasma volume, and therefore ions' concentration in plasma and the current of main discharge are also increased. The current of additional discharge is defined by concentration of charged particles in anode plasma and by the square of surface of plasma boundary. However, the simulation results shown, that increasing of plasma volume takes place only to the defined limits, and the minimum value of cathode-plasma distance d_{cp}^{min} defined by simple relation:

$$d_{cp}^{min} \approx d_{tr}. \quad (9)$$

The second conclusion is, that anode plasma position relative to the cathode d_{cp} is strongly depended from the residual pressure in discharge gap p_{a0} , but the dependence of d_{cp} from the acceleration voltage U_{ac} is, in contrary, very weak. Since d_{cp} is strongly influence to the current of formed electron beam and to the self-maintained

electron-ion optic in HVGD [1, 8, 12], it is clear, that in control systems, where HVGD current stabilized by changing the potential on additional electrode, the pressure in discharge gap also must be precisely stabilized.

With known size of anode plasma d_p ions concentration, as well as the currents of main and additional discharges also can be defined from equations (6, 7).

Defining the currents of main and additional discharges, as well as efficiency of electron gun. Since the longitudinal length of anode plasma d_p is known from the relations (8), ions concentration of ions in plasma can be calculated from following equation, which are obtained from the equation of discharge self-maintained (6) [7, 9, 11]:

$$C_1 = A_i U_{ac}^{-a_i} (1 + A_i U_{ac}^{-a_i}) (1 + \eta r_{tr}^{a_i} (1 - f(1 - d_p p_{a0} Q_{ep0}))) ,$$

$$C_4 = 3N_0 \alpha_i \sqrt{\frac{e(kT_e + eU_d)}{2\pi m_e}} , C_2 = \frac{\pi^2 H_0}{(d_p p_{a0})^2} \left(1 + \frac{\gamma d_{tr}}{\lambda_b}\right) - C_4 ,$$

$$C_3 = C_2 (kT_e + eU_d) e^{-\frac{U_i}{kT_e + U_d}} , \quad \eta_i = \frac{C_1}{C_3} , \quad (10)$$

where C_1, C_2, C_3 and C_4 is the additional variables.

From equations (8) and (10) can be obtained the simple relations for the currents of main and additional discharges. The current of additional discharge is defined as [11]:

$$I_d = en_i \pi r_{tr} (1 + \gamma) (r_{tr} + 2d_p) \sqrt{\frac{2eU_d}{m_i}} , \quad r_{tr} = \frac{d_{tr}}{2} , \quad (11)$$

where m_i – mass of the ions of operation gas. And the current of HVGD is defined as [7, 9]:

$$I_e = r_c^2 n_i (1 + A_i U_{ac}^{-a_i}) \sqrt{\frac{\pi e d_p (kT_e + eU_d)}{2m_e}} . \quad (12)$$

With known currents of the HVGD and of additional discharge from equations (11, 12) the energetic efficiency of triode GDEG can also be estimated. In the book [12] by analyze of energetic balance in the electrodes and in the diode discharge gap was shown, that energetic efficiency of diode GDEG can be defined by the following equations:

$$\eta_d = 1 - \frac{2 + k_d (1 + 2k_d \gamma \mu_{r0})}{2k_d (1 + \gamma k_d)} , \quad k_d = l p_{a0} \bar{Q}_0 . \quad (13)$$

Provided theoretical estimations and experimental researches of energetic efficiency of diode GDEG are shown, that the energy loses in the volume of discharge gap is very small, and it is caused by the low value of the residual pressure p_{a0} . Therefore the volume loses can be neglect, and total loses at the cathode and the anode in diodes high voltage glow discharge electrodes' systems are usually nearly 10% [12]. In such conditions, with known currents of main and additional discharges, which are defined by equations (8, 10–12), and considering also equations (13), energetic efficiency of triode glow discharge electron guns can be simply defined from following relation [7]:

$$\eta = \frac{\eta_b}{1 + \frac{\eta_b U_d I_d}{U_{ac} I_e}} . \quad (14)$$

Obtained simulation results and its discussion.

Obtained theoretical dependences of triode GDEG energetic efficiency from acceleration voltage, from the voltage on the additional electrode and from the residual pressure in the discharge gap are presented at the Fig. 3.

It is clear, that GDEG energetic efficiency is increased with increasing of acceleration voltage, with increasing

the voltage on the additional electrode, and with decreasing of operation pressure. In any case, the energetic efficiency of triode GDEG is very high value and lead in range 80–90%. That value is closed to corresponded parameter for the similar diode electrodes systems [8], therefore the energy loses in additional discharge really is not very high, its estimation level is few percent. It caused by the low voltage of additional discharge and by the high efficiency of gas ionization in it. Furthermore, reducing of pressure in the discharge gap in triode GDEG given the advanced possibilities of its applying in the modern electron-beam technologies, in such technological processes, where the high level of vacuum is necessary. For example, deposition of complex compositions from metals and dielectrics films in the microelectronic and nanoelectronic production is possible.

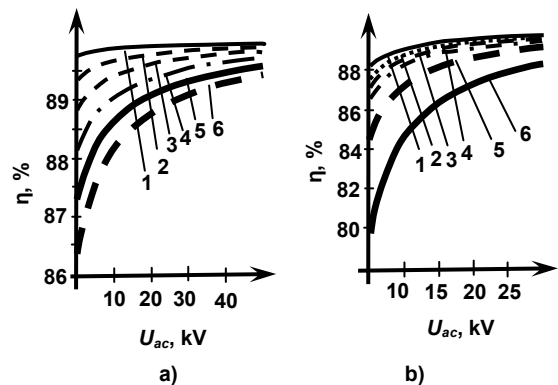


Fig. 3. Dependences of GDEG efficiency from acceleration voltage, voltage on additional electrode (a) and residual pressure (b):
 a – $p_{a0} = 0.5$ Pa; 1 – $U_d = 80$ V, 2 – $U_d = 70$ V, 3 – $U_d = 60$ V, 4 – $U_d = 50$ V, 5 – $U_d = 40$ V, 6 – $U_d = 30$ V;
 b – $U_d = 50$ V; 1 – $p_{a0} = 0.2$ Pa, 2 – $p_{a0} = 0.4$ Pa, 3 – $p_{a0} = 0.5$ Pa, 4 – $p_{a0} = 0.6$ Pa, 5 – $p_{a0} = 0.8$ Pa, 6 – $p_{a0} = 1$ Pa

Since the plasma size and the current of formed electron beam are strongly depended from the residual pressure in the discharge gap, with realizing of electric control and stabilization of beam power stabilization of residual pressure is also necessary. But in any case regulation time constant for HVGD systems with electric control is in range of tens' or hundreds microsecond, and this small value of time regulation constant is very suitable to thermal processes of modern electron-beam technologies [2, 5, 6, 14, 15].

Provided theoretical investigations and estimations are shown the high level of energetic efficiency of triode GDEG. Therefore these investigations confirmed that elaboration of industrial constructions of such guns and its applying in modern electron-beam technological equipment is very promising.

Conclusion. Proposed mathematical model of triode HVGD electrodes systems based on solving of analytical equations for defining plasma boundary position, its volume and the concentration of ions in it. All main physical processes are taking into account. Therefore, in spite of the simplified one-dimensional model of discharge gap, obtained results are very adequate. Experimental measurements of discharge current also have been provided, and disagreement between theoretical and experimental data was in range 15%. Therefore proposed model is very suitable to providing preliminary calculations in the first step of designing of industrial guns.

In any case, numerical simulation shown, that energetic efficiency of triode GDEG is in range 80–90% for different

acceleration voltage, voltage on the additional electrode and the residual pressure in the discharge gap. Therefore, taking into account the small time constant for electrical method of beam current control, such guns are very promising to application in modern electron-beam technological equipment. Creating of novel up-to-date technologies with using high-effective and cheap triode GDEG is also possible.

REFERENCE:

1. Model of Beam Formation in a Glow Discharge Electron Gun With a Cold Cathode / S. Denbnovetskiy, J. Felba, V. Melnik, I. Melnik // Applied Surface Science, 111 (1997). – P. 288–294.
2. Denbnovetskiy, S. High voltage glow discharge electron sources and possibilities of its application in industry for realising of different technological operations / S. Denbnovetskiy, V. Melnyk, I. Melnyk // IEEE Transactions on plasma science, 2003. – Vol. 31, № 5, October. – P. 987–993.
3. Denbnovetskiy S. Investigation of forming of electron beam in glow discharge electron guns with additional electrode / S. Denbnovetskiy, V. Melnik, I. Melnik, B. Tugay // XVIII-th International Symposium on Discharges and Electrical Insulation in Vacuum, August 17–21, 1998, Eindhoven, The Netherlands. – Proceedings. – Vol. 2. – P. 637–640.
4. Denbnovetskiy, S. Model of control of glow discharge electron gun current for microelectronics production applications / S. Denbnovetskiy, V. Melnyk, I. Melnyk, B. Tugay // Proceedings of SPIE. Sixth International Conference "Material Science and Material Properties for Infrared Optoelectronics", 2003. – Vol. 5065. – P. 64–76.
5. Electron-beam welding. / Ed. by B. Paton // Kyiv, 1987. (Published in russian).

6. Electron-beam melting in the foundry engineering / S. Ladohn, N. Levitskiy et al. // Kyiv, 2007. (Published in russian).
7. Melnik I. Generic methodology of simulation of triode high-voltage glow discharge electron sources / I. Melnik // Electronic Modelling, 2013. – Vol. 35, № 4. – P. 93–107. (Published in russian).
8. Melnik I. Numerical simulation of distribution of electric field and the particles trajectories in the high voltage glow discharge electron sources / I. Melnik // Radioelectronics and communication systems, 2005. – Vol. 48. – № 6. – P. 61–71.
9. Melnik I. Simulation of current-voltage characteristics of triode high voltage glow discharge electron sources / I. Melnik // Successes of Applied Physic, 2013. – Vol. 1, № 5. – P. 592–600. (Published in russian).
10. Melnik I. Analytical calculation of anode plasma boundary position in high voltage discharge gap with lighting of additional discharge / I. Melnik, S. Tuhai // Radioelectronics and communication systems, 2012. – Vol. 55, № 11. – P. 50–59.
11. Melnik I. Simulation of current-voltage characteristics of non-self-maintained additional discharge in triode gas discharge electron guns. / I. Melnik, S. Tuhai // Electronic Modelling, 2012. – Vol. 34, № 5. – P. 103–114. (Published in russian).
12. Novikov A. High-voltage glow discharge electron sources with anode plasma / A. Novikov // Moscow, 1983. (Published in russian).
13. Plasma processes in technological electron guns / M. Zavialov, Yu. Kreyndel, et al. – Moscow, 1989. (Published in russian).
14. High-temperature processes. Thermophysical bases // N. Rykalin, A. Uglovat et al. – Moscow, 1986. (Published in russian).
15. Shiller S. Elektronenstrahltechnologie // S. Shiller, Ul. Heisig, S. Panzer. – Dresden, 1976. (Published in german).

Submitted on 01.10.14

Денбновецький С., д-р техн. наук, Мельник І., д-р техн. наук,
Тугай С., канд. техн. наук, каф. електронних приладів та пристроїв, факультет електроніки,
Національний технічний університет України "КПІ", Київ

АНАЛІТИЧНІ СПІВВІДНОШЕННЯ ДЛЯ РОЗРАХУНКУ ЕНЕРГЕТИЧНОЇ ЕФЕКТИВНОСТІ ТРІОДНИХ ГАЗОРОЗРЯДНИХ ЕЛЕКТРОННИХ ГАРМАТ

Отримані та представлені у даній статті залежності енергетичної ефективності тріодних електронних гармат високовольтного тліючого розряду від прискорювальної напруги, тиску залишкового газу у розрядному проміжку, та від напруги на керувальному електроді. Запропонована математична модель сформована шляхом аналітичного розв'язування алгебраїчних рівнянь, отриманих як результат аналізу рівняння балансу іонів в анодній плазмі та рівняння самоозодження розряду. Отримані результати показали, що енергетична ефективність тріодних газорозрядних електронних гармат лежить в діапазоні 80–90%, тому такі гармати можуть успішно використовуватися у сучасних електронно-променевих технологіях.

Ключові слова: електронна гармата, електронно-променеві технології, високовольтний тліючий розряд, анодна плазма.

Денбновецький С., д-р техн. наук, Мельник І., д-р техн. наук,
Тугай С., канд. техн. наук, каф. електронних приборів и устройств, факультет електроніки,
Национальный технический университет Украины "КПИ", Киев

АНАЛИТИЧЕСКИЕ СООТНОШЕНИЯ ДЛЯ РАСЧЕТА ЭНЕРГЕТИЧЕСКОЙ ЭФФЕКТИВНОСТИ ТРИОДНЫХ ГАЗОРАЗРЯДНЫХ ЭЛЕКТРОННЫХ ПУШЕК

Получены и представлены в данной статье зависимости энергетической эффективности триодных электронных пушек высоковольтного тлеющего разряда от ускоряющего напряжения, остаточного давления в разрядном промежутке и от напряжения на управляющем электроде. Предложенная математическая модель получена путём аналитического решения алгебраических уравнений, полученных в результате анализа уравнения баланса ионов в анодной плазме и уравнения самосогласованности горения разряда. Полученные результаты показали, что энергетическая эффективность триодных газоразрядных электронных пушек лежит в диапазоне 80–90%, поэтому такие пушки могут успешно использоваться в современных электронно-лучевых технологиях.

Ключевые слова: электронная пушка, электронно-лучевые технологии, высоковольтный тлеющий разряд, анодная плазма.

UDC 538.9; 539.2

M. Zabolotnyy, Ph. D., Department Physics of functional materials, Faculty of Physics, Taras Shevchenko National University of Kyiv,
G. Dovbeshko, Doct. Sci., Institute of Physics, National Academy of Ukraine,
G. Solyanyk, Doct. Sci., R. E. Kavetsky Institute of Experimental Pathology, Oncology and Radiology, Y. Kondratskyy, Ph. D., Kyiv National Institute of cancer,
V. Estrela-Lyopis, Ph. D., Institute of Colloid and Water Chemistry,
M. Kulysh, Doct. Sci., O. Dmytrenko, Ph.D., T. Busko, Ph.D., N. Poluyan, stud.,
Department Physics of functional materials, Faculty of Physics,
Taras Shevchenko National University of Kyiv

MAIN PROBLEMS OF ANTICANCER DRUGS' MODIFICATION

Limit capabilities and low efficiency in the treatment of locally advanced and disseminated forms of cancer shows that anticancer drugs are need to be modified. This modification needs solving some special tasks. So there was created the program of their realization. There are main tasks and results, shared at this moment, shown in this article.

Keywords: cancer, oncodrugs, modification, radiation, bubstones.

The experience of anticancer chemotherapy has shown limit capabilities and low efficiency in the treatment of locally advanced and disseminated forms of cancer. One of the

most actual problem of modern pharmacology and oncology practice is an identification of new biologically active materials, studding of their physical-chemical and

© Zabolotnyy M., Dovbeshko G., Solyanyk G., Kondratskyy Y., Estrela-Lyopis V., Kulysh M., Dmytrenko O., Busko T., Poluyan N., 2014

therapeutic properties and creation of effective and low-toxic anticancer drugs [1, 2, 3]. Establishing of the relationship between the physical and medical - biological properties of anticancer drugs is important. The modification of the anticancer agents pharmacological properties direct to increasing of an efficiency and reduction of toxicity.

There is a basic tendency to individualization of cancer treatment since human body is unique.

Modern domestic practical oncology [1, 2, 3] makes it possible to determine the molecular profile of the tumor cells of each patient. As a result the individual and antitumor therapy must to be treated. And it is in contravention of medical standards.

According to current medical standards medical treatment of cancer patients provides by specific cycles of chemotherapy. It is extremely toxic and not all patients need of written standard treatment. It is know that individual sensitivity to therapeutic agents varying in 10–40 times [3], which requires consideration of this factor in determining of the optimal treatment scenario. A formation of drug resistance is another extremely serious problem for treatment.

Almost 80% of patients were sensitive to the intensive anticancer chemotherapy 40 years ago. Nowadays 40% of primary cancer patients are sensitive to chemotherapy and they lost one after 3–4 courses. Therefore, the creation and modification of new anticancer drugs is one of the most relevant in the modern oncology.

The absence of selectivity of drugs activity and their general toxicity stipulate to improve the efficiency, selectivity and safety. Also the modern methods of radiation medicine and nanophysics can involve the synergetic mechanisms of oncodrugs anticancer action. In most cases, for creation such nanocomposites components with properties of which are known in pharmacocorrection or in direct cytostatic action have used. Onrush development of molecular biology and chemistry provides rapid utilization of de novo synthesized drugs. Plants still are traditional and rich sources of pharmacologically active substances. Thus, almost half of modern drugs was derived from plant extract [4, 5].

Several plant-derived compounds have been approved as anticancer drugs: vinblastine, vincristine, etoposide, teniposide, taxol, taxotere, topotecan and irinotecan, just to name a few. The main bioactive agents of plants used in medicine for the treatment of malignant tumors are alkaloids.

The last exhibits pronounced cytostatic effect at the tumor cells. The crucial issue is the selection of the optimal nanostructured modifier [1–5]. Modification of the medical drug molecules by surface-active nanoparticles has a great theoretical and practical importance. It allows receiving active drugs with fixed size molecules and achieving biocompatibility with the human organism cells [2]. The selection of the modifying nanoimpurities essentially depends on the reason of the drug therapeutic action improvement. This can occur due to 1) the transfer of drug molecules in conformational state with increased activity, 2) the complex formation of the molecule drugs and molecule (nanoparticle) of modifying substances, 3) increasing sensitivity of patient injured points to drugs under modifying agents. In the last case the binary drugs with targeted action are created. The first two ways are the most relevant at this stage because their implementation is possible without detailed information about the specific biological mechanisms of drugs action.

In above cases, the lifetime of molecule drugs in newly formed states needs exceed the time of their therapeutic action. The following factors at choosing of modifying nanoparticles should be taken into account [2, 6]. The properties of nanoparticles depend on their size (size effect). For nanoparticles the percentage of surface atoms

increases as the particle size decreases and it leads to variation of chemical, physical, chemical, biological, pharmacological properties. The nanoparticles properties are determined by their surface tension and energy. These characteristics influence on another thermodynamic nanoparticles parameters. In nanoparticles can realize phases that do not exist in macroparticles. As the particle size decreases the specific surface energy increases.

One of the factors, which cause the modification of the nanoparticles thermodynamic properties are the boundaries change of the phonon frequency distribution function.

This leads to increase of the nanoparticles specific heat could be 10–15 times higher than for macro dimensional ones. The optical properties (frequency dependence of the absorption and reflection) of nanoparticles are significantly different. The propagation of light is likely to have the band character. Another important feature of nanoparticles is a strong dependence of their characteristics on the medium parameters. This property is cause by the relative number of surface atoms in nanoparticles. An alternative possibility to use doping medicines (or solutions) by nanoparticles is the use of high-energy radiation. The last one transfer molecule drugs in the metastable state, following which its conversion to a state of increased medical capacity [7]. Thereby, the modification of anticancer drugs needs solving the following tasks.

1. The creation of physical – health picture of oncodrugs, the studying of connection between the physical and pharmacological properties of drugs, development of methods of physical identification for their therapeutic suitability.

2. Examination of mechanisms of radiation and impurity modification of electronic, optical and therapeutic properties of biomolecules, nanostructures and their composites for drugs creation with low toxicity and high efficiency with respect to resistant tumors.

3. Determination of ways formation, properties and patterns of relationship of radiation defects (including bubblestones [6]) long life clusterization in biologically compatible liquid media.

4. Investigation of the double charged electrical layers formation surrounded by radiation-induced defects in liquid media with the specified structure of electric charge distribution.

5. The influence determination of electric surrounding of nanoparticles on their thermodynamic properties and stability nanocomposites conditions for their participation.

6. The ways identification of reconstruction structuring conformational state of the molecule oncology medicines under the influence of radiation induced defects in solvent.

7. Preparation of templates based on ordered nanostructures to enhance the efficiency and sensitization of oncology medicines.

The program realization was started within the range of budget subject at the Physics of functional materials department of Physics faculty of Kiev National Taras Shevchenko University at collaboration with R.E Kavetsky Institute of Experimental Pathology, Oncology and Radiology, Physics, F. D. Ovcharenko Institute of Biocolloidal Chemistry of National Academy of Science of Ukraine and National Cancer Institute at 2012. The main results are:

1. The calculus of approximations for range control conformational changes of polymer organic and biomolecules by using radiation and impurity modification were developed.

2. Methods of given conformational state realization of photosensitive organic biomolecules were created.

3. Physical mechanisms of the impurities effect of carbon nanostructures on pharmacological and biophysical properties of oncodrugs in order to develop methods for the modification of their medical properties were investigated.

4. The enhancement of the therapeutic effect of certain drugs at doping alkaloid in the presence of water-soluble fullerenes was registered.

5. The methods of template modification of physical-chemical and medical-biological parameters were proposed.

6. The influence of surface electric charge on the surface tension of some polymeric liquids was determined. The conditions of surface instability were established.

7. Based on the case study the perspective using of polysaccharides, doxorubicin alkaloids and some compounds of stilbene series for the creation of an effective anticancer drugs was proven.

These results show potential implementation of the above program.

REFERENCE:

1. *Bunkin N. F.* Quasi-stable clusters of nanobubbles of solved gas in water and water electrolytic solutions / Bunkin N. F. et al. // *Nanosystems, Nanomaterials, Nanotechnologies*, 2011. – Vol. 9, № 2. – P. 499–504.

2. *Chehun V. F.* Creation of new drugs based on nanocomposite materials for solving of contemporary oncologists problems / V. F. Chehun // *Nanosystems, Nanomaterials, Nanotechnologies*, 2011. – Vol. 9, № 1, P. 261–274.

3. *Chekman I. S.* Nanomedicine, nanopharmacology: pharmaceutical aspect / I.S. Chekman, M.I. Zagorodnyy // *Carpathian bulletin of T. Shevchenko scientific community*, 2011. – Vol. 4(16). P. 7–23.

4. *Chemotherapy individualization for stomach cancer patient.* / I. B. Schepotin, O.V. Vasilev, D.O. Rozumiy et al. // *Ukrainian medical periodical*, VII/VIII 2010. – Vol. 4 (78). – P. 67–69.

5. The method of application of aconitine agent as antiangiogenic anticancer remedy / Solyanik G. I., Fedorchuk O. G., Pyaskovska O. M. et al. // *Patent 48524 Ukraine, MPK A 61 K 35/76, A 61 P 35/04.* № u 2009 08954; application 28.08.2009; published 25.03.2010, № 6.

6. *Modification of alkaloid structure in the conium drug with fullerenes C60* / Zabolotnyy M.A., Momot A.I., Dovbeshko G.I. et al. // *Ukr. J. Phys.*, 2012. – Vol. 57, № 7. – P. 1739–1745.

7. *Klaessig F.* Current Perspectives in Nanotechnology Terminology and Nomenclature, Nanotechnology Standards / F. Klaessig, M. Marrapese, S. Abe // *Nanostructure Science and Technology*, 2011. – P. 21–52.

Submitted on 04.11.14

Заболотний М., канд. фіз.-мат. наук, Київський національний університет імені Тараса Шевченка,
Довбешко Г., д-р фіз.-мат. наук, Інститут фізики НАНУ,
Соляник Г., д-р фіз.-мат. наук, Інститут експериментальної патології, онкології та радіології ім. Р. Е. Кавецького,
Кондацький Ю., канд. мед. наук, Київський національний інститут раку,
Естрела-Льопис В., канд. хім. наук, Інститут колоїдної хімії та хімії води,
Куліш М., д-р фіз.-мат. наук, Дмитренко О., канд. фіз.-мат. наук, Момот А., канд. фіз.-мат. наук,
Буско Т., канд. фіз.-мат. наук, Полуян Н., студ., Київський національний університет імені Тараса Шевченка

ОСНОВНІ ПРОБЛЕМИ МОДИФІКАЦІЇ ПРОТИРАКОВИХ ПРЕПАРАТІВ

Обмежені можливості та низька ефективність у лікуванні місцево поширених та дисимінованих форм раку показує, що протиракові препарати потребують модифікації. Цей процес вимагає від лікарів та медичних фізиків вирішення деяких особливих задач. Тому було створено і запроваджено програму реалізації їх розв'язку. В цій статті представлено основні її завдання та результати отримані на даний момент.

Ключові слова: рак, онкопрепарати, модифікація, радіація, бабстони.

Заболотный М., канд. физ.-мат. наук, Киевский национальный университет имени Тараса Шевченка,
Довбешко Г., д-р физ.-мат. наук, Институт физики НАНУ,
Соляник Г., д-р физ.-мат. наук, Институт экспериментальной патологии, онкологии и радиологии им. Р. Е. Кавецького,
Кондацкий Ю., канд. мед. наук, Киевский национальный институт рака,
Естрела-Льопис В., канд. хим. наук, Институт коллоидной химии и химии воды,
Кулиш М., д-р физ.-мат. наук, Дмитренко О., канд. физ.-мат. наук, Момот А., канд. физ.-мат. наук,
Буско Т., канд. физ.-мат. наук, Полуян Н., студ. Киевский национальный университет имени Тараса Шевченко

ОСНОВНЫЕ ПРОБЛЕМЫ МОДИФИКАЦИИ ПРОТИВОРАКОВЫХ ПРЕПАРАТОВ

Ограниченные возможности и низкая эффективность в лечении местных и дисиминированных форм рака показывает, что противораковые препараты нуждаются в модификации. Этот процесс требует от врачей и медицинских физиков разрешения некоторых специальных задач. Для этого была разработана программа реализации их решения. В этой статье представлены ее основные задания и результаты, полученные на сегодняшний день.

Ключевые слова: рак, онкопрепараты, модификация, радиация, бабстоны.

UDC 537.86

I. Zavislyak, Dr. Sci., M. Popov, Ph.D.,

M. Movchan, post grad. stud.,

Quantum Radiophysics Department, Faculty of Radiophysics, Electronics and Computer Systems,
Taras Shevchenko National University of Kyiv

PASSIVE FERRITE RESONATOR-BASED MILLIMETER WAVE BAND COMPONENTS

The review of magnetodynamic resonances in ferrite resonators and their mm-wave band applications was given. Ferrite resonator eigenexcitations classification has been presented. The analytical theory for modes resonant frequencies calculations is stated and a number of prototype electronically tunable mm-wave devices, utilizing the "above" and "below FMR" magnetodynamic resonances, including isolator, phase shifter, band-pass and band-stop filters have been demonstrated.

Keywords: magnetodynamic modes; mm-wave devices; barium hexaferrite; nickel ferrite; yttrium-iron garnet.

Introduction. The mm-wave band of the electromagnetic spectrum is of particular importance for applications related to security systems, radars, radio astronomy, and satellite communication [14]. There is a need for device components such as isolators and phase shifters, and others for signal-processing devices working at these frequencies. Such low-loss components can be constructed using ferrites. Since ferrites are magnetic dielectrics, eigenoscillations of ferrite resonators, in general case, belong to magnetodynamic type. Magnetic nature of ferrites influences such oscillations most prominently in resonance region near ferromagnetic resonance (FMR) frequency, where dipole-exchange spin oscillations and waves can exist. Most known oscillations of such kind are the Walker modes. Their main peculiarities are wide-range

magnetic field tuning of frequency and fast spatial variations of rf-fields, which, in turn, makes retardation effects insignificant and allows miniaturizing resonator dimensions, which can be important for low-power microwave microelectronics. Theoretical analysis of Walker modes, at frequencies well below that of ferrite resonator main electromagnetic mode (assuming resonator is nonmagnetic dielectric), can be done in magnetostatic approximation.

Meanwhile, in such wide spread ferrite devices like circulators and isolators, ferrite resonator operates at frequencies far from FMR and its magnetic properties influence magnetodynamic modes [1, 3] due to, basically, Faraday effect. Such resonators have much larger dimensions, although can operate at higher power. A lot of research on ferrites resonators, mostly fabricated from

© Zavislyak I., Popov M., Movchan M., 2014

garnets and spinels, in the L – to Ka-bands has been performed [11, 2].

Some important properties of widely used ferrite materials are given in Table 1. The ferrites of choice for mm-wave FMR devices is M-type hexagonal ferrites which are characterized by a large uniaxial magneto-crystalline anisotropy field and FMR at 50 GHz or more with zero external magnetic field [6].

Table 1

Material	Magnetic parameters			
	$4\pi M_0$, Gs	ΔH , Oe	H_a , Oe	Minimum FMR frequency, GHz
$Y_3Fe_5O_{12}$	1800	≈ 1	50	≈ 1
$Ni_xZn_{1-x}Fe_2O_4$	3500–5000	≈ 5	100–250	≈ 3
$BaFe_{12}O_{19}$	4800	≈ 20	16800	47
$SrFe_{12}O_{19}$	4700	≈ 20	18700	51

We will divide frequency region of electromagnetic excitations in magnetized ferromagnetic media into three regions (see Fig. 1): 1) FMR region; 2) above FMR region – magnetodynamic resonances (MDR) with frequencies higher the approximately $\gamma(H_a + H_0 + 4\pi M_0)$ (here γ is gyromagnetic ratio, H_a – uniaxial anisotropy field, H_0 – bias magnetic field, $4\pi M_0$ – saturation magnetization); 3) below resonance region, MDR with frequencies smaller than $\gamma(H_a + H_0 - 4\pi M_0)$. From above mentioned ferrite materials, only hexaferrites, magnetized along easy axis can be explored in mm-wave band in all three regions, whereas spinels and garnets can operate only in "above FMR" region.

1. Mode splitting effect in disc ferrite resonators.

Let's consider resonator as a section of an open gyromagnetic rod waveguide with the tensor magnetic permeability in the demagnetized state.

$$\hat{\mu} = \begin{pmatrix} \mu & -i\mu_a & 0 \\ i\mu_a & \mu & 0 \\ 0 & 0 & \mu_z \end{pmatrix} \quad (1)$$

where $\mu_z = 1$, $\mu_a = \gamma 4\pi M_0 / \omega$ for garnets and spinels and $\mu = 1 - \frac{\gamma H_a (\gamma 4\pi M_0)}{\omega^2 - (\gamma H_a)^2}$, $\mu_a = \frac{\omega (\gamma 4\pi M)}{\omega^2 - (\gamma H_a)^2}$ in the case of hexaferrites, (M – is net magnetization).

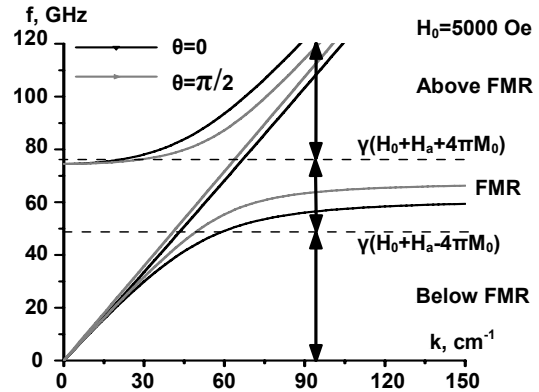


Fig. 1. Electromagnetic waves dispersion in magnetized ferrite media (barium hexaferrite, BaM), for waves propagating perpendicularly and parallel to the bias field direction

Expressions for electromagnetic field in such waveguides with tensor susceptibility in the form (1) in cylindrical coordinates are known [12]. After applying electromagnetic boundary conditions at the rod surface, the explicit dispersion equation (2) for guided electromagnetic waves can be found [4].

$$\begin{vmatrix} 1 & 0 & 1 & 1 \\ 0 & 1 & \theta_1 & \theta_2 \\ in \left(\frac{q_3}{ha_1} \right)^2 \frac{\mu_a}{\mu} & \frac{K'_n(ha_1)}{ha_1 K_n(ha_1)} \frac{1}{\mu_z} & \frac{\theta_{m1} J'_n(q_1 a_1)}{q_1 a_1 J_n(q_1 a_1)} - \frac{\mu_a n q_3^2}{\mu (q_1 a_1)^2} & \frac{\theta_{m2} J'_n(q_2 a_1)}{q_2 a_1 J_n(q_2 a_1)} - \frac{\mu_a n q_3^2}{\mu (q_2 a_1)^2} \\ \frac{1}{\varepsilon} \frac{K'_n(ha_1)}{ha_1 K_n(ha_1)} \frac{\mu_a}{\mu} & -j \frac{n}{(ha_1)^2} \frac{1}{\mu_z} & \frac{J'_n(q_1 a_1)}{q_1 a_1 J_n(q_1 a_1)} \frac{\mu_a}{\mu} + \frac{n \sigma_{m1}}{(q_1 a_1)^2} & \frac{J'_n(q_2 a_1)}{q_2 a_1 J_n(q_2 a_1)} \frac{\mu_a}{\mu} + \frac{n \sigma_{m2}}{(q_2 a_1)^2} \end{vmatrix} = 0, \quad (2)$$

where $q_3 = \frac{\beta}{k_0 \sqrt{\varepsilon}}$, $q_{1,2} = \frac{\chi_{1,2}}{k_0 \sqrt{\varepsilon}}$, $h = \frac{\tau}{k_0 \sqrt{\varepsilon}}$, $\theta_{m1,2} = \mu_{\perp} - \left(\frac{\varepsilon}{\varepsilon_z} q_{1,2}^2 + q_3^2 \right)$, $\tau = \sqrt{\beta^2 - k_0^2}$, $a_1 = a k_0 \sqrt{\varepsilon}$, $\sigma_{m1,2} = \frac{\theta_{m1,2}}{\mu} + \left(\frac{\mu_a}{\mu} \right)^2$,

$$|n|=0,1,2,\dots \chi_{1,2}^2 = \frac{1}{2} \left(k_0^2 \varepsilon (\mu_{\perp} + \mu_z) - \left(1 + \frac{\mu_z}{\mu} \right) \beta^2 \right) \pm \sqrt{\frac{1}{4} \left(k_0^2 \varepsilon (\mu_{\perp} - \mu_z) - \left(1 - \frac{\mu_z}{\mu} \right) \beta^2 \right)^2 + \beta^2 k_0^2 \varepsilon \mu_z \left(\frac{\mu_a}{\mu} \right)^2}, \mu_{\perp} = \frac{\mu^2 - \mu_a^2}{\mu}, k_0 = \omega \sqrt{\varepsilon_0 \mu_0}.$$

In order to define the longitudinal wave number β we replaced real experimental setup – sample of thickness S lying on the metal surface of rectangular waveguide – with simplified theoretical model, where perfect electric wall is substituted instead of lower metal wall and far lying upper metal wall is replaced with perfect magnetic wall, while sidewalls are completely removed. This led to the following discrete wave numbers $\beta_p = (2p-1)\pi/(2S)$, $p=1,2,\dots$

Experimental and theoretical frequency vs. bias field dependence for the two lowest MDR modes in before FMR region for BaM disc-shaped resonator with radius $a=1.2$ mm and $S=0.36$ mm is shown on Fig. 2 [5]. Comparison between experimental results and theoretical calculations in above FMR region for BaM magnetodynamic resonator with radius $a=0.62$ mm and $S=0.28$ mm is shown on Fig. 3 [4].

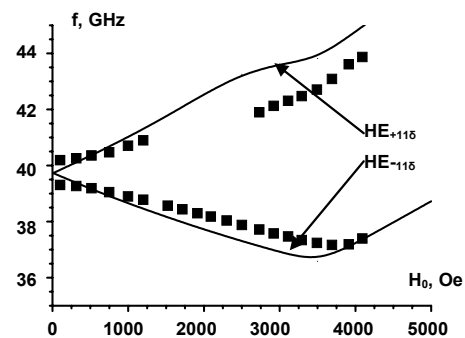


Fig. 2. Frequency vs. bias field dependence for the lowest MDR modes of the BaM disk located on the metal wall for magnetic field applied perpendicular to the disk: theoretical calculations (solid lines) and experiment (dots)

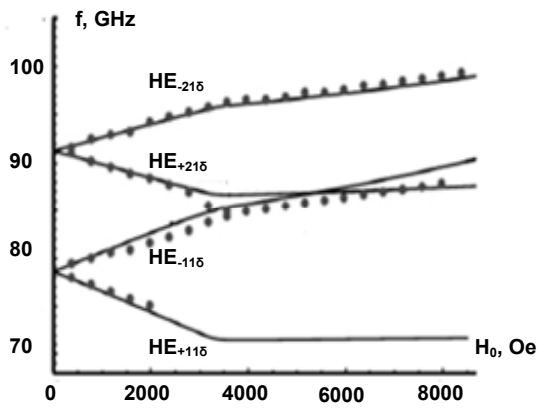


Fig. 3. Frequency vs bias field dependence for lowest MDR in barium hexaferrite disk resonator: theory (solid lines) and experiment (dots)

Since MDR frequencies depend on dielectric constant and resonator dimensions, magnetic field tunable devices utilizing MDR can operate in subterahertz band, at frequencies much higher, than attainable for FMR devices.

2. Hexaferrite, nickel ferrite and yttrium-iron garnet resonators utilizing HE_{±116} modes.

2.1. Millimeter wave waveguide isolator using single-crystal BaM disk. Typical waveguide-based prototype device setup is shown on Fig. 4. Disk sample (D=1.2 mm, S=0.17 mm) was situated inside a waveguide flange, with lateral position varied if necessary, fixed with foam and (possibly) with polyethylene layer, that allows for eigenfrequencies mechanical tuning and decrease losses due to eddy currents in metal wall. Magnetic field is perpendicular to the disk flat surface.

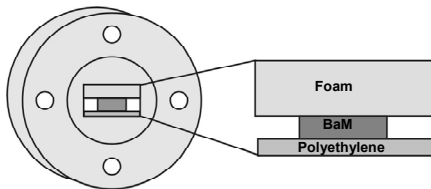


Fig. 4. Diagram showing a disc of single crystal BaM mounted inside a waveguide flange and sandwiched between a dielectric polyethylene layer and a foam slab

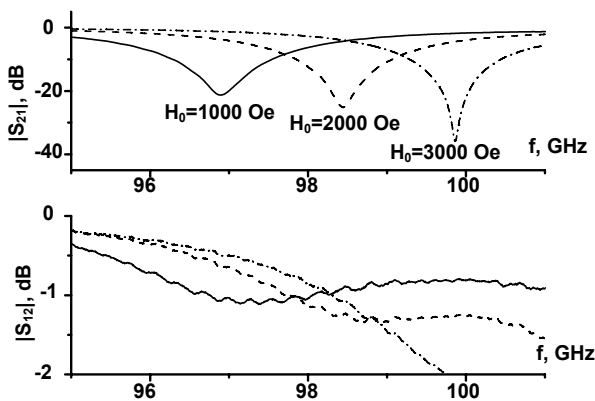


Fig. 5. Direct and reverse transmission characteristics of BaM isolator

Comparison between direct and reverse losses for BaM disk, shifted from the center of waveguide, approximately into the point, where waveguide H₁₀ mode have circular polarization, is shown on Fig. 5. An isolator effect is clearly visible; with isolation frequency is tunable with magnetic field in over 5 GHz range.

2.2. Single-crystal yttrium-iron garnet (YIG) disk waveguide band-stop filters. This device is based on D=1 mm, S=0.2 mm YIG disk, positioned on the center of flange. Its transmission characteristic, showing more than 2 GHz tunability with 100 GHz central frequency is presented on Fig. 6 [7].

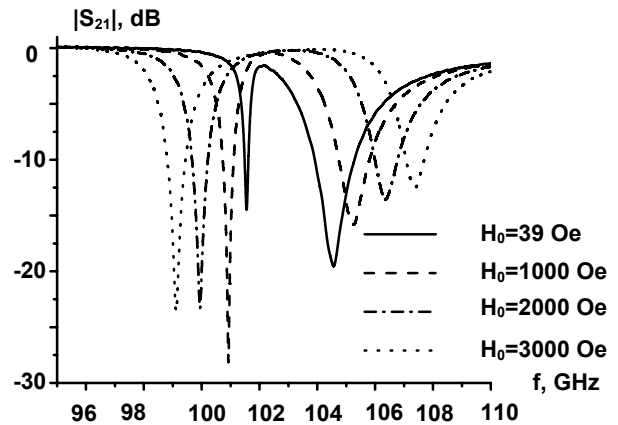


Fig. 6. Transmission characteristics of YIG disk band stop filter

2.3. Waveguide nickel ferrite-based tunable phase shifter. Phase vs. bias field characteristic of mm-wave poly-crystalline nickel ferrite oxide (NFO) disk-based tunable phase shifter (D=1 mm, S=0.25 mm) is shown on Fig. 7.

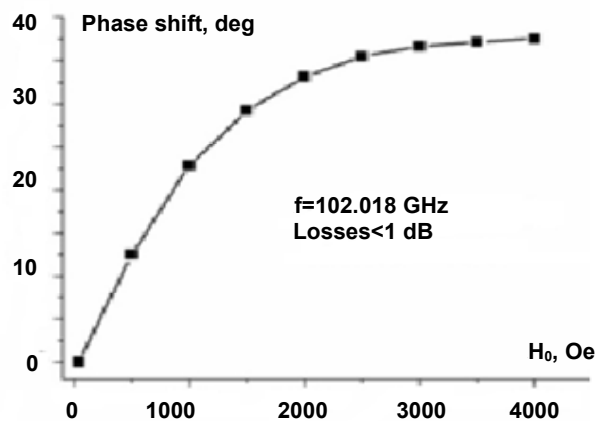


Fig. 7. Tunable insertion phase shift of NFO phase shifter

2.4. Stripline nickel ferrite-based tunable band-pass filter. A filter based on the magnetodynamic mode in NFO was designed and characterized. The microstripline filter shown on inset on Fig.8 was made from a 0.25 mm thick RT Duroid 5880 substrate and had a gap in the central strip. Power is transferred from input to output due to excitation of magnetodynamic resonance in the NFO disk. The scattering parameter S₂₁ vs. f measured for a series of H₀ are shown in Fig. 8 [8].

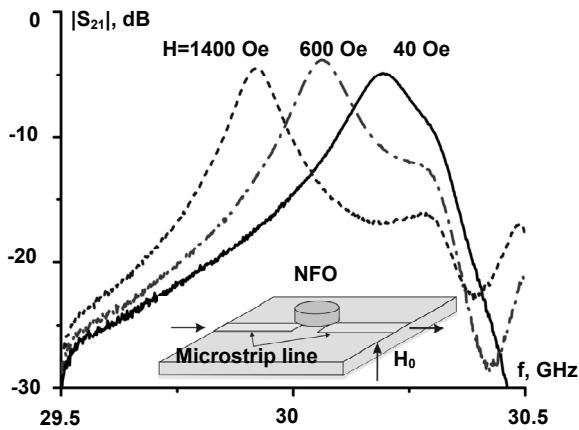


Fig. 8. Schematic diagram showing NFO dielectric resonator bandpass filter and profiles of scattering parameter S_{21} for different H_0

2.5. BaM nonreciprocal phase shifter with bistability effect. It was found, that when H_0 decreases from large values, sample stays saturated up to some critical field $H_{cr} \approx 2500$ Oe [9]. But then single-domain state becomes metastable, whereas multidomain state becomes energetically favorable, and at some point jump-type transition to unsaturated state is observed. This bistability leads to noticeable phase shift $\delta\varphi$ of transmitted electromagnetic wave in frequency region between resonance frequencies, when ferrite resonator is switched amongst a two states on the hysteresis curve (see Fig. 9).

From Fig. 9 one can see, that $\delta\varphi$ increase from 22° at 2700 Oe to 77° at 3700 Oe at middle frequency, but losses at the very same frequency also monotonically increase. Theoretical calculations, using HFSS and analytical theory (2) for frequency determination and equivalent circuit model for phase shift derivation, demonstrate rather satisfactory coincidence with experimental data.

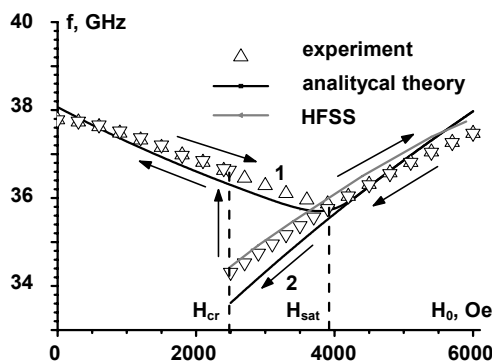
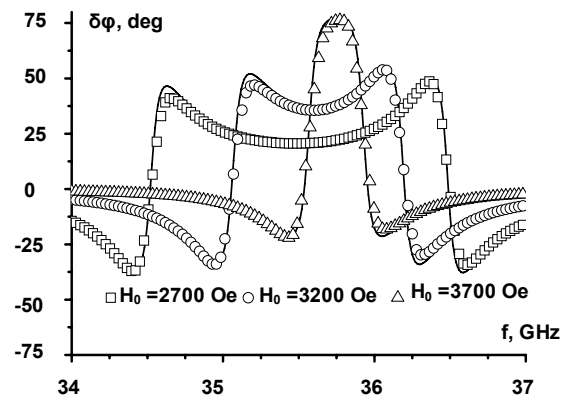


Fig. 9. Experimental (dots) and theoretical (lines) frequency vs. field dependence of main MDR, demonstrating high-frequency hysteresis and corresponding differential phase shift for different bias fields



2.6. BaM tunable devices in "below FMR" region. MDR modes properties in the below-FMR region mostly remain unexplored. Also, when operating in the below-FMR region, the spin-wave manifold is inevitably lying above the MDR frequency, hence 1) no spin wave modes would ever appear inside device bandwidth for any value of bias

magnetic field and 2) any possible nonlinear interactions between MDR and spin waves are also excluded.

An examples of phase shifter and isolator in the below-FMR region [10] made from BaM disks with radius $a=1.2$ mm, and thicknesses $S=0.36$ mm (№1) and $S=0.44$ mm (№2) are shown on Fig. 10.

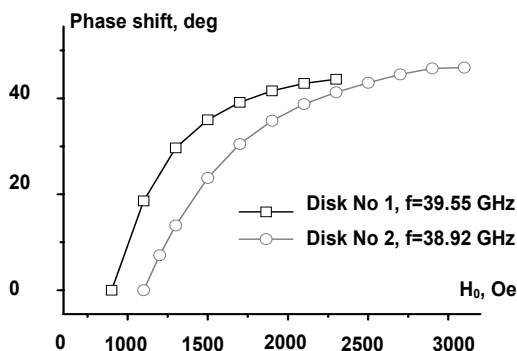
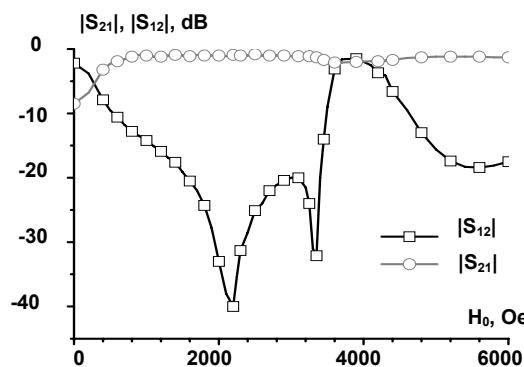


Fig. 10. Tunable differential phase shift for №1 and №2 BaM disk resonators; direct loss and isolation of resonance isolator (resonator №2), operating frequency 39.9–41.2 GHz, in the "below FMR" region



3. Hexaferrite magnetostatic resonators with dual magnetic and electric field tuning. The bilayer made from substituted barium hexaferrite bonded to piezoelectric lead zirconate titanate (PZT) was used for studies on millimeter-wave electric field tunable magnetostatic resonator. For an electric field E applied to

bilayer, the piezoelectric deformation leads to an internal magnetic field, proportional to mechanical strain. Thus, the condition for FMR, for H_0 perpendicular to the plane is

$$f_0 = \gamma (H_a + H_0 - 4\pi M_0) + AE \quad (3)$$

Figure 11 shows data on the E dependence of δf obtained for a bilayer with a ferrite thickness of 95 μm [13].

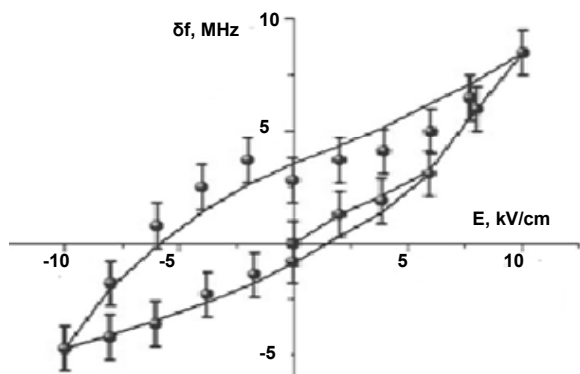


Fig. 11. Electric field induced frequency shift δf vs E for BaM/PZT bilayer for $H_0=6020$ Oe

A maximum frequency shift of 8 MHz was measured for $E=\pm 10$ kV/cm using vector network analyzer. Thus the magnetodielectric coupling constant $A=0.8$ MHz cm/kV.

Conclusions. In the frequency range 30–110 GHz tunable ferrite devices can be manufactured using any type of considered above excitations, however at higher frequencies, magnetic field tunable devices on the basis of magnetodynamic resonances in ferrite resonator seems to be the most promising option.

A number of prototype magnetic field tunable resonance millimeter wave devices (phase shifters, isolators and band-pass filter) utilizing magnetodielectric resonances were presented and their principal characteristics have been measured. With proper choice of ferrite resonator dimensions one can vary the device operating frequency in the below-FMR region as well as in the above-FMR frequency domain. Moreover, maximum operating frequency in the above-FMR region does not

depend on magnetic parameters of the ferrite and, in theory, can easily reach THz frequencies.

REFERENCE:

1. Bosma H. On stripline Y-circulation at UHF / H. Bosma // *IEEE Trans. MTT*, 1964. – Vol. MTT-12, Iss.1 – P. 61–72.
2. How H. Microwave phase shifter utilizing nonreciprocal wave propagation / H. How, C. Vittoria // *IEEE Trans. MTT*, 2004. – Vol. 52, Iss. 8. – P. 1813–1819.
3. Krupka J. Resonant modes in shielded cylindrical ferrite and single-crystal dielectric resonators / J. Krupka // *IEEE Trans. MTT*, 1989. – Vol. 37, Iss. 4. – P. 691–696.
4. Movchan N. N. Splitting Axially Heterogeneous Modes in Microwave Gyromagnetic and Gyroelectric Resonators / N. N. Movchan, I. V. Zavislyak, M. A. Popov // *Radioel. and Comm. Sys.*, 2012. – Vol. 55, Iss. 12 – P. 549–558.
5. Movchan N. N. Ferrite-dielectric resonators made of uniaxial ferrites in before-the-resonance region / N. N. Movchan, I. V. Zavislyak // *Radioel. and Comm. Sys.*, 2013. – Vol. 56, Iss. 12. – P. 553–559.
6. Nicholson D. B. Hexagonal ferrites for millimeter-wave applications / D. B. Nicholson // *Hewlett-Packard J.*, 1990. – Vol. 41, Iss. 10. – P. 59–61.
7. Popov M. A. Sub-THz dielectric resonance in single crystal yttrium iron garnet and magnetic field tuning of the modes / M. A. Popov, I. V. Zavislyak, G. Srinivasan // *J. Appl. Phys.*, 2011. – Vol. 110, Iss. 7 – P. 024112-1 – 024112-7.
8. Magnetic field tunable 18–36 GHz dielectric bandpass filter / M. A. Popov, D. V. B. Murthy, I. V. Zavislyak, G. Srinivasan // *Electronics Lett.*, 2012. – Vol. 48, Iss. 1 – P. 98–99.
9. Nonreciprocal millimeter wave latching phase-shifter utilizing magnetodielectric phase-frequency bistability effect / M. A. Popov, I. V. Zavislyak, N. N. Movchan, G. Srinivasan // *MOTL*, 2014. – Vol. 56, No. 8 – P. 1759–1764.
10. Mode Splitting in 37-42 GHz Dielectric Resonance in Barium Hexaferrite and Device Applications / M. A. Popov, I. V. Zavislyak, N. N. Movchan et al. // *IEEE Trans. Magn.*, 2014. – Vol. 50, Iss. 6. – P. 4004507-1 – 4004507-7.
11. Schloemann E. F. Circulators for microwave and millimeter-wave integrated circuits / E. F. Schloemann // *Proc. IEEE*, 1988. – Vol. 76, Iss. 2. – P. 188–200.
12. Schott F.W. Electromagnetic waves in longitudinally magnetized ferrite rods / F.W. Schott, T. F. Tao, R.A. Freibrun // *J. Appl. Phys.*, 1967. – Vol.38, Iss.7. – P. 3015–3022.
13. Srinivasan G. Millimeter-wave magnetoelectric effects in bilayers of barium hexaferrite and lead zirconate titanate / G. Srinivasan, I. V. Zavislyak, A.S. Tatarenko // *Appl. Phys. Lett.*, 2006. – Vol. 89, Iss. 10. – P. 152508-1 – 152508-3.
14. Vizard D. R. Millimeter-wave applications: from satellite communications to security systems / D. R. Vizard // *Microwave J.*, 2006. – Vol. 49, Iss. 6 – P. 22–36.

Submitted on 28.10.14

Зависляк І., д-р фіз.-мат. наук,

Попов М., канд. фіз.-мат. наук, Мовчан М., асп.

каф. квантової радіофізики, факультет радіофізики, електроніки та комп'ютерних систем
Київський національний університет імені Тараса Шевченка

ПРИСТРОЇ МІЛІМЕТРОВОГО ДІАПАЗОНУ НА ОСНОВІ ПАСИВНИХ ФЕРИТОВИХ РЕЗОНАТОРІВ

В огляді розглянуто магнітодинамічні коливання в феритових резонаторах та їх застосування в міліметровому діапазоні довжин хвиль. Дано класифікацію власних коливань феритових резонаторів. Запропонована аналітична теорія для розрахунку резонансних частот та продемонстровано ряд електрично перестроюваних пристроїв міліметрового діапазону, що використовують магнітодинамічні коливання в зарезонансній та дорезонансній областях, наприклад вентиля, фазообертачі, смугопротискаючі фільтри.

Ключові слова: магнітодинамічні моди, прилади міліметрового діапазону, гексаферрит барію, нікелевий ферит, залізо-ітрієвий гранат.

Зависляк И., д-р физ.-мат. наук,

Попов М., канд. физ.-мат. наук,

Мовчан Н., асп.

каф. квантовой радиофизики, факультет радиофизики, электроники и компьютерных систем
Киевский национальный университет имени Тараса Шевченко

ПРИБОРЫ МИЛЛИМЕТРОВОГО ДИАПАЗОНА НА ОСНОВЕ ПАСИВНЫХ ФЕРРИТОВЫХ РЕЗОНАТОРОВ

В обзоре рассмотрено магнитодинамические колебания в ферритовых резонаторах и их использование в миллиметровом диапазоне длин волн. Дана классификация собственных колебаний ферритовых резонаторов. Предложена аналитическая теория для расчета резонансных частот и продемонстрировано ряд электрически перестраиваемых приборов миллиметрового диапазона, которые используют магнитодинамические колебания в зарезонансной и дорезонансной областях, например вентиля, фазовращатели, полосопропускающие фильтры.

Ключевые слова: магнитодинамические моды, приборы миллиметрового диапазона, гексаферрит бария, никелевый феррит, железо-иттриевый гранат.

UDC 523.44

S. Zaitsev, Junior Researcher Fellow, N. Kiselev, D.Sc., V. Rosenbush, D.Sc.,
Main Astronomical Observatory of the National Academy of Sciences of Ukraine,
F. Velichko, Ph. D., Institute of Astronomy of Karazin Kharkiv National University,
N. Kolesnikov, Ph. D., Astronomical Observatory of Odessa Mechnikov National University

POLARIMERTY OF GALILEAN SATELLITES OF JUPITER NEAR OPPOSITION IN 2012–2014

We present results of new polarimetric observations of Galilean satellites of Jupiter Io, Ganymede, Europa, and Callisto carried out during 2012–2014. We used 2.6-m Shain telescope (Nauchny, Crimean Astrophysical Observatory) and 1-m RCC telescope (Simeiz, Crimean Astrophysical Observatory) equipped with one-channel photoelectric polarimeters. The measurements were performed at phase angles ranging from 0.03° to 3.46°. Our new observations confirmed the presence of the polarization opposition effect for high-albedo satellites Io, Europa, and Ganymede at phase angles less than 2°. We did not detect the polarization opposition effect for moderate-albedo satellite Callisto.

Keywords: polarization, satellite, polarization opposition effect.

Introduction. Measurements of the polarization of scattered light as functions of the phase angle is an important source of information about the physical properties of the surfaces of distant atmosphereless Solar System Bodies (asteroids, satellites, planetary rings). The phase-angle dependence of polarization near the opposition for different ASSBs are still in the focus of attention because the behavior of polarization at small phase angles is a key test for alternative models of light scattering by regolith surfaces.

High-albedo Jovian satellites Io, Europa, and Ganymede are among the ASSBs exhibiting the sharp opposition effect of brightness accompanied by the polarization opposition effect (POE). It is a sharp peak of negative polarization at small phase angles superimposed on the regular negative polarization branch [0]. Its existence was theoretically predicted by Mishchenko [0] as manifestation of coherent backscattering as one of the former mechanisms to explain the observed opposition effects for high-albedo ASSBs.

Polarimetric observations of the Galilean satellites in wide range of phase angles were started in 1960s [0]. The polarization opposition effect for high-albedo satellites Io, Europa, and Ganymede at phase angles less than 2° was originally discovered by Rosenbush et al. [0]. Later it was confirmed by Rosenbush and Kiselev [0], Kiselev et al. [0], and Zaitsev et al [0]. But so far the available polarimetric data are still not enough to trace because the behavior of polarization at small phase angles in details. It is very important to distinguish between "narrow" secondary minimum superimposed upon the regular negative polarization branch and "wide" asymmetric negative polarization branch. In order to archive it we need to obtain polarimetric data in phase angles range from 2.5° to 3.5° which are missing.

We present results of new polarimetric observations of the Galilean satellites at small phase angles.

Observations. Polarimetric observations of Galilean satellites Io, Ganymede, Europa, and Callisto were carried out during 7 night on November 29 – December 18, 2012, and 2 nights on January 4–5, 2014. We used 2.6-m Shain telescope equipped with a one-channel photoelectric photometer-polarimeter [0] and 1-m RCC telescope equipped with a one-channel photoelectric photometer-polarimeter [0] (Crimean Astrophysical Observatory). Both polarimeters are based on modulation principle with a rapidly rotating retarder. Observations were carried out in V and R spectral bands. The measurements were performed at phase angles ranging from 0.03° to 3.46°.

All our observations have been carried out in the mode of linear polarization measurements.

The Stokes parameters u and q were received from observations, and then the degree of linear polarization P and the position angle of the polarization plane θ were calculated, using the expressions:

$$P = \sqrt{u^2 + q^2},$$

$$\operatorname{tg} 2\theta = \frac{u}{q}.$$

The random error σ_P in degree of linear polarization P was calculated using mean square errors of the individual measurements of parameters q and u , which in turn are calculated using both statistics of recorded photons and their internal dispersion [0]. The larger of these two errors was adopted as an accuracy measure of the mean values of parameters of polarization P of measurements during the night.

The errors σ_θ in the position angle measurements were determined using the standard relation

$$\sigma_\theta = \frac{28.65 \sigma_p}{P}.$$

The instrumental polarization and the zero point of position angles were determined each night using standard stars with zero and large polarization [0, 0]. The errors in polarization degree due to uncertainties in the instrumental polarization and reductions to the standard system do not exceed 0.05%.

In all cases, the angle between the polarization plane and the plane perpendicular to the scattering plane φ according to the expression:

$$\theta_r = \theta - (\varphi \pm 90^\circ)$$

is close to 90°, i.e., the degree of polarization is negative, as it generally agreed.

Discussion. Fig. 1 represents phase-angle dependencies of linear polarization for the Galilean satellites in the V and R spectral bands at phase angles less than 7° according to this work (filled symbols) and previous works (open symbols) – Rosenbush et al. [0], Rosenbush and Kiselev [0], Kiselev et al. [0], Zaitsev et al. [0]. Circles represents data for leading hemispheres, and diamonds for trailing hemispheres. For Europa and Ganymede solid lines are the regular negative branches of polarization. For Io and Callisto solid and dashed lines are the regular negative branches of polarization for the leading and trailing hemispheres respectively [0].

Our new observations confirmed the presence of asymmetric secondary minimum of polarization (the polarization opposition effect) superimposed upon the negative polarization branch for high-albedo satellites Io, Europa, and Ganymede at phase angles less than 2°. The scatter of polarization data points is mainly the result of local inhomogeneities of the satellites surface, which is superimposed on the global distinctions of polarimetric properties of the leading and trailing hemispheres.

New observations fill the gap in our data in phase angles range from 2° to 4°. As one can see, in this phase angles range the behavior of polarization can be described by the regular negative branch of polarization.

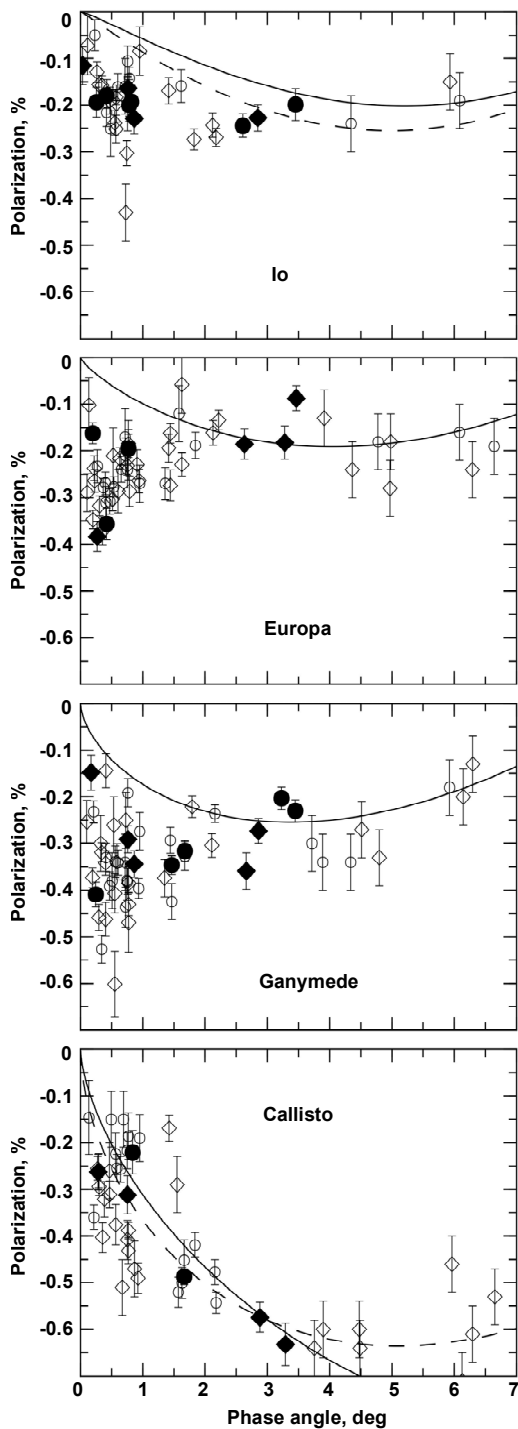


Fig. 1. Phase-angle dependencies of polarization for Galilean satellites in the V and R bands at phase angles less than 7° according to this work (filled symbols) and previous works (open symbols) – Rosenbush et al. [0], Rosenbush and Kiselev [0], Kiselev et al. [0], Zaitsev et al. [0].
 Circles represents data for leading hemispheres, and diamonds for trailing hemispheres

For now high-albedo Galilean satellites of Jupiter are the only outer planets satellites exhibiting secondary minimum of negative polarization at small phase angles as sharp peak superimposed on the regular negative polarization branch. The high-albedo moons of Saturn, including the bright side of Iapetus, exhibit deep and very asymmetric phase-angle curves of polarization without a separate secondary minimum near opposition [0,0], while they have albedo close to albedo of Europa. It seems that these distinctions may imply different microstructures of the upper layers of the satellites as well as different albedos can be caused by different processes. At the same time, Io, Europa, and Ganymede show bimodal branches of negative polarization similar to bimodal branch of negative polarization of high-albedo asteroid 64 Angelina [0], while the composition of their surfaces is different.

Conclusions. New polarimetric observations of the Galilean satellites of Jupiter in 2012–2014 are in a good agreement with our previous observations and confirm the presence of the polarization opposition effect for Io, Europa, and Ganymede in the range of phase angles smaller than 2°. Within the accuracy of the measurements we did not detect the polarization opposition effect for moderate-albedo satellite Callisto.

REFERENCE:

1. Afanasiev V. Polarimetry of Uranian satellites at the 6-m BTA telescope. / V. Afanasiev, V. Rosenbush, N. Kiselev // *Astrophys. Bull.*, 2014. – Vol. 69(2). – P.121–133.
2. Dollfus A. Optical polarimetry of the Galilean satellites of Jupiter. / A. Dollfus // *Icarus*, 1975. – Vol. 25. – P. 416–431.
3. Ejeta C. Spectro-polarimetry of the bright side of Saturn's moon Iapetus. / C. Ejeta, H. Boehnhardt, S. Bagnulo, G. Tozzi // *Astron. Astrophys.*, 2012. – Vol. 537. – A23.
4. Hsu J.-C. On standard polarized stars. / J.-C. Hsu, M. Breger // *Astrophys. J.*, 1982. – Vol. 262. – P. 732–738.
5. Kiselev N. Polarimetry of the Galilean satellites and Jupiter near opposition. / N. Kiselev, V. Rosenbush, F. Velichko, S. Zaitsev // *J. Quant. Spectrosc. Radiat. Transfer.*, 2009. – Vol. 110. – P. 1713–1718.
6. Mishchenko M. On the nature of the polarization opposition effect exhibited by Saturn's rings. / M. Mishchenko // *Astrophys. J.*, 1993. – Vol. 411. – P. 351–361.
7. Polarization properties of the Galilean satellites of Jupiter: Observations and preliminary analysis. / V. Rosenbush, V. Avramchuk, E. Rosenbush, M. Mishchenko // *Astrophys. J.*, 1997. – Vol. 487. – P. 402–414.
8. V. Rosenbush. Polarization opposition effect for the Galilean satellites of Jupiter. / Rosenbush V., Kiselev N. // *Icarus.*, 2005. – Vol. 179. – P. 490–496.
9. Serkowski K. Polarimeters for optical astronomy / K. Serkowski // In book: *Planets, stars and nebulae. Studied with photopolarimetry*, Ed. by T. Gehrels – Tucson., 1974. – P. 135–174.
10. Shakhovskoy N. Polarization observations of nonstable stars and extragalactic objects. I. Equipment and technique of observations and their processing. / N. Shakhovskoy, Y. Efimov // *Izv. Crimean Astrophys. Obs.*, 1972. – Vol. 45. – P.90–100.
11. Velichko S. Polarimetry and photometry of comet C/2004 Q2 (Machholz). / S. Velichko, N. Kiselev, F. Velichko // *Earth Moon Planets.* – 2005. – Vol. 97. – P. 379–86.
12. Polarimetric observations of the Galilean satellites near opposition in 2011. / S. Zaitsev, N. Kiselev, V. Rosenbush et al. // *Advances in Astronomy and Space Physics.*, 2012. – Vol. 2. – P. 177–179.
13. Polarimetry of the E-type asteroid 64 Angelina / S. Zaitsev, N. Kiselev, V. Rosenbush et al. // *Kinemat. Phys. Celest.*, 2014. – Vol. 30. – P. 155–160.

Submitted on 10.11.14

Зайцев С., мол. наук. співроб, Кисельов Н., д-р. фіз.-мат. наук, Розенбуш В., д-р. фіз.-мат. наук, Головна астрономічна обсерваторія Національної академії наук України, Величко Ф., канд. фіз.-мат. наук, НДІ астрономії Харківського національного університету ім. Каразіна, Колесніков С., канд. фіз.-мат. наук, НДІ "Астрономічна обсерваторія" Одеського національного університету ім. Мечнікова

ПОЛЯРИМЕТРІЯ ГАЛІЛЕЄВИХ СУПУТНИКІВ ЮПІТЕРА БІЛЯ ОПОЗИЦІЇ У 2012–2014 РОКАХ

Наводяться результати поляриметричних спостережень галілеєвих супутників Юпітера Іо, Європи, Ганімеда і Калісто, які проводилися у 2012–2014 рр. на 2.6-м телескопі ім. Шайна (с. Научний, Кримська астрофізична обсерваторія) і 1-м телескопі Цейсс-1000 (с. Сімеїз, Кримська астрофізична обсерваторія) за допомогою одноканальних фотометрів-поляриметрів. Діапазон фазових кутів складає 0.03°–3.46°. Наші нові спостереження підтверджують присутність поляриметричного опозиційного ефекта для високоальбедних супутників Іо, Європи і Ганімеда на фазових кутах, менших ніж 2°. Присутності поляриметричного опозиційного ефекта для Калісто не виявлено.

Ключові слова: поляризація, супутник, поляриметричний опозиційний ефект.

Зайцев С., мп. науч. сотр., Киселев Н., д-р. физ.-мат. наук,
 Розенбуш В., д-р. физ.-мат. наук, Главная астрономическая обсерватория Национальной академии наук Украины,
 Величко Ф., канд. физ.-мат. наук, НИИ астрономии Харьковского национального университета им. Каразина,
 Колесников С., канд. физ.-мат. наук, НИИ "Астрономическая обсерватория" Одесского национального университета им. Мечникова

ПОЛЯРИМЕТРИЯ ГАЛИЛЕЕВЫХ СПУТНИКОВ ЮПИТЕРА ВБЛИЗИ ОППОЗИЦИИ В 2012–2014 ГОДАХ

Представляются результаты поляриметрических наблюдений галилеевых спутников Юпитера Ио, Европы, Ганимеда и Каллисто, которые проводились в 2012-2014 гг. на 2.6-м телескопе им. Шайна (п. Научный, Крымская астрофизическая обсерватория) и 1-м телескопе Цейсс-1000 (п. Симеиз, Крымская астрофизическая обсерватория) с помощью одноканальных фотометров-поляриметров. Диапазон фазовых углов составлял $0.03^\circ - 3.46^\circ$. Диапазон фазовых углов Наши новые наблюдения подтверждают присутствие опозиционного поляриметрического эффекта для высококачественных спутников Ио, Европы, и Ганимеда на углах, меньших 2° . Присутствия поляриметрического опозиционного эффекта для Каллисто не обнаружено.

Ключевые слова: поляризация, спутник, поляриметрический опозиционный эффект.

UDC 537.226.4: 537.226.1: 537.226.83: 537.226.86

M. Zelenyuk, PhD stud., A. Susla, eng.,
 H. Guyvan, PhD, A. Slivka, Prof, Dr., V. Kedyulich, PhD
 Uzhhorod National University, Faculty of Physics

THE INFLUENCE OF AN EXTERNAL ELECTRIC FIELD AND UNIAXIAL PRESSURE ON THE DIELECTRIC PROPERTIES OF TGS+Cu²⁺ CRYSTALS

The results of an experimental study of the effect of uniaxial pressure and external electric field on dielectric properties of TGS crystals doped with metallic impurities of Cu²⁺ in the vicinity of the ferroelectric structural phase transition are presented. The obtained results are compared with published data for undoped TGS crystals. The results of experimental measurements shows that for the TGS crystals the uniaxial pressure σ_2 leads to a decrease in the maximum values of the dielectric constant and reducing the phase transition temperature and external electric fields leads to a decrease in the maximum values of the dielectric constant and increment of the phase transition temperature.

Keywords: TGS, external electric field, uniaxial pressure, metal impurities, dielectric constant, ferroelectric crystals.

Introduction. Among the ferroelectric crystals with hydrogen bonds triglycine sulfate (NH₂CH₂COOH)₃·H₂SO₄ (TGS), despite the complexity of the chemical formula and crystal structure, investigated the most fully. They are ferroelectrics with second order phase transition of "order-disorder" type. The crystal has monoclinic symmetry and belongs to centrosymmetric class 2/m above the Curie temperature $T_C = 322$ K. Below T_C the mirror plane disappears and the crystal belongs to the polar point group 2 of the monoclinic system.

The most important in understanding the mechanisms of phase transitions in ferroelectric crystals with hydrogen bonds is a study of their behavior under the influence of external factors such as pressure or electric field [1]. In particular, the external pressure is the only way to continuously modify the geometric characteristics of hydrogen bonds, break their equivalence etc., which makes it possible to investigate the role of hydrogen bonding in the mechanisms of the phase transition and dielectric response of crystals.

Significant part of ferroelectrics with hydrogen bonds has piezoelectric properties in the paraelectric phase. Applying the mechanical stress provides an opportunity to examine the piezoelectric interactions in phase transformations and formation of the physical characteristics of crystals [2].

To change the properties of the triglycine sulfate crystals they are doped by metallic or organic impurities.

The aim of this paper is to study the dielectric properties of TGS+Cu²⁺ crystals under the influence of an external electric field and uniaxial pressure. The concentrations of impurities for these crystals are 2%.

Experimental. The dielectric constant of the crystals was determined by the results of experimental measurements of the capacitance of samples and was calculated by using the formula for a plane capacitor. The capacitance of samples was directly measured by using an AC bridge LCR E7-12 at a frequency of 1 MHz with a measuring field of 1.25 V/cm.

Samples were made in the form of a parallelepiped, oriented according to the crystallographic axes. At the

edge, which are perpendicular to the polar direction, were applied electrical contacts with silver paste. Uniaxial mechanical stress was created by a spring dynamometer and was transferred on sample through a punch with floating heads (fig. 1).

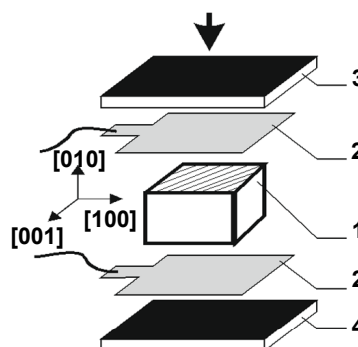


Fig. 1. Method of the investigations under the influence of uniaxial compression (1 – sample, 2 – cooper foil contacts, 3 – floating head punch, 4 – cell support)

The accuracy of registration of the uniaxial pressure was $\pm 5\%$. The samples were placed in a specially constructed thermostat which allowed to gradually adjust the temperature of sample. The temperature was measured by the copper-constantan thermocouple with an accuracy of ± 0.1 K. To improve heat transfer and to prevent contact with air the sample and thermocouple were filled by silicone oil.

The device for investigating the ferroelectric crystals under uniaxial pressure allows to perform measurements over a wide temperature range ($77 \div 370$ K) and efforts (up to 45 kg). Uniaxial pressure was applied along the ferroelectric axis b, which corresponds to the mechanical stress σ_2 [3].

Fig. 2 shows the temperature dependences of the dielectric constant of studied crystals under the influence of the external electric field.

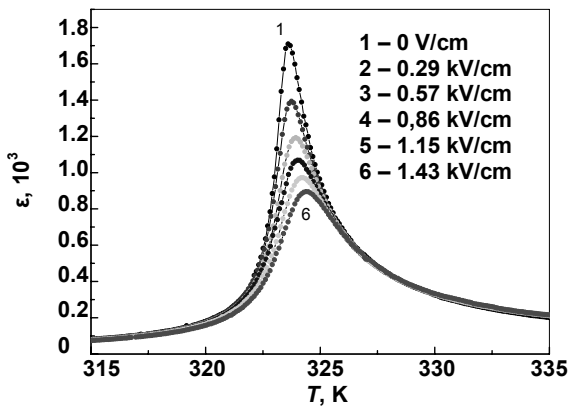


Fig. 2 Temperature dependences of the dielectric constant of TGS+Cu²⁺ crystals for different values of external electric fields

Fig. 3 shows the temperature dependences of the dielectric constant of studied crystals under the influence of the uniaxial pressure σ_2 .

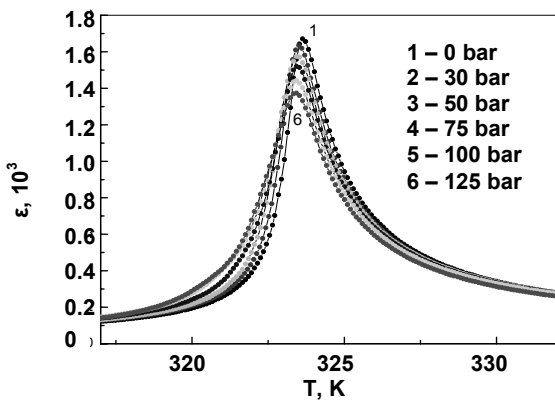


Fig. 3. Temperature dependences of the dielectric constant of TGS+Cu²⁺ crystals for different values of uniaxial pressure σ_2

It can be seen, that the application of mechanical stress and external electric field decreases the maximum value of the dielectric constant.

Fig. 4 shows the field dependences of the maximum temperature of the dielectric constant and the values of this maximum of TGS+Cu²⁺ crystals.

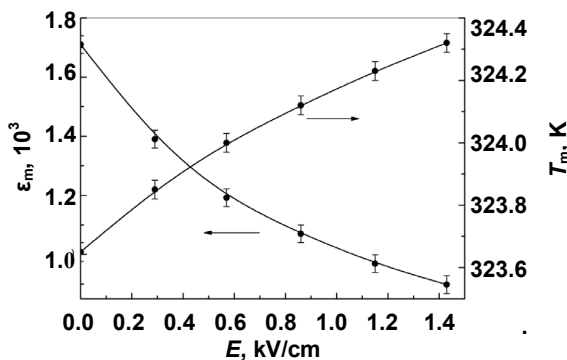


Fig. 4. The field dependences of the maximum temperature of the dielectric constant and the values of this maximum of TGS+Cu²⁺ crystals

Fig. 5 shows the phase σ_2 -T-diagrams of TGS+Cu²⁺ crystals. To construct the phase diagrams the extrapolating of the inverse temperature dependence of the dielectric constant to zero in the paraelectric phase was performed [2].

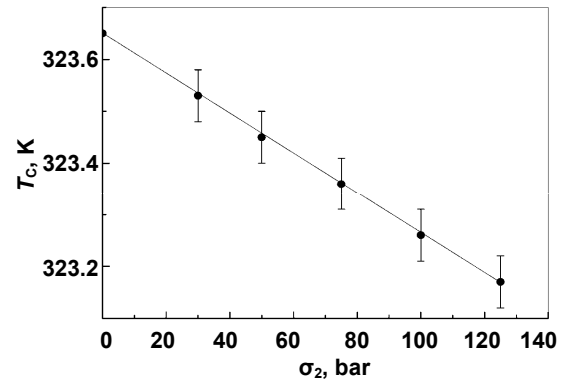


Fig. 5. The phase σ_2 -T-diagrams of TGS+Cu²⁺ crystals

The temperature of the maximum of the dielectric constant increases under the influence of an external electric field whereas it – decreases under the influence of uniaxial pressure.

It was shown that the increase in the atomic mass of doped impurities leads to the increase in the phase transition temperature. Thus, for TGS and TGS+Cu²⁺ crystals it was, respectively, 321,9 K and 323,6 K.

The pressure coefficients of the shift the phase transition temperature for Cu-doped TGS crystals is equal to -5.3 K/kbar. The displacement of the phase transition temperature under the influence of uniaxial pressure along the ferroelectric axis of doped crystals was less than for undoped ones.

This effect can be accounted for by the existence of internal electric fields in doped crystals, the value of which is determined by the presence of impurities [1, 4]. The nature of such internal fields has a relaxing character, and the presence of such internal field, along with the changes of the temperature maximum of dielectric constant, leads to the blurring of $\epsilon(T)$ dependencies.

Conclusions.

1. Established the reducing of displacement of the phase transition temperature of doped TGS crystals, due to the existence of internal electric fields, the value of which is determined by the presence of impurities (Cu²⁺).
2. The phase σ_2 -T-diagrams are constructed.
3. For the TGS+Cu²⁺ crystals the uniaxial pressure σ_2 leads to a decrease in the maximum values of the dielectric constant and reducing the phase transition temperature with a coefficient of $dT_C/d\sigma_2 = -5.3$ K/kbar.
4. Increasing the atomic mass of dopants leads to an increase in the phase transition temperature. Thus, for TGS and TGS+Cu²⁺ crystals it was, respectively, 321,9 K and 323,6 K.

REFERENCE:

1. Influence of spatially inhomogeneous electric fields on dielectric constant in ferroelectrics / V.M. Kedyulich, E.I. Gerzanich, A.G. Slivka, P.M. Lukach // Scientific Bulletin of the Uzhhorod University, ser. Physics (in Ukrainian). – 1999. – № 3. – P. 79–81.
2. Kiyoyasu I. Effect of Uniaxial Pressure on the Ferroelectric Phase Transition of Tri-Glycine Sulfate. / I. Kiyoyasu // Journal of the Physical Society of Japan. – 1974. – Vol. 36, №4.
3. Condensed Matter Physics / Kedyulich V.M. et al. – 2000. – Vol. 3, №4 (24). – P. 851–856.
4. Influence of electric field on the ferroelectric phase transition in Sn₂P₂S₆ / A.G. Slivka, V.M. Kedyulich, E.I. Gerzanich et al. // Ukr. fiz. j., 2000. – V. 45, № 3. – P. 328–331.

Зеленюк М., асп., Сусла А., пров. інж., Гуйван Г., канд. фіз.-мат. наук, доц.,
Сливка О., д-р фіз.-мат. наук, проф., Кедюлич В., канд. фіз.-мат. наук, доц.,
ДВНЗ "УжНУ", Фізичний факультет

ВПЛИВ ЗОВНІШНЬОГО ЕЛЕКТРИЧНОГО ПОЛЯ ТА ОДНОВІСНОГО ТИСКУ НА ДІЕЛЕКТРИЧНІ ВЛАСТИВОСТІ КРИСТАЛІВ TGS+Cu²⁺

Наведено результати експериментального дослідження впливу одновісного тиску та зовнішнього електричного поля на діелектричні властивості кристалів ТГС, легованих металічними домішками Cu²⁺, в околі структурного сегнетоелектричного фазового переходу. Отримані результати порівнюються з літературними даними для нелегованого домішками кристалу ТГС. Результати експериментальних вимірювань показали, що для кристалів ТГС+Cu²⁺ одновісний тиск σ_2 приводить до зменшення максимальних значень діелектричної проникності та зменшення температури фазового переходу, а зовнішнє електричне поле призводить до зменшення максимального значення діелектричної проникності і зростання температури фазового переходу.

Ключові слова: ТГС, зовнішнє електричне поле, одновісний тиск, металічні домішки, діелектрична проникність, сегнетоелектрики.

Зеленюк М., асп., Сусла А., вед. інж., Гуйван А., канд. фіз.-мат. наук, доц.,
Сливка А., д-р фіз.-мат. наук, проф., Кедюлич В., канд. фіз.-мат. наук, доц.,
ГВНЗ "УжНУ", Фізический факультет

ВЛИЯНИЕ ВНЕШНЕГО ЭЛЕКТРИЧЕСКОГО ПОЛЯ И ОДНООСНОГО ДАВЛЕНИЯ НА ДИЭЛЕКТРИЧЕСКИЕ СВОЙСТВА КРИСТАЛЛОВ TGS+Cu²⁺

Приведены результаты экспериментального исследования влияния одноосного давления и внешнего электрического поля на диэлектрические свойства кристаллов ТГС, легированных металлическими примесями Cu²⁺, в окрестности структурного сегнетоэлектрического фазового перехода. Полученные результаты сравниваются с литературными данными для нелегированного примесями кристалла ТГС. Результаты экспериментальных измерений показали, что для кристаллов ТГС+Cu²⁺ одноосное давление σ_2 приводит к уменьшению максимальных значений диэлектрической проницаемости и уменьшению температуры фазового перехода, а внешнее электрическое поле приводит к уменьшению максимального значения диэлектрической проницаемости и увеличению температуры фазового перехода.

Ключевые слова: ТГС, внешнее электрическое поле, одноосное давление, металлические примеси, диэлектрическая проницаемость, сегнетоэлектрики.

UDC 535.37; 53.044; 621.3.032.36

O. Ishchenko, Dr.Sci., A. Shkavro, Ph.D., O. Braiman, stud.,
D. Nechepurenko, stud., Institute of high technology
Taras Shevchenko National University of Kyiv

LUMINESCENT PROPERTIES OF ORGANIC DYES IN POLYMERS PEPK AND PVE

Sandwich-structures for the electroluminescence investigation were produced with the method of the organic dye applying to the glass substrate surface covered with ITO with spin-coating. Aluminium contacts were evaporated in the vacuum chamber. Samples for the photoluminescence investigation were produced simultaneously. The dependence of the change in position of the maxima of the photoluminescence spectra on the dye content and the matrix polymer type were investigated. Current-voltage characteristic of the produced structures were obtained and the dependence of integral electroluminescence intensity on the voltage on the sample was determined.

Key words: organic dye, PEPK, PVE, ITO, sandwich-structure, OLED, photoluminescence, electroluminescence, PPV.

Light emitting structures based on organic materials are widely used all over the world. In comparing to liquid crystal displays (LCD) OLED-displays need any external highlight, have a large viewing angle and wide working temperature range. OLED-technologies permit flexible displays creation. One of the fundamental materials for organic light emitting structure fabrication is PPV. The aim of this work is investigation of polymers PEPK and PVE, doped with an organic dye, as an alternative material for organic light emitting structures fabrication.

Samples for the electroluminescence investigation were made as a sandwich-structure (Fig. 1). On the glass substrate with ITO-layer sequentially were applied layers of PEDOT:PSS and polymer, doped with an organic dye using spin coating [2]. Chosen PEDOT:PSS is modified and has optimal conductivity and capacity [3]. PEDOT:PSS decreases ITO surface irregularity and enhance hole injection [4].

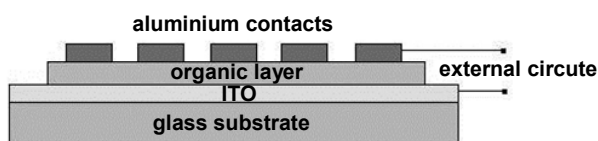


Fig. 1. Sandwich-structure

As an active layer we used polymers PEPK and PVE, doped with the organic dye DCM (1% and 10%). Structural formulas of the dyes DCM and N#1 are shown on figures 2

and 3 respectively. Aluminium electrodes were deposited through the mask on the polymer layer.

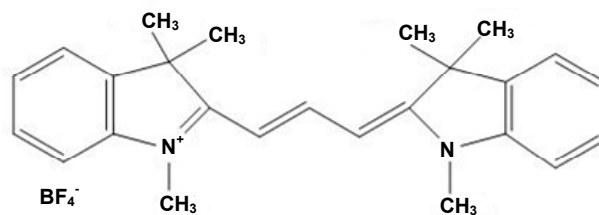


Fig. 2. Structural formula of the dye N#1

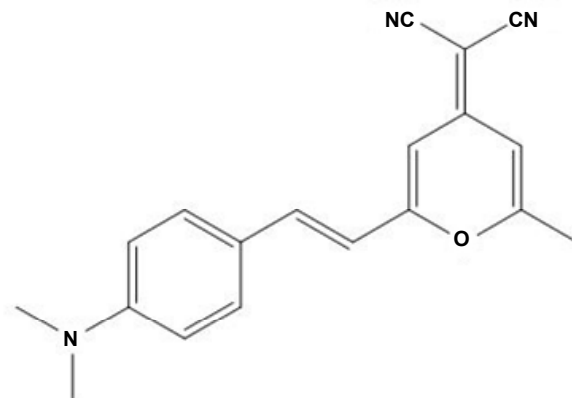


Fig. 3. Structural formula of the dye DCM

Simultaneously samples for photoluminescence investigation were created. To fabricate them the same solutions of the polymers, doped with organic dyes, were deposited on the glass substrate by coating.

Electrophysical and luminescent characteristics investigation of the samples was conducted on an automated installation, based on the aperture of the monochromator MDR-2 [1].

Photoluminescence spectra of investigated samples with DCM are shown on figure 4. Photoluminescence spectra depend on polymer type and dye concentration. The maximum intensity of photoluminescence when using 10% doping shifts toward the long-wave region compared to the photoluminescence maximum at 1% doping. ($\lambda = 40\text{nm}$).

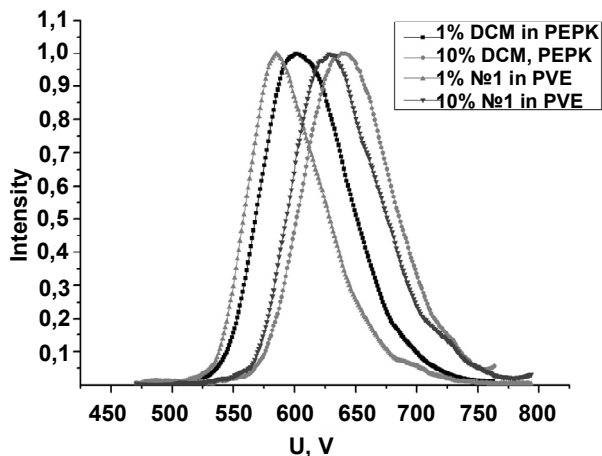


Fig. 4. Photoluminescence spectrum of 1% and 10% DCM in PEPK and PVE

Photoluminescence spectra of samples with the dye №1 are shown on the figure 5. Photoluminescence maxima sequence of the samples with the dye №1 is similar to the photoluminescence maximum sequence of the samples with the dye DCM. The maximum of the photoluminescence of the sample based on PVE with 1% organic dye concentration ($\lambda = 610\text{ nm}$) is located in the most shortwave region. Further is located the photoluminescence maximum of the sample based on PEPK with 1% organic dye concentration ($\lambda = 622\text{ nm}$). 1 nm further is the photoluminescence maximum of the sample based on PVE with 10% organic dye concentration ($\lambda = 623\text{ nm}$), and the last is the photoluminescence maximum of the sample based on PEPK with 10% organic dye concentration. It is difficult to determine which factor has the greater impact on the photoluminescence maximum shift: dye content change or matrix polymer change. The differences between different polymers photoluminescence maximum location with 1% and 10% dye content are 12 nm and 9 nm respectively. The differences between photoluminescence maximum of the samples with 1% and 10% dye content are 10 nm and 13 nm for the samples based on PEPK and PVE respectively.

Typical current-voltage characteristic of the investigated sandwich-structures is shown on the figure 6. Qualitatively it is similar to based on PPV OLED's characteristic.

Typical sandwich-structure ITO/1%DCM in PVE/Al electroluminescence integral intensity dependence is shown on figure 7. Emission begins at voltages on the sample near 3V and rapidly grows up with the increasing of voltage. At voltages more than 10–15 V there are instability and degradation of the structure's characteristics.

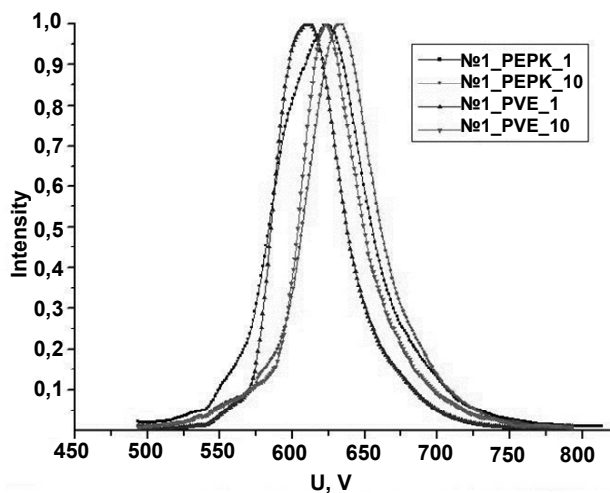


Fig. 5. Photoluminescence spectrum of 1% and 10% content of the dye №1 in PEPK and PVE

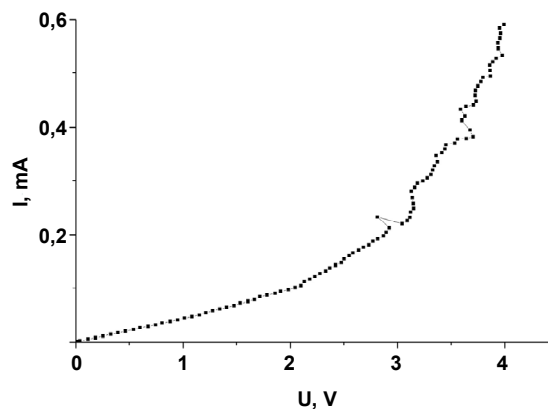


Fig. 6. Typical current-voltage characteristic of sandwich-structure ITO/1% DCM in PVE/Al

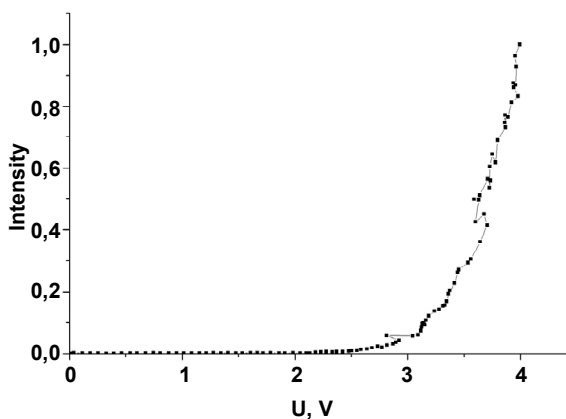


Fig. 7. Typical electroluminescence intensity of DCM in PEPK and PVE

Electroluminescence spectrum of the structure based on PPV is shown on the figure 8. Electroluminescence spectra of the investigated structures at voltages 15–25 V are analogous by form to electroluminescence spectra of the structures, based on PPV, and have a greater half-width.

Conclusions. Photoluminescence spectra maximum of the polymer 10% doped with the dye are shifted to the right approximately per 40 nm comparing to photoluminescence spectra maximum of the polymer 1% doped with the dye.

This value is 10 nm for polymers doped with the dye №1. Polymer PEPK doped with the dye DCM photoluminescence intensity maximum is shifted to the right per 10–15 nm from the analogous maximum for PVE. For polymers doped with the dye №1 this value is 9–12 nm.

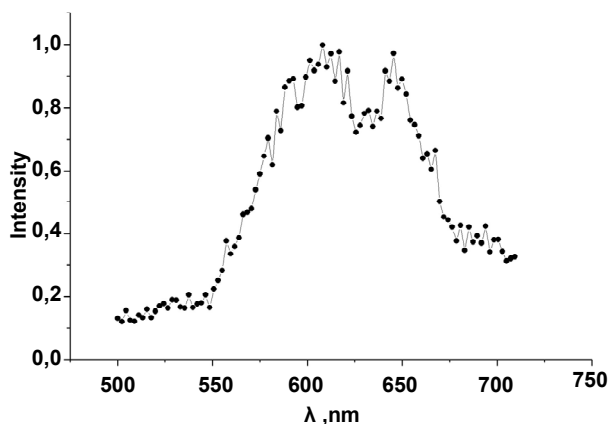


Fig. 8. Electroluminescence spectrum of the structure based on PPV at voltage $V = 30V$

Ищенко О., д-р. хім. наук, Шкавро А., канд. фіз.-мат. наук, Брайман О., студ., Нечепуренко Д., студ., Інститут високих технологій, Київський національний університет імені Тараса Шевченка

ЛЮМИНЕСЦЕНТНІ ВЛАСТИВОСТІ ОРГАНІЧНИХ БАРВНИКІВ У ПОЛІМЕРАХ РЕРК І PVE

Виготовлено сандвіч-структури для дослідження електролюмінесценції шляхом нанесення органічного шару методом центрифугування на скляну підкладку з ITO та напылення алюмінієвих контактів і зразки для дослідження фотолімінесценції. Досліджено залежність зміни положення максимумів спектрів фотолімінесценції від вмісту барвника і типу матричного полімеру. Знято вольт-амперні характеристики виготовлених сандвіч-структур та встановлено залежність інтегральної інтенсивності електролюмінесценції від напруги.

Ключові слова: органічний барвник, РЕРК, PVE, ITO, сандвіч-структура, OLED, фотолімінесценція, електролюмінесценція, PPV.

Ищенко А., д-р хім. наук, Шкавро А., канд. физ.-мат. наук, Брайман А., студ., Нечепуренко Д., студ., Інститут високих технологій, Киевский национальный университет имени Тараса Шевченко

ЛЮМИНЕСЦЕНТНЫЕ СВОЙСТВА ОРГАНИЧЕСКИХ КРАСИТЕЛЕЙ В ПОЛИМЕРАХ РЕРК И PVE

Изготовлено сандвич-структуры для исследования электролюминесценции нанесением органического слоя методом центрифугирования на стеклянную подкладку с ITO и напылением алюминиевых контактов и образцы для исследования фотолімінесценции. Исследовано зависимость изменения положения максимумов на спектрах фотолімінесценции от количества красителя и типа матричного полимера. Снято вольт-амперные характеристики изготовленных сандвич-структур и установлено зависимость интегральной интенсивности электролюминесценции от напряжения.

Ключевые слова: органический краситель, РЕРК, PVE, ITO, сандвич-структура, OLED, фотолімінесценция, электролюминесценция, PPV.

UDC 535.373, 538.958

The instability of electroluminescence and electrophysical characteristics of the samples at voltages more than 10–15 V are found. Polymers, doped with organic dyes demonstrate characteristics, which are analogous to based on PPV structure's characteristics and can be used as a material for OLED's active layer.

REFERENCE:

1. Prosta realizatsiya metodu pidrahunku fotoniv dlia doslidzhennia spectriv poverhnevobarjnyh nanogeterostruktur / S.V. Bunak, V.V. Ilchenko, O.M. Okoronko, A.G. Shkavro // Visnyk Kyivskogo universytetu, seria Fizyko-matematychni nauky, 2007. – № 4, P. 249–254.
2. Kelvin probe and ultraviolet photoemission measurements of indium tin oxide work function: a comparison / J.S. Kim, B. Lägél, E. Moons et al. // Synthetic Metals, 2000, Vol. 111–112, P. 311–314.
3. Structure and electronic properties of poly (3,4-ethylene-dioxythiophene) poly(styrene sulfonate) prepared under ultrasonic irremission / O. Yu. Posudievsky, N. V. Konoshchuk, A. G. Shkavro et al. // Synthetic Metals, 2014, Vol. 195, P. 335–339.
4. Issledovanie vliyania rasstvoriteley sopriazhennykh polimerov na harakteristiki planarnykh heterostruktur ITO/PEDOT:PSS/PF/AL I ITO/PEDOT:PSS/MEH-PPV/AL / V. M. Sorokin, Yu. V. Kolomzarov, M. A. Miniaylo et al. // Doklady BGUIR, 2011. – №3(57). – P. 81–86.

Submitted on 15.11.14

PL AND FTIR SPECTROSCOPY OF POWDERED SILICA AEROGEL $ar-SiO_x$

Optical and photoluminescent properties of powdered silica aerogel $ar-SiO_x$ have been investigated using FTIR spectroscopy and PL lifetime spectroscopy. Powdered silicagel was prepared from sodium silicate water solution using sol-gel technique. It was confirmed that the investigated material consists of two phases: stoichiometric SiO_2 and non-stoichiometric SiO_x . FTIR analyses reveal the presence of numerical hydroxyle groups which determines oxidative properties of the material and makes it a promising matrix for the incorporation of nanoparticles. The intense PL emission was detected in blue-green region with stipulated peaks at 1.9, 2.0, 2.2 and 2.6 eV. It was shown that emission properties of powdered silica aerogel $ar-SiO_x$ caused by the presence of numerical oxygen defect centres: oxygen hole centers, peroxide radicals and oxygen-deficient centers as well as siloxane and silane groups. It was also obtained that under UV treating by pulsed laser irradiation the transformation the integrated PL intensity is decreased. The PL quenching is caused by transformation of the defect structure during photo oxidation process.

Keywords: powdered silica aerogel, defect states, FTIR transmission spectroscopy, PL lifetime spectroscopy.

Introduction. It is considered that porous oxide materials, possessing a large specific surface area, high porosity and fine grain structure, can be used as a comprehensive matrix for nanoparticles incorporation and molecular adsorption in order to create luminescent nanocomposites, photodetectors, catalysts, waveguides, lasers and gas sensors [1, 5, 12, 15]. The considered

nanoporous materials are simple and inexpensive in preparation, the gas sensor sensitivity can be significantly increased due to the enlarged overall active surface area.

The fact that typical aerogels have more than 90% porosity gives them unusual characteristics: they are characterized by extremely high surface area, high thermal resistivity, low dielectric constant and low refractive index.

Depending on the preparation technique the silica aerogel demonstrates a strong visible PL in the blue–green region [3]. Numerous studies have been devoted to the investigation of the origin of luminescence in other SiO_2 based structures [2,17]. In fact, the structural and compositional features of the prepared silica aerogels, amorphous silica, silica xerogels and porous silica remain similar. In these materials, the ratio of surface atoms to bulk atoms is quite large, resulting in several potential light-emitting defect centres that are peculiar to the surface states. These surface related defect sites strongly affect the dynamics of the electronic transitions and will hence influence the related optical and PL properties.

In our earlier work [9] it was proved that silica aerogel has a high sensitivity with respect to liquid adsorbate and can be effectively used as transducer for chemical sensors. In this work optical and photoluminescence properties of powdered silica aerogel $ar - \text{SiO}_x$ have been investigated. The effect of UV irradiation on evolution of PL spectra has been studied.

Experiment. Powdered silica aerogel ($ar - \text{SiO}_x$) was prepared from sodium silicate water solution and an ethanol-based catalyst [11]. The drying process was carried out in an autoclave at supercritical parameters ($T=240^\circ\text{C}$ and $p=8 \cdot 10^6 \text{ Pa}$) in the presence of ethanol. These conditions are maintained for a short time with subsequent slow pressure reduction down to atmospheric pressure. As prepared material was then annealed at 450°C at oxygen atmosphere. The TEM image of porous $ar - \text{SiO}_x$ is presented on Fig. 1. In our earlier work using X-ray diffraction analyses it was observed that porous aerogel $ar - \text{SiO}_x$ is the mixture of amorphous and crystal phases that consists of cristobalite and quartz.

FTIR measurements were carried out using Fourier spectrometer "Perkin-Elmer Spectrum BX" in the range of $400\text{--}4000 \text{ cm}^{-1}$ with 4 cm^{-1} resolution.

The samples used for PL measurements were prepared by pressing of silica aerogel into pellets with diameter of about 12 mm and typical thickness of $0,2 \pm 0,3 \text{ mm}$ at a pressure of 13 MPa. The temporal domain PL spectra were measured at the room temperature using the analogous registration scheme [4]. The samples were excited with nitrogen laser pulses at 337 nm (3.68 eV), repetition rate 100 Hz, pulse duration $\tau=8 \text{ ns}$ and average power 20 mW. The proper band of emission was selected by a monochromator (MS2004, SOLAR TII) and registered by a combination of photomultiplier (HAMAMATSU C6270) and analog-to-digital board (up to 1 GHz sample rate). The signal was processed and analyzed by PC.

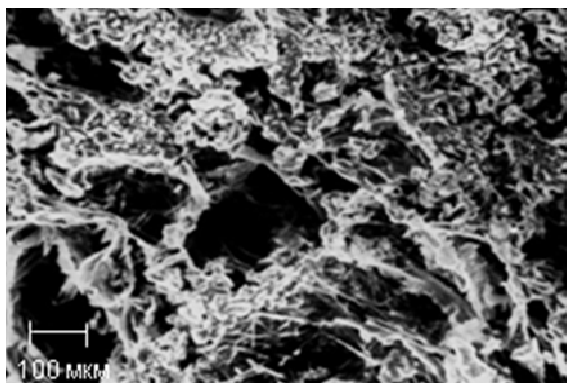


Fig. 1. TEM image of silica aerogel

FTIR spectroscopy. Fig. 2 shows FTIR transmittance spectrum of silica aerogel $ar - \text{SiO}_x$. There are absorption modes of Si-O-Si bonds with maxima at 1095, 780 and 460 cm^{-1} and a wide band in the $3000\text{--}3700 \text{ cm}^{-1}$ region. The last one is due to the presence of adsorbed water and surface OH groups (OH stretching vibrations at 3440 cm^{-1}) [6,14].

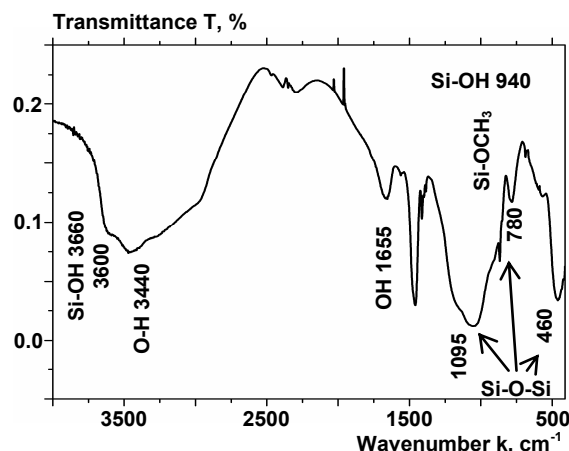


Fig. 2. FTIR transmittance spectrum of silica aerogel $ar - \text{SiO}_x$ correlated by KBr spectrum. Characteristic absorbing modes are indicated

The nature of surface groups of silica aerogel is strongly dependent on the conditions used during its preparation. In the considered aerogel $ar - \text{SiO}_x$ produced from water solution the surface is almost fully covered with hydroxyl groups.

Water molecules in interaction with silica surface groups effectively break Si-O-Si bonds forming a surface hydroxyl Si-OH groups, as a result FTIR spectrum reveals shoulders at 3600 and 940 cm^{-1} due to presence of bounded Si-OH groups.

A weaker Si-OH bending vibration band is revealed at 1650 cm^{-1} . The FTIR spectrum reveals also the presence of absorption modes of more complex structural groups such as Si-OCH_3 .

In Fig. 3 the result of Gaussian peak deconvolution is presented for absorption peak of Si-O-Si stretching vibration LO and TO groups. The peak in the region of $1300\text{--}850 \text{ cm}^{-1}$ has been revealed to have complex structure with maxima at 902, 1001, 1098 and 1201 cm^{-1} .

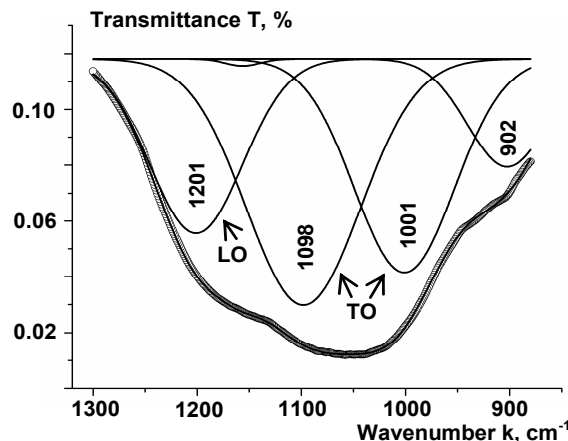


Fig. 3. The result of deconvolution into Gaussian profiles of stretching absorption Si-O-Si band of silica aerogel $ar - \text{SiO}_x$

The presence of stretching TO modes at 1098 and 1201 cm^{-1} having a large semiwidth (110 and 96 cm^{-1} correspondingly) suggests that investigated material consists of stoichiometric and non-stoichiometric phases $\text{SiO}_2 / \text{SiO}_x$.

This conclusion is consistent with the data of X-ray diffraction analyses obtained in [10]. The wavenumber of TO absorption peak is calculated from empirical solution $\nu(\text{SiO}_x) = 900 + 90x \text{ cm}^{-1}$ [6], so in our case x value varies from 1.1 to 2. Absorption peak at 1201 cm^{-1} is also shifted from 1250 cm^{-1} for stretching LO vibrations in stoichiometric SiO_x structures.

Taking into consideration the huge surface area and a number of surface hydroxyl groups, silica aerogel displays acidic properties and can be used as matrix for grafting of different molecules, e.g. for chemical sensors. In earlier work [17] it was proved that silica aerogel ar-SiO_x is characterized by significant sensor response under interaction with liquid adsorbates.

PL spectroscopy. The integrated PL spectrum of the freshly prepared ar-SiO_x sample is presented on Fig. 4. Gaussian peak decomposition of the PL spectrum reveals the presence of 4 basic peaks: Peak P1 at 1.89 eV with semiwidth (FWHM) $\Delta E = 0.11$ eV; Peak P2 at 2.08 eV ($\Delta E = 0.16$ eV); Peak P3 at 2.23 eV ($\Delta E = 0.35$ eV) and Peak P4 at 2.61 eV ($\Delta E = 0.99$ eV). The energy of all the maxima is smaller than the band gap of stoichiometric SiO_2 structure which is 8.2 eV. However, in the case of nonstoichiometric structure SiO_x the band gap is smaller and can reach 1.1 eV for $x=0$. The FTIR transmittance spectra revealed the combination of stoichiometric and nonstoichiometric phases in ar-SiO_x , so it should be considered that the aerogel emission is associated with the presence of a SiO_x structure ($1 < x < 2$) as well as with surface and bulk defect states in SiO_2 phase.

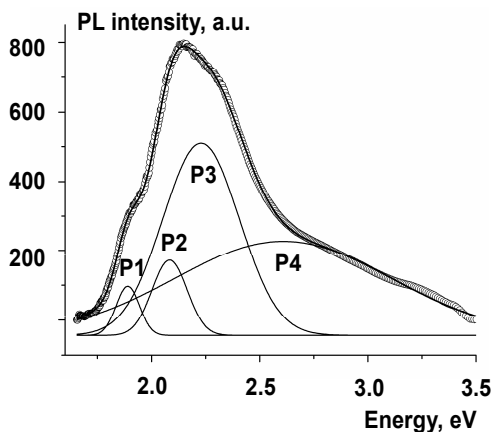


Fig. 4. Integrated PL spectrum of freshly prepared ar-SiO_x sample. Result of deconvolution into Gaussian profiles is shown

The structure of material and defect states are determined by preparation technology (temperature during the process of gel formation, concentration of reagents, pH level, etc.) [3,7,8]. Silica aerogels have several types of microstructural defects that can give contribution to the photoemission [3]. If PL excitation energy is 3.68 eV (nitrogen laser), the contribution to the photoemission of stoichiometric SiO_2 phase can produce only defects determined by the interaction within individual SiO_x tetrahedra. These include defects with dangling bonds: 1)

non-bounded oxygen hole center (NBOHC), which is described as follows: $\equiv \text{Si}-\text{O}\cdot$ where the dot means the unpaired electron; 2) peroxide radicals (POR) $\equiv \text{Si}-\text{O}_2\cdot$ and 3) oxygen-deficient centers (ODC) which include oxygen vacancies and divacancies and two-coordinate silicon (ODC(II)) [16].

Oxygen hole centers are responsible for emission in low-energy region at around 1.8–1.9 eV. (Peak P1), while the maximum at 2.7 eV (P4) is associated with the presence of two coordinate silicon in SiO_x matrix. The emission peak at 2.08 eV arises due to the presence of siloxane ($\equiv \text{Si}-\text{O}-\text{Si} \equiv$) and silane ($\equiv \text{Si}-\text{O}-\text{H}$) groups. These groups are formed from hydroxyl $\text{Si}-\text{OH}$ groups connected with hydrogen bonds during the dehydration process and due to the presence of silane (SiH and SiH_2) in hydrogenated aerogels [3]. Peak P3 at 2.23 eV results from radiative recombination processes in nonstoichiometric structure SiO_x [7]. There is also the emission peak of peroxide radicals in this range.

The influence of UV irradiation on luminescence properties of ar-SiO_x . It was shown in our earlier work [10] that emission properties of porous composite materials based on silica aerogel essentially depend on storage conditions and external factors such as temperature, atmospheric humidity etc. Taking into consideration the fact that the PL emission properties of ar-SiO_x mostly caused by the presence of oxygen bonds and oxygen centers in dielectric matrix it's important to study the influence of UV irradiation on PL properties material under investigation. For this purpose we used pulse laser irradiation ($\lambda = 337$ nm, $p = 20$ mW) focused on the sample surface with beam diameter of 3–4 mm. Fig. 5 shows the evolution of the integrated PL spectra with increasing of irradiation time.

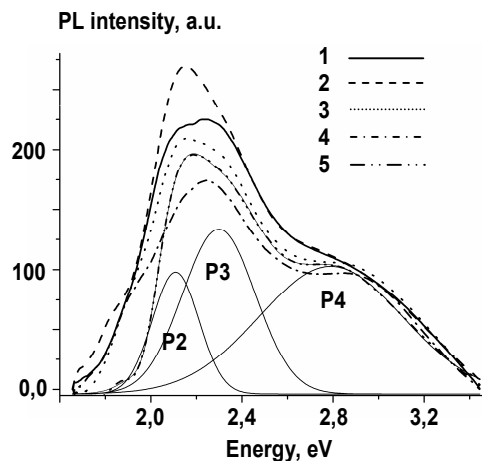


Fig. 5 The evolution of PL spectra under pulsed UV irradiation ($\lambda = 337$ nm) for ar-SiO_x sample: 1 – initial sample and after 2–4 min; 3–8 min; 4–12 min; 5–25 min irradiation. Result of deconvolution into Gaussian profiles for spectrum 5 is shown

Taking into consideration the obtained data, it can be concluded that the interaction between oxide matrix and UV irradiation caused the decreasing of PL integrated intensity as well as changes of the PL spectral composition. The most significant changes were observed for the low-energy peak at 1.87 eV (P1), namely, after UV irradiation during 16 min there is a complete quenching of emission peak. More detailed analyses have been made through the procedure of Gauss peak decomposition. Fig. 6 shows the evolution of peak positions during the UV irradiation.

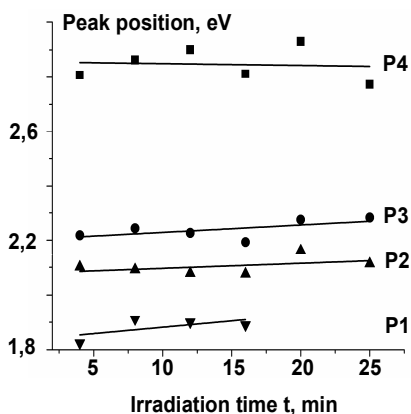


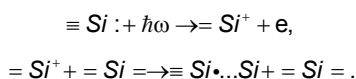
Fig. 6 The evolution of Gauss peak positions during UV irradiation for ar-SiO_x sample

It could be clearly seen that under photo oxidation process the peak positions are almost unchanged except for a small shift of PL peaks at 2.1 eV (P2) and 2.2 eV (P3) towards the high energy region. At the same time there are essential changes in the peak intensity at 1.87 and 2.2 eV, namely after 16 min irradiation the low-energy peak disappears and the P3 peak area noticeably decreases. For two another peaks (P2 and P4) essential changes haven't been observed.

Thus for powdered silica aerogel the evolution of PL spectra during photo oxidation process under UV irradiation is mainly due to the transformation of emission peaks at 1.87 and 2.2 eV.

As mentioned above, the low-energy PL emission caused by the presence of oxygen-hole centers. During photo oxidation process the transformation of these vacancies to peroxide radicals occurs according to reaction: $\equiv Si - O \cdot + O \rightarrow \equiv Si - O_2 \cdot$.

It's also well known [13,16] that in amorphous silicon-oxide matrix under laser excitation there is a structural reorganization, namely transformation of the oxygen vacancies type ODC(II), such as divalent silicon Si_2^0 , and the neutral oxygen vacancies (NOV) into defect type E' centers according to the scheme:



Since the E' centers can give a contribution to the photoemission under excitation energies of 5.8–6.3 eV, in our case, they are not active, which results in reducing of the peak intensity.

Thus, we can conclude that the decreasing of the integrated PL intensity of the powdered silica aerogel is caused by the transformation of the defect structure during photo oxidation process.

Карлаш А., канд. фіз.-мат. наук, каф. електрофізики, факультет радіофізики, електроніки та комп'ютерних систем Київський національний університет імені Тараса Шевченка

FTIR ТА ФЛ СПЕКТРОСКОПІЯ ПОРОШКОПОДІБНОГО АЕРОГЕЛЮ КРЕМНЕЗЕМУ ar-SiO_x

Було досліджено оптичні та фотолюмінесцентні властивості порошкоподібного аерогелю кремнезему з використанням FTIR спектроскопії пропускання та фотолюмінесцентної спектроскопії. Порошкоподібний аерогель кремнезему було виготовлено на основі водного розчину силікату з використанням технології золь-гель синтезу. Підтверджено, що досліджуваній матеріал складається з двох фаз: стехіометричної SiO₂ та нестехіометричної SiO_x. Аналіз FTIR спектрів пропускання виявив присутність значної кількості гідроксидних груп, що обумовлюють окиснювальні властивості матеріалу і визначають перспективність використання аерогелю кремнезему в якості ефективної матриці для інкорпорації наночастинок. Зареєстровано інтенсивну ФЛ у синьо-зеленій області спектру з максимумами при 1.9, 2.0, 2.2 та 2.6 еВ. Було показано, що емісійні властивості порошкоподібного аерогелю кремнезему ar-SiO_x обумовлені наявністю значної кількості кисневих дефектних центрів, таких як кисневі діркові центри, пероксидні радикали та киснево-дефіцитні центри, а також силосанових та силанових груп. Було також показано, що під впливом імпульсного лазерного УФ опромінення спостерігається зменшення інтегральної інтенсивності ФЛ. Гасіння ФЛ обумовлене трансформацією дефектної структури матеріалу в процесі фотоокиснення.

Ключові слова: порошкоподібний аерогель кремнезему, дефектні стани, FTIR спектроскопія пропускання, кінетика ФЛ.

Conclusions. In this work optical and photoluminescence properties of powdered silica aerogel ar - SiO_x have been investigated using FTIR and PL spectroscopy. It was confirmed that investigated material consists of stoichiometric SiO₂ and non-stoichiometric SiO_x phases. FTIR spectra revealed a presence of numerical hydroxyl groups such as bonded Si-OH and non-bonded -OH groups which determines oxidative properties of the material and makes it a promising matrix for incorporation of silicon nanoparticles.

Photoemission properties of investigated material are mainly due to the presence of oxygen defect states in non-stoichiometric SiO_x phase as well as siloxane and silane groups. It was shown that UV irradiation causes the decreasing of integrated PL intensity of silica aerogel mainly due to the transformation of its defect structure.

REFERENCE:

1. Porous silicon nanocrystals in a silica aerogel matrix / J. Amankosolpan, D. Wolverson, B. Goller et al. // *Nanoscale Research Letters.*, 2012. – Vol.7. – P. 397.
2. Ultraviolet excitation fine-tuning of luminescence bands of oxygen-deficient centers in silica / A. Anedda, C. Carbonaro, F. Clemente et al. // *J. App. Phys.*, 2002. – Vol. 92(6). – P. 3034.
3. Ayers M. Visibly photoluminescent silica aerogels / M. Ayers, A. Hunt // *J. Non-Cryst. Solids.*, 1997. – Vol. 217. – P. 229–235.
4. Influence of pH solution on photoluminescence of porous silicon / A. Benilov, I. Gavrilchenko, I. Benilova et al. // *Sens. Act. A.*, 2007. – Vol. 137. – P. 345–349.
5. Silicon nanoparticles in SiO₂ sol-gel film for nanocrystal memory device applications / A. Dima, F. Della Corte, C. Williams et al. // *Microelectronic Journal*, 2008. – Vol. 39. – P. 768–770.
6. Handbook of infrared spectroscopy of ultrathin films / Ed. by V. Tolstoy, I. Chernyshova, V. Skryshevsky. – N.J.: Wiley, 2003.
7. Hinić I. Influence of the synthesis conditions on the photoluminescence of silica gels / I. Hinić, G. Stanišić, Z. Popović // *J. of Serb. Chem. Soc.*, 2003. – Vol. 68(12). – P. 953–959.
8. Active Sites on Mesoporous and Amorphous Silica Materials and Their Photocatalytic Activity: An Investigation by FTIR, ESR, VUV-UV and Photoluminescence Spectroscopies / Y. Inaki, H. Yoshida, T. Yoshida et al. // *J.Phys.Chem. B.*, 2002. – Vol. 106(35). – P. 9098–9106.
9. Impedance spectroscopy of composites based on porous silicon and silica aerogel for sensor applications / A. Karlash, G. Kuznetsov, Yu. Milovanov et al. // *Functional Materials*, 2013. – Vol. 20, №1. – P. 110–117.
10. Evolution of visible photoluminescence of Si quantum dots embedded in silicon oxide matrix / A. Karlash, V. Skryshevsky, G. Kuznetsov et al. // *J. of Alloys and Compounds.*, 2013. – Vol. 577. – P. 283–287.
11. Photoluminescence properties of silica aerogel/porous silicon nanocomposites / A. Karlash, Yu. Zakharko, V. Skryshevsky et al. // *J.Phys.D: Appl. Phys.*, 2010. – Vol. 48. – P. 335–405.
12. Hierarchical nanostructured semiconductor porous materials for gas sensors / V. Moshnikov, I. Gracheva, V. Kuznezov et al. // *J. of Non-Cryst. Solids.*, 2010. – Vol.356(37–40). – P. 2020–2025.
13. Photoluminescence of oxygen-deficient-type defects in a-SiO₂ / N. Nishikawa, Y. Miyake, E. Watanabe et al. // *J. Non-Cryst.Sol.*, 1997. – Vol. 222. – P. 221–227.
14. Infrared studies of transition layers at SiO₂/Si interface / H. Ono, T. Ikarashi, K. Ando et al. // *J. Appl. Phys.*, 1998. – Vol. 84. – P. 6064–6069.
15. Optical gain in silicon nanocrystals / L. Pavezi, L. Dal Negro, C. Mazzoleni et al. // *Nature*, 2000. – Vol. 408. – P. 440–444.
16. Skuja L. Optically active oxygen-deficiency-related centers in amorphous silicon dioxide / L. Skuja // *J. of Non-Cryst. Solids.*, 1998. – Vol. 239. – P. 16–48.
17. Yamada T. Photoluminescence property of transparent silica glass prepared from nanometer-sized silica particles / T. Yamada, T. Uchino // *J. of Optoelectr. and Adv. Mater.*, 2005. – Vol. 7(4). – P. 1935–1940.

Submitted on 15.09.14

Карлаш А., канд. физ.-мат. наук,
каф. електрофізики, факультет радіофізики, електроніки і комп'ютерних систем
Київський національний університет імені Тараса Шевченка

FTIR И ФЛ СПЕКТРОСКОПИЯ ПОРОШКООБРАЗНОГО АЭРОГЕЛЯ КРЕМНЕЗЕМА α -SiO_x

Проведено исследование оптических и фотолюминесцентных свойств порошкообразного аэрогеля кремнезема с использованием FTIR спектроскопии пропускания и фотолюминесцентной спектроскопии. Порошкообразный аэрогель кремнезема изготавлялся на основе водного раствора силиката с использованием технологии золь-гель синтеза. Подтверждено, что исследуемый материал состоит из двух фаз: стехиометрической SiO₂ и нестехиометрической SiO_x. Анализ FTIR спектров пропускания обнаружил присутствие значительного количества гидроксидных групп, которые обуславливают окислительные свойства материала и определяют перспективность его использования в качестве матрицы для инкорпорирования наночастиц. Зарегистрирована интенсивная ФЛ в сине-зеленой области спектра с максимумами при 1.9, 2.0, 2.2 и 2.6 эВ. Было показано, что эмиссионные свойства порошкообразного аэрогеля кремнезема α -SiO_x обусловлены наличием значительного количества кислородных дефектных центров, таких как кислородные дырочные центра, пероксидные радикалы и кислородно-дефицитные центры, а также силиксоановые и силановые группы. Было также показано, что под воздействием импульсного лазерного УФ облучения наблюдается уменьшение интегральной интенсивности ФЛ. Гашение ФЛ обусловленное трансформацией дефектной структуры материала в процессе фотоокисления.

Ключевые слова: порошкообразный аэрогель кремнезема, дефектные состояния, FTIR спектроскопия пропускания, кинетика ФЛ.

UDC 537.622.4

V. Koronovskyy, Ph.D., Y. Vakyla, eng.
Department Electrophysics, Faculty of Radiophysics,
Taras Shevchenko National University of Kyiv

VISUALIZATION OF MAGNETO-ELECTRIC DISPLAYS IN FG/GGG EPITAXIAL STRUCTURES

Using the method of polarizing microscopy, under the combined effects of static and alternating electric fields and magnetic field, studied the reaction of the domain structure (DS) epitaxial ferrite garnet (FG) films, grown on single crystal substrates of gallium-gadolinium garnet (FG / GGG). In transmitted light visually detected a small effect of the profile changes ("smearing") of the individual local sites of the films domain wall (DW) because of a combination of three-channel external influence.

Keywords: magneto-electric effect, electric field, magnetic field, domain wall, domain structure, polarizing microscope.

Introduction. The change of magnetization under the influence of electric field or of electric polarization under the influence of magnetic field are called magnetoelectric (ME) effect. Study of the mechanism of interaction of electric and magnetic subsystems in magneto-electric materials has recently been the subject of many publications. This interest is driven by a need to establish a single fundamental theory of magneto-electric interactions in solids, and wide application possibilities of using magneto-electric materials in electronics.

The first explicit prediction of ME effect in a specific material was made by Dzyaloshinskii who showed that in Cr₂O₃ these effects are allowed by the magnetic symmetry [2]. Experimentally, the electrically induced ME effect was first observed by Astrov [1] on a crystal of Cr₂O₃ and later Rado and Folen [10]. The first observation of the ME effect in yttrium-iron-garnets (YIG) was reported by O'Dell [9] and later, the ME effect was studied in a number of papers [3÷8, 12]. The external electric field that connected to the crystal of certain magnetic symmetry (eg, YIG), can cause in crystal the manifestations induced optical phenomena, linear or nonlinear in the electric field. One of such phenomenon is the effect of the changes of light polarization plane Faraday rotation in an optically transparent dielectric crystal induced by an electric field, which the authors named as an electromagneto-optical (EMO) effect [8]. Using a highly sensitive method of optical polarimetry, it is possible to measure the changes of light polarization plane rotation in an external electric field, as well as to carry out visual observations of the domain structure of the sample using a polarizing microscope.

Iron garnets are a large class of ferrimagnetic oxides with high Curie temperature ($T_c > 500\text{K}$) and have been applied to magneto-optical devices and magnetic bubble memories [11, 13]. The active interest in the structural, magnetic, and magneto-optical properties of garnet films has been related to the fact that all these properties can be widely varied by changing the composition and orientation. Although the parent garnet crystal structure is characterized as the cubic centrosymmetric space group the studies of film structure and magnetic properties have revealed that films tend to have uniaxial or orthorhombic

symmetry. The origin of this symmetry lowering is due to growth anisotropy and mismatch between the lattice parameters of the films and substrates. The crystallographic orientation of the substrate is also of primary importance. Garnet crystals are well known to play an important role in technological devices.

Domain structure (DS) of ferrite garnets is periodically interspersed with small regions of antiparallel magnetization direction, which are separated by domain walls. In DW is changing the direction of the orientation of the spins in the same domain to the direction in the nearby. In ferrite garnets it is possible to visualize processes occurring in them due to the magneto-optical Faraday effect.

In this paper, we report the results of studies ME manifestations in epitaxial ferrite garnet films in a two-channel and three-channel external influence. In particular, visual observations were made for the DS of the film with the use of magneto-optical polarization microscopy with high optical permission based on the Faraday effect in two experimental versions: 1) under the joint action of the alternating electric field and constant magnetic field; 2) under the joint action of DC and AC electric field and a constant magnetic field. Investigated epitaxial films grown on (111) substrates of gallium-gadolinium garnets (GGG). The domain structure of the films studied under the polarizing microscope looks like high contrast, which indicates about significant deviation of domain magnetization vectors from the film plane.

Experimental. The test sample was placed between two optically transparent electrodes. The electrodes were deposited by spraying on the inner surfaces of the two thin glass plates. Separately or simultaneously to the sample plugged in the AC and DC voltage. External constant magnetic field was oriented along the plane of the film. The thickness of the film was about 10 μm , the width of domains was about 14 μm at $H=0$, and the domain-wall width was about 0.5 μm . The test sample we previously several times been the iterative process of quasi-static magnetization in the magnetic field in both directions. The reproducibility of the overall picture domain labyrinth structure in this case was not observed. DW motion occurred intermittently due to the interaction with micro-

defects and for each area of the DW was of probabilistic nature. The stripe domains are randomly bent and DW located in different places in the film, indicating that complete isotropy of the properties of this film in its plane.

Results and discussion. By visual observation of the domain structure of the following was revealed. For small values of the constant electric field (from 0 to 1.6 kV/mm) significant changes in the domain structure was not observed. Domain structure remained the same as in the initial state – a disordered maze. Connection to the sample while still a magnetic field, oriented in the plane of the sample, did not lead to any visually observed changes in the domain array of the film. Connection of the third control channel – low-frequency (950 Hz) AC electric field with strength up to 3.5 kV/mm, did not cause changes in the DS of the sample also. But, starting with the value 1.8 kV/mm in the constant electric field and the fixed values of the magnetic and alternating electric fields, DC stability was broken. The general domains picture that observed in the microscope has not changed. However, some small, curved portions of domain heads (domain head is a part of stripe domains, where DW is curved and the radius of curvature of the head is approximately equal to half the width of the domain) of the individual domains became slightly visually "blurry", which can be seen when analyzing the micro-photo. In this case, the geometric shape of the domain did not change and the domain structure remained through the maze, the DW displacement from their equilibrium positions were not observed. For computer processing exposed micro-photo where observe individual domain head, in the same location of the investigated film, but for different values of the constant electric field. The results of analysing of the images where shown in Fig. 1. On the plot (Fig. 1) we can see the estimates of the number of the width changing (h) of the domain wall that we obtained for "blurring" domain head in static electric field E_1 (for fixed values of the alternating electric E_2 and a constant magnetic field H). As can be seen from Fig. 1, changes in the width of the local section of the DW when considering a three-channel external effect on the sample is not significant (the width of the domain wall in the absence of external fields was about 0.5 microns).

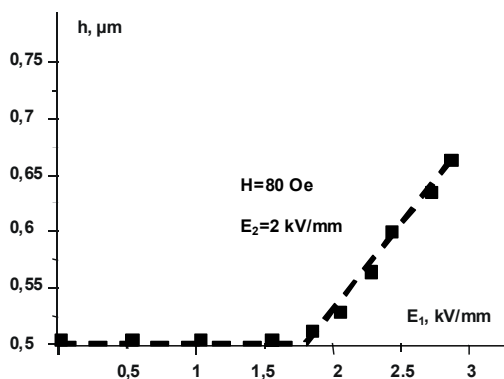


Fig. 1. Estimated dependence for changing of width of local DW site (domain head) from intensity of constant electric field E_1 , at the fixed values of variable electric ($E_2 = 2\text{ kV/mm}$) and constant magnetic ($H = 80\text{ Oe}$) fields

Figure 2 shows the evaluation results after computer processing of visual observations of this domain local area in a two-channel head of external influence – an alternating electric field E_2 , with frequency of 950 Hz and a constant magnetic field H .

Spatial fields orientations was the same as in the previous case. As can be seen from Fig. 2, the alternating

electric field as at $H = 0$ and when $H \neq 0$ does not cause a visually observable changing of width for investigate domain head or offset.

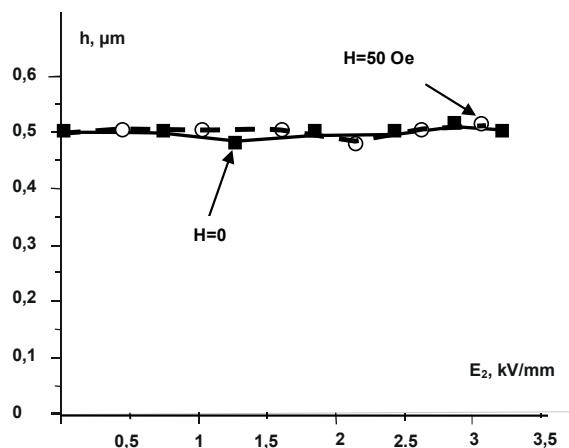


Fig. 2. Results of visual supervision over changes of width for a investigated domain head in the conditions of two-channel external influence - variable electric field E_2 (frequency of 950 Hz) and constant magnetic field H ($H = 0$ and $H = 50\text{ Oe}$)

Best of all, the response of domain head for simultaneous connection of the electric fields (alternating and constant) are be seen when connected still a magnetic field, that oriented in the plane of the film (Fig. 3). Even for small values of the magnetic field, as can be seen from Fig. 3, viewed curved portions DW become sensitive to external influence electrical fields.

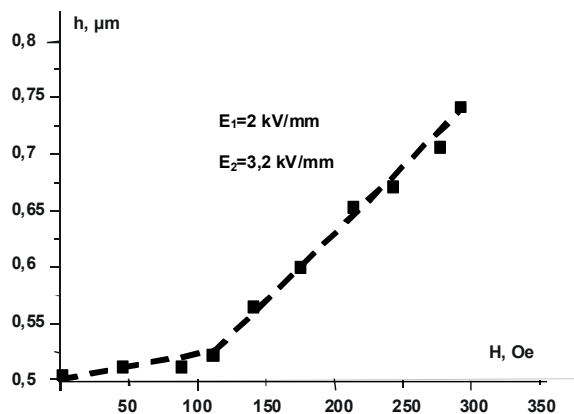


Fig. 3. Estimated dependence of changes of domain head width from intensity of a constant magnetic field, at the fixed values of variable electric ($E_2 = 3.2\text{ kV/mm}$) and constant electric ($E_1 = 2\text{ kV/mm}$) fields

Feature of the observed local "smearing" of DS is the fact that it was shown only on shorter (curved, irregular shape) regions of the labyrinthine DS - domain heads. Direct (long) segments of DS remained dimensionally stable and their reaction to considering complex external action is not sufficient for direct visual observation. Possible reason for these differences in the response may be some differences in the micro-magnetic structure of the DW in these areas. In the labyrinthine domain in the absence of external fields, in addition to long sections of the DW with the structure of the Bloch type, there are shorter sections with Neel structure. In general, as is known, the DW of magneto-uniaxial films is

non-planar interface between adjacent domains. DW is a three-dimensional structured element of finite extent of the domain of the array with a nonuniform distribution of the magnetization vector in them as in thickness, and developed the film plane. The structure of the DW uniaxial films, such a study, is referred to as the twisted type, i.e. is neither Bloch nor Neel. In our experiments, the external magnetic field is applied in the film plane perpendicular to the easy axis (EA) and the DW motion in a magnetic field when it is not. Probably, in the magnetic field changes occur in the structure of the twisted DW and change the ratio in the initial balance between Bloch and Neel components. The magnetization of the wall with increasing magnetic field deviates more and more from the Bloch orientation, i.e. there is a certain structural "imbalance". At the same time, structural changes in the domain heads led to the fact that they were more susceptible to the influence of an external electric field (which changes the parameters of the magnetic anisotropy of the film), oriented parallel to the normal to the sample surface as compared with the more direct, the length of the labyrinth of the DW. The question about the local response of individual sections of the DW to an external electric field, more research is needed.

Conclusions. Thus, our results of imaging studies of magneto-electric interaction manifestations in FG/GGG epitaxial structures with typical maze domain structure showed the following. A very small impact on the value of the joint action of alternating and static electric fields on the domain wall is shown only when the additional connection of a static magnetic field, oriented in the plane of the sample. Visually observed a small effect of the local "smearing" of individual sections of the domain wall can be

seen, probably, as a small distortion of the DW profile without DW displacement as a whole.

Reference

1. *Astrov D. N.* The magnetoelectric effect in antiferromagnetics / *D. N. Astrov* // *Sov. Phys.-JETP.*, 1960. – 11. – P. 708–709.
2. *Dzyaloshinskii I. E.* On the magneto-electrical effects in antiferromagnets / *I. E. Dzyaloshinskii* // *Sov. Phys.-JETP.*, 1959. – 10. – P. 33–35.
3. *Fiebig M.* Revival of the magnetoelectric effect / *M. Fiebig* // *J. Phys. D: Appl. Phys.*, 2005. – 3. – P. 123–152.
4. *Koronovskyy V. E.* Electromagneto-optical effects on local areas of a ferrite-garnet film / *V. E. Koronovskyy, S. M. Ryabchenko, V. F. Kovalenko* // *Phys. Rev. B.*, 2005. – 71. – P. 172402–172406.
5. *Koronovskyy V. E.* Influence of an external mechanical strain on the character of the magneto-electric effect in epitaxial films of yttrium iron garnet / *V. E. Koronovskyy* // *Phys. Stat. Sol. (a)*, 2006. – Vol. 203, №. 8. – P. 2007–2011.
6. *Koronovskyy V. E.* Influence of powerful laser irradiation on electromagneto-optical dependences of yttrium iron garnets / *V. E. Koronovskyy* // *J. Appl. Phys.*, 2009. – 106. – P. 063914–063916.
7. *Koronovskyy V. E.* The electromagneto-optical effect in local areas of single magnetic domains in epitaxial films of yttrium iron garnet / *V. E. Koronovskyy, N. D. Gorchinski* // *Functional Materials*, 2011. – Vol. 18, №1. – P. 37–41.
8. *Krichevstov B. B.* The electromagneto-optical effect in yttrium iron garnets $Y_3Fe_5O_{12}$ / *B. B. Krichevstov, R. V. Pisarev, A. G. Selitskij* // *JETP Lett.*, 1985. – 41. – P. 317–319.
9. *O'Dell T. H.* The electro-dynamics of magneto-electric media / *T. H. O'Dell* – *Philos. Mag.*, 1967.
10. *Rado G. T.* Anisotropy of the magnetoelectric effect in Cr_2O_3 / *G. T. Rado, V. J. Folen* // *Phys. Rev. Lett.*, 1961. – 6. – P. 141–147.
11. *Scott G. B.* Absorption spectra of $Y_3Fe_5O_{12}(YIG)$ and $Y_3Ga_5O_{12}:F_3+$ / *G. B. Scott, D. E. Lacklison, J. L. Page* // *Phys. Rev. B.*, 1974. – 10. – P. 971–974.
12. *Magneto-electric properties of Yttrium Iron Garnet* / *G. Velleaud, B. Sangare, M. Mercier, G. Aubert* // *Solid State Commun.*, 1984. – Vol. 52. – P. 71–74.
13. *Optical properties of epitaxial Iron garnet thin films* / *S. H. Wemple, S. L. Blank, J. A. Seman, W. A. Biolsi* // *Phys. Rev. B.*, 1974. – 9. – P. 2134–2137.

Submitted on 30.09.14

Коронівський В., канд. фіз.-мат. наук, Вакула Ю., інж.,
каф. електрофізики, радіофізичний факультет,
Київський національний університет імені Тараса Шевченка

ВІЗУАЛІЗАЦІЯ МАГНІТОЕЛЕКТРИЧНИХ ПРОЯВІВ У ЕПІТАКСІЙНИХ СТРУКТУРАХ ФГ/ГГТ

Використовуючи метод поляризаційної мікроскопії, в умовах одночасного впливу постійного і змінного електричних полів і магнітного поля, досліджувалась реакція доменної структури (ДС) епітаксіальних плівок феритових гранатів (ФГ), вирощених на підкладниках з галій-гадолінієвого гранату (ФГ/ГГТ). У прохідному світлі, візуально виявлено малий ефект "розмиття" профілю окремих локальних ділянок доменних меж (ДМ) плівок в умовах комбінованого трьохканального впливу.

Ключові слова: магніто-електричний ефект, електричне поле, магнітне поле, доменні межі, доменна структура, поляризаційний мікроскоп.

Коронівський В., канд. физ.-мат. наук, Вакула Ю., инж.,
каф. электрофизики, радиофизический факультет,
Киевский национальный университет имени Тараса Шевченко

ВИЗУАЛІЗАЦІЯ МАГНІТОЕЛЕКТРИЧЕСКИХ ПРОЯВЛЕНИЙ В ЭПИТАКСИАЛЬНЫХ СТРУКТУРАХ ФГ/ГГТ

Используя метод поляризационной микроскопии, в условиях совместного воздействия постоянного и переменного электрических полей и магнитного поля, исследовалась реакция доменной структуры (ДС) эпитаксиальных пленок ферритовых гранатов (ФГ), выращенных на монокристаллических подложках из галлий-гадолиниевый граната (ФГ/ГГТ). В проходящем свете, визуально обнаружен малый эффект "размытия" профиля отдельных локальных участков доменных границ (ДГ) пленок в условиях комбинированного трехканального внешнего воздействия.

Ключевые слова: магнито-электрический эффект, электрическое поле, магнитное поле, доменные границы, доменная структура, поляризационный микроскоп

UDC 53; 547.136.13; 576.535; 577.037

M. Kulish, Dr. Sc., Prof., O. Dmytrenko, Ph. D.,
O. Melnyk, stud., Taras Shevchenko National University of Kyiv,
E. Malyi, post grad. stud., M. Pinkovska, Ph. D.,
V. Tartachnyk, Dr. Sc., Prof., Institute for Nuclear Research of NASU,
V. Shlapatska, Ph. D., Institute of Physical Chemistry of NASU

EVALUATION OF DOSE DISTRIBUTION IN PENUMBRA AREA BY USING LIGHT EMITTING STRUCTURES

A light-emitting diodes possess some essential advantages, compared to all other sources of previous generations, such as low energy consumption, small size, high operating speed, reliability. Dosimetry of radiation field in the penumbra area must be carried out with sensor of minimal size and maximal sensitivity. Gallium phosphide light emitting diode of less than 1mm^2 size. It is appropriate to use LEDs due to their low cost and emitting ability in visible region of spectrum.

Keywords: gallium phosphide, penumbra, LEDs, light-emitting diodes, dosimetry, spectra.

© Kulish M., Dmytrenko O., Melnyk O., Malyi E., Pinkovska M., Tartachnyk V., Shlapatska V., 2014

Introduction. Modern light emitting sources are the special types of high spectral purity illuminators useful in wide spectral range (from infrared to ultraviolet light). The devices possess some essential advantages, compared to all other sources of previous generations, such as low energy consumption, small size, high operating speed, reliability and low cost. The scope of these devices is constantly expanding: precision instrumentation, production of household appliances, and also medicine.

Gallium phosphide, the wide-zone semiconductor of $A^{III}B^V$ group, due to simple and inexpensive technologies allows creating p-n- transition by growing epitaxial films and doping them chemically. The doping of material by isoelectronic (concerning phosphorus) nitrogen impurity causes an appearing of electron traps. A negatively charge center attracts a free hole and form Vanye-Mott exciton of a large radius. The level of its ground state is $E_c - 0,20$ meV, which makes it possible at essential excitation to observe emitting even at room temperature (green narrow band with $h\nu = 2.10$ eV).

Simultaneous doping of GaP crystal by zinc and oxygen forms analogous emitting center. At sufficient doping levels of both atoms, zinc and oxygen as isovalence impurities in gallium and phosphorus sublattices accordingly, are situated nearby and due to the lattice deformation form exciton traps. Annihilation of an exciton, bound to Zn-O pair, causes emitting in the red range of the spectrum ($h\nu = 1.80$ eV) [3–4].

Experiment. Emitting spectra of p-n structures of both doping types (at room temperature) are given in figures 1–2. From the dependence of the emitting intensity on the current through the transition it is possible to adjust device brightness by changing the level of injection of minority carriers.

Irradiation of GaP LEDs leads to monotonic decrease in the intensity of luminescence due to stable at room temperature phosphorus and gallium vacancies of annealing activation energies of 1.5 and 2.0 eV, respectively. The center of annealing stage of Vp is $150 \div 160^\circ C$, and $V_{Ga} - 250 \div 270^\circ C$, that provides the thermal stability of the accumulated information .

We studied diodes irradiated with 2 MeV electrons and had shown that dose dependences of emitting brightness at different currents had the form of monotonic curves; at low doses ($\Phi < 10^{14} \text{ cm}^{-2}$) they were nearly linear (Figure 3).

Discussion. It is known that forming of dose field of complex configuration on the body of the patient is performed with the help of system of wedges and bolus of specific profile. Owing to the particles' diffraction and the source size influence the penumbra effect inevitably appears which evokes the overexposure of the healthy tissue.

The problem of protection has become especially alert, if critical organ is situated near irradiation zone.

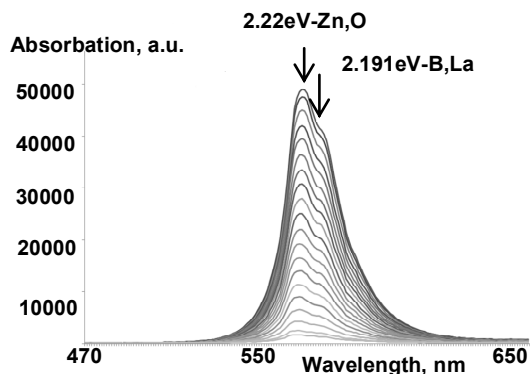


Fig. 1. Emitting spectra of green LED at different currents through p-n –transition at room

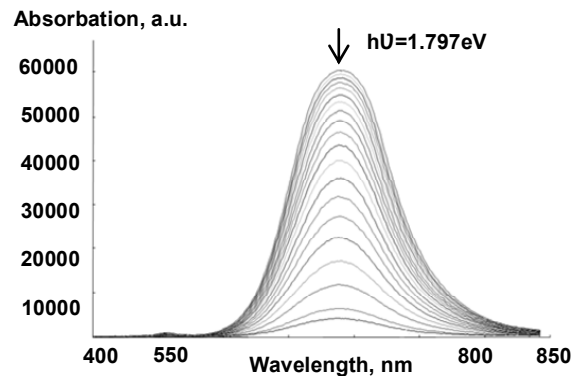


Fig. 2. Emitting spectra of red LED at different currents through p-n –transition at room temperature

Radiobiological effect is known to have two stages. At the first stage interaction of penetrating radiation with a cell is rapid and is accompanied by visible changes. Further morphological and functional effects can appear in a few minutes or even a few years after exposure.

To this day the effect of small doses in humans still remains unclear. Therefore, the problem of accurate dosimetry is closely associated with the prediction of the impact of long-term effects of radiation on the patient's health in the future and also with the dose circumscription in the critical organs.

Accurate assessment of the effects of radiation in biological object with active repair damages and opposite action of cumulative effect is possible only with high quality dosimetry measurements.

In passing, it should be noted that the function of cell survival varies exponentially with the dose, confirming the importance of accurate determination of this parameter. In beam radiotherapy the problem of beam's coupling is one of the most difficult. It is in this case an important role of a minimal source size and its high sensitivity.

It is advisable also to mention the method of photodynamic therapy, which is based on photochemical reactions in the dye, previously introduced into the tumor. The products of decomposition of the dye in the light cause the destruction of oncology cell.

A special technique monitors the level of accumulation in cells sensitizer, then the tumor is illuminated by the source of a certain wavelength.

Modern LEDs unlike lasers cover almost continuously the entire visible region of the spectrum, including infrared and ultraviolet light, and being introduced into the tumor, can provide the process of photochemical cytotoxic reactions with the formation of singlet oxygen and subsequent destruction of diseased cells.

The main purpose of our research is to offer a method and using of gallium phosphide p-n- transition in radiation medicine practice in order to measure the tissue-absorbed doses.

Dosimetry of radiation field in the penumbra must be carried out by the sensor of minimal size and maximal sensitivity. Light emitting diode of less than 1mm^2 size and high penetrating radiation sensitivity provided by exciton recombination mechanism, in our opinion, fits the best. It is appropriate to use gallium phosphide LEDs due to their low cost and emitting ability in visible region of spectrum.

Dose dependence of GaP LED's emitting intensity, carried out during irradiation by electrons with $E = 2$ MeV, is linear to the $5 \times 10^{14} \text{ cm}^{-2}$, which can be useful for the dosimeter of especially small doses.

In order to build the dosimetric map one needs some samples with similar output emitting intensity. One of them had to be previously graded at the accelerator,

which henceforth will be used in clinical practice. Experience suggests that change of emitting intensity of proposed diode owing to irradiation should be monitored by the simple silicon photocell without stationary spectrometry equipment.

For this purpose the lightproof camera is designed connected to regulated source of LED's supply and photocell setting-up. The tissue absorbed dose is evaluated based on the known values of the weighting factors for its and for the beam.

In order to restore the diode emitting intensity after the first dose one should increase the current through the diode.

An advantage of the proposed dosimetry method is the ability to process information "on line" during target irradiation as well as during adjustment of irradiation outfit.

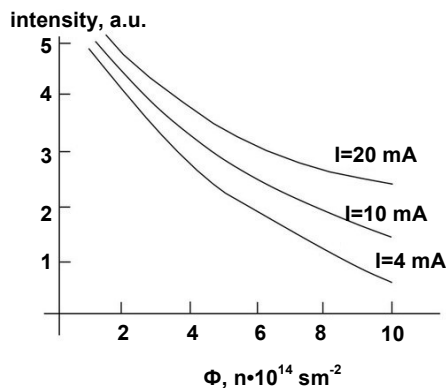


Fig. 3. Dose dependences of emitting intensity of red LED irradiated with 2 MeV electrons at different currents through p-n –transition at room temperature

For example, in order to input sensor into area of the inner cavity of the body, one can use the cable system of

Куліш М., д-р. фіз.-мат. наук., проф., Дмитренко О., канд. фіз.-мат. наук,
Мельник О., студ., Київський національний університет імені Тараса Шевченка,
Малий Є., асп., Пінковська М., канд. фіз.-мат. наук,
Тартачник В., д-р. фіз.-мат. наук, проф., Інститут ядерних досліджень НАН України,
Шлапацька В., канд. фіз.-мат. наук, Інститут фізичної хімії НАН України

ОЦІНКА ДОЗОВОГО РОЗПОДІЛУ В ОБЛАСТІ ПЕНУМБРИ З ВИКОРИСТАННЯМ СВІТЛОДІОДНИХ СТРУКТУР

Світлодіоди володіють деякими істотними перевагами порівняно з усіма іншими видами джерел попередніх поколінь. Світлодіодним структурам властиві – низька енергоємність, мініатюрність, швидкодія, надійність. Дозиметрія радіаційного поля у межах напівтіні повинна здійснюватися датчиком мінімального розміру та максимальної чутливості. Саме таким елементом може бути структура розміром менше 1мм². З нашого погляду найдоцільнішим є використання епітаксціальних фосфід-галієвих р-п-переходів з огляду на їхню низьку вартість та випромінювання у видимій області спектру.

Ключові слова: фосфід галію, напівтінь, світлодіоди, дозиметрія, спектр.

Кулиш Н., д-р. физ.-мат. наук., проф., Дмитренко О., канд. физ.-мат. наук,
Мельник О., студ., Киевский национальный университет имени Тараса Шевченко,
Малий Е., асп., Пинковская М., канд. физ.-мат. наук,
Тартачник В., д-р. физ.-мат. наук, проф., Институт ядерных исследований НАН Украины,
Шлапацкая В., канд. физ.-мат. наук, Институт физической химии НАН Украины

ОЦЕНКА ДОЗОВОГО РАСПРЕДЕЛЕНИЯ В ОБЛАСТИ ПЕНУМБРЫ С ИСПОЛЬЗОВАНИЕМ СВЕТОДИОДНЫХ СТРУКТУР

Светодиоды обладают некоторыми существенными преимуществами по сравнению со всеми другими видами источников предыдущих поколений. Светодиодным структурам присущи – низкая энергоёмность, миниатюрность, быстродействие, надёжность. Дозиметрия радиационного поля в пределах полутени должна осуществляться датчиком минимального размера и максимальной чувствительности. Именно таким элементом может быть структура размером менее 1мм². С нашей точки зрения наиболее целесообразным является использование эпитаксциальных фосфид-галлиевых р-п-переходов, учитывая их низкую стоимость и излучения в видимой области спектра.

Ключевые слова: фосфид галлия, полутень, светодиоды, дозиметрия, спектр.

the hard radiation source supply, used in brachytherapy, while replacing the radioactive preparation by the LED. Then during external wide field gamma-irradiation the change of luminescence intensity of diode responds the quanta fluence in a particular dot area of the target. In the case the optoelectronic pair serves as the sensor, than the dynamics of irradiation process can be recorded electronically.

The accuracy of location of apparatus with the sensor can be controlled by means of X-ray television.

Conclusions. Electroluminescent dosimeter is particularly useful in modeling of proton irradiation or its planning in tissue-equivalent phantom. In this method the accuracy to determine the Bragg peak position is of the great importance. So when several of LED sensors are placed in the controled area, the location of the diode with a maximum level of degradation is the localization of the Bragg peak.

In multiple-field irradiation the proposed method can help to combine the Bragg peaks of different beams on the same target.

Note also that the GaP sensors allow storing information at room temperature for a long time, as the minimum temperature of radiation defects' recovery in this material is 150⁰ C [1–2].

REFERENCE:

1. Brailovsky E. Y., Defects in GaP electron-irradiated / E. Y. Brailovsky, I.D. Konozenko, V.P. Tartachnyk, // Fizika i tekhnika poluprovodnikov. – 1975. – Vol. 9. – p. 769–771.
2. Brailovsky E. Y., Radiation defects in GaP under electron irradiation with E = 50 MeV / E. Y. Brailovsky, G. N. Yeritzyan, V. P. Tartachnyk // Fizika i tekhnika poluprovodnikov. – 1975. – Vol. 9. – p. 1805–1807.
3. Schubert E. Light-emitting diodes / E. Schubert – K., 2006.
4. "LED". The American heritage science dictionary. Houghton Mifflin Company., 2005.

Submitted on 09.11.14

K. Lavrenko, stud., I. Kolomiets, post. grad. stud.
S. Savenkov, Dr. Sci., Ye. Oberemok, Ph. D., A. Klimov, Ph. D.
Faculty of Radiophysics, Electronics and Computer Systems
Taras Shevchenko National University of Kyiv

THE EVOLUTION OF POLARIZATION STATE IN LONGITUDINALLY INHOMOGENEOUS MEDIUM WITH LINEAR BIREFRINGENCE

The Features of formation of anisotropy in longitudinally inhomogeneous media with linear birefringence were considered and studied. Equivalent model of representation of this class of media as a series of identical action of phase plates rotated relative to each other by the same angle was used. The method of differential Mueller matrices to describe the polarization properties of the medium was used. Evolution of the Stokes vector on the basis of differential Mueller matrix and vector transport equation was derived. Evolution of azimuth and angle of ellipticity in the direction of light propagation in this class of media was obtained and studied. Period of changes of polarization ellipse parameters were determined. Comparison of the features of evolution of polarization state with relevant features in the homogeneous media with elliptical birefringence was made. Effective value of optical activity for any state of polarization of light propagating in the medium was found. Features of rotation of the polarization plane of privileged waves were considered.

Keywords: Mueller matrix, birefringence, azimuth, angle of ellipticity, longitudinally inhomogeneous media, polarization state.

Introduction. Development of liquid crystal technology has led to the fact that one of the actually problems of modern polarimetry is to study the polarization properties of longitudinally inhomogeneous medium with linear birefringence. In particular, such media include twisted nematic and cholesteric, which used in the creation of liquid crystal displays [6, 11]. In the works [7–9] were considered problems related to the features of eigenwaves which propagating in such media and orthonalization properties of such media. Another important problem related to study of anisotropic properties of longitudinally inhomogeneous medium with linear birefringence are features of the evolution of polarization state of light [4, 6]. The study of with problem associated with the fact that this class of media against a background of linear birefringence and due to the special structure arises effective circular birefringence (optical activity) [5].

In view of the problems, the aim of this paper is to investigate the features of formation anisotropy in longitudinally inhomogeneous media with linear birefringence and its effect on the evolution of polarization state at the light propagating in the direction of the helical axis.

The matrix model of the medium. Nondepolarizing longitudinal inhomogeneous medium with linear birefringence can be equivalent representation as a sequence of molecular planes which consist of elongated molecules, oriented parallel to each other [3]. Each of such molecular planes can be present as a thin phase plate with linear birefringence [4]. Fast (slow) axis of the plate is parallel (perpendicular) to the direction along which direct the plane of the molecules what is considered, and lies entirely in this plane. Considering the totally polarized light propagating along the axis perpendicular to the molecular plane (helical axis), we assume that the direction of this axis coincides with the direction of the axis z of some Cartesian rectangular coordinate system. Axes x and y coincide with the main (fast and slow) axes of birefringence of input molecular plane (Fig. 1).

In such media, the motion in the direction perpendicular to the molecular planes the direction of anisotropy axis of each molecular layer returns (twisted) compared to the previous by some angle α_0 [3, 4]:

$$\alpha_0 = \frac{2\pi}{p} \tag{1}$$

where p – a step of helical structure of medium (the smallest distance between the planes with the same orientation of molecules). Then the molecular orientation of the plane in distance z from the input can be defined as:

$$\alpha = \alpha_0 z \tag{2}$$

Anisotropic properties of one molecular layer of such medium are described by the differential Mueller matrix [1]:

$$m = \begin{bmatrix} 0 & 0 & 0 & 0 \\ 0 & 0 & 0 & -\delta_0 \sin(2\alpha_0 z) \\ 0 & 0 & 0 & \delta_0 \cos(2\alpha_0 z) \\ 0 & \delta_0 \sin(2\alpha_0 z) & -\delta_0 \cos(2\alpha_0 z) & 0 \end{bmatrix} \tag{3}$$

This matrix is similar to the corresponding differential Mueller matrix for a homogeneous medium with linear birefringence [1]. The only difference between the matrices is (2), i. e. the angle α is a function of the coordinates z .

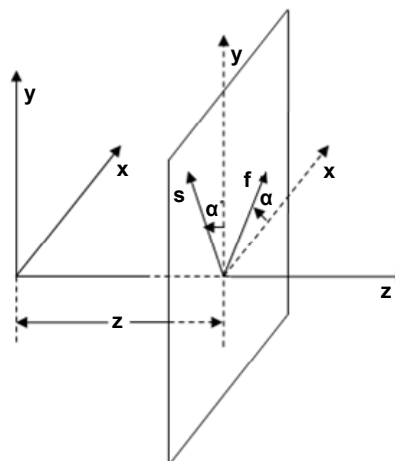


Fig. 1. Molecular plane of longitudinally inhomogeneous medium at a distance z from the input plane. f and s – directions of fast and slow axes of birefringence, which for incoming planes coincide with axes x and y coordinate systems

The evolution of Stokes parameters. Now we will study the evolution of the polarization state of waves propagating in a given class of media. As the example will choose a linearly polarized light, as it is the simplest and yet the most common case of using in polarimetry as a tool to study the anisotropy of the medium [12]. The Stokes vector of light in the case of linear polarization with azimuth of orientation of the electric field θ_{inp} is following [4]:

$$S_{inp} = (1 \quad \cos 2\theta_{inp} \quad \sin 2\theta_{inp} \quad 0)^T \tag{4}$$

The main equations describing the evolution of the Stokes vector (and hence the corresponding state of polarization) is the transport equation of light through anisotropic medium [1]:

$$\frac{dS}{dz} = mS \tag{5}$$

where S is a Stokes vector which describes the polarization state of the light, m is a differential Mueller matrix describing the anisotropic properties of medium (3). Vector differential equation (5) can be represented as a system of four scalar differential equations for the individual Stokes parameters S_1, S_2, S_3, S_4 . Solving this system of four differential equations with initial conditions (4), the result can be represented as the ratio:

$$S_{1,2,3,4}(z) = f(m_{ij}, S_{1,2,3,4}(0), z); \overline{i, j} = 1, 4 \tag{6}$$

where $S_{1,2,3,4}(z)$ – Stokes parameters of light at the output layer anisotropic medium with thickness z , $S_{1,2,3,4}(0)$ – Stokes parameters of light at the input layer of anisotropic medium (initial conditions (4)), m_{ij} – elements of the differential Mueller matrix.

The evolution of polarization state. Solutions are presented in the form (6) describes the evolution of the polarization state with coordinate z in the direction of light propagation in a medium whose anisotropy is given a particular view of the differential matrix m . At propagation of the light in a medium is very informative the evolution of parameters of the polarization ellipse as a function of z , i.e. azimuth θ_0 and angle of ellipticity e_0 which are defined as follows [4]:

$$\theta_0 = \frac{1}{2} \operatorname{arctg} \left[\frac{S_{out(3)}}{S_{out(2)}} \right], \tag{7}$$

$$e_0 = \frac{1}{2} \operatorname{arctg} \left[\frac{S_{out(4)}}{\sqrt{S_{out(2)}^2 + S_{out(3)}^2}} \right]$$

Graphical interpretation of equation (7), describing the evolution of the azimuth and angle of ellipticity of the input polarization (4) are shown in Figure 2.

Analyzing Fig. 2 we can see that the azimuth is non-linear and non-periodic function of the coordinate z . Changing the azimuth at the minimum to the maximum value corresponds to the mathematical features of functions \arctan . The angle of ellipticity changing with coordinate z periodic and the period does not coincide with the period of helical structure of cholesteric p and equal:

$$Z = \frac{2\pi}{\sqrt{4\alpha_0^2 + \delta_0^2}} \tag{8}$$

in the case considered in Fig. 2 $Z = 4,62$ (μm). Moreover, the relation (8) can be obtained from the condition $\delta = \arccos(M_{44}) = 0$ [8].

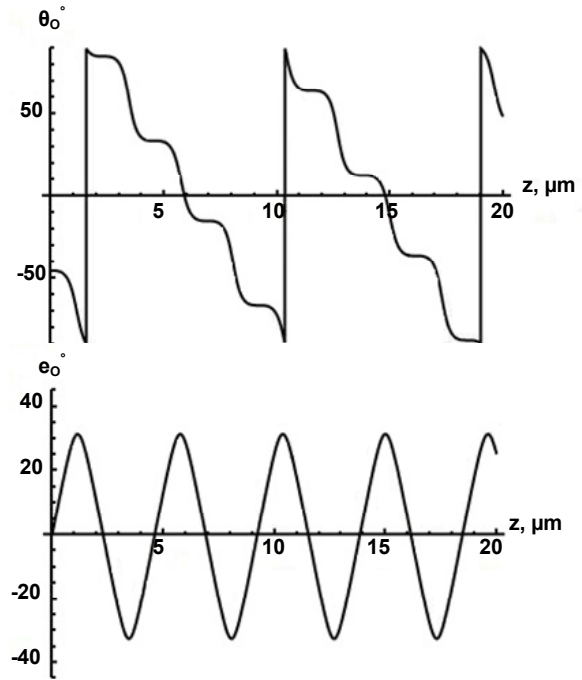


Fig. 2. Evolution of azimuth θ_0 and angle ellipticity e_0 of light with azimuth $\theta_{mp} = -0,8(\text{rad})$ with z coordinates in longitudinally inhomogeneous medium with linear birefringence and parameters: $\delta_0 = 1,22$ ($\text{rad}/\mu\text{m}$), $\alpha_0 = 0,3(\text{rad}/\mu\text{m})$

The periodic changing of angle of ellipticity with coordinate's z can be explained by the fact that this class of media with changing z may exhibit properties of linear, circular or elliptical phase anisotropy. However, as is well known [2, 10] with the change of angle of ellipticity caused only a linear phase anisotropy. That is, the changing of the angle of ellipticity in this case is such as in the media with linear phase anisotropy. It should also be noted that both parameters changed similarly as in a homogeneous medium with elliptical birefringence in the case commensurate with parameters of linear and circular birefringence [10]. So it should be noted that this class of longitudinally inhomogeneous medium characterized by effective circular birefringence which can be determined by applying solutions of inverse problems to the corresponding integral Mueller matrix [1] (3):

$$\varphi^{\text{eff}} = \frac{\operatorname{ArcCos} \left[-1 + 2\cos[z\alpha]^2 \cos \left[\frac{1}{2}z\sqrt{A} \right]^2 + \frac{8\alpha^2 \sin[z\alpha]^2 \sin \left[\frac{1}{2}z\sqrt{A} \right]^2}{A} + \frac{2\alpha \sin[2z\alpha] \sin[z\sqrt{A}]}{\sqrt{A}} \right] \left(\pm 2\alpha\sqrt{A} \cot[za] + A \cot \left[\frac{1}{2}z\sqrt{A} \right] \right)}{2z\delta\sqrt{A} \sqrt{\frac{4\alpha^2 \cot[z\alpha]^2 - 4\alpha\sqrt{A} \cot[z\alpha] \cot \left[\frac{1}{2}z\sqrt{A} \right] + A \cot \left[\frac{1}{2}z\sqrt{A} \right]^2 + \delta^2 \operatorname{Csc}[2\alpha]^2}{\delta^2}}} \tag{9}$$

where $A = 4\alpha^2 + \delta^2$.

and privileged waves propagating in a given class of media as a homogeneous optically active medium "not feeling" linear birefringence, and the ratio (9) is simplified to the form:

$$\varphi^{\text{eff}} = 2\alpha_0 z \tag{10}$$

where φ^{eff} – effective circular birefringence.

Conclusions. It is shown that the changing of the polarization state of the wave propagating in longitudinally inhomogeneous medium with linear birefringence is similar to the corresponding law, for the case of a homogeneous medium with elliptical birefringence. The latter can be described as the emergence of an effective circular birefringence (optical activity) for the state of polarization of the incident wave. In the case of privileged waves propagation this class of media is equivalent to a homogeneous optically active medium with the appropriate size of the circular birefringence.

REFERENCE:

1. Azzam R. M. A. Propagation of partially polarized light through anisotropic media with or without depolarization. A differential 4×4 matrix calculus / R. M. A. Azzam // J. Opt. Soc. Am., 1979. – Vol. 68. – P. 1756–1767.
2. Azzam R. M. A. Trajectories Describing the Evolution of Polarized Light in Homogeneous Anisotropic Media and Liquid Crystals / R. M. A. Azzam, N. M. Bashara, B. E. Merrill // J. Appl. Opt., 1973. – Vol. 12. – P. 764–771.
3. Azzam R. M. A. Simplified Approach to the Propagation of Polarized Light in Anisotropic Media-Application to Liquid Crystals / R. M. A. Azzam, N. M. Bashara // J. Opt. Soc. Am., 1972. – Vol. 62. – P. 1252–1257.
4. Azzam R. M. A. Ellipsometry and polarized light / R. M. A. Azzam, N. M. Bashara – New-York, 1977.
5. Born M. Principles of Optics / M. Born, E. Wolf. – M., 1973.

6. Transmission type twisted nematic liquid crystal display for three gray-level phase-modulated holographic data storage systems / B. Das, S. Vyas, J. Joseph et al. // Opt. and Las. in Eng., 2009. – Vol. 47. № 11. – P. 1150–1159.

7. Kolomiets I. The Studing of orthogonalization properties of longitudinally inhomogeneous nondepolarizing medium / I. Kolomiets, S. Savenkov, Ye. Oberemok // Registration, data storage and processing. – 2013. – Vol 15, No 1. – P. 23–30.

8. The solution of the spectral problem for longitudinally inhomogeneous nondepolarizing media / I. Kolomiets, S. Savenkov, Ye. Oberemok, A. Klimov // Metallofiz. Noveishie Tekhnol. 2013. – Vol. 35, No. 9. – P. 1197–1208.

9. Studying anisotropic properties of longitudinal inhomogeneous nondepolarizing media with elliptical phase anisotropy / I. S. Kolomiets, S. N. Savenkov, Ye. A. Oberemok, A. S. Klimov // Semiconductor Physics, Quantum Electronics & Optoelectronics, 2013. – Vol. 16. – № 4. – P. 366–373.

10. Kolomiets I.S. Observation of polarization evolution in homogeneous medium with two types of anisotropy / I. S. Kolomiets, S. N. Savenkov, Ye. A. Oberemok // XI International Young Scientists' Conference On Applied Physics, 15–18 June 2011, Kyiv, Ukraine p. 35–36.

11. Progress in the development of polymer cholesteric liquid crystal flakes for display applications / T. Z. Kosci, K. L. Marshalla, A. Trajkovska-Petkoska et al. // Displays, 2004. – V. 25. – Iss. 5. – P. 171–176.

12. Shurkliff W. Polarized Light. / W. Shurkliff. – M., 1965.

Submitted on 23.09.14

Лавренко К., студ., Коломієць І., асп.,
Савенков С., д-р фіз.-мат. наук, доц.,
Оберемок Є., канд. фіз.-мат. наук, асист.
Клімов О., канд. фіз.-мат. наук, наук. співроб.,
факультет радіофізики, електроніки і комп'ютерних систем
Київський національний університет імені Тараса Шевченка

ЕВОЛЮЦІЯ СТАНУ ПОЛЯРИЗАЦІЇ В ПОЗДОВЖНЬО НЕОДНОРІДНОМУ СЕРЕДОВИЩІ З ЛІНІЙНИМ ДВОПРОМЕНЕЗАЛОМЛЕННЯМ

Розглянуті та проаналізовані особливості формування анізотропії в поздовжньо неоднорідному середовищі з лінійним двоприменезаломленням. Була застосована еквівалентна модель представлення даного класу середовищ послідовною дією однакових фазових пластинок кожна з яких повернута на однаковий кут по відношенню до попередньої. Для представлення поляризаційних властивостей середовища був використаний диференціальний матричний метод Мюллера. Було отримано еволюцію вектора Стокса на основі диференційної матриці Мюллера та векторного рівняння переносу. Отримано та вивчено еволюцію азимута та кута еліптичності в напрямку розповсюдження світла в даному класі середовищ. Визначено період зміни параметрів еліпса поляризації. Було проведено порівняння особливостей еволюції стану поляризації з відповідними особливостями в поздовжньо однорідному середовищі з еліптичним двоприменезаломленням. Визначено ефективне значення оптичної активності для довільного стану поляризації світла, що розповсюджується в середовищі. Були розглянуті особливості обертання площини поляризації преваляючої хвилі.

Ключові слова: матриця Мюллера, двоприменезаломлення, азимут, кут еліптичності, поздовжньо неоднорідне середовище, стан поляризації.

Лавренко К., студ., Коломієць І., асп.,
Савенков С., д-р фіз.-мат. наук, доц.,
Оберемок Є., канд. фіз.-мат. наук, асист.,
Клімов О., канд. фіз.-мат. наук, наук. сотр.,
факультет радіофізики, електроніки і комп'ютерних систем
Київський національний університет імені Тараса Шевченка

ЕВОЛЮЦІЯ СОСТОЯНИЯ ПОЛЯРИЗАЦИИ В ПРОДОЛЬНО НЕОДНОРОДНОЙ СРЕДЕ С ЛИНЕЙНЫМ ДВУЛУЧЕПРЕЛОМЛЕНИЕМ

Рассмотрено и проанализировано особенности формирования анизотропии в продольно неоднородной среде с линейным двулучепреломлением. Была применена эквивалентная модель представления сред данного класса последовательным действием фазовых пластинок каждая, из которых повернута относительно предыдущей на один и тот же угол. Для представления поляризационных свойств сред был использован дифференциальный матричный метод Мюллера. Было получено эволюцию вектора Стокса на основе дифференциальной матрицы Мюллера и векторного уравнения переноса. Получено и изучено эволюцию азимута и угла эллиптичности в направлении распространения света в данном классе сред. Определен период изменения параметров эллипса поляризации. Было осуществлено сравнения особенностей эволюции состояния поляризации с соответственными особенностями в продольно однородной среде с эллиптическим двулучепреломлением. Определено эффективное значения оптической активности для произвольного состояния поляризация света распространяющегося в среде. Были рассмотрены особенности вращения плоскости поляризации преваляющих волн.

Ключевые слова: матрица Мюллера, двулучепреломление, азимут, угол эллиптичности, продольно неоднородные среды, состояния поляризации.

UDC 535.515; 535.56; 535.46; 535.012.21

M. Lavrenko, stud., I. Kolomiets, post. grad. stud.,
S. Savenkov, Dr. Sci., Ye. Oberemok, Ph. D.,
Faculty of Radio physics, Electronics and Computer Systems
Taras Shevchenko National University of Kyiv

RELATION BETWEEN THE ANISOTROPY PARAMETERS OF MULTIPLICATIVE AND HOMOGENEOUS MODEL FOR MEDIUM WITH ELLIPTICAL BIREFRINGENCE

The features of application of multiplicative and homogeneous models were described. Relations between anisotropy parameters describing the simultaneous (homogeneous models) and sequential (multiplicative model) effects of mechanism of anisotropy in a medium with elliptical birefringence were found. Cases of different ratios between the values of different mechanisms of anisotropy were reviewed.

Keywords: Muller matrix model, 1-st equivalence Jones theorem, linear and circular birefringence, anisotropic media, parameters of anisotropy, multiplicative and homogeneous models.

Introduction. Polarimetry as high precision research instrument without destroying anisotropic media has many applied uses today [6]. However, the development of modern polarimetry closely connected with the peculiarities of specific classes of studied objects [11]. Polarization properties of the medium with one mechanism of anisotropy are the simplest case which has been totally studied [1]. Therefore, considerable interest is paid to the properties of the medium in which there are several mechanisms of anisotropy [2]. Today in matrix polarimetry there are two main methods for modelling properties of such media. The question about the features of the polarization properties of such media was the study of the α - SiO_2 crystal in which in the direction perpendicular to the optical axis distributed two elliptically polarized eigenwaves [9–10]. This indicates the presence in the crystal anisotropy of two mechanisms: linear and circular birefringence. These mechanisms are determined by the anisotropy of different phase velocity of the eigenwaves that in the first case are linear, and the second are circular. In polarimetry for the quantitative analysis of the properties of these mediums consider the following parameters: $\delta = 2\pi(n_o - n_e)z/\lambda = \delta_0 z$ – phase shift between the two linearly polarized eigenwaves, α – azimuth and circular phase anisotropy with phase shift: $\varphi = \pi(n_l - n_r)z/\lambda = \varphi_0 z$ where n_o, n_e, n_l, n_r – refractive indices of the medium for ordinary, extraordinary, left and right circularly polarized waves respectively, δ_0, φ_0 – the value of the relative phase shift per unit length in the direction of light propagation z .

Examples of such media are crystals α - SiO_2 and TeO_2 [10]. For studying and analyzing of the polarization properties of the medium with complex anisotropy are prevalent matrix methods, including the method of Jones and Mueller [1]. Within these methods, the anisotropic properties of the medium are described by a matrix of 2x2 or 4x4, which for the above mentioned class of media is a function of the anisotropy parameter δ, φ, α . Mueller matrix models for media in which there is a mechanism of anisotropy were constructed in [4]. To analyze the media in which there are two mechanisms of anisotropy associated with birefringence [2] was proposed the 1-st equivalence Jones theorem, the essence of which is that any sequence of optical elements with linear or circular birefringence can be represented by a set of two elements with appropriate mechanisms of anisotropy. In fact, based on this theorem was built multiplicative model of homogeneous anisotropic media in which the presence in the media of linear and circular birefringence can be represented as sequential effect of these mechanisms of anisotropy and the order of their following is discussed in [3, 10]. Mueller matrix under the multiplicative model is the product of matrices Müller,

describing some of the mechanisms of anisotropy. In particular, it was shown that the phase shift δ, φ the same in both orders of following optical elements and orientation α is different by the value φ .

In the framework of homogeneous model of representing of anisotropic media [7], it was shown [8] that the electrodynamic parameters δ, φ, α do not coincide with the corresponding effective parameters of multiplicative model.

Applying the method presented in [9] obtained the following relationship between the parameters of multiplicative $\delta_M, \alpha_M, \varphi_M$ and homogeneous $\delta_0, \varphi_0, \alpha$ models:

$$\delta_M = \arctan \left(\frac{\delta_0 (\Delta S(2\alpha) S(z\Delta) - 2\varphi_0 C(2\alpha) (C(z\Delta) - 1))}{(4\varphi_0^2 + \delta_0^2 C(z\Delta)) S(\alpha_M)} \right),$$

$$\alpha_M = \frac{1}{2} \arctan \left(\frac{-2\varphi_0 C(2\alpha) (C(z\Delta) - 1) + \Delta S(2\alpha) S(z\Delta)}{2\varphi_0 S(2\alpha) (C(z\Delta) - 1) + \Delta C(2\alpha) S(z\Delta)} \right), \quad (1)$$

$$\varphi_M = \frac{1}{2} \arctan \left(\frac{4\varphi_0 \Delta S(z\Delta)}{\delta_0^2 + (\delta_0^2 + 8\varphi_0^2) C(z\Delta)} \right)$$

where $\Delta = \sqrt{\delta_0^2 + 4\varphi_0^2}$ – relative phase shift between eigenwaves per unit length z , $C(x) = \cos(x)$, $S(x) = \sin(x)$. From relations (1) can be noted that the values δ_M, α_M are a function of all three parameters $\delta_0, \varphi_0, \alpha$ of the homogeneous model and thickness z , while the value φ_M does not depend on the orientation of the axis of birefringence α in the framework of homogeneous model. This indicates that the circular birefringence even in the multiplier is still independent of the orientation of the plane of polarization. Let us analyze the obtain relation (1) for different ratios between the parameters of linear and circular birefringence. First, consider the case where the predominant linear birefringence. In particular, this case is realized for crystals α - SiO_2 and TeO_2 , which are characterized by the values of unit parameters of anisotropy: $\delta_0 = 5,14^\circ / \mu\text{m}$, $\varphi_0 = -8,5 \times 10^{-3} / \mu\text{m}$ and $\delta_0 = 86,97^\circ / \mu\text{m}$, $\varphi_0 = 3,55 \times 10^{-2} / \mu\text{m}$ for $\lambda = 0,63$ and $\alpha = 0$ respectively. Substituting the above mentioned parameters of crystals α - SiO_2 , and TeO_2 , in the direction perpendicular to the optical axis in equation (1) we obtain the dependence of the parameters of anisotropy of the multiplicative model $\delta_M, \alpha_M, \varphi_M$ on coordinate z , which are represented together with the parameters of anisotropy of homogeneous model δ, φ, α in Fig. 1.

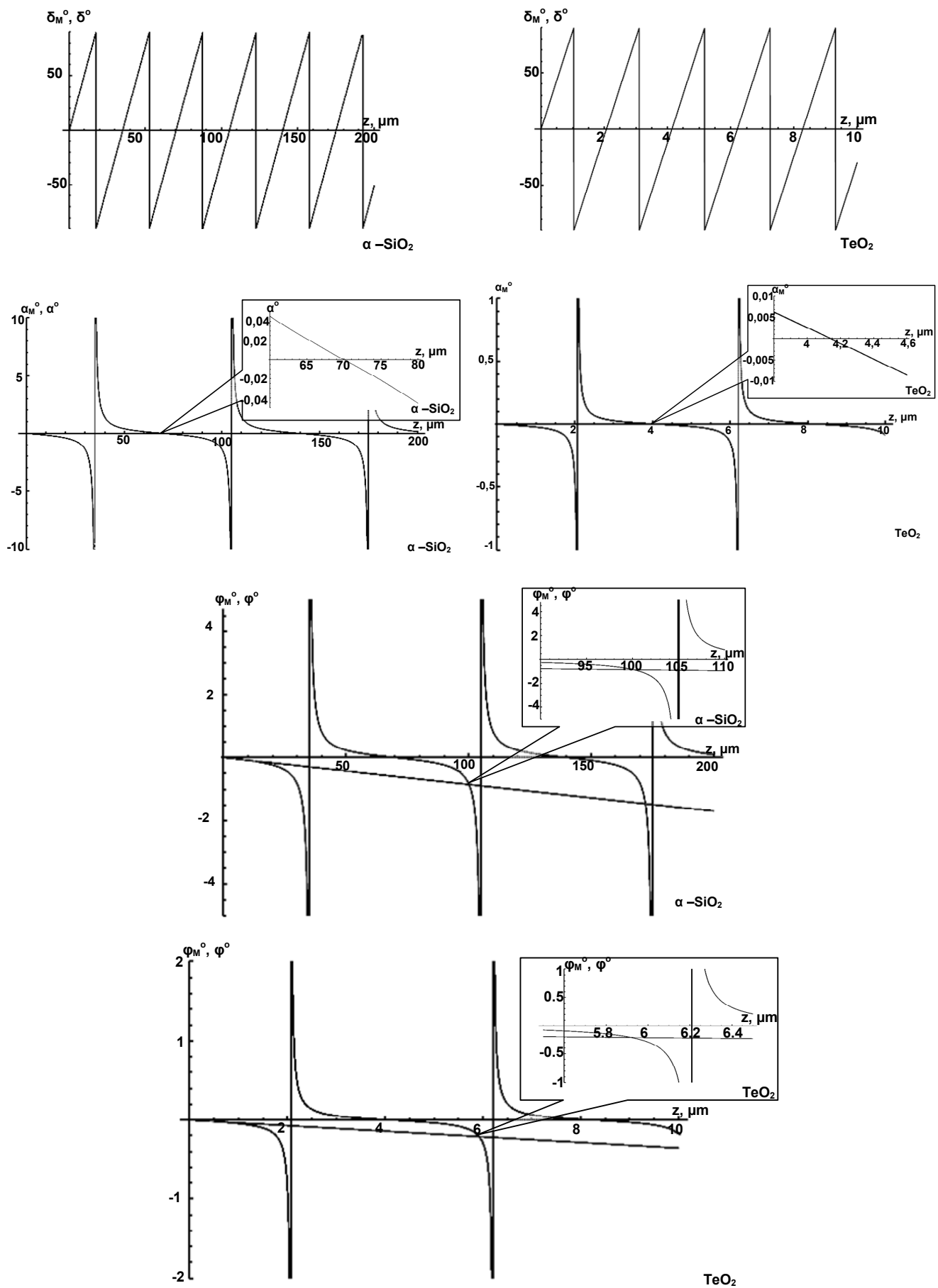


Fig. 1. The dependence of anisotropy parameters of multiplicative and homogeniuse models on thickness z in direction of light propagation for crystals $\alpha\text{-SiO}_2$ and TeO_2

Graphical interpretation of Eqs. (1) for other different ratios between δ_0 and φ_0 for crystal $\alpha - SiO_2$ shown in Fig. 2. It turns out that in extreme cases $\delta_0 \gg \varphi_0$ or $\delta_0 \ll \varphi_0$ the appropriate parameters of anisotropy of multiplicative and homogeneous models $\delta_M = \delta_0$ or

$\varphi_M = \varphi_0$ coincides. While all the other parameters of the model in this cases do not coincides. In the most general case, when $\delta_0 \approx \varphi_0$ none parameters of anisotropy of homogeneous and multiplicative model does not coincides.

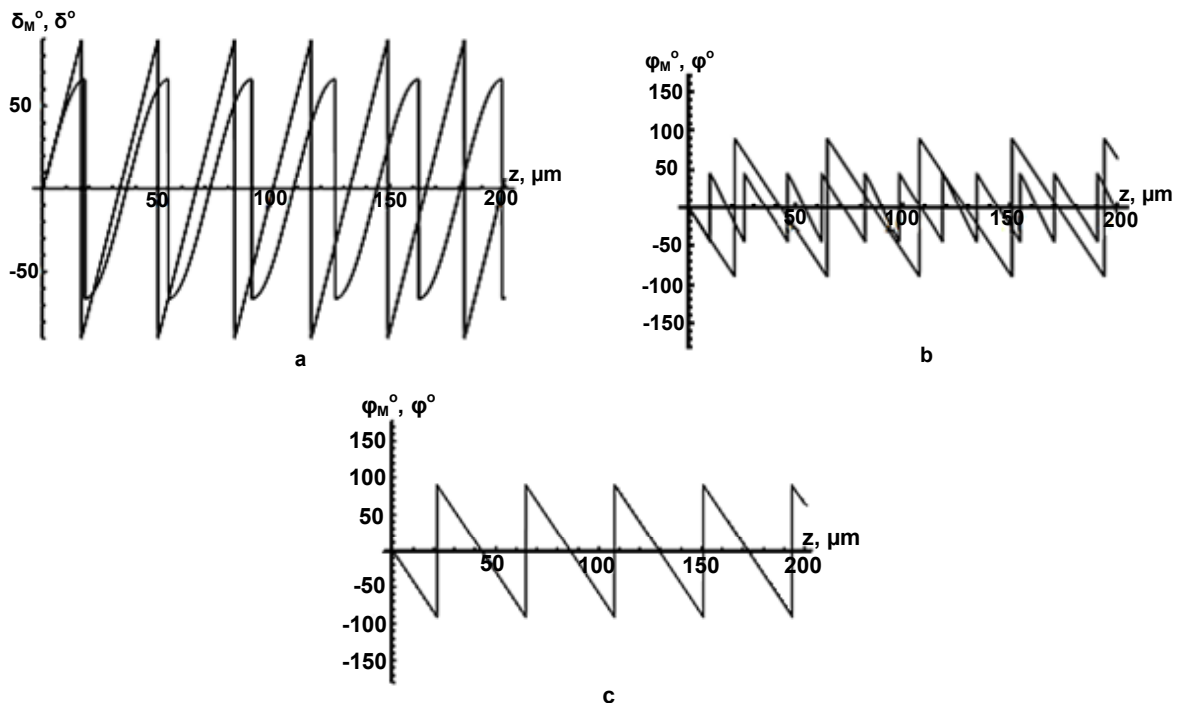


Fig. 2 The dependence of anisotropy parameters of multiplicative and homogeneous models on thickness z in direction of light propagation for the cases a), b) $\delta_0 = 5,43^\circ / \mu m$, $\varphi_0 = -4,18^\circ / \mu m$,
c) $\delta_0 = 7,3 \times 10^{-3}^\circ / \mu m$, $\varphi_0 = -4,18^\circ / \mu m$

Conclusions. In general for the medium with elliptical birefringence the parameters of anisotropy of sequences effect of anisotropy mechanisms (multiplicative model) do not coincident with parameters of anisotropy of simultaneous effects of mechanisms (homogeneous model) of anisotropy. So in general case the multiplicative model characterized by some effective anisotropy parameters. However, in extreme cases, when the value of one mechanism of anisotropy dominates over the other, there is a coincidence of this value of anisotropy in both models. Case $\delta_0 \gg \varphi_0$ for example sold for trigonal crystal system which includes in particular: $\alpha - SiO_2$ and TeO_2 in direction of optical axis.

REFERENCE:

1. Azzam R. M. Ellipsometry and Polarized Light / R. M. Azzam, N. M. Bashara. – New York: North-Holland Publishing Company, 1977. – 584 p.
2. Hurwitz H. A new calculus for the treatment of optical systems II. Proof of three general equivalence theorems / H. Hurwitz, R.C. Jones // J. Opt. Soc. Am. – 1941. – Vol.31. – P. 493–499.
3. Jones R. C. A new calculus for the treatment of optical systems. VII, Properties of the N – matrices / R. C. Jones // J. Opt. Soc. Am. – 1948. – Vol.38. – P. 671–685.

4. Jones R. C. A new calculus for the treatment of optical systems III. The Sohncke Theory of Optical Activity / R. C. Jones // J. Opt. Soc. Am. – 1941. – Vol.31. – p. 500–503.
5. Jones R. C. A new calculus for the treatment of optical systems IV / R. C. Jones // J. Opt. Soc. Am. – 1942. – Vol.32. – P. 486–493.
6. Kokhanovsky A. A. Light Scattering Media Optics: Problems and Solutions / A. A. Kokhanovsky. – Chichester: Springer-Praxis Books in Environmental Sciences, 2nd Edition, 2001. – 365 p.
7. Kolomiets I. S. Eigenpolarizations orthogonality conditions for the first and second Jones equivalence theorems, in the approximation of homogeneous and layered medium / I. S. Kolomiets, Y. A. Oberemok, S. N. Savenkov // Metal physics and the newest technology. – 2011, – Vol. 33. – P. 493–502.
8. Kolomiets I. S. Difference between homogeneous and multiplicative mueller matrix model / I. S. Kolomiets, S. N. Savenkov, Y. A. Oberemok, // XII International Young Scientists' Conference On Applied Physics, 23-26 May 2012, Kyiv, Ukraine. – P. 12–13.
9. Lavreno M. L. Comparison of polarization properties of media with elliptical phase anisotropy under homogeneous and multiplicative models / M. L. Lavreno, I. S. Kolomiets, S. N. Savenkov, Y. A. Oberemok, A. S. Klimov // Lashkaryovskiy Chytannya – 2014, 2–4 April 2014 Kyiv, Ukraine. – P. 8–10.
10. Nye J. F. Physical Properties of Crystals: Their Representation by Tensors and Matrices / Nye J. F. – Oxford: Clarendon Press, 1957. – 322 p.
11. Savenkov S. N. Optimization and structuring of the instrument matrix for polarimetric measurements / S. N. Savenkov // Optical Engineering. – 2002. – Vol. 41. – No.5. – P. 965–972.

Submitted on 17.11.14

Лавренко М., студ., Коломієць І., асп., Савенков С., д-р фіз.-мат. наук, доц., Оберемок Є., канд. фіз.-мат. наук, асист., факультет радіофізики, електроніки та комп'ютерних систем, Київський національний університет імені Тараса Шевченка

ПОРІВНЯННЯ РОЗВ'ЯЗКІВ ОБЕРНЕНОЇ ЗАДАЧІ ПОЛЯРИМЕТРІЇ ПРИ ПОСЛІДОВНІЙ ТА ОДНОЧАСНІЙ ДІЇ МЕХАНІЗМІВ АНІЗОТРОПІЇ СЕРЕДОВИЩ З ЕЛІПТИЧНИМ ДВОПРОМЕНЕЗАЛОМЛЕННЯМ

Було описано особливості застосування мультиплікативних і однорідних моделей. Були знайдені співвідношення між параметрами анізотропії, що описують одночасну (однорідна модель) і послідовну (мультиплікативна модель) дію механізмів анізотропії в середовищі з еліптичним двоприменезаломленням. Випадки різних співвідношення між значеннями різних механізмів анізотропії були розглянуті.

Ключові слова: матрична модель Мюллера, 1-ша теорема еквівалентності Джонса, лінійне та циркулярне двоприменезаломлення, анізотропне середовище, параметри анізотропії, мультиплікативна і однорідна моделі.

Лавренко М., студ., Коломиец И., асп., Савенков С., д-р физ.-мат. наук, доц., Оберемок Е., канд. физ.-мат. наук, асист., факультет радиофизики, электроники і компьютерных систем, Киевский национальный университет имени Тараса Шевченко

СРАВНЕНИЕ РЕШЕНИЙ ОБРАТНОЙ ЗАДАЧИ ПОЛЯРИМЕТРИИ ПРИ ПОСЛЕДОВАТЕЛЬНОМ И ОДНОВРЕМЕННОМ ДЕЙСТВИИ МЕХАНИЗМОВ ФНИЗОТРОПИИ СРЕД С ЭЛЛЕПТИЧЕСКИМ ДВУЛУЧЕПРЕЛОМЛЕНИЕМ

Было описано особенности применения мультипликативных и однородных моделей. Были найдены соотношения между параметрами анизотропии, описывающих одновременную (однородная модель) и последовательную (мультипликативная модель) действие механизма анизотропии в среде с эллиптической двулучепреломления. Случаи различных соотношениях между значениями различных механизмов анизотропии были рассмотрены.

Ключевые слова: матричная модель Моллера, 1-я теорема эквивалентности Джонса, линейное и циркулярное двулучепреломление, анизотропная среда, параметры анизотропии, мультипликативная и однородная модели.

УДК 372.853;372.862;621.37

С. Левитський, д-р фіз.-мат. наук, проф.
Київський національний університет імені Тараса Шевченка

ЧИ МОЖНА ВИЯВИТИ БУДЬ-ЯКІ СЛІДИ СИГНАЛУ ДО ЙОГО ПОЧАТКУ?

Розглядається методичне питання до курсу з гармонічного аналізу про можливість виявлення слідів сигналу до його початку, оскільки розкладання ведеться на гармоніки, що простягаються від мінус до плюс нескінченності у часі. Показано, що для будь-яких реальних фільтрів, які складаються з LRC-елементів. це неможливо, тоді як для ідеального фільтру (який практично не може бути реалізований) така можливість існує.

Ключові слова: спектр, ідеальний фільтр, реальний LRC-фільтр

При вивченні деяких розділів курсу з гармонічного аналізу сигналів у студентів часто виникають питання, зайти відповіді на які буває досить складно. Іноді такі питання стосуються навіть певних парадоксів, як, наприклад, зазначене вище "Чи можна виявити будь-які сліди сигналу до його початку?" І хоча таке питання у студентів природно виникає, відповіді на нього в навчальній літературі, переліченій наприкінці даної статті, нам знайти не вдалось.

Наша інтуїція, що ґрунтується на принципі причинності, категорично відхиляє таку можливість. Проте, оскільки ми розкладали сигнал на гармонічні складові, що простягаються у часі від мінус нескінченності до плюс нескінченності, то виходить, що для сигналу, який розпочався у певний скінчений момент часу (наприклад, в момент $t = 0$), гармонічні складові повинні існувати і до його початку. Зрозуміло, окрему дискретну гармонічну складову неперіодичного сигналу виявити неможливо, бо її амплітуда нескінченно мала. Взяті ж разом всі складові до початку сигналу мають давати в сумі нуль, оскільки саме з цієї умови робиться добір їх амплітуд і фаз. Та чи можна за допомогою будь-якого фільтру "вирізати" з усього спектру деяку смугу частот, котрі в сумі не давали б нуль до початку сигналу?

У загальному випадку вираз для сигналу на виході деякого лінійного чотириполюсника має вигляд

$$f_2(t) = \frac{1}{2\pi} \int_{-\infty}^{\infty} \dot{s}_1(\omega) K(\omega) e^{j\omega t} d\omega = \frac{1}{2\pi} \int_{-\infty}^{\infty} K(\omega) e^{j\omega t} d\omega \int_{-\infty}^{\infty} f_1(\theta) e^{-j\omega\theta} d\theta \quad (1)$$

де $f_1(\theta)$ і $\dot{s}_1(\omega)$ – сигнал і його спектр на вході чотириполюсника, а $K(\omega)$ – передавальна функція чотириполюсника. Змінюючи порядок інтегрування в (1), одержуємо

$$f_2(t) = \frac{1}{2\pi} \int_{-\infty}^{\infty} f_1(\theta) d\theta \int_{-\infty}^{\infty} K(\omega) e^{j\omega(t-\theta)} d\omega \quad (2)$$

Візьмемо як приклад звичайний коливний контур (рис. 1), для якого передавальна функція має вигляд:

$$K(\omega) = \frac{\omega_0^2}{\omega_0^2 - \omega^2 + 2j\omega\delta} \quad (3)$$

де ω_0 – власна частота контуру, а δ – його згасання.

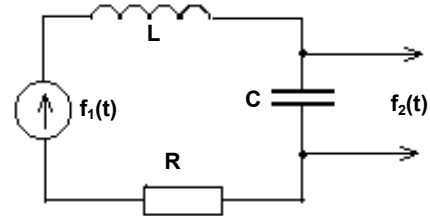


Рис. 1. Схема фільтру

Для обчислення другого інтегралу в (2) слід скористатися методом лишків, перетворивши його у контурний інтеграл.

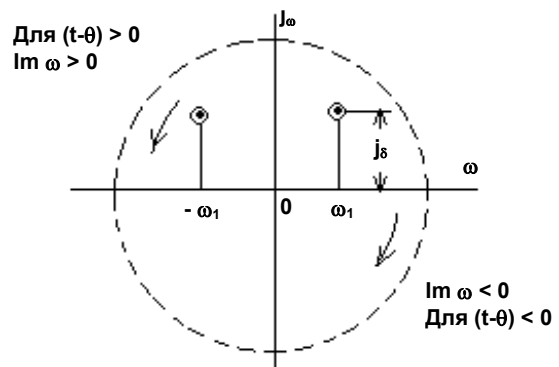


Рис. 2. Контур на комплексній площині

З цією метою слід замкнути шлях інтегрування на площині комплексної змінної ω (Рис.2) таким чином, щоб додаткова частина шляху інтегрування нічого б не додавала до значення нашого інтегралу. Це можна зробити, проводячи замикаючу лінію через область, де $|Im \omega| = \infty$. Тоді, щоб виконати вказану вище умову для $t - \theta > 0$ (тобто для моментів часу після початку сигналу), замикаючу лінію слід проводити у верхній напівплощині, де $Im \omega = +\infty$, бо лише у цьому випадку $e^{j\omega(t-\theta)}$ на цій додатковій ділянці контуру інтегруванні дорівнюватиме нулю і нічого не додасть до нашого

інтегралу. А для моментів $t - \theta < 0$ (тобто до початку сигналу) контур інтегрування слід замикати через нижню напівплощину.

Але полюси $K(\omega)$ (Тобто значення ω , при яких $K(\omega)$ перетворюється на нуль) відповідають значенням

$$\omega = j\delta \pm \sqrt{\omega_0^2 - \delta^2}$$

і лежать у верхній напівплощині (рис. 2). Тому при обході контуру по нижній напівплощині (тобто для моментів до початку сигналу) $f_2(t)$ завжди дорівнюватиме нулю для будь-яких $f_1(t)$. На відміну від цього при обході контуру по верхній напівплощині контур охопить обидва полюси і лишок інтегралу не буде нульовим.

Ці міркування залишаються справедливими і для будь-яких фільтрів, складених з LRC елементів. Всі подібні фільтри мають позитивне згасання і полюси їх передавальних функцій повинні лежати в верхній напівплощині. Лише для систем з негативним згасанням полюси можуть лежати в нижній напівплощині і давати $f_2(t) \neq 0$ при $t - \theta < 0$. Але такі системи є нестійкими і в них можливе самозбудження коливаль.

Таким чином можна вважати доведеним, що маючи справу з реальними фільтруючими колами, складеними з LRC елементів, до початку сигналу будь-яких його слідів виявити неможливо.

Інша справа, якщо ми задамося фільтруючим пристроями, котрі неможливо реалізувати. Так, наприклад, для ідеального фільтра, який має передавальну функцію

$$K(\omega) = \begin{cases} 0, & \omega < \omega_0 - \Delta\omega \\ e^{-j\omega t_0}, & \omega_0 - \Delta\omega < \omega < \omega_0 + \Delta\omega \\ 0, & \omega > \omega_0 + \Delta\omega \end{cases} \quad (4)$$

зображену на рис. 3, при поданні на його вхід гармонічного сигналу $U_1(t)$, що починається в момент часу $t = 0$, тобто

$$\dot{U}_1(t) = 1(t) \cdot e^{j\omega_0 t}. \quad (5)$$

Тоді на виході фільтру об'єднана сигналу буде

$$U_{m2}(t) = \frac{1}{2} + \frac{1}{\pi} Si[\Delta\omega t'], \quad t' = t - t_0 \quad (6)$$

Левитский С., д-р физ.-мат. наук, проф.
Киевский национальный университет имени Тараса Шевченко

МОЖНО ЛИ ОБНАРУЖИТЬ КАКИЕ-ЛИБО СЛЕДЫ СИГНАЛА ДО ЕГО НАЧАЛА?

Рассматривается методический вопрос курса по гармоническому анализу о возможности обнаружения следов сигнала до его начала, поскольку разложение ведется на гармоники, которые располагаются от минус до плюс бесконечности по времени. Показано, что для любых реальных фильтров, которые состоят из LRC-элементов, это невозможно, тогда как для идеального фильтра (который практически не может быть реализован) такая возможность существует.

Ключевые слова: спектр, идеальный фильтр, реальный LRC-фильтр

Levitsky S., Dr.Sci., Prof.
National Taras Shevchenko University of Kyiv

ON THE POSSIBILITY TO DETECT ANY TRACES OF SIGNAL BEFORE IT'S BEGINNING

Methodological issues are considered for the rate of harmonic analysis on the possibility to detect some traces of the signal before it starts, because the decomposition is implemented at harmonics that extends from minus to plus infinity in time. It is shown that for any real filters, which consist of LRC-elements, this is impossible, whereas for an ideal filter (which can not practically be implemented) this possibility exists.

Key words: spectrum, ideal filter, real LRC-filter

Ця функція має вигляд зображений на рис. 4. Тут

$$Si(x) = \int_0^x \frac{\sin z}{z} dz - \text{інтегральний синус.}$$

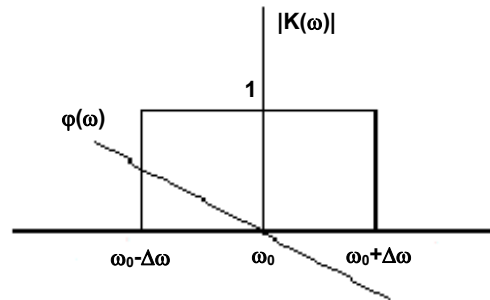


Рис. 3. Частотні характеристики

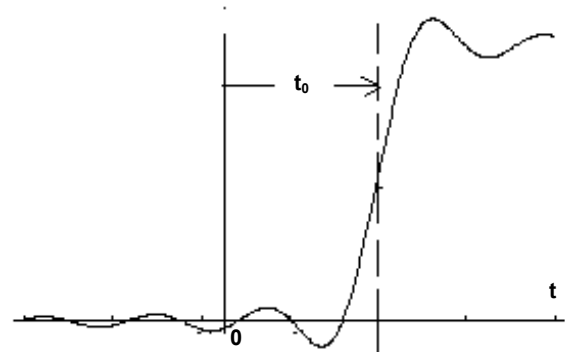


Рис. 4. Сигнал на виході фільтру

Як видно, $U_2(t)$ може бути відмінною від нуля і для $t < 0$, тобто до початку вхідного сигналу. Зміст цього парадоксу полягає в тому, що ідеальний фільтр з передавальною функцією (4), що має нескінченно різкі границі, практично не може бути реалізований і його слід віднести до "фантастичних" пристроїв, які спроможні давати "фантастичні" результати.

Submitted on 10.06.14

UDC 519.815

E. Martysh, D. Sc., Prof.
 Taras Shevchenko National University of Kyiv,
 Medical Radio Physics Department
 V. Yatsenko, D. Sc., Prof.
 Space Research Institute of NASU-SSAU

AUTONOMOUS RENDEZ-VOUS WITH UNCOOPERATIVE SPACE OBJECTS

Traditionally, relative navigation vision systems for rendezvous and docking in space have relied on cooperative targets such as retro-reflectors installed on the spacecraft to capture. While reliable, target based systems have operational limitations, as targets must be installed on the targeted payload. Unfortunately, tasks such as autonomous rendezvous and docking, planetary probe landing and robot navigation require higher levels of autonomy. A vision system for these applications would need to be operational under a wider range of conditions. Comparison of two most successive missions with rendezvous and docking in 2014 provides interesting designations for future systems development.

Keywords: satellite rendezvous and docking, space vision system, robot navigation

Introduction. The new generation of deep-space-investigation and Earth-orbit-servicing missions which are under considerations not only by several national and international space agencies, but has some commercial projects. For example, OLEV (Orbital Life Extension Vehicle) is a commercial project under development by a consortium formed by Swedish Space Corporation, Kayser-Threde and SENER, aimed to extend the operational life of geostationary telecommunication satellites by supplying them control, navigation and guidance services. OLEV is planned to use a set of cameras to determine the angular position and distance to the client satellite during the complete phases of rendezvous and docking, thus enabling the operation with satellites not equipped with any specific navigational aid to provide support during the approach.

These projects are driving the demand to efficiently approach and rendezvous with non-cooperative on-orbit objects. Strategic applications of this technology are in the frame of space situational awareness, orbital lifetime prolongation, and science among others. Common to these missions is the necessity to approach a non-cooperative passive target from large distances (e.g., > 30 km) in a fuel efficient, safe, and accurate manner [1].

November 12, 2014 yr the lander Philae from space probe Rosetta made a first controlled landing on a comet 67P – Fig. 1. This comet opened on October 23, 1969 in Kyiv, astronomer Klim Churyumov while watching another comet photographic plates – 32P, which a month earlier Svetlana Gerasimenko starred in Alma-Ata Observatory. The size of the comet's nucleus is 3x5 km, orbital period - 6.6 years. After that it has a name Comet Churyumov-Gerasimenko.

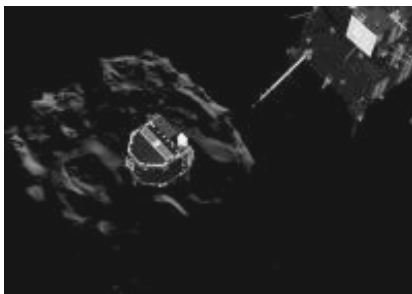


Fig. 1. The landing Philae on Comet 67P

ESA is trying to solve the problem of convergence of future spacecraft with "uncooperative" objects, such as fragment on low-Earth orbits, capsule with samples from Mars or comet and asteroid. The main experiments are connected with set of spaceships ATV (Automated Transfer Vehicle). Since the launch of the first ATV in 2008, each time units produce flawless docking with the space

station, using satellite navigation over long distances and optical sensors – in the Middle. It was reviewed at [2], in comparison of Russian system "KURS". But the last – ATV-5 (Georges Lemaître) made splendid rendezvous process with traditional but modernized devices and docking at August 8, 2014 yr. It has also the prototype LIRIS (Laser InfraRed Imaging Sensors) – the regular step to solve the problem on the new base.

It is obviously that practical the same requirements exist for deep space investigations where space vehicle docking with comets and asteroids is modern problem. The comparative examination of traditional methods and modern results in space exploration is useful from this point of view. The set of traditional devices are following:

Videometer. Used by the Jules Verne ATV (Automated Transfer Vehicle). The ATV vehicle was conceived as a resupply and reboost vehicle capable of performing a fully automated docking with the International Space Station. The ATV, which has recently performed its first mission with remarkable success, uses as primary sensor at close-ranges videometers to determine its distance and orientation relative to its target. Based on the design of a star tracker, the videometer is the first automatic optical operational system ever used for spacecraft navigation. It operates by emitting a pulsed laser beam, which is reflected by an arrangement of passive retro-reflectors (26, in the ISS) installed in the client satellite. Analysis of the time of flight and the pattern of reflected light enables to determine the distance and direction to the docking port. To add redundancy and a safety margin to the critical rendezvous operations, the relative distance and orientation to the client satellite is also computed by a secondary independent sensor, a telegoniometer.

Radiofrequency. Radiofrequency (RF) has also been used in space missions to sense distance and direction to a given target. An especially relevant example based in RF sensors is the Russian KURS system, which has been used for rendezvous navigation for a long time. This system was designed to provide all required navigation measurements during the entire approach from a few hundreds of kilometres down to contact, and operates in the S-band, using wavelengths of the order of 10 cm in continuous and modulated signals. In the SHF approach, a modulated signal is generated by a transmitter and is directed by an antenna towards the target. Part of the signal's power is reflected by the target back in the direction of the transmitter, or the signal is re-transmitted by a transponder at the target, and is received by the antenna at the transmitter's location. The typical maximum range of RF docking sensors is on the order of 100 Km, fitting well with the long and medium range of the approach, whereas the very short range would require a substantial effort to mitigate disturbances and provide the required performance. Other important drawbacks of the RF technology are the substantial power consumption and

mass of the antennas required to operate over long distances to the target, making this choice of sensor less used in modern systems.

Light Detection and Ranging (Lidar). This is an optical remote sensing technology that measures properties of scattered light to find range and/or other information of a distant target. The prevalent method to determine distance to an object or surface is to use laser pulses in a similar way to radar technology, which uses radio waves instead of light. The range to an object is determined by measuring the time delay between transmission of a pulse and detection of the reflected signal. LIDAR enables technology for Lunar Science, Exploration and Resource Prospecting. For in space and on orbit rendez-vous, the powerful flash LIDAR LASER pulse can be used to acquire and range targets from a distance of up to 10–20 km. For docking applications, flash LIDAR provides real-time three dimensional video of the target spacecraft under any lighting conditions. This provides six degree of freedom pose as well as velocity and spin rate data. Inclusion of a flash LIDAR system also allows for redundant video guidance capabilities [3].

There have been other missions (like Rosseta ESA's mission, Gemini or NEAR NASA's mission or Japan's Hayabusa mission) trying to reach passive (non-cooperative) targets in space. Most of them used cameras as one of the main optical instruments to successfully perform the rendez-vous, but supporting it with secondary optical instruments like a laser range finder to get distance measurements.

AVGS (Advanced Video Guidance Sensor). Another video sensor for rendez-vous and docking operations is the AVGS (Advanced Video Guidance Sensor), used in the Dart and Orbital Express demonstration missions. Dart was developed as part of NASA's Space Exploration Initiative, and was launched on April 15, 2005, aboard an Orbital Sciences Pegasus Launch Vehicle. The Dart mission included performing autonomous proximity operations on a target satellite using as primary sensor the AVGS. DART performed as planned during the first eight hours through the launch, early orbit, and rendez-vous phases of the mission, accomplishing all objectives up to that time. However, during proximity operations, the spacecraft began using much more propellant than expected. As DART detected its propellant source was approaching exhaustion, it began a series of manoeuvres for departure and retirement. DART finally collided with its client satellite 3 minutes and 49 seconds before initiating retirement. The Orbital Express mission was funded by DARPA and NASA with the goal of validating the technical feasibility of robotic, autonomous on-orbit refueling and reconfiguration of satellites. Orbital Express consists of a robotic servicing spacecraft (ASTRO) and NextSat, a prototypical modular next-generation serviceable client spacecraft. The tests performed in orbit included connection through the robotic arm, fuel transference, formation flying and autonomous rendezvous, and were completed successfully.

The AVGS system combines an imaging sensor, integrated laser sources, and narrow-band-filtered retro-reflective targets with sophisticated signal processing and optical correlation to develop six-degree-of-freedom estimates of the relative state between two spacecraft engaged in proximity operations. The AVGS sensor is equipped with four multiplexed 1 watt diode lasers illuminating a 24° aperture in front of the target vehicle. Laser light is reflected by reflective corner cubes mounted on the target satellite, and arranged in a triangle pattern with the optical axis of all three corner cubes pointing in the same direction. The reflected light is collected by an imaging lens and projected onto a 1024 x 1024 CMOS

detector. Pattern recognition algorithms identify the spot centroids of each corner cube to determine range, bearing, and attitude of the chaser vehicle with respect to the target satellite. The use of sensors such as the videometer or the AVGS obviously requires the previous installation of the set of retro-reflectors on the client satellite. This precludes their use in a mission such as OLEV, conceived to operate with satellites already in orbit, and generally un-equipped with any specific means to ease the rendez-vous and docking operation.

There have been other missions (like Rosseta ESA's mission, Gemini or NEAR NASA's mission or Japan's Hayabusa mission) trying to reach passive (non-cooperative) targets in space. Most of them used cameras as one of the main optical instruments to successfully perform the rendez-vous, but supporting it with secondary optical instruments like a laser range finder to get distance measurements.

The LAMP (LAsER MaPper). Used in the ST6 NASA mission launched in early 2004, this sensor is a laser radar. It operates by emitting short high power laser pulses, which bounce off an internal gimbaled mirror that determines the azimuth and elevation of the outgoing beam. When the laser pulse hits a target, a small amount of the light is reflected back to the instrument. The returned laser pulse bounces off the internal mirror and is collected by a telescope. On the way out, a laser actuated trigger starts a counter that is stopped by the return pulse. By sweeping the internal gimbaled mirror through a number of angles, it is possible to form a 3-dimensional image of the space in front of LAMP. The laser beam has been shaped to have a 0,02° (0.35 mrad) divergence. For a target surface with a 0.1m area, the detection range is 2.5 km. The LAMP telescope itself has a 5 cm aperture and is a classical Cassegrain type [4].

It is well-known that rocket with Rosetta still launched in 2004, it immediately brought the device into an interplanetary orbit, which needed a fourth stage of the launcher. He led the probe directly to the earth's gravity endpoint. After the vehicle was flying in a spiral, from time to time making gravitational maneuvers - acceleration or deceleration, flying past the Earth and Mars. The chemical engine, which is set to Rosetta, only needed to point inclusions for the correction of its movement. Somewhere about a year ago apparatus "put to sleep" due to energy savings. The flight lasted for inertia. In the spring of this year, the unit again "wake up", and he was involved in the work. The fact that he still got to comet 67P, - a very good result of celestial mechanics.

Rosetta spent a decade flying to comet 67P/Churyumov-Gerasimenko, and spent three months mapping its surface to prepare for Philae's touchdown. But the landing didn't go as planned. The three systems designed to attach Philae to the surface: a gas thruster, harpoons and ice screws – all failed, so the spacecraft bounced twice before coming to a halt, angled against a shadowed cliff with one leg in the air. Without enough sunlight to recharge its batteries, Philae went into a deep sleep. There is a chance it could revive as the comet moves closer to the sun, but for now researchers are busy dissecting the wealth of data Philae managed to upload before it shut down.

Readings from radar instrument that linked Philae with Rosetta before the lander ran out of power, have narrowed potential landing spots to a 350 metre by 30 metre strip on the comet's head – Fig. 2. Scientists at the ESA are now searching images from Rosetta's cameras to see if they can spot Philae, but it is in a region of deep shadow and is only likely to show up when light bounces off its solar panels [5].

As for Philae's drill, it was one of the last instruments to be activated before the lander switched off. Mission managers know the drill operated as expected, but because the probe was sitting at angle they don't know whether it delivered a sample to the instrument, which was designed to study molecules from the comet by heating material in an oven and measuring the resulting gas.



Fig. 2. Surface appearance of the comet 67P from a distance of 40 meters

Rosetta is now ramping up its scientific mission. The ESA has placed the spacecraft back into a higher orbit, 30 kilometres above the comet, but it will dip to 20 kilometres on 3 December for 10 days to gather data on the increasing dust and gas spewing from 67P as it nears the sun. The plan is to stay as close to the comet as possible without putting Rosetta at risk from the comet's increasing activity.

Мартиш Є., д-р фіз.-мат. наук, Київський національний університет імені Тараса Шевченка,
Яценко В., д-р техн. наук, Інститут космічних досліджень НАН та НКА України

АВТОНОМНЕ СТИКУВАННЯ З НЕКООПЕРОВАНИМИ КОСМІЧНИМИ ОБ'ЄКТАМИ

Традиційно, системи відносної навігації та бачення для зближення і стикування в космосі покладалися на кооперовані об'єкти, такими що мали світловідбивачі, встановлені на космічному кораблі. Тому надійні системи на цільовій основі мають експлуатаційні обмеження, як цілі повинні бути встановлені на корисному навантаженні. Такі завдання, як автономне зближення і стикування, планетарні посадки зонда і навігації роботів вимагають більш високого рівня автономії. Системи бачення для цих застосувань необхідно буде ввести в експлуатацію відповідно з більш широким діапазоном умов. Порівняння двох успішних місій зі зближенням і стикуванням в 2014 році дає цікаві позначення для розвитку майбутніх систем.

Ключові слова: супутникова зближення і стикування, система космічного бачення, автоматична навігація

Мартыш Е., д-р физ.-мат. наук, Киевский национальный университет имени Тараса Шевченко,
Яценко В., д-р техн. наук, Институт космических исследований НАН та НКА Украины

АВТОНОМНАЯ СТЫКОВКА С НЕКООПЕРИРОВАННЫМИ КОСМИЧЕСКИМИ ОБЪЕКТАМИ

Традиционно системы относительной навигации и видения для сближения и стыковки в космосе полагались на кооперированные объекты, такие, что имели световотражатели, установленные на космическом корабле. Поэтому надежные системы на целевой основе имеют эксплуатационные ограничения, так как цели должны быть установлены на целевой нагрузке. Такие задачи, как автономное сближение и стыковка, планетарные посадки зонда и автоматической навигации требуют более высокого уровня автономии. Системы видения для этих приложений необходимо будет ввести в эксплуатацию в соответствии с более широким диапазоном условий. Сравнение двух самых успешных миссий с сближения и стыковки в 2014 году дает интересные направления для развития будущих систем.

Ключевые слова: спутниковые сближения и стыковки, система космического видения, автоматическая навигация

UDC 535.36

A. Machulansky, Ph.D., B. Babych, stud.
Microelectronics department, Faculty of Electronics,
National Technical University of Ukraine Kiev Polytechnic Institute

SELECTIVE ENERGY-SAVING METAL-DIELECTRIC NANOCOMPOSITE COATINGS BASED ON COPPER

Spectral selective characteristics of metal-dielectric nanocomposite coverings on the basis of copper are investigated. The computing algorithm of determination of coefficients of reflection and a transmission of nanocomposite metal-dielectric structures on the basis of copper in dielectric matrixes of SiO₂ is developed. Numerical modeling of their optical characteristics in the spectral range from 0.3 to 3 microns for various options of structures is executed. Possibilities of practical realization and application of nanocomposite structures on the basis of copper as the energy saving are discussed.

Keywords: metal-dielectric structure, spectral-selective properties, nanocomposite coatings, energy saving.

Introduction. Scientific and technological research on the development of energy-saving coatings in many countries belong to the priority areas of science and technology as the main attention is paid to date save energy resources.

Such coatings can be used as transparent heat filters, photothermal and photovoltaic cells with improved efficiency [2].

Special interest are transparent nanocomposite coatings with energy-saving properties based on nanoscale metal layers on optically transparent dielectric substrate to reduce energy losses due to light gaps [5, 6].

Analysis of the current state of energy consumption shows that the order of half the energy consumption accounts for the maintenance of thermal and lighting comfort indoors. Of these, 40% is lost through the light transparent gaps. In Ukraine such losses equivalent to the annual expenses of gas in 8 billion cubic meters in May 2014 prices, equivalent to 4 billion dollars. About 50% of energy loss accounts for the thermal radiation of glass of light gaps in the near infrared (IR) wavelengths. Removal of such losses is possible only through the use of heat-reflective filters based on transparent surfaces. By the experimental data are listed energy saving coating reduces heat losses from 50% to 2%.

Energy-saving coatings is being implemented mainly based on multilayer structures formed from thin films of silver and dielectric. These coatings have a high cost due to the use of precious materials. These coatings have significant drawbacks: high cost; possibility of degradation characteristics of multilayer coatings; insufficient mechanical strength; sophisticated manufacturing techniques and control parameters of multilayer structures; limited choice of materials for energy-saving features, etc. [2, 5, 6]. To avoid a large part of these drawbacks is proposed by the manufacture of nanocomposite metal-dielectric structures with energy-saving features based on the widely used in microelectronic technology metals, including copper [3, 8].

The aim of this work is to develop nanocomposite metal-dielectric coatings based on copper for use in energy-saving technologies.

Experiment technique. For the numerical simulation of optically transparent nanocomposite coatings used metal-dielectric structure consisting of thin layers of dielectric and metal on a dielectric substrate.

To calculate the parameters of spectral-selective characteristics of the electromagnetic response of each layer and the whole system is developed computational algorithm based on transfer matrix method [3, 4, 9]. This method is based on the theory of plane electromagnetic waves in a layered system [1].

An advantage of the method is that it does not impose any restrictions on the number of layers and can be used to calculate both the multilayer and single layer structures.

The calculations were performed under the following approximations:

- Layered structure consists of N plane-parallel, homogeneous, isotropic layers;
- Each layer is characterized by the effective thickness d_i (i – the index of the layer), the spectral complex electromagnetic parameters ϵ_i^* and μ_i^* ;
- Coating located between two semi-infinite homogeneous isotropic medium (in this case there is air with a refractive index equal to unity).

In accordance with [4, 9], we represent the tangential terms of $E_t(z_i)$ and $H_t(z_i)$ are the electric E and magnetic H fields in the form of a two-dimensional vector:

$$G_i(z_i) = \begin{pmatrix} E_t(z_i) \\ H_t(z_i) \end{pmatrix} \quad (1)$$

The nature of electromagnetic wave propagation in layered environments will be determined by the terms of the continuity of E and H :

$$G_i(z_i) = G_{i+1}(z_{i+1}) \quad (2)$$

Given the continuity conditions (2) in [1] that the vectors $G_i(z_i)$ and $G_i(z_{i+1})$ are related as follows:

$$G_i(z_i) = M_i G_i(z_{i+1}) \quad (3)$$

or

$$G_i(z_i) = \begin{pmatrix} M_{11} & iM_{12} \\ iM_{21} & M_{22} \end{pmatrix} G_i(z_{i+1}) \quad (4)$$

The characteristic matrix M of i -layer provided homogeneity is [4, 9]:

$$M_i = \begin{pmatrix} \cos D_i & i \left(\frac{1}{u_i} \right) \sin D_i \\ i u_i \sin D_i & \cos D_i \end{pmatrix}, \quad (5)$$

where

$$u_i = \begin{cases} n_i \cos \varphi - s - \text{components,} \\ \frac{n_i}{\cos \varphi} - p - \text{components,} \end{cases} \quad (6)$$

$$D_i = \frac{2\pi}{\lambda} n_i d_i \cos \varphi_i \quad (7)$$

where λ is the wavelength of electromagnetic radiation; φ_i is the angle of refraction of a i -environment; s is the polarization component of the electric field in a perpendicular plane to the plane of incidence; p is the polarization component in the plane of incidence.

Owing to a condition of continuity (2) on limit of the section of two environments the transfer matrix through border is single.

The transfer matrix through all layered structure of M , according to [1, 9] presents work of characteristic matrixes of separate layers in it to M_i , starting with that on which the wave falls:

$$M = \prod_{i=1}^N M_i \quad (8)$$

The full matrix of transfer of layered structure, as shown in work [9] has an appearance:

$$W_{(N+1),0} = V_{N+1} M V_0^{-1} \quad (9)$$

where

$$V_i = \frac{1}{2} \begin{pmatrix} 1 & \frac{1}{u_i} \\ 1 & -\frac{1}{u_i} \end{pmatrix}, \quad V_i^{-1} = \begin{pmatrix} 1 & 1 \\ u_i & -u_i \end{pmatrix}. \quad (10)$$

Elements of a matrix W of layered structure are Fresnel amplitude coefficients of a transmission and reflection. For limit of the section between i and m layers the matrix of transfer is defined by a ratio:

$$W_{im} = \frac{c_{im}}{t_{im}} \begin{pmatrix} 1 & -r_{im} \\ r_{im} & d_{im} \end{pmatrix} \quad (11)$$

where

$$d_{im} = t_{im} t_{im} - r_{im} r_{im} \quad (12)$$

$$c_{im} = \begin{cases} 1 - s - \text{components,} \\ \cos \varphi_i - p - \text{components,} \\ \cos \varphi_m \end{cases} \quad (13)$$

where $t_{im}, r_{im}, r_{im}, r_{im}$ are respectively the amplitude transmission and reflection coefficients for a beam incident from the i -environment on the border with the m - environment.

Thus, on the basis of ratios (9) we find amplitude coefficients of a transmission and reflection of multilayered structure, using data about electromagnetic parameters and thickness of separate layers.

Energy monochromatic coefficients of a transmission of T_λ and R_λ reflections from a covering for unpolarized light according to [4, 9] are represented by ratios:

$$T_\lambda = \frac{n_2 \cos \varphi_2}{n_1 \cos \varphi_1} \left(\frac{|t_{\lambda s}|^2 + |t_{\lambda p}|^2}{2} \right), \quad (14)$$

$$R_\lambda = \left(\frac{|r_{\lambda s}|^2 + |r_{\lambda p}|^2}{2} \right), \quad (15)$$

where $r_{\lambda s}, r_{\lambda p}$ are the monochromatic Fresnel amplitude coefficients of reflection for s- and p-polarized light components from the coating; $t_{\lambda s}, t_{\lambda p}$ are the monochromatic Fresnel amplitude coefficients of transmission for s- and p-polarized light components; $\cos \varphi_1$ and $\cos \varphi_2$ are cosines of the angles formed by the

ray and the normal to the surface of the environment, with the refractive index n_1 and n_2 .

Value of $\cos \varphi_2$ is defined by the expression given [8]:

$$\cos \varphi_2 = \frac{1}{n_2} \sqrt{n_2^2 - n_1^2 \sin^2 \varphi_1} \quad (16)$$

On a basis above the presented ratios the algorithm of calculation in the program MATLAB environment is developed for power coefficients of a transmission and reflection of metal-dielectric structures.

The initial data for the calculation of dielectric structures with energy-saving properties apply values of the optical parameters of thin-film layers of copper and dielectric layers SiO_2 [7].

Results. Results of numerical modeling of spectral dependences of coefficients of reflection and transmission in the range from 0.3 to 3 microns of lengths of waves metal-dielectric structures with nanoscale layers of copper and anti-reflect layers on the basis of oxide of silicon (SiO_2 -Cu- SiO_2) are given in Fig. 1, 2 and 3.

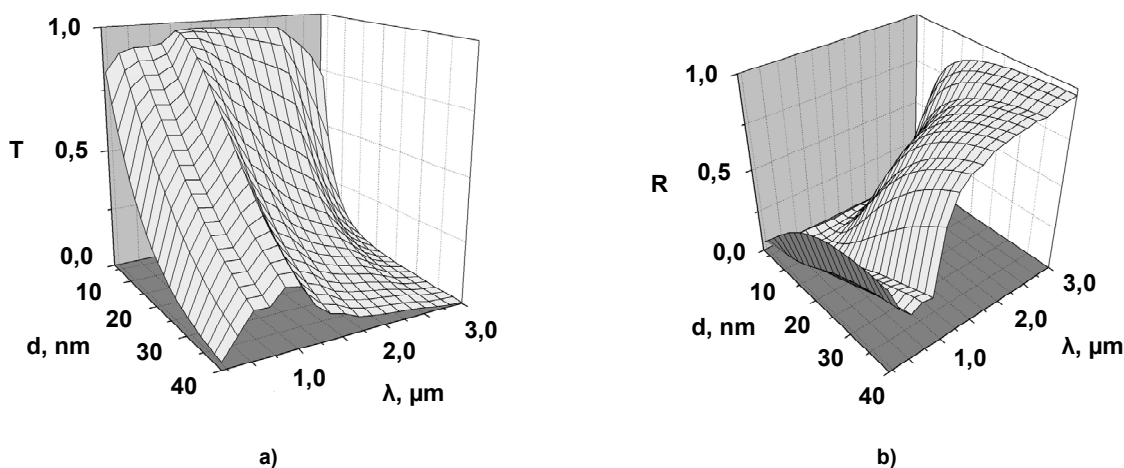


Fig. 1. Spectral dependence of coefficient of reflection of R (a) and coefficient of a transmission of T (b) of structure of SiO_2 -Cu- SiO_2 (the top layer of $\text{SiO}_2 = 50$ nanometers) at various values of thickness of a metal layer

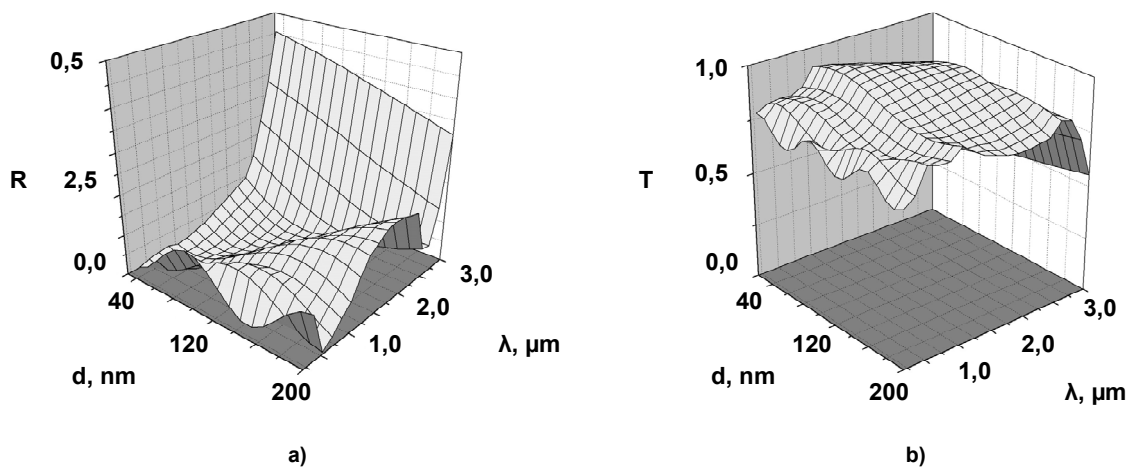


Fig. 2. Spectral dependence of coefficient of reflection of R (a) and coefficient of a transmission of T (b) of structure of SiO_2 -Cu- SiO_2 (Cu=4 nanometers) at various values of thickness of a dielectric layer

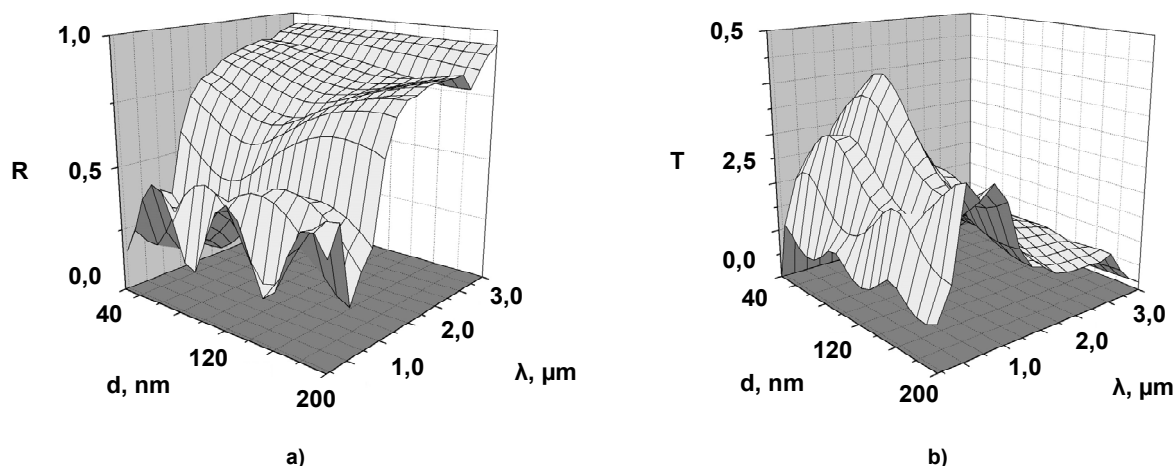


Fig. 3. Spectral dependence of coefficient of reflection of R (a) and coefficient of a transmission of T (b) of structure of $\text{SiO}_2\text{-Cu-SiO}_2$ (Cu=30 nanometers) at various values of thickness of a dielectric layer

Follows from Fig. 1 that in the spectral range of $0.3\div 0.7$ microns for copper layer thickness to 40 nanometers values of coefficient of reflection are observed low (to 0.2). Thus, in the spectral range over 2 microns for a copper layer more than 15 nanometers of value of coefficient of reflection increase to 0.9.

From Fig. 2 and 3 it is visible that change of thickness of the clarifying layer of SiO_2 doesn't lead to essential change of nature of spectral dependence of coefficient of reflection and a transmission.

Representation results show that changing parameters of structure of a metal-dielectric covering on the basis of copper it is possible to change values of coefficient of reflection and a transmission in the spectral range from 0.3 to 3 microns. The obtained results make it possible to determine the parameters of metal-dielectric structures to provide the necessary spectral-selective characteristics. Analysis of the results of numerical simulations show the possibility of using metal-dielectric structures based on copper as energy-saving coatings of various practical applications.

Structures of $\text{SiO}_2\text{-Cu-SiO}_2$ with nanoscale layers of copper up to 5 nanometers thick and with the clarifying layer to 170 nanometers can recommend to be used as energy saving low-issue coverings for a frigid climate (Fig. 2). And for copper thickness about 15 nanometers and with the clarifying layer of 50 nanometers – as energy saving low-issue coverings for warm climate (Fig. 1).

For structures with thickness of a nanoscale layer of copper of 30 nanometers it is characteristic values of coefficient of a transmission at the level about 0.5 in the spectral range of $0.3\div 0.76$ microns. It allows recommending for use such metal-dielectric structures as reflex coverings for warm climate (Fig. 3).

Conclusions. The computing algorithm of calculation of spectral dependences of coefficients of reflection and

transmission of nanocomposite coverings with metal and dielectric components on the basis of a method of matrixes of transfer is developed.

Numerical modeling of spectral characteristics of metal-dielectric structures on the basis of nanoscale films of copper with transparent dielectric layers is carried out.

Recommendations of practical application of metal-dielectric structures on the basis of nanoscale films of copper as transparent heat-reflecting filters in energy saving technologies are made.

REFERENCE:

1. Abeles F. Recherches sur la propagation des ondes electromagneticique sinusoidal dans les milieu stratifies / F. Abeles // Ann. Phys., 1950. – V.5. – P. 596–606.
2. Agnihotri O. Selektivnyye poverhnosti solnechnykh ustanovok / O. Agnihotri, B. Gupta. – M., 1984, 273 s.
3. Optical losses of multi component glasses for fibers and methods of their reduction / A. V. Anan'ev, V. N. Bogdanov, L. V. Maksimov et al. // Optics and Optoelectronics. Proc. SPIE. Warsaw. Poland. 2006. – Vol. 5951. – P. 59510E-1 – 59510E-9.
4. Born M. Osnovy optiki / M. Born, D. Volf – M.: Nauka, 1973. – 719 s.
5. Dietrich A. Bendable silver-based low emissivity coating on glass / A. Dietrich, K. Hartig, J. Szczyrbowski // Solar Energy Materials, 1989. – V.19. – P. 43–53.
6. High transmittance, low emissivity coating for substrates / E. Eby, S. Green et al. // U.S. Patent. № 5.302.449. Apr. 12. 1994.
7. Zolotarev V. M. Opticheskie postoyannyye prirodnykh i tehnikeskikh sred. / V. M. Zolotarev, V. N. Morozov, E. V. Smirnova. – L.: Himiya, Leningradskoe otdelenie, 1984. – 215 s.
8. Machulyanskiy A. V. Elektromagnitnyye karakteristiki nanokompozitov na osnove nanorazmernykh metallicheskih vklucheniyy / A. V. Machulyanskiy // Tehnichna elektrodinamika, 2012. – Ch.2. – S. 193–197.
9. Rozenberg G. V. Optika tonkosloynnykh pokrytiyy / G. V. Rozenberg. – M.: Nauka, 1958. – 570 s.
10. Tellen O. Konstruirovaniye mnogoslouynnykh interferentsionnykh svetofiltrov / O. Tellen // Fizika tonkih plenok / Pod red. G. Hassa., R.E.Tuna. T.5. – M.: Mir, 1972. – S. 46–83.

Submitted on 09.10.14

Мачулянський О., канд. техн. наук, Бабич Б., студ.,
каф. мікроелектроніки, факультет електроніки,
Національний технічний університет України "Київський політехнічний інститут"

ЕНЕРГОЗБЕРІГАЮЧІ НАНОКОМПЗИТНІ ПОКРИТТЯ НА ОСНОВІ МІДІ

Досліджено спектрально-селективні характеристики металодіелектричних нанокмпозитних покриттів на основі міді. Розроблено обчислювальний алгоритм визначення коефіцієнтів відбиття та пропускання нанокмпозитних металодіелектричних структур на основі міді в діелектричних матрицях SiO_2 . Виконано чисельне моделювання їх оптичних характеристик в спектральному діапазоні від 0,3 до 3 мкм для різних варіантів структур. Обговорюються можливості щодо практичної реалізації та застосування нанокмпозитних структур на основі міді в якості енергозберігаючих.

Ключові слова: металодіелектричні структури, спектрально-селективні характеристики, нанокмпозитні покриття, енергозбереження.

Мачулянський А., канд. техн. наук, Бабыч Б., студ.
 каф. мікроелектроніки, факультет електроніки,
 Національний технічний університет України "Київський політехнічний інститут"

ЭНЕРГОСБЕРЕГАЮЩИЕ НАНОКОМПОЗИТНЫЕ ПОКРЫТИЯ НА ОСНОВЕ МЕДИ

Исследованы спектрально-селективные характеристики металлodieлектрических нанокomпозитных покрытий на основе меди. Разработан вычислительный алгоритм определения коэффициентов отражения и пропускания нанокomпозитных металлodieлектрических структур на основе меди в диелектрических матрицах SiO₂. Выполнено численное моделирование их оптических характеристик в спектральном диапазоне от 0,3 до 3 мкм для различных вариантов структур. Обсуждаются возможности практической реализации и применения нанокomпозитных структур на основе меди в качестве энергосберегающих.

Ключевые слова: металлodieлектрические структуры, спектрально-селективные характеристики, нанокomпозитные покрытия, энергосбережения.

UDC 621.382:62-1/-9(045)

O. Melnyk, Ph.D., V. Kozarevych, Assist., A. Sobchenko, Stud.,
 Department Electronic, Institute of Air Navigation,
 National Aviation University of Kyiv

SYNTHESIS OF NANOELECTRONIC DEVICES WITH PROGRAMMABLE STRUCTURES

The synthesis of reliable programmable nanoelectronic devices based on the technology of quantum automata has been described. While constructing majority circuits of combinational and sequential types the theory of finite automats is using. The order of construction and programming of various types of arithmetic-logic devices has been analyzed.

Keywords: quantum nanodots, majority elements, field programmable gate array.

Introduction. The contradictions between specialization and universality can be eliminated through the development of field programmable gate array (FPGA), which algorithms of work can be changed at the request of the designer of a particular computer equipment, that is by creating the arithmetic logic circuits with programmable features.

Relevance of research. The development of theory and practice of using a majority principle is an urgent problem at present time, because the performance of nanoelectronic computing systems with programmable structures significantly reduces their cost and greatly simplifies the phase of automated circuit design. One programmable nanocircuit replaces from 30 to 150 integrated circuits with medium scale of integration.

Problem statement. The problem of developing the design principles of the reliable computer technology is very important nowadays. Application of mathematical and circuit analysis along with computer aided design can significantly improve the reliability of designing devices.

Main material. The most promising area of nanoelectronics is creation of multi-functional subsystems when one module combines a large number of logic elements into a single functional unit, intended to implement complex logic functions. These subsystems must satisfy the following basic requirements:

- have a minimum number of external connections;
- have a hardware compatibility;
- use the same type of cells if it is possible;
- have a property extension, that is to have a flexible structure.

To implement systems with variable structure (adaptive system), besides, it needs to be able to programmatically change the technical parameters of the subsystems during or before work. In terms of cheapening of nanoelectronic subsystems and improving the reliability of their work they should be performed on the same type of cells with the same configuration of connections between cells [1].

Programmable nanoelectronic device, which consists of three universal majority elements (UME), duly connected to each other (fig. 1), can be used as such cell to build majority adaptive systems (MAS). Informational (x_3, x_2, x_1, x_0) and control signals (r_2, r_1, r_0) are submitted to the inputs of UME [2].

With the help of FPGA of this type all the functions of two or three arguments can be implemented, including functions of sum, difference, carry and loan, functions of one, two and three memory elements, and some functions

of four or five arguments. The feature of FPGA is that its logical possibilities and connections may be changed by the program that allows it to be used for constructing of MAS. The most important functions in majority basis, implemented on the base of FPGA, are shown in table 1.

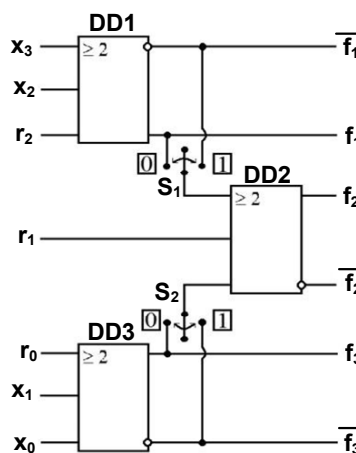


Fig.1. Block diagram of a universal programmable nanoelectronic device

FPGA is a functionally complete unit, because in its composition are functionally complete UME.

Synthesis of majority systems on the base of FPGA is recommended to do according to the following order:

1. The boolean functions, which are specified or obtained, are presented in majority basis.
2. The minimization of obtained majority function is performed.
3. The row, which is equivalent to the minimum form of the majority function, is sought in table 1.
4. A block diagram of the given subsystem is created, considering the opportunities of UME and specified number of inputs.

The functioning of the systems on quantum cellular automata (QCA) is based on the interaction of Coulomb forces of quantum dots for performing logic functions. They are designed to reduce the use of transistors and to solve the problems of density and connection of devices. The cellular automata consists of grouped quantum dots, connected with tunnel junctions and capacitors. Quantum

dots are regions of low potential, which are surrounded by a ring of high potential. There are several methods of their formation, but the most common ones is metallization. In cellular automata four quantum dots are placed in the corners of a square. Each automata contains two

electrons, which are placed diagonally, because of the action of Coulomb repulsion forces, in opposite corners (fig. 2). Two possible location of these electrons are marked as polarization of cells $P = -1$ and $P = +1$ [1].

Table 1

Examples of the most important functions that can be implemented on FPGA

No	r_2	r_1	r_0	f_1	f_2	f_3	Numb. of output func.
1	0	0	0	$\text{maj}(x_3, x_2, 0)$	$\text{maj}(x_3 x_2, x_1 x_0, 0)$	$\text{maj}(x_1, x_0, 0)$	24
2	0	0	1	$\text{maj}(x_3, x_2, 0)$	$\text{maj}(x_3 x_2, x_1 \vee x_0, 0)$	$\text{maj}(x_1, x_0, 1)$	24
3	0	1	0	$\text{maj}(x_3, x_2, 0)$	$\text{maj}(x_3 x_2, x_1 x_0, 1)$	$\text{maj}(x_1, x_0, 0)$	24
4	0	1	1	$\text{maj}(x_3, x_2, 0)$	$\text{maj}(x_3 x_2, x_1 \vee x_0, 1)$	$\text{maj}(x_1, x_0, 1)$	24
5	1	0	0	$\text{maj}(x_3, x_2, 1)$	$\text{maj}(x_3 \vee x_2, x_1 x_0, 0)$	$\text{maj}(x_1, x_0, 0)$	24
6	1	0	1	$\text{maj}(x_3, x_2, 1)$	$\text{maj}(x_3 \vee x_2, x_1 \vee x_0, 0)$	$\text{maj}(x_1, x_0, 1)$	24
7	1	1	0	$\text{maj}(x_3, x_2, 1)$	$\text{maj}(x_3 \vee x_2, x_1 x_0, 1)$	$\text{maj}(x_1, x_0, 0)$	24
8	1	1	1	$\text{maj}(x_3, x_2, 1)$	$\text{maj}(x_3 \vee x_2, x_1 \vee x_0, 1)$	$\text{maj}(x_1, x_0, 1)$	24
9	0	0	x_4	$\text{maj}(x_3, x_2, 0)$	$\text{maj}(x_3 x_2, \text{maj}(x_1, x_0, x_4), 0)$	$\text{maj}(x_1, x_0, x_4)$	44
10	0	x_4	0	$\text{maj}(x_3, x_2, 0)$	$\text{maj}(x_3 x_2, x_1 x_0, x_4)$	$\text{maj}(x_1, x_0, 0)$	40
11	0	x_4	x_5	$\text{maj}(x_3, x_2, 0)$	$\text{maj}(x_3 x_2, \text{maj}(x_1, x_0, x_5), x_4)$	$\text{maj}(x_1, x_0, x_5)$	76
12	x_4	0	0	$\text{maj}(x_3, x_2, x_4)$	$\text{maj}(\text{maj}(x_3, x_2, x_4), x_1 x_0, 0)$	$\text{maj}(x_1, x_0, 0)$	44
13	x_4	0	x_5	$\text{maj}(x_3, x_2, x_4)$	$\text{maj}(\text{maj}(x_3, x_2, x_4), \text{maj}(x_1, x_0, x_5), 0)$	$\text{maj}(x_1, x_0, x_5)$	48
14	x_4	x_5	0	$\text{maj}(x_3, x_2, x_4)$	$\text{maj}(\text{maj}(x_3, x_2, x_4), x_1 x_0, x_5)$	$\text{maj}(x_1, x_0, 0)$	76
15	x_4	x_5	x_6	$\text{maj}(x_3, x_2, x_4)$	$\text{maj}(\text{maj}(x_3, x_2, x_4), \text{maj}(x_1, x_0, x_6), x_5)$	$\text{maj}(x_1, x_0, x_6)$	80
16	1	f_2	0	$\text{maj}(x_3, x_2, 1)$	$\text{maj}(x_3 \vee x_2, x_1 x_0, f_2)$	$\text{maj}(x_1, x_0, 0)$	Trigger with control inputs
17	f_1	0	f_3	$\text{maj}(x_3, x_2, f_1)$	$\text{maj}(\text{maj}(x_3, x_2, f_1), \text{maj}(x_1, x_0, f_3), 0)$	$\text{maj}(x_1, x_0, f_3)$	Two triggers
18	f_1	f_2	f_3	$\text{maj}(x_3, x_2, f_1)$	$\text{maj}(\text{maj}(x_3, x_2, f_1), \text{maj}(x_1, x_0, f_3), f_2)$	$\text{maj}(x_1, x_0, f_3)$	Three triggers
19	f_2	f_2	\bar{f}_2	$\text{maj}(x_3, x_2, f_2)$	$\text{maj}(\text{maj}(x_3, x_2, f_2), \text{maj}(x_1, x_0, \bar{f}_2), f_2)$	$\text{maj}(x_1, x_0, \bar{f}_2)$	Accum. adder

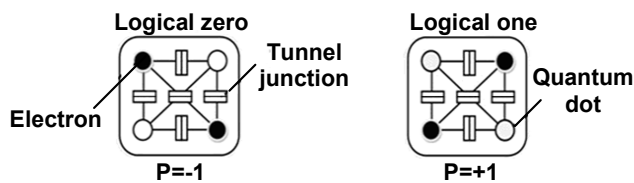


Fig. 2. Quantum cells in states of logical zero and logical one

In table. 1 $x_6, x_5, x_4, x_3, x_2, x_1, x_0$ – input informational signals, represented either in direct or inverse code; r_2, r_1, r_0 – control signals; f_3, f_2, f_1 – output signals.

Let us synthesize the function of logical adding of four arguments, using aided design system QCA Designer [3]:

$$f_2 = \text{maj}(x_3 \vee x_2, x_1 \vee x_0, 0), \quad (1)$$

which corresponds to the majority equivalent in the sixth row in table. 1.

Functions of logical addition of two of the four arguments are formed on two additional outputs of FPGA:

$$f_1 = x_3 \vee x_2 = \text{maj}(x_3, x_2, 1), \quad (2)$$

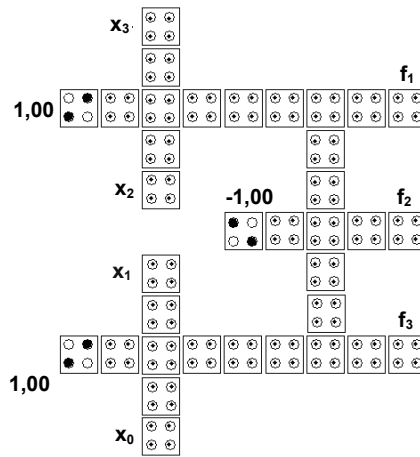
$$f_3 = x_1 \vee x_0 = \text{maj}(x_1, x_0, 1). \quad (3)$$

Simulation results. To program the functions (1), (2) and (3) keys S_1 and S_2 in block diagram of FPGA (fig. 1.) must be set in the state 0, and the programmable inputs must be set in the polarizations $+P = 1$ for $r_2 = r_0 = 1$, and polarizations $-P = -1$ for $r_0 = 0$ [2].

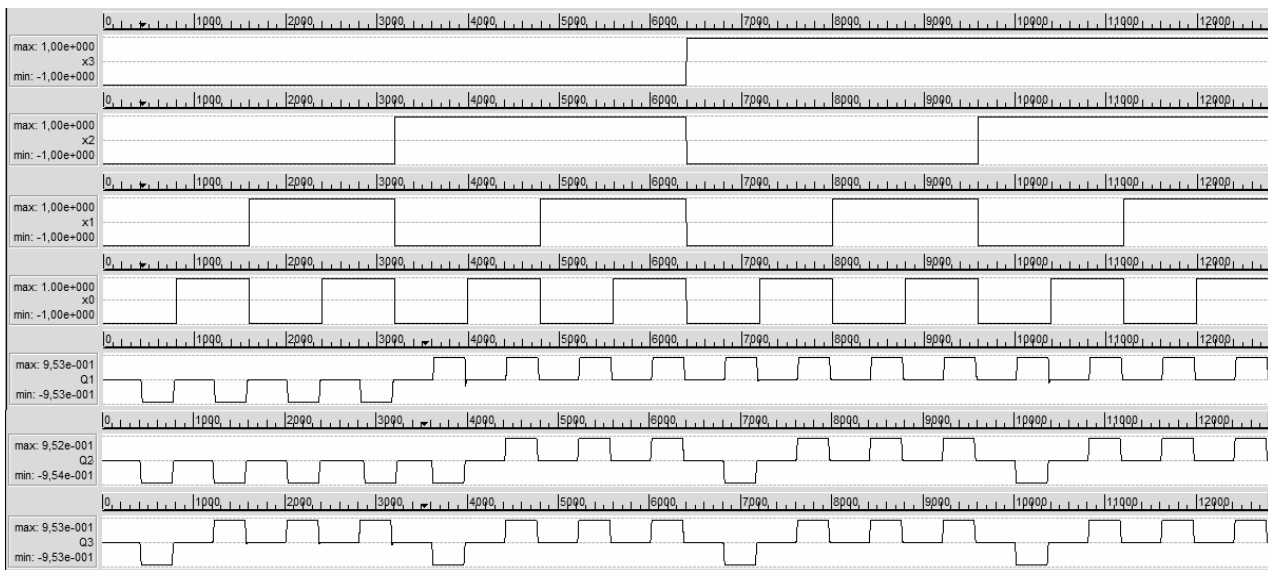
The fig. 3, a shows a block diagram of FPGA, which is built on the working field of QCA Designer [3]. It consists of 55 quantum cells, which have size 18×18 nm, with 4 quantum dots about 5 nm in diameter and 20 nm distance between their centers. The total size of FPGA is (198×218) nm. It has four informational inputs x_3, x_2, x_1 and x_0 , three programmable inputs with polarizations $+P = 1$ and $-P = -1$, and three pairs of complementary outputs f_1, f_2 and f_3 .

The results of computer-aided design of FPGA time characteristics are shown on fig. 3, b. Positive pulses correspond to positive polarizations $+P = 1$, and negative – negative polarizations $-P = 0$. The corresponding truth table of FPGA for this programming mode is shown in table 2.

With the change of polarization of the inputs r_2, r_1, r_0 and set the keys S_1 and S_2 in different positions FPGA with seven inputs (fig. 1) can be programmed for 192 logical functions of two and four inputs combinational circuits.



a)



b)

Fig. 3. Computer-aided design of combinational FPGA on QCA

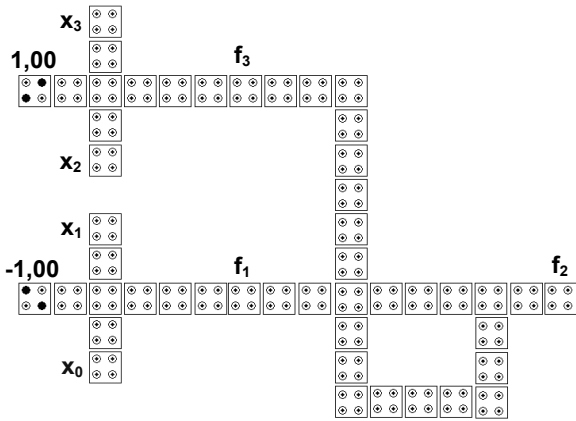
Table 2
Truth table of functions $\text{maj}(x_3, x_2, x_1, x_0, 0)$

x_3	x_2	x_1	x_0	f_1	f_2	f_3
0	0	0	0	0	0	0
0	0	0	1	0	0	1
0	0	1	0	0	0	1
0	0	1	1	0	0	1
0	1	0	0	1	0	0
0	1	0	1	1	1	1
0	1	1	0	1	1	1
0	1	1	1	1	1	1
1	0	0	0	1	0	0
1	0	0	1	1	1	1
1	0	1	0	1	1	1
1	0	1	1	1	1	1
1	1	0	0	1	0	0
1	1	0	1	1	1	1
1	1	1	0	1	1	1
1	1	1	1	1	1	1

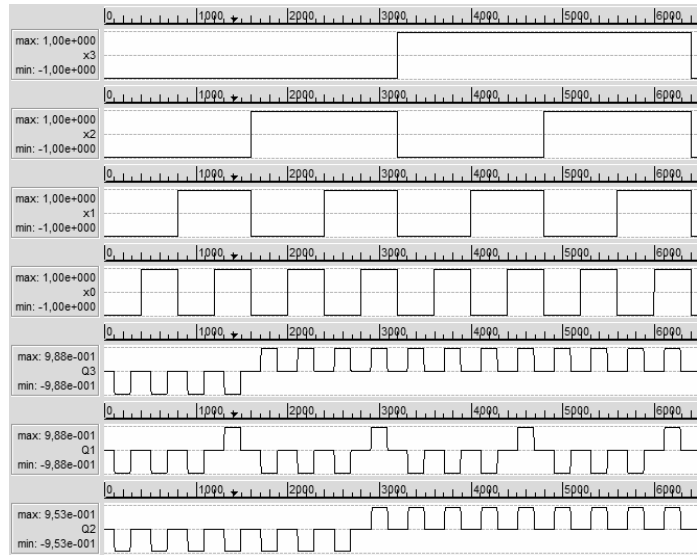
With the change of polarization of the inputs r_2, r_1, r_0 and set the keys S_1 and S_2 in different positions FPGA with seven inputs (fig. 1) can be programmed for 192 logical functions of two and four inputs combinational circuits.

Now lets synthesize the circuit for the 16th row of the table 1, which consists of two majority elements with separate inputs x_3, x_2 and x_1, x_0 . Direct outputs f_1 and f_3 of these majority elements are combined into RS-triggers, covered with feedback f_2 (fig. 1). On fig. 4, a built this sequential nanoelectronic circuit in the form of QCA Designer, and the results of time simulation are shown on fig. 4, b. It has a size (350x240) nm and consists of 48 quantum dot automatas.

The results of computer-aided design of FPGA time characteristics are shown on fig. 3, b. Positive pulses correspond to positive polarizations $+P=1$, and negative – negative polarizations $-P=0$. The corresponding truth table of FPGA for this programming mode is shown in table. 2.



a)



b)

Fig. 4. Computer-aided design of sequential FPGA on QA

Verification table of FPGA states are given in table 3.

Table 3

Truth table of functions $maj(maj(x_3, x_2, 1), maj(x_1, x_0, 0), f_2)$

x_3	x_2	x_1	x_0	f_1	f_2	f_3
0	0	0	0	0	0	0
0	0	0	1	0	0	0
0	0	1	0	0	0	0
0	0	1	1	0	0	1
0	1	0	0	1	0	0
0	1	0	1	1	0	0
0	1	1	0	1	0	0
0	1	1	1	1	1	1
1	0	0	0	1	1	0
1	0	0	1	1	1	0
1	0	1	0	1	1	0
1	0	1	1	1	1	1
1	1	0	0	1	1	0
1	1	0	1	1	1	0
1	1	1	0	1	1	0
1	1	1	1	1	1	1

Conclusions. In the nearest ten years semiconductor components of big integrated circuits will achieve quantum technological limitations and will not meet the increasing performance requirements of computer technology. Therefore, new nanotechnologies are developing so actively, that would provide significantly higher performance. One of such developments is the quantum cellular automata and created on its basis systems with programmable structures. As shown above, such devices will provide realization of full system of logic functions for both combinational and sequential arithmetical and logical computing devices.

REFERENCE:

1. Melnyk O. S. Synthesis programmable nanoelectronic divaces / O.S. Melnyk, S. V. Todavchych // Electronics and Control systems – 2013. – P. 89–94.
2. Pakulov N. I Majoritary principle design of reliable devices of computer / N.I. Pakulov, V.F. Uhanov, P.N. Chernyshov // Moscow: Sov. Radio, 1974. - 184 p. (in Russian).
3. Walus K. QCA Designer: A Rapid Design and Simulation Tool for QCA / K. Walus // Internet journal of Nanotech. and Appl. – 2005. – Vol. 2 – № 1 – P. 1–7.

Submitted on 29.10.14

Мельник О., канд. техн. наук, доц., Козаревич В., асист., Собченко А., студ., каф. електроніки, Інститут аеронавігації, Національний авіаційний університет

СИНТЕЗ ПРОГРАМОВАНИХ НАНОЕЛЕКТРОННИХ ПРИСТРОЇВ

Описаний синтез надійних програмованих наноелектронних пристроїв на базі технології квантових автоматів. При побудові мажоритарних схем комбінаційного та послідовностного типів використовується теорія кінцевих автоматів. Проаналізовано порядок побудови та програмування різних типів арифметико-логічних пристроїв.

Ключові слова: квантові автомати; мажоритарні елементи; логічні елементи, програмовані користувачем.

Мельник А., канд. техн. наук, доц., Козаревич В., ассист., Собченко А., студ., каф. електроніки, Институт аэронавигации, Национальный авиационный университет

СИНТЕЗ ПРОГРАММИРУЕМЫХ НАНОЭЛЕКТРОННЫХ УСТРОЙСТВ

Описан синтез надежных программируемых нанозлектронных устройств на базе технологии квантовых автоматов. При построении мажоритарных схем комбинационного и последовательностного типов используется теория конечных автоматов. Проанализированы порядок построения и программирования различных типов арифметико-логических устройств.

Ключевые слова: квантовые автоматы; мажоритарные элементы; логические элементы, программируемые пользователем.

UDC 53.082.77

S. Miroshnichenko, Dr. Sc., Teleoopic PRA
 O. Motolyga, post. grad. stud., Physics Faculty,
 Taras Shevchenko National University of Kyiv,
 A. Nevgasimii, Ph.D., Teleoopic PRA

S. Senchurov, Ph.D., Physics Faculty, Taras Shevchenko National University of Kyiv

**THEORETICAL ESTIMATION OF THE RECONSTRUCTED SLICE THICKNESS
 IN DIGITAL TOMOSYNTHESIS**

The theoretical estimation of the dependence of the digital tomosynthesis reconstructed slice thickness on the sweep angle is presented. The dependence of the slice thickness on the in-plane object size is shown.

Keywords: Digital X-ray tomosynthesis, Slice thickness, Biomedical imaging.

Introduction. Digital tomosynthesis is one of the emerging technologies in medical imaging. It allows the reasonable compromise between image quality, 3D reconstruction and patient dose. Today on market are several models of digital tomosynthesis equipment, mainly general purpose tomosynthesis equipment and mammographic tomosynthesis equipment.

Present study deals with general purpose digital tomosynthesis equipment. Table 1 summarizes some characteristics of equipment.

Table 1

**Electromechanical characteristics
 of general purpose digital tomosynthesis equipment**

Model/ Manufacturer	Number of projection images	Angular scan range, degrees	Source-to- detector distance SID, cm	Anode voltage, kV
General Electric Definium 8000/ VolumeRAD	60	±15°	180	120
Shimadzu SoniaVision Safire	75	±20°	180	120
Amico FluoroProGraf 7000	30...60	±20°	120	70...90

Characteristics of mammographic tomosynthesis equipment are summarized in [1, 2].

Technically there is possibility to use numerous variants of X-ray tube and digital receptor movement and variety of the reconstruction algorithms. During the design of the digital tomosynthesis system we need some estimations of the relationship between the angular scan range, number of projection images, and the reconstruction quality. The aim of our study is to obtain corresponding theoretical dependencies.

Tomosynthesis slice thickness and angular scan range. There are at least two approaches to calculate slice thickness depending on the angular scan range. Both of them give similar results. First approach is derived from the Radon transform and central slice theorem and is discussed in [1, 2]. Slice thickness is calculated from the Fourier space.

We will use normal space to calculate the slice thickness. The idea of slice thickness calculation is given in Figure 1. We assume, that

1. Incident X-rays are collimated to parallel;
2. There is no divergence of a single X-ray;
3. X-ray source is a point-like source;
4. Reconstruction is done by a simple backprojection algorithm.

Slice thickness is assumed the distance between reconstructed planes, where the intensity of the in-plane object decreases two times.

From the simple geometrical consideration we derive the following relation for the slice thickness h :

$$h = \frac{d}{2 \operatorname{tg} \gamma} \tag{1}$$

The most interesting conclusion from this equation is than slice thickness depends on the size of the in-plane object. So the slice thickness of large objects is bigger than thickness of small ones. This conclusion corresponds to results, obtained in [1, 2].

The physical nature for this result is that the projection angular range is less than π .

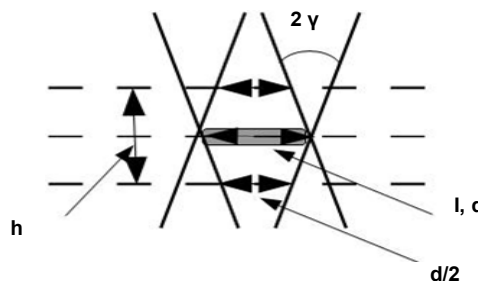


Fig. 1. Calculation of the slice thickness of the tomosynthesis object. Backprojection algorithm is used. Gray rectangle denotes the planar reconstructed object. d is size of the object in tomosynthesis plane, I is the intensity of the reconstructed in-plane object, 2γ is angular scan range, h is the slice thickness

Number of projections and number of voxels. Another problem which appears during the design of the tomosynthesis system is the relation between the number of voxels and the number of projections. The situation is illustrated by Figure 2. A group of voxels is projected vertically (Projection 1) and at a minimal angular interval (Projection 2). The densities of neighbouring black and white voxels, which superpose in Projection 1, in Projection 2 can be distinguished only if corresponding shadows cover different pixels.

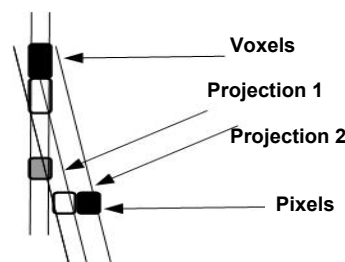


Fig. 2. Calculation of the minimal angular scanning interval

This means that if v is the voxel height or slice thickness, b is the projection pixel dimension and $\Delta\gamma$ is the minimal angular scanning interval, than

$$v = \frac{b}{\operatorname{tg} \Delta\gamma} \quad (2)$$

If H is the total height of the reconstructed volume, then the number of voxels should be

$$N_{\text{vox}} = \frac{H}{h} N_{\text{pix}} = \frac{H}{b} \operatorname{tg} \Delta\gamma N_{\text{pix}}, \quad (3)$$

where N_{pix} is a number of pixels in projection.

On the other hand, in algebraic reconstruction technique to calculate the X-ray densities of N_{vox} different voxels, we need at least the equivalent number of equations. When the total angular scanning range is 2γ , the corresponding number of equations is

$$N_{\text{eq}} = N_{\text{pix}} \frac{2\gamma}{\Delta\gamma} = N_{\text{pix}} N_{\text{proj}}, \quad (4)$$

where N_{proj} is the total number of projections. From equations **Ошибка! Источник ссылки не найден.**, **Ошибка! Источник ссылки не найден.** and **Ошибка! Источник ссылки не найден.**, we obtain

$$N_{\text{proj}} \geq \frac{H}{v} \quad (5)$$

For instance, if we take angular scanning range $2\gamma = 90^\circ$, $b = 0.25 \text{ mm}$ which corresponds 2 lp/mm , and $\Delta\gamma = 1^\circ$, then $h \approx 14 \text{ mm}$ and for $H = 200 \text{ mm}$ minimum number of projections, needed for reconstruction, is about 14. Making more projections decreases the relative noise and increases patient dose.

Conclusions. The relationship between the angular scan range and the tomosynthesis slice thickness obtained. Slice thickness appears to be proportional to the in-plane object dimension. The number of projections necessary for the reconstruction of the given number of voxels was calculated. Number of projections is inverse proportional to the projection pixel size.

REFERENCE:

1. Image Artifact in Digital Breast Tomosynthesis and Its Dependence on System and Reconstruction Parameters / Yue-Houng Hu, Wei Zhao, Thomas Mertelmeier and Jasmina Ludwig // Digital Mammography. Proc. 9th International Workshop, IWDM 2008 Tucson, AZ, USA, July 20–23, 2008, pp 628–634.
2. Yue-Houng Hu. Image artifacts in digital breast tomosynthesis: Investigation of the effects of system geometry and reconstruction parameters using a linear system / Yue-Houng Hu, Bo Zhao, Wei Zhao // Medical Physics – 2008 – V. 35(12): 5242–5252.

Submitted on 07.11.14

Мірошніченко С., д-р техн. наук, НВО Телеоптик,
Мотоліга О., асп., каф. молекулярної фізики, фізичний факультет,
Київський національний університет імені Тараса Шевченка,
Невгасимий А., канд. техн. наук, НВО Телеоптик, Сенчуров С., канд. фіз.-мат. наук,
каф. молекулярної фізики, фізичний факультет,
Київський національний університет імені Тараса Шевченка

ТЕОРЕТИЧНА ОЦІНКА ТОВЩИНИ РЕКОНСТРУЙОВАНОГО ЗРІЗУ ПРИ ЦИФРОВОМУ ТОМОСИНТЕЗІ

Представлено теоретичну оцінку залежності товщини реконструйованого зрізу при цифровому томосинтезі від куту розвороту. Показано залежність товщини зрізу від розміру об'єкту в площині зрізу.

Ключові слова: Цифровий рентгенівський томосинтез, товщина зрізу, медичні зображення.

Мирошниченко С., д-р техн. наук, НПО Телеоптик,
Мотолыга А., асп., каф. молекулярной физики, физический факультет,
Киевский национальный университет имени Тараса Шевченко,
Невгасимый А., канд. техн. наук, НПО Телеоптик, Сенчуров С., канд. физ.-мат. наук,
каф. молекулярной физики, физический факультет,
Киевский национальный университет имени Тараса Шевченко

ТЕОРЕТИЧЕСКАЯ ОЦЕНКА ТОЛЩИНЫ РЕКОНСТРУИРОВАННОГО СРЕЗА ПРИ ЦИФРОВОМ ТОМОСИНТЕЗЕ

Представлено теоретическую оценку толщины реконструированного среза при цифровом томосинтезе в зависимости от угла разворота. Показано зависимость толщины среза от размера объекта в плоскости среза.

Ключевые слова: Цифровой рентгеновский томосинтез, толщина среза, медицинские изображения.

УДК 620.18:546.28

N. Nakhodkin, Dr. Sc., Prof., acad. of NAS of Ukraine,
N. Kulish, Dr. Sc., Prof., Member of NAS of Ukraine, Taras Shevchenko National University of Kyiv
P. Lytvyn, Ph.D., Lashkaryov Institute of Semiconductor Physics, National Academy of Sciences of Ukraine
T. Rodionova, Ph.D., A. Sutyagina., stud., Taras Shevchenko National University of Kyiv

SPECIAL JOINTS OF GRAIN BOUNDARIES IN NANOSILICON FILMS WITH EQUIAXED AND FIBROUS STRUCTURES

Atomic force microscope was used for investigation of grain boundaries joints in undoped nanosilicon films. It was shown that in films with equiaxed and fibrous structure joints differ in the number and mutual arrangement of special boundaries $\Sigma = 3^n$ and of the general type boundaries.

Key Words: nanosilicon films; structure; joints of grain boundaries

Introduction. Nanosilicon films are one of the leading electronic materials for large-area application as solar cells or switching electronics used for flat-panel displays. As is known [3, 8], the characteristics of the electronic devices that use nanosilicon films are directly connected with the structural properties of the films, in particular, their grain boundary and grain boundary joints. Grain boundary joints in

a polycrystalline microstructure correspond to the one-dimensional regions of space where three or more grain boundaries meet. In total volume of nanocrystalline material part of the grain boundaries and joints of grain boundaries is $\geq 50\%$. It is evident that the joints influence the film structure formation and properties of the films. This effect is different for various joints and is structure-dependent.

© Nakhodkin N., Kulish N., Lytvyn P., Rodionova T., Sutyagina A., 2014

Of particular interest is the investigation of special grain boundary joints that result from interaction of special grain boundaries. These joints possess a low energy, weak trend to impurity adsorption, low diffusive penetration and so on. As compared to joints of general type, the special joints are more stable, because mobility of special grain boundaries is low [2].

It is well known [5] that in thick polysilicon films (≥ 500 nm), relative amount of special joints is defined by the film structure type (equiaxed, dendritic, fibrous). As for undoped nanosilicon films, in previous studies it has been shown [4] that there are two structural modification of nanosilicon films, depending on their thickness, namely, equiaxed (at thickness < 70 nm) and fibrous (at thickness ≥ 70 nm). It is reasonably to suggest that grain boundary structures of these films are different.

In this work grain boundaries joints in undoped equiaxed and fibrous nanosilicon films were investigated by atomic force microscope (AFM)

Experimental procedure. Nanosilicon films were prepared by low-pressure chemical vapour deposition from a silane/argon mixture. Films were deposited on thermally oxidized (100) single-crystal silicon wafers. The deposition temperature was equal to 630°C . The film thickness was ranged from 3 to 100 nm.

AFM has been used to obtain a set of statistical data in studies of grain boundary joints. The film surface images

were obtained using a scanning atomic force microscope NanoScope IIIa in the periodic contact mode.

Joints attributed to one or another type, depending on the joint configuration and, more importantly, depending on the angles between grain boundaries that form the joint. The values of angles were compared with the values of the angles between the corresponding crystallographic planes [9] and the values of the angles between the twins of different orders [2] in the face-centered cubic lattice.

Results and Discussion. AFM studies show that several types of triple and multiple joints are observed in nanosilicon films. These joints differ by grain boundary orientation.

AFM-images and corresponding schematic drawing in Table 1 show several types of triple grain boundary joints in nanosilicon films. The following types of triple joints were observed:

1. 3a joint is a contact of three grain boundaries of general type (GBGT). Dihedral angles between boundaries can be arbitrary, and in equilibrium state close to 120° .

2. 3b joint is a contact of two GBGT grain boundaries and twin boundary $\Sigma=3$ (Σ is the inverse density of coincidence sites in the coincidence site lattice (CSL) [5]). Dihedral angles between GBGT boundaries close to 180° .

3. 3c joint is a contact of three coherent twin boundaries $\Sigma=3^n$. This joint is discussed in detail in [6].

Table 1

Types of triple joints in nanosilicon films

Joints type	3a	3b	3c
AFM-images			
Schematic drawing			
<p>— grain boundaries of the general type (GBGT); special grain boundaries (Σ)</p>			

Table 2

Types of multiple joints in nanosilicon films

Joint type	4a	4b	4c	5d
AFM images				
Schematic drawing				
<p>— grain boundaries of the general type (GBGT); special grain boundaries (Σ)</p>				

Joints, in which four or more grain boundaries meet (multiple joints), were considered in [2,5] for metals and thick (thickness ≥ 500 nm) polysilicon films, respectively. Table 2 represents AFM-images and corresponding schematic drawing of multiple joint types for nanosilicon films. The following types of multiple joints were observed:

1. 4a joint is a contact of three GBGT boundaries and twin boundary $\Sigma = 3$. In this case the line of joint lies along the close-packed directions [110], [211], [321].

2. 4b joint is a contact of two GBGT grain boundaries and two coherent twin boundaries $\Sigma = 3$. As bypassing the joint following alternation takes place: $GBGT_1 \rightarrow \Sigma = 3_1 \rightarrow \Sigma = 3_2 \rightarrow GBGT_2$. Joint line is always lies along the [110] direction, which is the intersection of the {111} planes of coherent twin boundaries $\Sigma = 3_1$ and $\Sigma = 3_2$. Dihedral angle between the boundaries $\Sigma = 3$ is 70.5° , or 109.5° . The angle between the $GBGT_1$ and $GBGT_2$ boundaries is generally much less than 180° .

3. 4c joint is a contact of two GBGT grain boundaries and two coherent twin boundaries $\Sigma = 3$. However, unlike the junction 4b, alternation of boundaries another: $GBGT_1 \rightarrow \Sigma = 3 \rightarrow GBGT_2 \rightarrow \Sigma = 3$. Dihedral angle between the $\Sigma = 3$ boundaries can be arbitrary. Joint line strictly coincides with the [211], [321], [431], but [110] direction never found.

4. 5d joint. The interaction between the boundaries $\Sigma = 3^n$ creates joints of five boundaries 5d, among which the most widespread is: $\Sigma = 3 \rightarrow \Sigma = 3 \rightarrow \Sigma = 3 \rightarrow \Sigma = 3 \rightarrow \Sigma = 81$. 5d joints line is always lies along the direction [110], which is common to all boundaries in joint [5].

Analysis of AFM images shown that the relative number of various types of grain boundary joints changes under transformation from equiaxed film structure to fibrous. Fig. 1 shows the changes in the relative number of triple and multiple joints with increasing the film thickness from 10 nm to 100 nm. As is seen from the Fig. 1, for all films thickness that was tested, the number of triple junctions dominates. Analysis of statistical data shows that at the early stages of film growth ($d = 100$ nm), the relative number of multiple joints of all types is only 15% (Fig. 1). As shown above (Table. 1 and Table 2), triple and multiple joints differ from one another by the number of boundaries of general type and special ($\Sigma = 3^n$) boundaries. Fig. 2 shows the thickness dependence of

relative number of different types of triple and multiple joints. With film thickness increasing number of special boundaries increases and the boundaries of general type is reduced. Thus, the decrease of free surface energy under film growth is not only by reducing the surface area of the grain boundaries, but also by the quality of the boundaries. Primarily disappear boundaries of general type, which have a high specific surface energy, and special boundary are the longer, the lower their energy [1] We can assume that this increasing in the relative number of special boundary $\Sigma = 3^n$ causes the increase in the number of joints of special type 3b and 3c, as well as multiple joints of all types. It can be assumed that the increasing in the relative number of chance meeting of special boundaries between themselves and with the boundaries of the general type leads to an increasing in the relative number of special multiple joints. For films with a thickness of 50 nm it is 35 %.

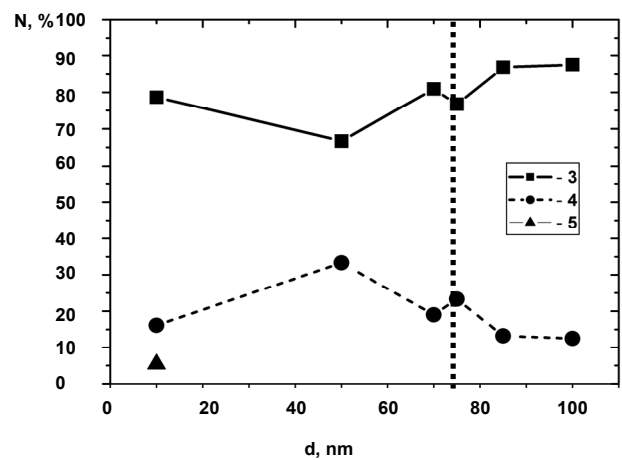
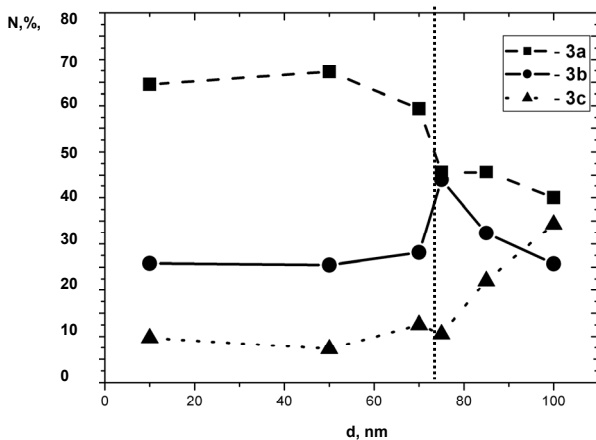
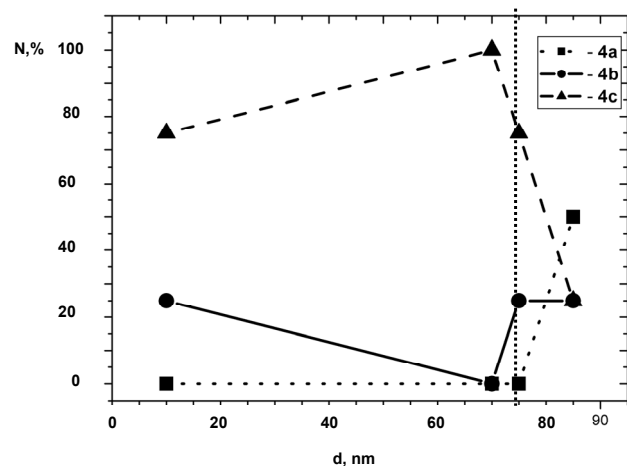


Fig. 1. The relative number of triple and multiple grain boundaries joints in nanosilicon films, depending on the film thickness (dashed line separates the areas of film thickness of equiaxed ($d < 70$ nm) and fibrous ($d \geq 70$ nm) structures)



a



b

Fig. 2. The relative number of different types of triple (a) and multiple (b) grain boundaries joints in nanosilicon films, depending on the film thickness (dashed line separates the areas of film thickness of equiaxed ($d < 70$ nm) and fibrous ($d \geq 70$ nm) structures)

Attention is drawn to the fact that in equiaxed nanosilicon films (film thickness < 70 nm) joint lines lie along different directions, in particular, [211], [321], [431], [110]. This correlates with the absence of texture in these films. At the same time, in fibrous films (thickness ≥ 70 nm) joint lines always coincide with the direction [110], which correlates with the presence of preferred orientation [110] in these films [7].

Conclusions

1. Triple and multiple joints of grain boundaries are observed in nanosilicon films. Crystallographic classification of multiple joints carried out.

2. As triple and multiple grain boundaries joints are divided in joints of general type and special joints.

3. There are several types of special grain boundaries joints, which differ in the number and mutual arrangement of special boundaries $\Sigma = 3^n$.

4. In films with equiaxed structure (thickness < 70 nm) joint lines lie along different directions, in particular, [211] [321] [431] and [110] that corresponds to a disordered film structure.

5. In films with fibrous structure (thickness ≥ 70 nm) joint lines coincide that correlates with the presence of texture [110] in these films.

REFERENCE:

1. Dillon S. J. Mechanism for the development of anisotropic grain boundary character distributions during normal grain growth / S. J. Dillon, G. S. Rohrer // *Acta Materialia*, 2009. – Vol. 57. – P. 1–7.
2. Kopetsky Ch. V. Grain boundaries in pure materials / Ch. V. Kopetsky, A. N. Orlov, L. K. Fionova – Moscow: Nauka, 1987. – 158 p. [in Russian].
3. Mukhopadhyay S. Nanocrystalline silicon: A material for thin film solar cells with better stability / S. Mukhopadhyay, A. Chowdhury, S. Ray // *Thin Solid Films*, 2008. – Vol. 516, Issue 20. – P. 6824–6828.
4. Nakhodkin N. G. Effect of thickness on structural characteristics of nanosilicon films / N. G. Nakhodkin, N. P. Kulish, T. V. Rodionova, A. S. Sutyagina // *Bulletin of Taras Shevchenko National University of Kyiv Series Physics & Mathematics*, 2012. – V. 1. – P. 285–288.
5. Nakhodkin N. G. Troinye i mnozestvennye spetsialnie styki zeren v polikremniyevykh plenkach s raznym tipom struktury / N. G. Nakhodkin, N. P. Kulish, P. M. Lytvyn, T. V. Rodionova // in Coll. of Sci. works on Nanosystems, Nanomaterials, Nanotechnologies, Kiev, 2004. – V. 2, № 3. – P. 793–801.
6. Costantini S. Cleri F. Triple junctions and elastic stability of polycrystalline silicon / S. Costantini, P. Alippi, L. Colombo // *Phys. Rev. B*, 2001. – Vol. 63, Issue 4. – P. 045302-1–045302-4.
7. Nakhodkin, N. G. Formation of different types of polysilicon film structures and their grain growth under annealing / N. G. Nakhodkin, T. V. Rodionova // *Phys. Status Solidi A*, 1991. – Vol. 123, № 2. – P. 431–439.
8. Rath J. K. Low temperature polycrystalline silicon: a review on deposition, physical properties and solar cell applications / J. K. Rath // *Sol. Energy Mater. Sol. Cells*, 2003. – Vol. 76, № 4. – P. 431–487.
9. Хирш П. Электронная микроскопия тонких кристаллов / П. Хирш, А. Хови, Р. Николсон, Д. Пэшли, М. Уэлан / Пер. с англ. Под ред. Утевского Л.М. – М.: Мир., 1968. 574 с.

Submitted on 20.03.14

Находкін М., д-р фіз.-мат. наук, проф., акад. НАНУ, Куліш М., д-р фіз.-мат. наук, проф., чл.-кор. НАНУ, Київський національний університет імені Тараса Шевченка, Литвин П., канд. фіз.-мат. наук, Інститут фізики напівпровідників імені В. С. Лашкарєва НАН України, Родіонова Т., канд. фіз.-мат. наук, Сутягіна А., студ., Київський національний університет імені Тараса Шевченка

СПЕЦІАЛЬНІ СТИКИ ГРАНИЦЬ ЗЕРЕН У НАНОКРЕМНІЄВИХ ПЛІВКАХ З РІВНООСЬОВОЮ ТА ВОЛОКНИСТОЮ СТРУКТУРОЮ

Методами атомної силової мікроскопії досліджено спеціальні стики границь зерен в нанокремнієвих плівках. Показано, що в плівках з рівноосьовою та волокнистою структурою стики відрізняються кількістю та взаємним розташуванням спеціальних границь $\Sigma = 3^n$ та границь загального типу.

Ключові слова: нанокремнієві плівки; структура; стики границь зерен

Находкин Н., д-р физ.-мат. наук, проф., акад. НАНУ, Кулиш Н., д-р физ.-мат. наук, проф., чл.-кор. НАНУ, Киевский национальный университет имени Тараса Шевченко, Литвин П., канд. физ.-мат. наук, Институт физики полупроводников имени В. Е. Лашкарева НАН Украины, Родионова Т., канд. физ.-мат. наук, Сутягина А., студ., Киевский национальный университет имени Тараса Шевченко

СПЕЦИАЛЬНЫЕ СТИКИ ГРАНИЦ ЗЕРЕН В НАНОКРЕМНИЕВЫХ ПЛЕНКАХ С РАВНООСНОЙ И ВОЛОКНИСТОЙ СТРУКТУРОЙ

Методами атомной силовой микроскопии исследованы стики границ зерен в нанокремниевых пленках. Показано, что в пленках с равноосной и волокнистой структурой стики отличаются количеством и взаимным расположением специальных границ $\Sigma = 3^n$ и границ общего типа.

Ключевые слова: нанокремниевые пленки; структура; стики границ зерен

UDC 53; 547.136.13; 576.535; 577.037

Ye. Oberemok, Ph.D.
Department Quantum Radiophysics,
Faculty of Radio Physics, Electronics and Computer Systems
Taras Shevchenko National University of Kyiv

THE MUELLER MATRIX STRUCTURE OF MEDIA WITH ORTHOGONAL EIGENPOLARIZATIONS

The Mueller matrix structure and relationships between its elements for media with orthogonal eigenpolarizations were studied. Relations has been derived were verified on basic types of anisotropy and mixtures of ones. It was shown that Mueller matrix of medium with orthogonal eigenpolarizations has less than twelve independent elements. In addition the conditions which determine the values of anisotropy parameters for the eigenpolarizations to be orthogonal have been derived and examined for several characteristic mixtures of anisotropies. In particular it was founded that the orthogonality of eigenpolarization is always possible in mixtures of four basic types of anisotropy by properly fitted birefringent part. Finally the symmetry of the Mueller matrix, resulted from eigenpolarizations orthogonality, was established and analyzed for optimal measurement.

Keywords: Mueller matrix, eigenpolarizations orthogonality, parameters of anisotropy.

Introduction. It is well known that in optics and electrodynamics the crystalline medium are characterized by the types of eigenpolarizations that this medium possesses. Eigenpolarizations are those polarization

states of light that do not change when passing through a medium. The amplitude and the overall phase of the beam of light with an eigenpolarization do, however, change. These changes are described by the corresponding

eigenvalues. In scope of this research we intend to study the conditions, under which homogeneous anisotropic medium has in general case the orthogonal eigenpolarizations (eigenmodes). It is known, that all four basic types of anisotropy, circular and linear birefringence and circular and linear dichroism, each taken separately, possess orthogonal eigenpolarizations. Generalized birefringence, i.e. the case of medium exhibiting linear and circular birefringence simultaneously, is characterized by unitary matrix model and has orthogonal eigenpolarizations. At the same time, simultaneous presence of dichroism and birefringence in a medium may lead to nonorthogonal eigenpolarizations. However, to the best of our knowledge, so far there has been no systematic study of conditions under which such medium possesses orthogonal eigenpolarizations. Ascertainment of generalized conditions for orthogonality of medium's eigenpolarizations allows determining the structure and symmetry of matrix model for such class of media.

Given input and scattering directions and wavelength of input radiation, medium anisotropy properties are completely described by 4x4 real Mueller matrix. The measurement of complete Mueller matrix oriented to the case when all 16 elements of the Mueller matrix are independent. However, in practice, all 16 elements may very frequently not be independent. Some are zero and some are identical to others, depending on the symmetry and certain properties of the studied medium. A typical example of such situation is the deterministic class of crystalline media [1, 3, 6, 7] with Mueller matrices consisting in general of 7 independent elements – degrees of freedom. Measuring all 16 elements of the Mueller matrix for this class of media one consequently makes more than 50% “uninformative” measurements. In practice the part of uninformative measurements is even higher. This means that determination of the symmetry of inner structure of Mueller matrix model of medium, that is, the determination of the number and location of independent, informative elements in matrix, is perspective way to increase the speed of measurements. Furthermore, analysis carried out by us earlier shows that the measurement of incomplete matrix is characterized by higher precision than that of complete matrix.

Thus, relying on model symmetry which will be determined in scope of intended research; it will be possible to determine the incomplete Mueller matrices which are sufficient for full description of media with orthogonal eigenpolarizations in general case and for solving of corresponding classes of the inverse problems. In its turn, this allows to determine the scheme of polarimeter which is optimally fit for the measurement of these structures of incomplete Mueller matrices. This would permit to increase both the speed and accuracy of polarimetric measurements. This has ultimate importance for imaging Mueller polarimetry as well.

Methods, Assumptions and Procedures. To describe the linear interaction of polarized radiation with the medium, the Jones and Mueller matrix methods, which is uniquely related in case of a homogeneous anisotropic media [2], are used.

When Jones matrix method is used than

$$\mathbf{E}^{\text{out}} = \mathbf{T} \cdot \mathbf{E}^{\text{in}}, \quad (1)$$

where $\mathbf{E}^{\text{in(out)}}$ is the Jones vector of input (output) radiation, and \mathbf{T} denotes the Jones matrix.

Jones matrix \mathbf{T} (2x2 matrix with complex elements t_{mn}) describes anisotropic properties of homogeneous medium:

$$\mathbf{T} = \begin{bmatrix} t_{11} & t_{12} \\ t_{21} & t_{22} \end{bmatrix}; \quad \text{where } t_{mn} = |t_{mn}| \exp(-i\varphi_{mn}). \quad (2)$$

Eigenpolarizations χ of such matrix can be obtained as:

$$\chi_{1,2} = \frac{1}{2} \frac{t_{22} - t_{11} \pm \sqrt{(t_{22} - t_{11})^2 + 4t_{12} \cdot t_{21}}}{t_{21}}, \quad (3)$$

where $\chi = E_x / E_y$ – complex variable [2]; $E_{x,y}$ – components of the Jones vector \mathbf{E} .

For orthogonal eigenpolarizations the following relation:

$$\chi_1 \chi_2^* = -1, \quad (4)$$

is satisfied.

In experimental studies the Mueller method is used for description of interaction between electromagnetic radiation and medium because it operates with intensities of radiation that can be directly measured.

Then, in scope of the Muller matrix method (1) can be rewritten as:

$$\mathbf{S}^{\text{out}} = \mathbf{M} \mathbf{S}^{\text{in}}, \quad (5)$$

where $\mathbf{S}^{\text{in(out)}}$ – denotes input (output) Stokes vectors.

The definition of Stokes vector is follows:

$$\mathbf{S} = (I \ p \ \cos(2\theta) \ \cos(2\varepsilon) \ \ I \ p \ \sin(2\theta) \ \cos(2\varepsilon) \ \ I \ p \ \sin(2\varepsilon))^T, \quad (6)$$

where I – overall intensity of radiation; p – polarization degree; θ – azimuth and ε – ellipticity angle of polarization ellipse; T – transposing.

In accordance with (5) the Mueller matrix \mathbf{M} is a 4x4 matrix with real elements

$$\mathbf{M} = \begin{bmatrix} m_{11} & m_{12} & m_{13} & m_{14} \\ m_{21} & m_{22} & m_{23} & m_{24} \\ m_{31} & m_{32} & m_{33} & m_{34} \\ m_{41} & m_{42} & m_{43} & m_{44} \end{bmatrix}. \quad (7)$$

This matrix, as well as Jones matrix, describes completely anisotropic properties of homogeneous medium for a given input and output (scattering) directions and wavelength of input radiation.

Direct solving of the spectral problem in scope of Mueller formalism, i.e., finding the conditions on Mueller matrix elements for eigenpolarizations to be orthogonal, is quite complicated task because of Mueller matrix dimension. However, this problem, as it was demonstrated in [8], can be solved in scope of the Jones formalism both in terms of matrix. Taking into account the fact that Mueller \mathbf{M} and Jones \mathbf{T} matrices for homogeneous medium are interconnected by relation

$$\mathbf{M} = \mathbf{A}(\mathbf{T} \otimes \mathbf{T}^*) \mathbf{A}^{-1}, \quad (8)$$

where $*$ – conjugation; \otimes – Kronecker product; and

$$\mathbf{A} = \begin{bmatrix} 1 & 0 & 0 & 1 \\ 1 & 0 & 0 & -1 \\ 0 & 1 & 1 & 0 \\ 0 & i & -i & 0 \end{bmatrix},$$

all results, which are obtained for the Jones formalism, can be translated to the Mueller formalism with 8). Note that the main condition for that is the medium under consideration does not depolarize input radiation.

It is important to note that any 2x2 matrix could be called "Jones matrix", i.e., arbitrary 2x2 matrix with complex elements describes always a physical realizable transformation of polarization through the (1). The same can not be said about any 4x4 matrix with real elements. To be named as "Mueller matrix" this matrix has to meet an ample of requirements [4].

Due to above conditions the solving of spectral problem even for Mueller-Jones matrix (which is determined by (8)) case is generally difficult. We can write it in the following form:

$$\mathbf{M}(v_1^{-1}\mathbf{S}_1 + v_2^{-1}\mathbf{S}_2) = (1 \ 0 \ 0 \ 0)^T. \quad (9)$$

Conditions on matrices elements. In [8] was established that for orthogonality of eigenpolarizations the following relations between amplitudes and phases of Jones matrix elements need to be satisfied:

$$|t_{12}| = |t_{21}|, \quad (10)$$

$$2\phi_{22-11} = \phi_{12} + \phi_{21} \pm n\pi, \quad (11)$$

$$2\phi_{21+12} = \phi_{12} + \phi_{21} \pm n\pi, \quad (12)$$

$$2\phi_{i(21-12)} = \phi_{12} + \phi_{21} \pm n\pi. \quad (13)$$

where $\varphi_{mn\pm kl} = \arg(t_{mn} \pm t_{kl})$, $\varphi_{i(mn\pm kl)} = \arg(i(t_{mn} \pm t_{kl}))$.

Using interrelation (8) between Jones and Mueller methods, (10)-(12) and description of spectral problem as (9) we can also study symmetry of the Mueller matrix for medium with orthogonal polarizations.

In particular, from (8) it follows:

$$\begin{aligned} |t_{21}| &= \sqrt{\frac{m_{11} - m_{21} + m_{12} - m_{22}}{2}}, \\ |t_{12}| &= \sqrt{\frac{m_{11} + m_{21} - m_{12} - m_{22}}{2}}, \\ |t_{11}| &= \sqrt{\frac{m_{11} + m_{21} + m_{12} + m_{22}}{2}}, \\ |t_{22}| &= \sqrt{\frac{m_{11} - m_{21} - m_{12} + m_{22}}{2}}, \end{aligned} \quad (14)$$

$$\begin{aligned} \cos(\varphi_{12}) &= \frac{m_{13} + m_{23}}{2|t_{11}||t_{12}|}; \quad \sin(\varphi_{12}) = \frac{m_{14} + m_{24}}{2|t_{11}||t_{12}|}; \\ \cos(\varphi_{21}) &= \frac{m_{31} + m_{32}}{2|t_{11}||t_{21}|}; \quad \sin(\varphi_{21}) = \frac{m_{41} + m_{42}}{2|t_{11}||t_{21}|}; \\ \cos(\varphi_{22}) &= \frac{m_{33} + m_{44}}{2|t_{11}||t_{22}|}; \quad \sin(\varphi_{22}) = \frac{m_{43} - m_{34}}{2|t_{11}||t_{22}|}. \end{aligned} \quad (15)$$

Here we assumed that all phases of Jones matrix elements (2) are normalized on phase of the first matrix element (i.e. $\varphi_{mn} \rightarrow \varphi_{mn} - \varphi_{11}$). Thus, in this case the phase of element t_{11} is $\varphi_{11} \rightarrow 0$.

Condition (4) for orthogonality of eigenpolarizations of medium in terms of Jones matrix elements can be transformed using (14) into relation:

$$m_{11} - m_{21} + m_{12} - m_{22} = m_{11} + m_{21} - m_{12} - m_{22},$$

or

$$m_{12} = m_{21}. \quad (16)$$

Considering (10)–(12) as equivalent $2\phi_{11+22} = 2\phi_{(21+12)} = 2\phi_{i(21-12)} = \phi_{12} + \phi_{21} \pm n\pi$ we can write:

$$\frac{\text{Im}(t_{22} - t_{11})}{\text{Re}(t_{22} - t_{11})} = \frac{\text{Im}(i(t_{21} - t_{12}))}{\text{Re}(i(t_{21} - t_{12}))} = \frac{\text{Im}(t_{21} + t_{12})}{\text{Re}(t_{21} + t_{12})}, \quad (17)$$

then, invoking (14) and (15) we'll get:

$$\begin{aligned} \frac{m_{13} + m_{23} - m_{31} - m_{32}}{m_{41} + m_{42} + m_{14} + m_{24}} &= \frac{m_{41} + m_{42} - m_{14} - m_{24}}{m_{13} + m_{23} + m_{31} + m_{32}}, \\ &= \frac{m_{43} - m_{34}}{m_{11} + m_{21} + m_{12} + m_{22} - m_{33} - m_{44}}, \end{aligned} \quad (18)$$

and

$$(m_{13} + m_{23})^2 - (m_{31} + m_{32})^2 = (m_{41} + m_{42})^2 - (m_{14} + m_{24})^2 \quad (19)$$

After exploiting of relation (8) we tried to expand (9) in assumption that polarization degree of eigenpolarizations is $p=1$, i.e. $s_1^2 = s_2^2 + s_3^2 + s_4^2$.

From (9) for normalized Stokes vectors we can write:

$$\mathbf{S}_1 = (1 \ s_2 \ s_3 \ s_4)^T, \quad \mathbf{S}_2 = (1 \ -s_2 \ -s_3 \ -s_4)^T \quad (20)$$

As the Stokes vectors (20) are eigenvectors of Mueller matrix \mathbf{M} it is right that:

$$\begin{aligned} \mathbf{M} \cdot \mathbf{S}_{1,(2)} &= \begin{pmatrix} m_{11} \pm m_{12}s_2 \pm m_{13}s_3 \pm m_{14}s_4 \\ m_{21} \pm m_{22}s_2 \pm m_{23}s_3 \pm m_{24}s_4 \\ m_{31} \pm m_{32}s_2 \pm m_{33}s_3 \pm m_{34}s_4 \\ m_{41} \pm m_{42}s_2 \pm m_{43}s_3 \pm m_{44}s_4 \end{pmatrix} = \\ &= \underbrace{(m_{11} \pm m_{12}s_2 \pm m_{13}s_3 \pm m_{14}s_4)}_{v_{1(2)}} \mathbf{S}_{1,(2)} \end{aligned} \quad (21)$$

From (21) it follows:

$$\begin{cases} m_{21} + m_{22}s_2 + m_{23}s_3 + m_{24}s_4 - s_2 v_1 = 0 \\ m_{31} + m_{32}s_2 + m_{33}s_3 + m_{34}s_4 - s_3 v_1 = 0 \\ m_{41} + m_{42}s_2 + m_{43}s_3 + m_{44}s_4 - s_4 v_1 = 0 \\ m_{21} - m_{22}s_2 - m_{23}s_3 - m_{24}s_4 - s_2 v_2 = 0 \\ m_{31} - m_{32}s_2 - m_{33}s_3 - m_{34}s_4 - s_3 v_2 = 0 \\ m_{41} - m_{42}s_2 - m_{43}s_3 - m_{44}s_4 - s_4 v_3 = 0 \end{cases} \quad (22)$$

Combining (22) we obtain:

$$\begin{aligned} m_{21} &= s_2(m_{12}s_2 + m_{13}s_3 + m_{14}s_4), \\ m_{31} &= s_3(m_{12}s_2 + m_{13}s_3 + m_{14}s_4), \\ m_{41} &= s_4(m_{12}s_2 + m_{13}s_3 + m_{14}s_4). \end{aligned} \quad (23)$$

Multiplying (23) by s_2, s_3, s_4 , respectively, and, taking into account that for completely polarized light $(s_2^2 + s_3^2 + s_4^2)^{1/2} = 1$, we have:

$$s_2(m_{21} - m_{12}) + s_3(m_{31} - m_{13}) + s_4(m_{41} - m_{14}) = 0 \quad (24)$$

$$m_{21}(m_{21} - m_{12}) + m_{31}(m_{31} - m_{13}) + m_{41}(m_{41} - m_{14}) = 0, \quad (25)$$

$$\frac{m_{12}^2 + m_{13}^2 + m_{14}^2}{m_{12}m_{21} + m_{13}m_{31} + m_{14}m_{41}} = 1. \quad (26)$$

As for homogeneous media it is true that [1,4]

$$m_{12}^2 + m_{13}^2 + m_{14}^2 = m_{21}^2 + m_{31}^2 + m_{41}^2. \quad (27)$$

From (26) and (27) we can get that:

$$(m_{12} - m_{21})^2 + (m_{13} - m_{31})^2 + (m_{14} - m_{41})^2 = 0. \quad (28)$$

From (28) it results that:

$$m_{12} = m_{21}, \quad m_{13} = m_{31}, \quad m_{14} = m_{41}. \quad (29)$$

From (30) it follows that for complete description of anisotropy of medium with orthogonal eigenpolarizations the knowledge of second, third and fourth columns(rows) of Mueller matrix is sufficient. This result can be used during optimization of polarimeter for studying of given polarization class of media.

Conditions on anisotropy. To derive orthogonality condition in terms of anisotropy parameters we use the matrix model of arbitrary homogeneous anisotropy that has recently been presented in [6] and combines both mathematical generality and physical interpretability:

$$\mathbf{T}(\varphi, \Delta, \alpha, R, P, \gamma) = \mathbf{T}^{CP}(\varphi) \mathbf{T}^{LP}(\Delta, \alpha) \mathbf{T}^{CA}(R) \mathbf{T}^{LA}(P, \gamma), \quad (30)$$

where: value of linear dichroism is in the range $P \in [0;1]$ and the azimuth of maximum transition is in the range $\gamma \in \left[-\frac{\pi}{2}; \frac{\pi}{2}\right]$; value of circular dichroism $R \in [-1;1]$; value of linear birefringence $\Delta \in [0;2\pi]$ with it's fast axis orientation $\alpha \in \left[-\frac{\pi}{2}; \frac{\pi}{2}\right]$; value of optical activity is $\varphi \in [-\pi; \pi]$.

Let write next useful relations:

$$t_{22} - t_{11} = (a_1 + ib_1) \exp\left(-i \frac{\Delta}{2}\right), \quad (31)$$

$$t_{21} - t_{12} = (a_2 + ib_2) \exp\left(-i \frac{\Delta}{2}\right), \quad (32)$$

$$t_{21} + t_{12} = (a_3 + ib_3) \exp\left(-i \frac{\Delta}{2}\right). \quad (33)$$

In compliance with (31) parameters a_i and b_i have the following form:

$$\begin{aligned} a_1 &= (1+P)R \sin \frac{\Delta}{2} \sin(2\alpha - \varphi) - (1-P) \cos \frac{\Delta}{2} \cos(2\gamma - \varphi), \\ b_1 &= (1-P)R \cos \frac{\Delta}{2} \sin(2\gamma - \varphi) - (1+P) \sin \frac{\Delta}{2} \cos(2\alpha - \varphi), \\ a_2 &= (1-P)R \sin \frac{\Delta}{2} \cos(2\alpha - 2\gamma - \varphi) - (1+P) \cos \frac{\Delta}{2} \sin(\varphi), \\ b_2 &= (1+P)R \cos \frac{\Delta}{2} \cos(\varphi) - (1-P) \sin \frac{\Delta}{2} \sin(2\alpha - 2\gamma - \varphi), \\ a_3 &= (1+P)R \sin \frac{\Delta}{2} \cos(2\alpha - \varphi) + (1-P) \cos \frac{\Delta}{2} \sin(2\gamma - \varphi), \\ b_3 &= (1-P)R \cos \frac{\Delta}{2} \cos(2\gamma - \varphi) + (1+P) \sin \frac{\Delta}{2} \sin(2\alpha - \varphi), \end{aligned} \quad (34)$$

From (34) and (10) can be written:

$$a_2 a_3 + b_2 b_3 = 0; \quad (35)$$

(11)–(13) are transformed to:

$$a_1 b_3 - a_3 b_1 = 0, \quad (36)$$

$$a_1 b_2 + a_2 b_1 = 0. \quad (37)$$

(35)–(37) can be used for determination of anisotropy parameters. In particular we had got that for media have orthogonal eigenpolarizations its dichroism can be arbitrary but birefringence need to satisfy:

$$\begin{aligned} \operatorname{tg} \frac{\Delta}{2} &= -\frac{1}{2R} \frac{P-1}{P+1} \left[A - \sqrt{A^2 + 4R^2} \right], \\ \varphi &= \alpha - \gamma + \frac{1}{2} \arccos \left[\cos 2(\alpha - \gamma) \frac{R^2 - 1}{R^2 + 1} \right] - \frac{\pi}{2}, \end{aligned} \quad (38)$$

where $A = (1 - R^2) \sin 2(\alpha - \gamma)$.

It turns convenient to determine the parameters Δ and φ , while other four parameters are fixed in a range of definition. For example:

$$\begin{aligned} T(9.4^\circ, 51.8^\circ, 84^\circ, 0.7, 0.2, 25^\circ) &= \\ &= \begin{bmatrix} 0.803+0.61i & 0.457+0.098i \\ 0.188+0.428i & 0.261+0.168i \end{bmatrix} \end{aligned} \quad (39)$$

It is easy to see that eigenpolarizations $\chi_{1,2}$ of the Jones matrix (39) are orthogonal

$$\begin{aligned} \chi_1 &= 0.446+0.228i; \quad \chi_2 = -1.777-0.908i; \\ \chi_1 \chi_2^* &= -1. \end{aligned} \quad (40)$$

Taking to account (8) and (30), in terms of Mueller matrix we can obtain:

$$M(\varphi, \Delta, \alpha, R, P, \gamma) = \begin{bmatrix} 1.000 & 0.593 & 0.707 & 0.361 \\ 0.593 & 0.436 & 0.394 & 0.155 \\ 0.707 & 0.356 & 0.568 & 0.260 \\ 0.361 & 0.229 & 0.197 & 0.238 \end{bmatrix} \quad (41)$$

Eigenpolarizations of the Mueller matrix \mathbf{M} :

$$\mathbf{S}_1 = (1 \quad 0.599 \quad 0.713 \quad 0.365)^T;$$

$$\mathbf{S}_2 = (1 \quad -0.599 \quad -0.713 \quad -0.365)^T;$$

$$\mathbf{S}_1 + \mathbf{S}_2 = (1 \quad 0 \quad 0 \quad 0)^T. \quad (42)$$

Summary. Summarizing obtained results we can formulate next conclusions. Anisotropy of homogeneous media with orthogonal eigenpolarizations has limitations. In particular when we use for modeling such media an equivalence theorem in form (30) eigenpolarizations will be orthogonal always if linear Δ and circular birefringence φ will have values as (38), whereas other four anisotropy parameters (R, P, γ, α) can take an arbitrary values. In other words a media with orthogonal eigenpolarizations can demonstrate all six possible anisotropy behaviors as separately as simultaneously. One exclusion need to be taking into account: when the medium has simultaneously only two dichroismes (circular and linear) it can't have orthogonal eigenpolarizations under no conditions.

Limited anisotropy of media with orthogonal eigenpolarizations leads to symmetry in Mueller matrix (see (29)) and to other more difficult relations between elements on those matrices. These relations can be useful for simplify an analysis of properties of objects and utilized for optimization of measurement procedure. In last context we have used an equality of first column and row of Mueller matrix of studied objects to reduction measurement time with saving accuracy on polarimeter with four LC-transducers [5]. If we could to remove limitation on shift of LC transducers than measurement error limit could be reduced to $\delta m_{13} = 1.9\%$, in comparison $\delta m_{16} = 2.1\%$.

REFERENCE:

1. Anderson D.G. Necessary and sufficient conditions for a Mueller matrix to be derivable from a Jones matrix / *D.G. Anderson, R. Barakat // J.Opt. Soc.Am.A.*, 1994. – Vol. 11. – P. 2305–2319.
2. Azzam R.M.A. Ellipsometry and Polarized Light / *R.M.A. Azzam, N.M. Bashara / Ed by R.M.A. Azzam. – NY., 1987.*
3. Cloude S.R. Group theory and polarization algebra // *Optik (Stuttgart)*. – 1986. – Vol. 75. – P. 26–36.
4. Hovenier J.W. Structure of a general pure Mueller matrix / *J.W. Hovenier // Applied Optics*. – 1994. – Vol.33. – No.36. – P. 8318–8325.
5. Optimized Mueller polarimeter with liquid crystal / *A. De Martino, Y. K. Kim, E. Garcia-Caurel at all. // Opt. Letters*, 2003. – Vol.28. – P. 616–618.
6. Generalized matrix equivalence theorem for polarization theory / *S.N. Savenkov, V.V. Marienko, Y.A. Oberemok at. all // Phys.Rev.* – 2006. – Vol.E 74. – P. 056607 (1–8).
7. Savenkov S.N. Optimization and structuring of the instrument matrix for polarimetric measurements / *S.N. Savenkov // Opt.Eng.* – 2002 – 41. – P. 965–972.
8. Savenkov S.N. Generalized conditions of eigenpolarizations orthogonality: Jones matrix calculus / *S.N. Savenkov, Y.A. Oberemok // Proceedings of SPIE.* – 2008. – Vol.6972. – P. 697210.

Submitted on 31.01.14

Оберемок С., канд. фіз.-мат. наук,
каф. квантової радіофізики, факультет радіофізики, електроніки та комп'ютерних систем,
Київський національний університет імені Тараса Шевченка

СТРУКТУРА МАТРИЦІ МЮЛЛЕРА СЕРЕДОВИЩ З ОРТОГОНАЛЬНИМИ ПОЛЯРИЗАЦІЯМИ ВЛАСНИХ ХВИЛЬ

В роботі досліджено зв'язок між елементами матриці Мюллера однорідних анізотропних середовищ з ортогональними поляризаціями власних хвиль. Отримані співвідношення перевірено для випадку середовищ з простими та змішаними типами анізотропії. Встановлено, що ортогональність поляризацій власних хвиль зменшує кількість незалежних елементів матриці Мюллера до 12. Досліджено зв'язок між параметрами анізотропії такого типу середовищ та встановлено, що їх анізотропія може утворюватись поєднанням всіх чотирьох елементарних типів дихроїзму та двопронезаломлення, проте, з обмеженим співвідношенням. Зокрема, показано, що за довірливих значень дихроїзму, міри лінійного та циркулярного двопронезаломлення можуть приймати тільки конкретні значення. З огляду на встановлену симетрію матриці Мюллера, вимірювання тільки необхідної кількості її елементів дозволяє скоротити час вимірювання зберігши або підвищивши точність.

Ключові слова: Матриця Мюллера, ортогональність власних поляризацій, параметри анізотропії.

Оберемок Е., канд. физ.-мат. наук,
каф. квантовой радиофизики, факультет радиофизики, электроники и компьютерных систем,
Киевский национальный университет имени Тараса Шевченко

СТРУКТУРА МАТРИЦЫ МЮЛЛЕРА СРЕД С ОРТОГОНАЛЬНЫМИ ПОЛЯРИЗАЦИЯМИ СОБСТВЕННЫХ ВОЛН

В работе исследована связь между элементами матрицы Мюллера однородных анизотропных сред с ортогональными поляризациями собственных волн. Полученные соотношения проверены для случая сред с простыми и смешанными типами анизотропии. Установлено, что ортогональность поляризацій собственных волн уменьшает число независимых элементов матрицы Мюллера до 12. Исследована связь между параметрами анизотропии такого типа сред и установлено, что их анизотропия может образовываться сочетанием всех четырех элементарных типов дихроизма и двулучепреломления, однако, с ограниченным соотношением. В частности, показано, что при произвольных значениях дихроизма, значения линейного и циркулярного двулучепреломления могут принимать только конкретные значения. Учитывая установленную симметрию матрицы Мюллера, измерения только необходимого количества ее элементов позволяет сократить время измерений, сохранив или повысив точность.

Ключевые слова: Матрица Мюллера, ортогональность собственных поляризацій, параметры анизотропии.

UDC 004.62

I. Shyian, post. grad. stud., G. Chuiko, Dr.Sci.,
A. Pavlenko, stud., Medical Systems and Devices Department,
Faculty of Ecology and Medical Sciences
Petro Mohyla Black Sea State University

DIGITAL PROCESSING OF MEDICAL IMAGE WITH MAPLE

Typical medical images are most often in gray scale and their matrices of pixel intensities are convenient for digital processing. Recent versions of popular computer mathematics system Maple have special program packages for this aim. We are going to illustrate the possibilities of these packages by example of usual medical image. Our case study presents the discrete dyadic wavelet analysis (DWT), block thresholding of detail coefficients and evaluations of quality for reconstructed image. We investigated in addition the dependences of quality parameters on the digital filters used within DWT procedure.

Keywords: medical image, discrete wavelet analysis, dyadic decomposition, block thresholding, factors of image quality, image compression

Introduction. Digital processing is important for many applications that involve huge data storage, transmission and retrieval such as for multimedia, documents, videoconferencing, and medical imaging. Uncompressed images require considerable storage capacity. The objective of image compression technique is to reduce redundancy of the image data in order to be able to store or transmit data in an efficient form. This results in the reduction of file size and allows more images to be stored in a given amount of disk or memory space [1].

Medical image compression may be based on wavelet decomposition. It can produce notably better medical image results compared to the compression results that are generated by Fourier transform based methods such as the discrete cosine transform (DCT) used by JPEG [6].

The aim of this paper is to illustrate how discrete dyadic wavelet analysis (DWT) and block thresholding may be applied in medical image compression to reduce the volume of data.

Experimental. If we consider the quadratic image with sizes $N \times N = 2^m$, we can get at least $m = 2 \log_2 N$ consecutive Wavelet-Transformations (so called the scale levels). In practice, usually from two to six scale levels are enough for useful analysis [3]. We were starting with image size $N = 224$ and $m = 2$ (see Fig. 1).



Fig. 1. A medical image before (A) and after processing (B)

Two-dimensional wavelet transform can be represented as a composition of one-dimensional wavelet decompositions in rows and columns of the matrix image.

Image after single-level wavelets transformation in rows and columns is divided into four frequency blocks with different interpretation (Fig. 2) [5]:

1. LL-blok is top left block of approximation coefficients, which were filtered out in the analysis (decomposition) with two low-pass filters. The block contains a copy of the primary image with half resolution.

2. HL/LH blocks, bottom left and top right blocks, contain the detail coefficients, which were filtered by a low pass filter and a high pass filter. Block LH contains vertical edges, while the block HL – horizontal edges of the image.

3. HH-block, lower left. It contains detail coefficients twice filtered by high pass filters. We can interpret this block as an area which contains the edges of the original image in the diagonal direction.

A large number of wavelet detail coefficients will be small in absolute value (module) after decomposition since the neighboring pixels of images have mostly similar intensity values. As a result, the only part of the wavelet coefficients, especially those that are located in the so-called block LL of upper scale, chiefly represents the energy of image.

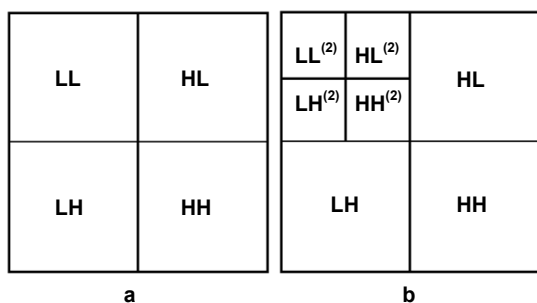


Fig. 2. Frequency blocks of wavelet coefficients for different numbers of levels of decomposition: A – single-level wavelet decomposition of the image; B – two-level (dyadic) wavelet decomposition

The following expression determines the image energy

$$E = \sum_{r=0}^{N-1} \sum_{c=0}^{N-1} (x_{r,c})^2 \tag{1}$$

here $0 \leq x_{r,c} \leq 1$ is intensity of a pixel.

The usefulness of the DWT is the large number of zero (or close to zero) wavelet coefficients in the matrix of decomposition. Most of small wavelet-coefficients may be neglected by shrinking (replaced by zeros). Such a procedure is known as thresholding [3]. This last may deal either with every wavelet coefficient or with blocks of them. We used here the second kind of this procedure. If we are going to neglect all wavelet coefficients of so-called LH, HL and HH sub-matrices of decomposition matrix then the percent of these increases with the scale levels as [7]:

$$N(m) = 100 \cdot (1 - \frac{1}{2^{2m}}) \tag{2}$$

The percentage of negligible coefficients increases with the number of scale levels as it is evident from Figure 2.

Table 1 shows that for dyadic decomposition ($m = 2$) it gives 93.75 % of zeros in decomposition matrix.

Table 1

Maximum percentage of zeros for thresholding of the matrix of wavelet coefficients depending on the number of the scale levels

the number of the scale levels (m)	1	2	3	4	5
percentage of zeros for thresholding (%)	75	93.75	98.44	99.61	99.90

Thus, only few percent of wavelet coefficients were in use for reconstruction of image (see Fig. 1B).

Figure 3 shows the intensity distribution of pixels on frequency blocks of wavelet coefficients for the two-level decomposition.

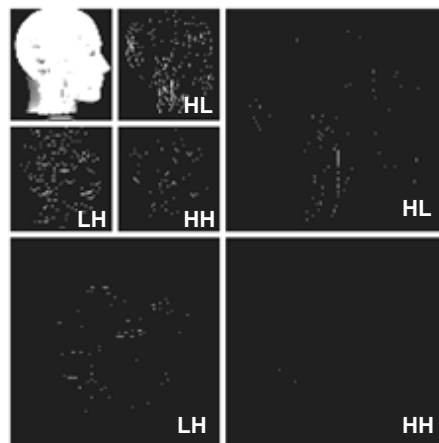


Fig. 3. Two-level refined from 93% of small detail coefficients image

Thus, there are only less than 7 % of non-zero wavelet coefficients, so the restored image will be significantly compressed. Such a radical reduction of information can be very useful in many cases, under condition that it is not accompanied by significant losses in image quality.

The evaluation of reconstructed image quality is possible with well-known factors: root of mean square error (rmse), peak signal to noise ratio (PSNR), entropy, coefficients of correlation between original and reconstructed images [2].

The root mean square error (rmse) measures the amount of change per pixel due to the processing. The rmse between a reference image and the compressed image is given by

$$rmse = \sqrt{mse} \tag{3}$$

Where mse is the mean square error

$$mse = \frac{\sum (r_{i,j} - s_{i,j})^2}{wh} \tag{4}$$

Here r, s are the reconstructed and source images, i, j range over all pixels, and w, h are the width and height [2, 8].

PSNR is most commonly used to measure the quality of reconstruction of compressed image. PSNR is usually expressed in terms of the logarithmic decibel scale.

$$PSNR = 10 \log_{10} \left(\frac{peak^2}{mse} \right) \tag{5}$$

Where mse is the mean square error and $peak$ is the maximal intensity of a pixel in the image [2, 8]. For our evaluations $peak = 1$.

Entropy H is a scalar value representing the entropy of grayscale image. Entropy is a statistical measure of randomness that can be used to characterize the texture of the input image.

The entropy of image is equal to

$$H = - \sum_{i=1}^M p_i \log_2 p_i \tag{6}$$

Here M is number of equal intervals between boundary intensities 0 and 1 (normally $M = 256$).

Coefficients of correlation characterize correlation of pixels of original and reconstructed images [2].

The Table 2 presents these factors and their dependences on the length of digital filters of Symlet wavelet family. The Symlet wavelet family is one of the set of orthogonal wavelets offered by Maple. Symlets are also known as the Daubechies least asymmetric wavelets. Their construction is very similar to the Daubechies wavelets. The Symlet wavelet of size $2n$ has n vanishing moments.

Table 2

Factors of image quality vs. length of digital filters

Filter length	2	4	6	8	10	12
rmse	0.060	0.050	0.046	0.045	0.045	0.044
PSNR (dB)	24.45	26.07	26.66	26.90	26.91	27.05
Entropy (bit)	5.921	6.218	6.288	6.256	6.290	6.276
Correlation	0.981	0.987	0.989	0.989	0.989	0.990

Note: Entropy of original image is equal to 6.425877

Digital filters, more correctly the bank of digital filters (low-pass and high-pass), are main thing as for real DWT of image. You can know nothing about graphics of wavelet or its properties but you are able to make a DWT if you have a digital filter bank [7]. One can see that quality factors shown in Tabl. 2 are better for lengthier digital filters, nonetheless this gain is quite moderate. There should be found a compromise between the quality factors (longer filters) and the duration of computing (shorter filters).

One more problem is the optimal choice of wavelet family for decomposition. The Tabl.3 presents the collection of quality factors for different orthogonal wavelets with equal lengths ($n = 12$) of digital filters.

Table 3

Factors of image quality for different orthogonal wavelets

Wavelet families	Daubechies, 12	Coiflet, 12	Symlet, 12
rmse	0.045274	0.044845	0.044407
PSNR (dB)	26.882917	26.965637	27.05098
Entropy (bit)	6.334132	6.256444	6.276446
Correlation	0.989195	0.989403	0.989611

Now the reader can independently estimate the results of the switch from one family of orthogonal wavelets to another. This effect does not look extremely strong, from our point of view.

For processing images besides orthogonal wavelets are also widely used biorthogonal wavelets. The biorthogonal wavelets introduced by Cohen, Daubechies, and Feauveau contain in particular compactly supported biorthogonal spline wavelets with compactly supported duals. In biorthogonal wavelets, separate decomposition and reconstruction filters are defined and hence the responsibilities of analysis and synthesis are assigned to two different functions (in the biorthogonal case) as opposed to a single function in the orthonormal case [4].

The bank of wavelets of computer mathematics system Maple has the only biorthogonal wavelet Cohen-Daubechies-Feauveau (CDF) (9, 7) [8]. However, digital filters can be obtained by the algorithm outlined in the [7]. For processing we have chosen particularly biorthogonal spline (2, 2). Fig. 4, 5 shows the low-pass and the high-pass filters of biorthogonal spline (2, 2) for analysis and synthesis.

Table 4 displays evaluations of reconstructed image quality processed by orthogonal and biorthogonal wavelets with different number of digital filters.

As you see, biorthogonal wavelets have not advantages over orthogonal wavelets in this case.

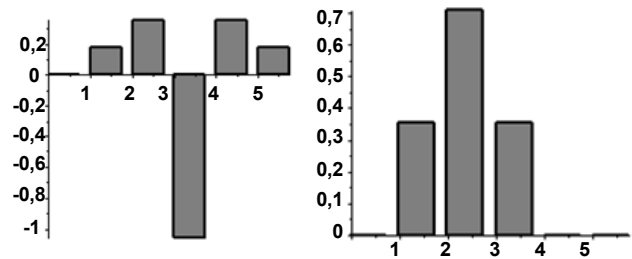


Fig. 4. Digital low-pass and high-pass filters of biorthogonal spline (2, 2) used for analysis

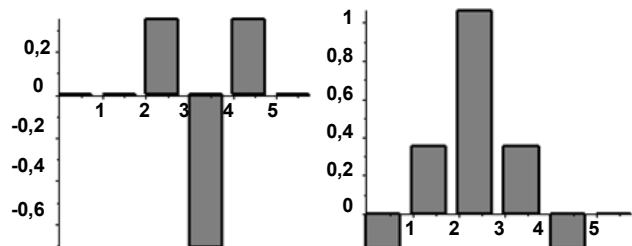


Fig. 5. Digital low-pass and high-pass filters of biorthogonal spline (2, 2) used for synthesis

Table 4

Comparison of factors of image quality for orthogonal and biorthogonal wavelets

Wavelet families	Orthogonal wavelets			Biorthogonal wavelets		
	Coiflet 12	Daubechies 12	Symlet 12	CDF 5/3	Biorthog. Spline 5/3	CDF 9/7
vanishing moments	6	6	6	2, 2	2, 2	4, 4
rmse	0,045	0,045	0,044	0,052	0,066	0,054
PSNR (dB)	26,97	26,88	27,05	25,71	23,65	25,34
Entropy (bit)	6,256	6,334	6,276	5,955	6,194	5,853
Correlation	0,989	0,989	0,990	0,986	0,977	0,985

Conclusions. Image compression and its clearing by method discrete wavelet transform can significantly reduce the size of a 2-D image (up to 6 times). Such a radical reduction of information can be very useful in many cases, under condition that it is not accompanied by significant losses in image quality.

Many scientists working in this field, are trying to find the optimal wavelet for image processing. However, the analysis showed that the reconstructed image quality parameters for different families of wavelets are almost indistinguishable. Besides, comparison of factors of image quality for orthogonal and biorthogonal wavelets shows, that biorthogonal wavelets have not advantages over orthogonal wavelets in our case study.

Research has shown that with increasing length of the digital filters factors of image quality are better. However, a compromise between quality factors (longer filters) and the computing duration (shorter filters) needs to be found.

REFERENCE:

1. Chowdhury M. H. Image Compression Using Discrete Wavelet Transform / M.H. Chowdhury, A. Khatun // International Journal of Computer Science Issues. – 2012. – Vol. 9(1). – P.327–330.
2. Dammavalam S. R. Quality assessment of pixel-level image fusion using fuzzy logic / S.R. Dammavalam, S. Maddala, K. Prasad // International Journal on Soft Computing (IJC). – 2012. – Vol.3(1). – P.13–25.
3. Jana D. Wavelet Thresholding for Image Noise Removal (Different Techniques of Thresholding Used for Wavelet Image Denoising) / D. Jana,

K. Sinha // International Journal on Recent and Innovation Trends in Computing and Communication (IJRITCC). – 2014. – Vol. 2(6). – P. 1400–1405.

4. Loganathan R. Medical Image Compression Using Biorthogonal Spline Wavelet With Different Decomposition / R. Loganathan, Y.S. Kumaraswamy // (IJCS) International Journal on Computer Science and Engineering. – 2010. – Vol. 2(9). – P. 3003–3006.

5. Monika. Lifting Scheme Using HAAR & Biorthogonal Wavelets For Image Compression / Monika, P. Chaudhary, G. Lalit // International Journal of Engineering Research and Applications (IJERA). – 2013. – Vol. 3(4). – P. 474–478.

6. Introduction to wavelet-based compression of medical images / D. F. Schomer, A. A. Elekes, J. D. Hazle et al. // Radiographics. – 1998. – Vol. 18(2). P. 469–481.

7. Vorobiov V. I.; Gribunin V. G. Theory and practice of the wavelet transform / V.I. Vorobiov; V.G. Gribunin. – Saint Petersburg, 1999.

8. Wavelets Examples and Applications. © – 2012, Maplesoft.

Submitted on 12.11.14

Шиян І., асп., Чуйко Г., д-р фіз.-мат. наук,

Павленко А., магістрант, каф. медичних приладів і систем, факультет еколого-медичних наук
Чорноморський державний університет імені Петра Могили

ЦИФРОВА ОБРОБКА МЕДИЧНИХ ЗОБРАЖЕНЬ ЗАСОБАМИ СКМ MAPLE

Більшість медичних зображень зазвичай представлені в сірих відтінках, а їх матриці інтенсивностей пікселів зручні для цифрової обробки. Останні версії популярної системи комп'ютерної математики Maple мають спеціальні програмні пакети для вирішення таких задач. В даній роботі проілюстровані можливості цих пакетів на прикладі типового медичного зображення. Для цифрової обробки зображення використовувалися засоби дискретного вейвлет-перетворення, процедури трешолдінгу (так званого "жорсткого порогу") та проводилася оцінка якості відновленого зображення. Крім того в роботі проведений аналіз залежності параметрів якості зображення від цифрових фільтрів, використовуваних у процедурі дискретного вейвлет-перетворення.

Ключові слова: медичне зображення, дискретне вейвлет-перетворення, дворівневе розкладання, трешолдінг, параметри оцінки якості зображення.

Шиян И., асп., Чуйко Г., д-р физ.-мат. наук,

Павленко А., магистрант, каф. медицинских приборов и систем, факультет эколого-медицинских наук,
Черноморский государственный университет имени Петра Могили

ЦИФРОВАЯ ОБРАБОТКА МЕДИЦИНСКИХ ИЗОБРАЖЕНИЙ МЕТОДАМИ СКМ MAPLE

Большинство медицинских изображений обычно представлены в серых оттенках, а их матрицы интенсивностей пикселей удобны для цифровой обработки. Последние версии популярной системы компьютерной математики Maple имеют специальные программные пакеты для решения таких задач. В данной работе проиллюстрированы возможности этих пакетов на примере типового медицинского изображения. Для обработки изображений использовались средства дискретного вейвлет-преобразования, процедуры трешолдинга (так называемого "жесткого порога") и проводилась оценка качества восстановленного изображения. Кроме того, в работе проведен анализ зависимости параметров качества изображения от цифровых фильтров, используемых в процедуре дискретного вейвлет-преобразования.

Ключевые слова: медицинское изображение, дискретное вейвлет-преобразование, двухуровневое разложение, трешолдинг, параметры оценки качества изображения.

UDC 539.1

V. Iakovenko, Ph.D., High Energy Physics Department,
Kiev Institute for Nuclear Research, Cancer Center "Innovacia";
A. Kovalchuk, Chief engineer, V. Pugatch, Prof., O. Okrimenko,
Lead engineer, High Energy Physics Department, Kiev Institute for Nuclear Research;
I. Sorokin, Ph.D., High Energy Physics Department, Kiev Institute for Nuclear Research,
3GSI Helmholtz Centre for Heavy Ion Research; Y. Prezado, Ph.D., I. Martinez-Rovira, Ph.D.,
Department of Imaging and Modeling in Neurobiology and Oncology, CNRS, France;
A. Iliukhina, stud., Physical Faculty, Taras Shevchenko National University of Kyiv

METAL MICRO-DETECTORS FOR IMAGING AND BEAM PROFILE MONITORING IN RADIATION THERAPY

Metal micro-detector (MMD) has been developed at Kiev Institute for Nuclear Research (KINR). Physics and techniques of this detector applied for monitoring and imaging of charged particles beams are presented. To provide the precise beam profile monitoring a 128-channel X-Y MMD was produced. Test studies with this detector were performed for 20 MeV electrons (Cancer Center "Innovacia") and high energy hadrons (protons, ¹²C-ions and ¹⁶O-ions, Heidelberg Ion-Beam Therapy Center). Results of these studies are discussed in this work. The results of our studies suggest the possibility of MMD application in clinical practice.

Key words: metal micro-detectors, beam profile monitoring, online dose monitoring, mini-beam radiation therapy.

Introduction. The main goal of radiotherapy is to deposit a high dose of ionizing radiation in a tumor while keeping the absorbed dose in the surrounding healthy tissue at a tolerant level [1]. The monitoring of the beam position and absorbed dose are essential. Current developments in radiation therapy require non-destructive beam profile monitoring in real time, as beam diagnostics provides information on the status of the beam, monitoring of critical parameters and alarming in case of emergency. For low intensity beams a proper approach could be realized by using silicon micro-strip detectors. However, radiation hardness aspect makes this approach rather limited.

A Metal Foil Detector (MFD) technology developed at Kiev Institute for Nuclear Research makes possible the production of radiation hard monitoring devices that are able to take a challenge and fulfill the needs of modern radiotherapy.

The general physics and registration principles of the MFD are discussed in details elsewhere [2]. Charged particles (or photons) hitting the metal sensor-foil initiate Secondary Electron Emission at 10–50 nm surface layers. The charge generated in a sensor is measured by a sensitive Charge Integrator.

MFD technology was successfully explored for the design and production of a novel thin metal micro-strip beam profile monitors of charge particles and synchrotron radiation beams. Through an innovative plasma-chemistry etching process, thin (about 1 μm) metal micro-strips are aligned, without any other materials in the working area. The main advantages of MMD are: low thickness of detecting material; good position resolution (up to few μm); low operating voltage (~ 20 V); high radiation tolerance (at gigarads level). MMD were tested at the Minibeam Radiation Therapy (MBRT) setup (Bio-Medical Beamline

ID17, European Synchrotron Radiation Facility) [3]. **Experimental setup. MMDw detector.** To provide the precise beam profile monitoring a (64 x 64)-channel X-Y MMDw was produced at KINR. Thin metal wires are used to create the strip structure of a sensor. Simple technology of production, low cost and reliable operation are main advantages of the MMDw. The read-out electronics is based on the commercial data acquisition system XDAS (SENS-TECH, UK) providing sensitivity of about 10^3 particles/strip and dynamic range up to 10^5 being connected with micro-strip metal detectors (Fig. 1).

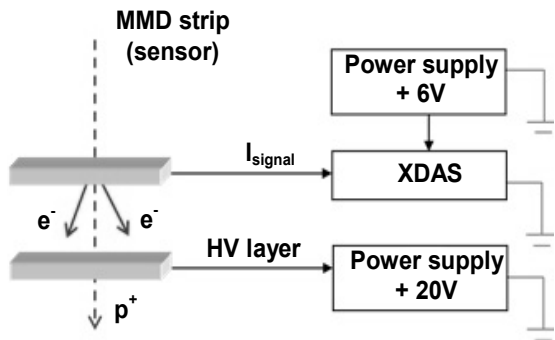


Fig. 1. Incident particles on the strips initiate secondary electron emission.
Readout is provided by X-DAS system

XDAS allows creating large detector arrays with high speed readout in digital format. It consists out of Detector Head Boards with analog output modules and Signal Processing Boards with 16-bit digital output.

Each detector head board acquires 128 channels of data, using a charge integrating ASIC and sends it via a local data bus to the signal processing board. The signal processing board converts the data into 14-bit format. On-board processing enables up to 4 data samples to be taken and added to produce a 16-bit output. This is transmitted via a data interface board to the host processor via USB2, data I/O, Ethernet or frame-grabber card. A system can handle more than 20000 channels with an exposure time from 100 μ s to 100 ms, depending on the number of channels.

Experiment at Heidelberg Heavy-Ion Therapy Center (HIT). To fully exploit the focused energy deposition of ^{12}C in carbon ion therapy, a high accuracy on dose location is required. It has been shown that the detection of nuclear reaction products resulting from the interaction of the beam with atomic nuclei of the tissue (can be positron emitting nuclides, prompt photons or light charged particles) provides relevant information that can be used for the verification of the delivered dose. The experiment in HIT was devoted to collect experimental data of distributions of different types of secondary emission with the best possible beam control. Schematic view of the experimental setup is presented on Fig. 2.

At HIT the treatment can be performed by protons, α -particles, ^{12}C and ^{16}O ions at different energies (from 50 to 430 MeV/nucleon) and intensities (from 10^6 to $2 \cdot 10^9$ particles/s). Fig. 3 illustrates the response of MMDw on the ^{12}C beam with the energy 86.7 MeV/nucleon and intensity $6 \cdot 10^6$ particles/s.

Experiment at Innovacia Cancer Center. The series of test measurements were performed at Innovacia Cancer Center with linear accelerator Varian Clinac 2100C. Preliminary results with 20 MeV electrons are presented on Fig. 4.

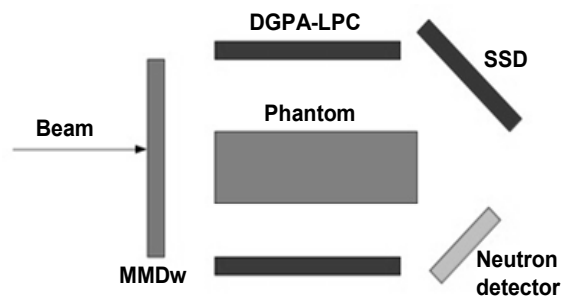


Fig. 2. HIT experimental setup.

The overall beam intensity was monitored by the MMDw. The annihilation photons were recorded by the DGPA-LPC (large acceptance pixelated detector) detectors placed following the beam direction in the plane $z=0$ ($\theta=90^\circ$), and by the in-beam PET system at HIT ($\theta=0^\circ$)

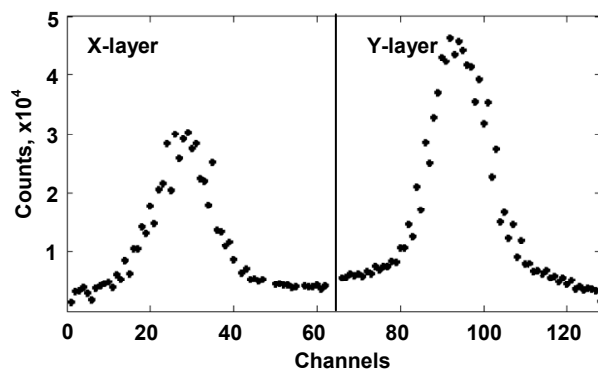


Fig. 3. MMDw response to ^{12}C beam with energy 86.7 MeV/nucleon and intensity $6 \cdot 10^6$ particles/s.
1-64 Channels correspond to the X-plane of MMDw, while 65-128 – Y-plane

Experiment at Innovacia Cancer Center. The series of test measurements were performed at Innovacia Cancer Center with linear accelerator Varian Clinac 2100C. Preliminary results with 20 MeV electrons are presented on Fig. 4.

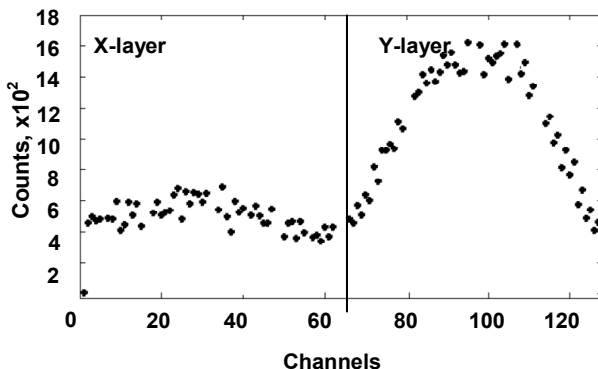


Fig. 4. MMDw response on the 20 MeV electrons at intensity of 100 MU/m. 1-64 Channels correspond to the X-plane of MMDw, while 65-128 – Y-plane.
The beam $5 \cdot 5 \text{ cm}^2$ was focused in the center of the detector

The influence of MMDw on the dose distribution for the 20 MeV electron beam was estimated. We performed absolute dosimetry measurements with and without detector

in the beam. We mentioned a higher absorbed dose on 0.4% for the measurements with detector inside the beam.

Conclusions. Advantages of MMD allow to create a reliable radiation monitoring systems for radiation therapy applications. Their implementation will improve beam delivery to tumor tissue, fast imaging and evaluation of data, optimization of treatment regimes. Commercially available read-out systems can be applied to build high efficient monitoring system for hadron radiation therapy. MMD has shown reliable performance for online beam profile monitoring. Once calibrated, the detector could also be used for dose monitoring in real time. This is one of the main tasks for the further measurements.

Acknowledgements. The authors thank ULICE TNA campaign within the FP7 European Programme and the Grant Agreement no 228436 for the allocated beamtime at HIT. We thank Collaboration MEDIPIX for TimePix

detectors. This work has been partially supported by the NASU grant CO-4-1-2014.

REFERENCE:

1. *Martinez-Rovira I.* Monte Carlo-based dose calculation engine for minibeam radiation therapy / *I. Martinez-Rovira, J. Sempau, Y. Prezado* // *Physica Medica: European Journal of Medical Physics.* – 2013. – Vol. 30. – Issue 1. – P. 57–62.
2. *Micro-strip metal detector for the beam profile monitoring / Pugatch V., Aushev V., Fedorovitch O. et al.* // *Nuclear Instruments and Methods.* – 2007. – Vol. A 581. – P. 531.
3. *Metal Micro-detector TimePix imaging synchrotron radiation beams at the ESRF Bio-Medical Beamline ID17 / Pugatch V., Campbell M., Chau A. et al.* // *Nuclear Instruments and Methods A.* – 2012. – Vol. 682. – P. 8–11.

Submitted on 07.11.14

Яковенко В., канд. фіз.-мат. наук, відділ фізики високих енергій, Інститут ядерних досліджень НАН України, Медична клініка "Інновація"; Ковальчук О., голов. інж., Пугач В., проф., Охріменко О., пров. інж., Сорокін Ю., канд. фіз.-мат. наук, відділ фізики високих енергій, Центр дослідження важких іонів імені Гельмгольца, Інститут ядерних досліджень НАН України; Презадо Й., канд. фіз.-мат. наук, Мартінез-Ровіра І., канд. фіз.-мат. наук, відділення зображення і моделювання в нейробіології та онкології, CNRS, Франція Ілюхіна А., студ., фізичний факультет, Київський Національний Університет імені Тараса Шевченка

МЕТАЛЕВІ МІКРО-ДЕТЕКТОРИ ДЛЯ ВІЗУАЛІЗАЦІЇ ТА МОНІТОРИНГУ ПРОФІЛЮ ПУЧКА В РАДІАЦІЙНІЙ ТЕРАПІЇ

Металеві мікро-детектори (ММД) розроблені в Інституті ядерних досліджень НАН України. В роботі представлені фізика та техніка таких детекторів для дозиметрії, реєстрації та візуалізації пучків заряджених частинок. Для забезпечення точного моніторингу профілю пучка виготовлений 128-канальний X-Y ММД. Проведено тестові вимірювання з цим детектором для електронів з енергією 20 MeV (Медична клініка "Інновація"), а також високоенергетичних адронних пучків (протони, іони ^{12}C та ^{16}O , Хайдельберг, Центр важко-іонної терапії). Результати цих досліджень обговорюються у роботі. Результати наших досліджень вказують на можливість застосування ММД в клінічній практиці.

Ключові слова: металеві мікро-детектори, моніторинг профілю пучка, моніторинг дози онлайн, міні-пучкова променева терапія.

Яковенко В., канд. физ.-мат. наук, отдел физики высоких энергий, Институт ядерных исследований НАН Украины, Медицинская клиника "Инновация"; Ковальчук А., глав. инж., Пугач В., проф., Охрименко А., вед. инж., Сорокин Ю., канд. физ.-мат. наук, отдел физики высоких энергий, Центр исследования тяжелых ионов имени Гельмгольца, Институт ядерных исследований НАН Украины; Презадо И., канд. физ.-мат. наук, Мартінез-Ровіра И., канд. физ.-мат. наук, Отделение изображения и моделирования в нейробиологии и онкологии, CNRS, Франция Ілюхіна А., студ., физический факультет, Киевский Национальный Университет имени Тараса Шевченко

МЕТАЛЛИЧЕСКИЕ МИКРО-ДЕТЕКТОРЫ ДЛЯ ВИЗУАЛИЗАЦИИ И МОНИТОРИНГА ПРОФИЛЯ ПУЧКА В РАДИАЦИОННОЙ ТЕРАПИИ

Металлические микро-детекторы (ММД) разработаны в Институте ядерных исследований НАН Украины. В работе представлены физика и техника таких детекторов для дозиметрии, регистрации и визуализации пучков заряженных частиц. Для обеспечения точного мониторинга профиля пучка изготовлен 128-канальный X-Y ММД. Проведены тестовые измерения с этим детектором для электронов с энергией 20 MeV (Медицинская клиника "Инновация"), а также высокоэнергетических адронных пучков (протоны, ионы ^{12}C и ^{16}O , Хайдельберг, Центр тяжело-ионной терапии). Результаты этих исследований обсуждаются в данной работе. Результаты наших исследований свидетельствуют о возможности применения ММД в клинической практике.

Ключевые слова: металлические микро-детекторы, мониторинг профиля пучка, мониторинг дозы онлайн, мини-пучковая лучевая терапия.

UDC 535.1

A. Ivanisik, Ph.D., O. Isaienko, post-grad. stud.,
P. Korotkov, D.Sci., Taras Shevchenko national university of Kyiv,
Faculty of Radiophysics, Medical Radiophysics Department,
G. Ponezha, Ph.D., National academy of statistics, accounting and auditing,
Faculty of Economy and Statistics

SELF-PHASE MODULATION OF LASER PULSE IN STRATIFIED SELF-FOCUSING MEDIUM

Self-phase modulation at quasi-stationary self-focusing in stratified Kerr liquid that is divided by an optically homogenous (non-scattering) layer has been considered. Instantaneous frequency of the laser radiation pulse at transition of the self-focusing area through a thin transparent layer is calculated. In addition, absorption of the light in the layer is taken into account.

The transition radiation on the layer (a glass partition or a similar structure), located in the self-focusing medium, has analogous characteristics with the radiation at the exit border of the medium. The frequency shift of the transition radiation, originated on the layer, is smaller than the shift of the laser radiation at the exit border of the medium. However, considering that the number of layers can be more than one, it could be concluded that introduction of the layers simplifies the experimental observation of the transition radiation and its usage.

Keywords: laser, self-focusing, phase self-modulation, transition effect

Introduction. Combination of Stimulated Raman Scattering (SRS) as an effective method of laser radiation frequency tuning [5], and self-focusing (SF) as a method of

spatial scanning by powerful pulses of electromagnetic field at a velocity close to the speed of light [4], allows transforming the initial pulse of laser radiation into a

© Ivanisik A., Isaienko O., Korotkov P., Ponezha G., 2014

random sequence of sub-pulses with a controlled duration and frequency of each sub-pulse [3]. To achieve this, the laser pulse has to be guided through a sample made of transverse layers of different SRS-active self-focusing materials with a specified thickness. However, implementation of this idea faces major physical challenges related with the effect of phase modulation on the laser radiation. This paper is dedicated to analyzing these physical challenges.

Phase self-modulation in self-focusing cell divided by a transparent layer. Let's consider the case of a thin non-absorbing layer, which is located in a self-focusing medium. We assume that this layer does not have a light field induced shift Δn and the value n_0 of its linear refractive index is approximately equal to the refractive index of SRS-active medium. Such situation can be achieved in a cell filled with self-focusing (Kerr) liquid, which contains thin optically transparent glass partition. Under such conditions, SF in Kerr medium occurs without dissipation of laser radiation in the layer.

The model proposed in [1] can be used to calculate the phase shift $\Delta\varphi$ of Gaussian pulse, with duration $\tau=1$ ns and normalized power $\tilde{P} = P/P_{cr}$ (P_{cr} is a critical power of SF), at the exit from the medium with length L . This model takes into account alteration in time t , which occurs in the focal area position, and its geometrical dimensions depending on the radiation intensity. Self-induced phase shift was calculated using expression:

$$\Delta\varphi(t) = k_0 \tilde{P}(t) \frac{(1.22\lambda_0)^2}{16n_0} \left(\int_0^{L_\ell} a_z^{-2} dz + \int_{L_\ell}^L a_z^{-2} dz \right), \quad (1)$$

where $k_0 = 2\pi/\lambda_0$, λ_0 is a wave length of the excitation pulse in vacuum, L_ℓ is a distance between the entrance border of the cell and the thin layer of linear optical medium with thickness ℓ , a_z is a radius of the laser beam at longitudinal coordinate z . When calculating using expression (1), it is assumed that the beam propagates linearly across the thin layer of non-active medium, thus ℓ has to be adequate with a confocal parameter of the focal area. With initial radius of the entry beam $a_0 = 113 \mu\text{m}$, minimum radius of the beam at the focal area $a_f = 5 \mu\text{m}$, and $\lambda_0 = 0.69 \mu\text{m}$, the focal area size changes from 14 mm to 0.7 mm, if \tilde{P} varies in the range from $\tilde{P}_{min} = 1.3$ to $\tilde{P}_{max} = 3.6$.

Self-phase modulation induces the corresponding frequency shift of the laser pulse. Instantaneous frequency shift (in inverse centimeters) equals:

$$\Delta\nu(t) = - (2\pi c)^{-1} \partial(\Delta\varphi)/\partial t, \quad (2)$$

where c is the speed of light in vacuum (in cm/sec).

The paper [2] states that when the self-focusing focal point crosses the border of two mediums (in [2] it is a "medium-vacuum" border), there the transition radiation appears at the frequency, which is shifted ($\sim \pm 140 \text{ cm}^{-1}$) relative to the excitation pulse of laser radiation. However, the transition radiation has a low ($\sim 0.5\%$) spectral density in comparison with the spectral density of the initial pulse. Bigger spectral density of the transition radiation can be achieved at the moments of time, which correspond to the highest instantaneous power of the laser pulse. Therefore, the layer must be located near a stop point of the focal area.

Self-induced phase shift and instantaneous frequency shift, which appear during self-modulation of the laser pulse in toluene-filled cell with length $L = 30$ cm and a thin

transparent layer of non-active medium ($\ell = 3$ mm, $L_\ell = 7$ cm) near the stop point $z_{f_{min}} \approx 6$ cm (minimal distance of the self-focusing focal area at $\tilde{P}_{max} = 3.6$), are shown in Fig. 1 and Fig. 2.

Self-induced phase shift (Fig.1) has two local minimums near $t=0$, which correspond to the moment when the focal area crosses the thin layer of non-active medium. When the layer thickness ℓ and distance L_ℓ increase, the width and the depth of the minimums also increase. Other parts of the plot shown in Fig.1 look identical to the phase shift, which occurs under SF in the homogenous (without a partition) medium [1].

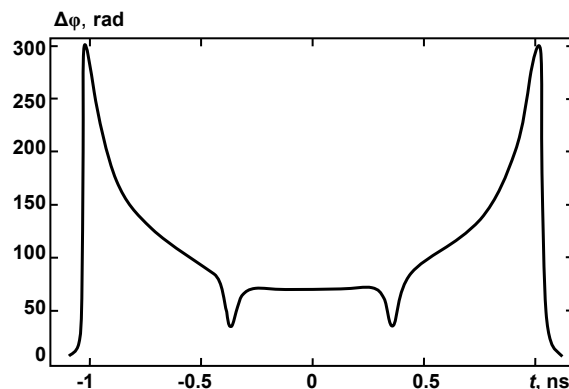


Fig. 1. The self-induced phase shift of the laser pulse at the exit of a toluene-filled cell divided by the transparent partition
($L = 30$ cm; $L_\ell = 7$ cm; $\ell = 3$ mm; $\tau = 1$ ns; $\tilde{P}_{max} = 3.6$)

The transparent layer induces additional instantaneous frequency shift. The frequency shift is presented in Fig. 2.

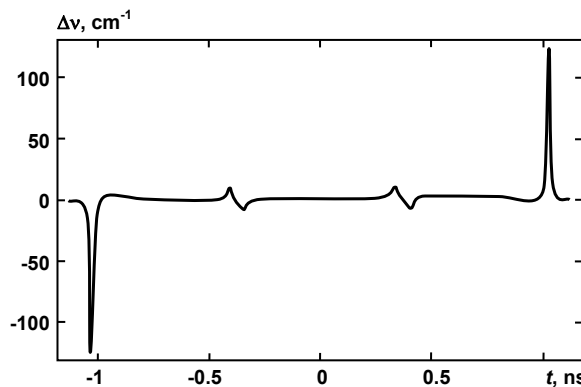


Fig. 2. The instantaneous frequency shift of the laser pulse at the exit of a toluene-filled cell divided by the transparent partition
($L = 30$ cm; $L_\ell = 7$ cm; $\ell = 3$ mm; $\tau = 1$ ns; $\tilde{P}_{max} = 3.6$)

Phase self-modulation in self-focusing cell divided by an absorption layer. Presume that the self-focusing medium contain an infinitely thin absorbing partition with a dissipation factor k . When the beams pass through the partition under SF, the laser pulse loses a part of its energy $k = 1 - (\tilde{P}_\ell(t)/\tilde{P}(t))$, where $\tilde{P}(t)$ and $\tilde{P}_\ell(t)$ are the power of laser pulse at a front and behind the partition.

The laser pulse passes the partition with different in time convergence angles and loses part of its energy. Therefore, the laser beam focuses at another point than

without the absorbing partition. With usage of [1, 6], the dependence of the beam radius a_z from the coordinate z after the partition can be approximately expressed as:

$$a_z = \sqrt{a_\ell^2 \left| -\frac{z^2}{\gamma_\ell^2 a_\ell^4} + \left(1 + \left(\frac{da}{dz} \right)_{z=L_\ell} \frac{z}{a_\ell} \right)^2 \right|^{\mu_\ell/2}} + a_f^2, \quad (3)$$

where a_ℓ is the beam radius at the partition, $(da_z/dz)_{z=L_\ell}$ is derivative at the partition, a_f is the minimum beam radius at the center of the focal area, γ_ℓ and μ_ℓ are parameters depended on the instantaneous power $\tilde{P}_\ell(t)$:

$$\gamma_\ell = 0.367n_0k_0 \left/ \left[\left(\sqrt{\tilde{P}_\ell} - 0.852 \right)^2 - 0.0219 \right]^{0.5} \right., \quad (4)$$

$$\mu_\ell = 2.9\tilde{P}_\ell^{-0.5} + \tilde{P}_\ell^{-1} + 1, \quad (5)$$

Dependencies in Fig. 3 and Fig. 4 present the self-induced phase shift of the laser pulse and the instantaneous frequency, respectively, when the partition is located at distance $L_\ell = 7$ cm from the entrance of the cell and has the dissipation factor $k = 0.73$.

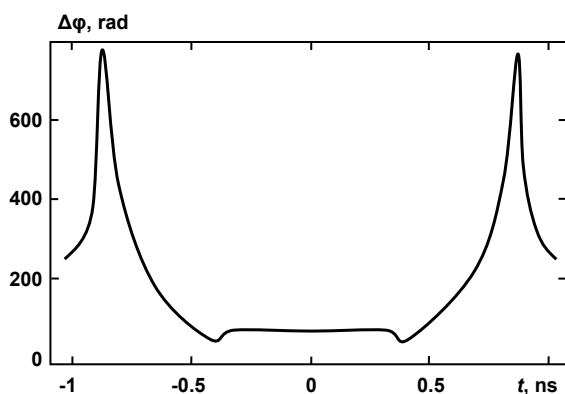


Fig. 3. The self-induced phase shift of the laser pulse at the exit of a toluene-filled cell divided by the thin absorbing partition
($L = 30$ cm; $L_\ell = 7$ cm; $k = 0.73$; $\tau = 1$ ns; $\tilde{P}_{\max} = 3.6$)

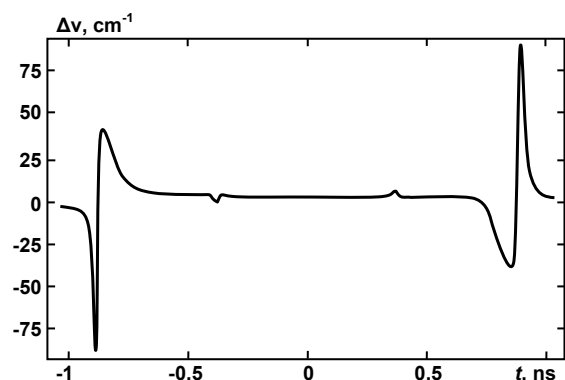


Fig. 4. The instantaneous frequency shift of the laser pulse at the exit of a toluene-filled cell divided by the thin absorbing partition
($L = 30$ cm; $L_\ell = 7$ cm; $k = 0.73$; $\tau = 1$ ns; $\tilde{P}_{\max} = 3.6$)

The self-induced phase shift in Fig. 3 has two distinct maximums and minimums (the minimum at $t = 0$ is almost unnoticeable).

A movement of the focal area behind the thin absorbing partition causes addition instantaneous frequency shift of laser pulse. Obviously, the plots in Fig. 2 and Fig. 4 have distinctive features.

In addition, it is possible to consider a local inhomogeneity of the "bubble" type, which in the simplest case is located on the axis of the laser beam path and has a radius, adequate with the geometrical dimensions of the focal area, but is smaller than the radius of the beam at the entrance of the medium. The beam appears "bubble" and dissipates during its intersection. The dissipation is as higher, as close the focal area is to the inhomogeneity. There comes a moment, when the inhomogeneity appears in a focal area. At that moment, when the focal area disappears for a short period, instantaneous frequency shift of laser pulse will be the same as at the exit of the cell.

Conclusions. In general practice, the layers combine properties of both described structures. This complicates the calculation of the laser pulse spectra. Nevertheless, the self-induced frequency shift of the laser pulse at the layers or local inhomogeneities in the self-focusing medium can be described by combining the two models described above.

There is small difference between the physical mechanisms related with the generation of the transition radiation in the transparent non-self-focusing layers, with definite width, and in the infinitely thin absorbing layers. In the first case, the radiation is generated due to the focal area entering and exiting the self-focusing medium near the layer. The second case takes place due to the change of the focal area length, when it crosses the absorbing thin layer.

The frequency shifts of the laser pulse originated at the layers are lower than the frequency shifts of the transition radiation originated from the border of the medium. However, there's observed a general trend of the radiation energy increase, which is almost inversed to the value of the frequency shift. Taking into account that the number of layers can be rather high, it could be considered that introduction of the layers greatly facilitates the experimental observation of the transition radiation. To some extent this can be compared with the transition radiation in the "foam" structures, which are used to increase the power of the transition and Cherenkov radiation in the applicable particle counters.

The stand-alone group of inhomogeneities, which lead to the generation of the intense transition radiation due to phase modulation, is inhomogeneities as scattering or absorbing "bubble", which size $\sim 1 \mu\text{m}$ is close to the focal area diameter. Such inhomogeneities can occur naturally in medium. Despite the relatively small size of the inhomogeneities (this provides sufficient optical quality of the medium and makes possible the self-focusing in general) their role in the generation of the transition radiation can be exceptional. This is result of short-term collapse in formation of the focal area, similar to the intersection of the medium borders by the focal area.

Reference

1. Borisenko A. D., Dudka S. O., Ivanisik A. I. Quasi-stationary phase self-modulation of the laser pulses in Kerr liquids // Bulletin of T. Shevch. Nat. Univ. of Kyiv. Series: Physics and Mathematics. – 2003. – №.1. – P. 259–267.
2. Dudka S. O., Ivanisik A. I., Konopatskiy A. V., Korotkov P. A. Transition effect at the medium-vacuum interface under the self-phase modulation of a light pulse // Ukr. J. Phys. – 2006. – Vol. 51, №2. – P. 140–146.
3. Ivanisik A. I., Maliy V. I., Ponezha G. V. Stimulated Raman scattering in the self-focusing mediums: new methods of experimental research // Bulletin of T. Shevch. Nat. Univ. of Kyiv. Series: Physics and Mathematics. – 1997. – №.4. – P. 239–248.
4. Ivanisik A. I., Korotkov P. A., Ponezha G. V. Temporal dynamics of focal point location under self-focusing of nanosecond laser pulses // Ukr. J. of Phys. Opt. – 2013. – Vol. 15, №1. – P. 1–8.

5. Yao J., Wang Y. Nonlinear optics and solid-state lasers: advanced concepts, tuning-fundamentals and applications series.– Springer Series in Optical Sciences, 2012.– 688 p.

6. Shen Y. R. The Principles of nonlinear optics: translated from english.– M.: Nauka, 1989.– 560 p.

Submitted on 30.01.14

Іванісік А., канд. фіз.-мат. наук, Ісаєнко О., асп., Коротков П., д-р фіз.-мат. наук, радіофізичний факультет, кафедра медичної радіофізики Київський національний університет імені Тараса Шевченка, Понежа Г., канд. фіз.-мат. наук, економіко-статистичний факультет, Національна академія статистики, обліку та аудиту

ФАЗОВА САМОМОДУЛЯЦІЯ ЛАЗЕРНОГО ІМПУЛЬСУ В ШАРУВАТИХ САМОФОКУСУЮЧИХ СЕРЕДОВИЩАХ

У роботі розглянуто фазову само модуляцію за квазістаціонарного самофокусування у шаруватій керрієській рідині, розділеній оптично однорідним (нерозсіюючим) прошарком. Обраховано миттєву частоту імпульсу лазерного випромінювання в момент перетину області самофокусування тонкого прозорого шару. Додатково враховано поглинання світла на шарі.

Перехідне випромінювання на прошарку (скляній пластинці або подібній структурі), розміщеному в самофокусуєчому середовищі, має спільні характеристики з випромінюванням на виході із середовища. Зсув частоти перехідного випромінювання, що вийшло із шару, менший за зсув частоти лазерного випромінювання на виході із середовища. Враховуючи, що прошарків може бути кілька, виявляється, що введення шарів у середовище спрощує експериментальне дослідження та застосування перехідного випромінювання.

Ключові слова: лазер, самофокусування, фазова само модуляція, перехідний ефект

Иванисик А., канд. физ.-мат. наук, Исаенко А., асп., Коротков П., д-р физ.-мат. наук, радиофизический факультет, кафедра медицинской радиофизики, Киевский национальный университет имени Тараса Шевченко, Понежа Г., канд. физ.-мат. наук, экономико-статистический факультет, Национальная академия статистики, учета и аудита

ФАЗОВАЯ САМОМОДУЛЯЦИЯ ЛАЗЕРНОГО ИМПУЛЬСА В СЛОИСТЫХ САМОФОКУСИРУЮЩИХ СРЕДАХ

В работе рассмотрена фазовая само модуляция в случае квазистационарной самофокусировки в слоистой керровской жидкости, разделенной оптически однородным (нерассеивающим) слоем. Рассчитана мгновенная частота импульса лазерного излучения в момент перехода области самофокусировки через тонкий прозрачный слой. Дополнительно учтено поглощение света на слое.

Переходное излучение на слое (стеклянной пластинке или подобной структуре), размещенном в самофокусирующей среде, имеет общие характеристики с излучением на выходе из среды. Смещение частоты переходного излучения, вышедшего из слоя, меньше сдвига частоты лазерного излучения на выходе из среды. Учитывая, что слоев может быть несколько, оказывается, что введение слоев в среду упрощает экспериментальное исследование и применение переходного излучения.

Ключевые слова: лазер, самофокусировка, фазовая само модуляция, переходный эффект

UDC 532,533, 533.9, 530.182

P. Kostrobij, Sc.D., B. Markovych, Ph.D., R. Tokarchuk, assist., Department of Applied Mathematics, Institute of Applied Mathematics and Fundamental Sciences, Lviv Polytechnic National University, Yu. Chernomorets, Ph.D. stud., Department of Nonequilibrium Processes Theory, Institute for Condensed Matter Physics, NAS of Ukraine M. Tokarchuk, Sc.D., Department of Applied Mathematics, Institute of Applied Mathematics and Fundamental Sciences, Lviv Polytechnic National University, Department of Nonequilibrium Processes Theory, Institute for Condensed Matter Physics, NAS of Ukraine

STATISTICAL THEORY OF ELECTRO-DIFFUSION PROCESSES OF IONS INTERCALATION IN "ELECTROLYTE – ELECTRODE" SYSTEM

A statistical theory of classical-quantum description of electro-diffusion processes of intercalation in "electrolyte-electrode" system is proposed. Using the nonequilibrium statistical operator method the generalized transport equations of Nernst-Planck type for ions and electrons in the "electrolyte-electrode" system are obtained. These equations take into account time memory effects and spatial heterogeneity. A one-dimensional simplified model of intercalation of ions into the electrode structure with taking the dielectric polarization into account is proposed.

Keywords: electrolyte, electrode, intercalation, nonequilibrium statistical operator .

1. Introduction. Theoretical studies of electro-diffusion transport processes of ions and electrons in the "electrode-electrolyte" systems remain actual nowadays [6, 16, 19]. They are linked with a need to describe nonequilibrium processes of intercalation as well as to develop a theory suitable for practical application to predicting and controlling these processes. The difficulties in describing processes at electrode are first of all related with surface phenomena at electrolyte-electrode interface. In this region, complicated processes of adsorption and diffusion take place which are connected with a problem of charge accumulation at battery electrodes. In the system "electrode (anode)-electrolyte-electrode (cathode)", the anode plays role of the source of both electrons, which move to cathode by the corresponding electric circle, and lithium ions in electrolyte. A cathode is typically a metallic

system (nickel, for example) covered with active material containing carbon and in which lithium ions intercalate from the solution. Herewith, an important issue is the following one. The electrochemical processes in electrolyte solution can be described using methods of classical statistical mechanics, whereas in the region near the electrolyte-electrode interface and inside the electrodes, description of diffusion and intercalation processes should be implemented by means of the modern methods of quantum statistical physics. In this field, the electrochemical impedance studies [4, 1, 8] of electro-diffusion transport processes in Li-ion batteries [18, 9, 10] were carried out and intercalation/deintercalation processes were investigated using nonequilibrium thermodynamics [19, 9, 2, 17]. The theoretical and experimental studies of chemical diffusion coefficient for lithium ions in intercalation

processes into various electrode materials are actively carried out [12, 20, 5, 7, 15]. A complicated dependence of chemical diffusion coefficient on a degree of electrochemical intercalation and on alteration of structure of cathode material is analyzed as well. In particular, in Ref. [12] based on a detailed analysis of experimental investigations for various materials an important conclusion was drawn: the structure of intercalated material has the main influence on the chemical diffusion coefficient. Consequently, it is important to take into account to some extent the altering of microstructure of cathode material, in particular, via its polarization properties.

2. Generalized transport Nernst-Planck equations

$$\frac{\partial}{\partial t} \delta n_{\alpha}(\vec{r}_i; t) = \frac{\partial}{\partial \vec{r}_i} \cdot (\vec{j}_{\alpha}^{(1)}(\vec{r}_i; t) + \vec{j}_{\alpha}^{(2)}(\vec{r}_i; t) + \vec{j}_{\alpha}^{(3)}(\vec{r}_i; t)),$$

where the ion flows have the following structure [19]:

$$\begin{aligned} \vec{j}_{\alpha}^{(1)}(\vec{r}_i; t) &= \sum_{l' \gamma} \int d\vec{r}_{l'} \int_{-\infty}^t e^{\varepsilon(t'-t)} \beta D_{jj}^{\alpha \gamma}(\vec{r}_i, \vec{r}_{l'}; t, t') \times \frac{\partial}{\partial \vec{r}_{l'}} Z_{\gamma} e \phi(\vec{r}_i; t') dt' - \int d\vec{r}_{s'} \int_{-\infty}^t e^{\varepsilon(t'-t)} \beta D_{jj}^{\alpha e}(\vec{r}_i, \vec{r}_{s'}; t, t') \cdot \frac{\partial}{\partial \vec{r}_{s'}} e \phi(\vec{r}_{s'}; t') dt' \\ \vec{j}_{\alpha}^{(2)}(\vec{r}_i; t) &= \sum_{l' \gamma} \int d\vec{r}_{l'} \sum_{l'' \alpha'} \int d\vec{r}_{l''} \int_{-\infty}^t e^{\varepsilon(t'-t)} \beta D_{jj}^{\alpha \alpha'}(\vec{r}_i, \vec{r}_{l''}; t, t') \times \frac{\partial}{\partial \vec{r}_{l''}} [\tilde{\Phi}_d^{-1}(\vec{r}_i, \vec{r}_{l''}; t')]_{\alpha, \gamma} \delta n_{\gamma}(\vec{r}_{l''}; t') dt' \\ &\quad - \int d\vec{r}_{s'} \int d\vec{r}_{s''} \int_{-\infty}^t e^{\varepsilon(t'-t)} \beta D_{jj}^{\alpha e}(\vec{r}_i, \vec{r}_{s''}; t, t') \times \frac{\partial}{\partial \vec{r}_{s''}} [\tilde{\Phi}_d^{-1}(\vec{r}_i, \vec{r}_{s''}; t')]_{ee} \delta \bar{n}_e(\vec{r}_{s''}; t') dt' \\ \vec{j}_{\alpha}^{(3)}(\vec{r}_i; t) &= \sum_{l' \gamma} \int d\vec{r}_{l'} \sum_{l'' \alpha'} \int d\vec{r}_{l''} \int_{-\infty}^t e^{\varepsilon(t'-t)} \beta \times \bar{D}_{jjn}^{\alpha \alpha' \gamma}(\vec{r}_i, \vec{r}_{l''}; t, t') \cdot \frac{\partial}{\partial \vec{r}_{l''}} Z_{\alpha'} e \phi(\vec{r}_{l''}; t') \delta n_{\gamma}(\vec{r}_{l''}; t') dt' + \sum_{l' \gamma} \int d\vec{r}_{l'} \int d\vec{r}_{s'} \int_{-\infty}^t e^{\varepsilon(t'-t)} \beta \bar{D}_{jjn}^{\alpha \gamma e}(\vec{r}_i, \vec{r}_{l'}, \vec{r}_{s'}; t, t') \\ &\quad \times \frac{\partial}{\partial \vec{r}_{l'}} Z_{\gamma} e \phi(\vec{r}_{l'}; t') \delta \bar{n}_e(\vec{r}_{s'}; t') dt' - \sum_{l' \gamma} \int d\vec{r}_{l'} \int d\vec{r}_{s'} \int_{-\infty}^t e^{\varepsilon(t'-t)} \beta \bar{D}_{jjn}^{\alpha \gamma}(\vec{r}_i, \vec{r}_{s'}; t, t') \\ &\quad \times \frac{\partial}{\partial \vec{r}_{s'}} e \phi(\vec{r}_{s'}; t') \delta n_{\gamma}(\vec{r}_{l'}; t') dt' - \int d\vec{r}_{s'} \int d\vec{r}_{s''} \int_{-\infty}^t e^{\varepsilon(t'-t)} \beta \bar{D}_{jjn}^{\alpha ee}(\vec{r}_i, \vec{r}_{s''}; t, t') \times \frac{\partial}{\partial \vec{r}_{s''}} e \phi(\vec{r}_{s''}; t') \delta \bar{n}_e(\vec{r}_{s'}; t') dt' \end{aligned}$$

Here z_{γ} is ion of valence and e is the electron charge; $\phi(\vec{r}_i; t')$ and $\phi(\vec{r}_{s'}; t')$ are scalar potentials of the electromagnetic field, which during the charging/discharging of batteries are the driving forces of transport processes of ions in the electrolyte and intercalated ions and electrons in the electrode.

These equations take into account the time memory effects and spatial heterogeneity. An important contribution to the generalized Nernst-Planck type equations are provided by the transport kernels which, unlike the generalized diffusion coefficients, are the third-order correlation functions and enter into equations via terms of second order in the parameters which describe the dynamic correlations between the field and a density.

$$D_{jj}^{\alpha \gamma}(\vec{r}_i, \vec{r}_{l'}; t, t') = \langle (1 - P(t)) \hat{j}_{\alpha}(\vec{r}_i) T_q(t, t') (1 - P(t')) \hat{j}_{\gamma}(\vec{r}_{l'}) \rangle_{q'}^t$$

is the generalized diffusion coefficient of ions as a function of coordinates and time. When $l = f$ and $l' = f'$, we have diffusion coefficient in electrolyte solution.

$$\hat{j}_{\alpha}(\vec{r}_i) = \frac{1}{m_{\alpha}} \sum_{j=1}^{N_{\alpha}} \vec{p}_j \delta(\vec{r}_i - \vec{r}_j)$$

is the current density of ions of species α in the electrolyte solution. When $l = s$ and $l' = s'$, we have a cross-diffusion coefficient for ions in the electrolyte solution and electrode. In this case,

$$\hat{j}_{\alpha}(\vec{r}_s) = \frac{1}{m_{\alpha}} (\hat{\psi}_{\alpha}^{+}(\vec{r}_s) \nabla_s \hat{\psi}_{\alpha}(\vec{r}_s) - \nabla_s \hat{\psi}_{\alpha}^{+}(\vec{r}_s) \hat{\psi}_{\alpha}(\vec{r}_s))$$

is the operator of current density of ions in the electrode

We proposed a statistical theory of classical-quantum description of electro-diffusion transport processes of ions and electrons in the "electrolyte-electrode" system [13] using the D. Zubarev nonequilibrium statistical operator (NSO) method [14, 21]. The presented theory takes the spatial heterogeneity and memory effects into account. The model and corresponding Hamiltonian are formulated and the nonequilibrium statistical operator for the "electrolyte-electrode" system as the functional of the corresponding parameters of the reduced description of the nonequilibrium processes (observable parameters) is obtained. In this approach, we receive the generalized transport equations such as Nernst-Planck equation for electrons and ions in the "electrolyte-electrode" system using the method of nonequilibrium statistical operator:

structure. When $l = s$ and $l' = s'$, we have the generalized quantum diffusion coefficient for ions in the electrode subsystem:

$$\begin{aligned} D_{jj}^{\alpha e}(\vec{r}_i, \vec{r}_{s'}; t, t') &= \langle (1 - P(t)) \hat{j}_{\alpha}(\vec{r}_i) T_q(t, t') \\ &\quad \times \int_0^1 d\tau \rho_{\phi}^{-\tau}(t') (1 - P(t')) \hat{j}_{e}(\vec{r}_{s'}) \rho_{\phi}^{\tau}(t') \rangle_{\phi}^t \end{aligned}$$

defines a generalized of ion-electron diffusion, herewith, ion can be in the electrolyte subsystem or in the electrode one. $\rho_{\phi}(t')$ is the quasiequilibrium statistical operator. In the generalized Nernst-Planck equations an important role belongs to transport kernels

$$\begin{aligned} D_{jjn}^{\alpha \alpha' \gamma}(\vec{r}_i, \vec{r}_{l'}, \vec{r}_{l''}; t, t') &= \sum_{l'' \alpha''} \int d\vec{r}_{l''} \langle (1 - P(t)) \hat{j}_{\alpha}(\vec{r}_i) T_q(t, t') \\ &\quad \times (1 - P(t')) \hat{j}_{\alpha'}(\vec{r}_{l''}) \hat{n}_{\alpha''}(\vec{r}_{l''}) \rangle_{\phi}^t [\tilde{\Phi}_d^{-1}(\vec{r}_i, \vec{r}_{l''}; t')]_{\alpha, \gamma} \end{aligned}$$

Unlike the transport kernels related with the generalized coefficient, they are the correlation functions of the third order and enter into the equations via the second order in the parameters $\phi(\vec{r}_i; t') \delta n_{\gamma}(\vec{r}_{l''}; t')$, $\phi(\vec{r}_i; t') \delta \bar{n}_e(\vec{r}_{s'}; t')$, $\phi(\vec{r}_{s'}; t') \delta \bar{n}_e(\vec{r}_{s''}; t')$. We also obtained the system of equations for the flows of ions and electrons from which the conditions of the existence of stationary processes can be determined. Approximate calculation of diffusion coefficients by means of the method of moments in Gaussian approximation provides us the relationship between the unary and pair distribution functions of quasiequilibrium state.

3. One-dimensional model of intercalation of ions into the electrode structure with taking the dielectric polarization into account In the generalized Nernst-Planck equations that describe the transport processes of ions and electrons in the "electrolyte-electrode" system with spatial heterogeneity and memory effects in time polarization processes are taken into account [13] by the averaged Maxwell's equations for the electromagnetic field. Based on this approach, we consider a simplified model of ion intercalation based on the Nernst-Planck equation, excluding electronic component and memory effects in time. That is, we consider a one-dimensional model with diagram shown in Figure

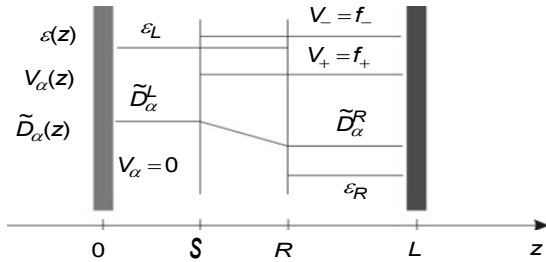


Fig. 1. Diagram of the "electrode-electrolyte" systems

We describe transport processes of ions between the electrodes by the Nernst-Planck equations

$$\frac{\partial}{\partial t} n_{\alpha}(z;t) = \frac{\partial}{\partial z} [\tilde{D}_{\alpha}(z;t) [\frac{\partial}{\partial z} n_{\alpha}(z;t) + n_{\alpha}(z;t) (\frac{\partial}{\partial z} V_{\alpha}(z) + Z_{\alpha} e \frac{\partial}{\partial z} \varphi(z;t))]]$$

where $\tilde{D}_{\alpha}(z;t)$ is the mobility of ions of class α , $V_{\alpha}(z)$ is the surface potential of two phases electrolyte-electrode, $\varphi(z;t)$ is the electric potential which satisfies the Poisson equation

$$-\frac{\partial}{\partial z} (\varepsilon(z) \frac{\partial}{\partial z} \varphi(z;t)) = 4\pi \sum_{\alpha} Z_{\alpha} e n_{\alpha}(z;t)$$

under the conditions $\bar{j}_{\alpha}(0;t) = \bar{j}_{\alpha}(L;t)$, $\varphi(0) = \varphi_0$, $\varphi(L) = \varphi_L$. The time dependence of the potentials on electrodes we present in the form

$$\varphi_0(t) = -\varphi_L(t) = \varphi^{st} + \frac{1}{2} (\varphi e^{i\omega t} + c.c.),$$

where φ^{st} is a static potential, and $\varphi_0(\omega) = \frac{\varphi}{2}$. Then the voltage between the electrodes is equal to

$$U(t) = \varphi_0(t) - \varphi_L(t) = 2\varphi^{st} + U(\omega) e^{i\omega t} + c.c.$$

$U(\omega) = \varphi$. Using Gauss's law for vector of the electric displacement $D(z;t)$ at $z=0$ we find the density of the surface charge:

$$\sigma_0(t) = -\frac{\varepsilon(0)}{4\pi} \frac{\partial}{\partial z} \varphi(z;t)|_{z=0} = D(0;t) = \sigma_0^{st} + \frac{1}{2} (\sigma_0^{am} e^{i\omega t} + c.c.),$$

σ_0^{am} is the peak value. Next we narrow the model of two-component ionic solution $Z_{\alpha} = Z_{+}, Z_{-}$ with the interfacial area $z = R$, $z = S$ and with the corresponding values of the dielectric function and surface potential:

$$\varepsilon(z) = \begin{cases} \varepsilon_L, & z < R \\ \varepsilon_R, & z > R \end{cases}$$

$$V_{\pm}(z) = \begin{cases} 0, & z < S \\ f_{\pm}, & z > S \end{cases}$$

where $|R-S| \ll L$, and f_{\pm} is the ions solubility in the corresponding phase. The mobility of ions is specified in each phase:

$$\tilde{D}_{\pm} = \begin{cases} \tilde{D}_{\pm}^L, & z < \min(R, S) \\ \tilde{D}_{\pm}^R, & z > \max(R, S) \end{cases}$$

First we consider the case of constant voltage over time:

$$\varphi_0(t) = -\varphi_L(t) = \varphi^{st},$$

with the condition $j_{\pm}(0;t) = j_{\pm}(L;t)$. In the homogeneous case a Poisson equation has the form:

$$-\frac{\partial}{\partial z} (\varepsilon(z) \frac{\partial}{\partial z} \varphi_{\text{hom}}(z;t)) = 0.$$

Its analytical solution can be represented as:

$$\varphi_{\text{hom}}(z) = \begin{cases} \frac{A_L}{\varepsilon_L} z + B_L, & z < R \\ \frac{A_R}{\varepsilon_R} z + B_R, & z > R \end{cases}$$

with the conditions of the continuity

$$\begin{aligned} D(R^-;t) &= D(R^+;t) = \varepsilon_L \frac{\partial}{\partial z} \varphi(z;t)|_{z=R^-} \\ &= \varepsilon_L \frac{\partial}{\partial z} \varphi(z;t)|_{z=R^+} \end{aligned}$$

$\varphi(R^-;t) = \varphi(R^+;t)$. As a result, the solution will look like:

$$\varphi_{\text{hom}}(z;t) = \begin{cases} -\frac{2\varphi^{st}}{\varepsilon_L} \left(\frac{R}{\varepsilon_L} + \frac{L-R}{\varepsilon_R}\right)^{-1} z + \varphi^{st}, & z < R \\ \frac{2\varphi^{st}}{\varepsilon_R} \left(\frac{R}{\varepsilon_L} + \frac{L-R}{\varepsilon_R}\right)^{-1} (L-z) - \varphi^{st}, & z > R \end{cases}$$

Then we find the solution of the inhomogeneous Poisson equation using the Green's functions method:

$$\frac{\partial}{\partial z} (\varepsilon(z) \frac{\partial}{\partial z} G(z, z')) = -4\pi \delta(z - z')$$

with the boundary conditions

$$G(0, z') = 0 \quad G(R^-, z') = G(R^+, z')$$

$$G(L, z') = 0 \quad \varepsilon_L \frac{\partial}{\partial z} G(z = R^-, z') = \varepsilon_R \frac{\partial}{\partial z} G(z = R^+, z').$$

The result is:

$$G(z, z') = \begin{cases} -\frac{4\pi}{\varepsilon_L} \Theta(z - z')(z - z') - \frac{C(z')}{\varepsilon_L} z, & z < R \\ -\frac{4\pi}{\varepsilon_R} \Theta(z - z')(z - z') - \frac{C(z')}{\varepsilon_R} z, & z > R \\ +\frac{4\pi}{\varepsilon_R} (L - z') + \frac{L}{\varepsilon_R} C(z'), & z > R \end{cases}$$

where

$$C(z') = \frac{4\pi}{\varepsilon_R - \varepsilon_L} \frac{1}{R} [\Theta(R - z')(R - z') \left(\frac{1}{\varepsilon_L} - \frac{1}{\varepsilon_R}\right) + (L - z') \frac{1}{\varepsilon_R}]$$

Then the solution of Poisson's equation for the selected model can be represented as:

$$\varphi(z;t) = \varphi_{\text{hom}}(z;t) + \int_0^L dz' G(z, z') (n_+(z';t) - n_-(z';t)).$$

Thus, substituting present solution to the Nernst-Planck equation, we get a closed system of equations:

$$\begin{aligned} \frac{\partial}{\partial t} n_{\alpha}(z;t) &= \frac{\partial}{\partial z} [\Omega_{\alpha}(z;t) \left[\frac{\partial}{\partial z} n_{\alpha}(z;t) + \right. \\ n_{\alpha}(z;t) \left(\frac{\partial}{\partial z} V_{\alpha}(z) + Z_{\alpha} e \frac{\partial}{\partial z} (\phi_{\text{hom}}(z;t) + \right. & \quad (1) \\ \left. \left. \int_0^L dz' G(z,z') (n_{+}(z';t) - n_{-}(z';t)) \right) \right] \end{aligned}$$

under the certain mobilities of ions $\tilde{D}_{\alpha}(z;t)$ and the surface potential $V_{\alpha}(z)$. The system of equations is nonlinear. An important step is to study the solutions of the system of equations close to equilibrium when $n_{\alpha}(z;t) = n_{\alpha}^{\text{st}}(z)$ is static distribution of ions in the "electrolyte-electrode" system. Solutions of the system of equations (1) for the approximate calculation $\tilde{D}_{\alpha}(z;t) \approx \frac{\beta}{m_{\alpha}} n_{\alpha}(z;t)$ through the moments [13] may be important that requires some mathematical research.

4. Conclusions. Summarizing, we proposed a statistical theory of classical-quantum description of electrodiffusion transport processes of ions and electrons in the "electrolyte- electrode" system using the NSO method. The presented theory takes the spatial heterogeneity and memory effects into account. In this approach, we receive the generalized transport equations such as Nernst-Planck equation for electrons and ions in the "electrolyte-electrode" system using the method of nonequilibrium statistical operator. These equations take into account the time memory effects and spatial heterogeneity. An important contributions to the generalized Nernst-Planck type equations are provided by the transport kernels $\tilde{D}_{jn}^{\alpha\alpha\gamma}$, which, unlike the generalized diffusion coefficients, are the third-order correlation functions and enter into equations via terms of second order in the parameters $\varphi(\vec{r}_i;t) \delta n_{\gamma}(\vec{r}_i;t)$, $\varphi(\vec{r}_i;t) \delta \bar{n}_{\alpha}(\vec{r}_s;t)$, $\varphi(\vec{r}_s;t) \delta \bar{n}_{\alpha}(\vec{r}_s;t)$ which describe the dynamic correlations between the field and a density.

In this approach, we have considered a one-dimensional simplified model of intercalation of ions into the electrode structure with taking the dielectric polarization into account.

An important open issue consists in the appearance of bound states of Li ions with electrons and Li ions inside electrode. For description of such processes, the transport equations should be complemented with the equations for "ion-ion", "ion-electron" and "electron-electron" nonequilibrium pair distribution functions within the electrode structure. These problems we will consider in our future works. Besides, within the classical description of an electrolyte we did not consider explicitly polar molecules of solvent which, evidently, can significantly effect the polarization processes due to their orientational movement and can be transported into the porous structure of electrode (what leads to a decrease of porosity and cleavage). This needs a separate study as well.

Reference

1. Barsoukov E., Macdonald J.R. Impedance spectroscopy. Theory, experiment and application. – Canada, 2005.
2. Bazant M.Z. Theory of Chemical Kinetics and Charge Transfer based on Nonequilibrium Thermodynamics. arXiv, 1208.1587V2. cond – mat.mtrl-sci, 2013, 17 p.
3. Biesheuvel P.M., Bazant M.Z. Diffuse charge and Faradaic reactions in porous electrodes // Phys. Rev. E. – 2011. – vol. 83, P. 061507.
4. Bisquet J., Compte A. Theory of the electrochemical impedance of anomalous diffusion // J. Electroanalytical Chem. – 2013. – vol. 499, P. 112.
5. Determination of the diffusion coefficient of lithium ions in nano-Si / Ding N. Xu J. et al. // Solid State Ionics. – 2009. – vol. 180, P. 222.
6. Ferguson T. R., Bazant M. Z. Nonequilibrium Thermodynamics of Porous Electrodes // J. Electrochem. Soc. – 2012. – vol. 159, P. 1967.
7. Goncalves W. D., Iost R.M., Crespiho F.N. Diffusion Mechanisms in Nanoelectrodes: Evaluating the Edge Effect // Electroch. Acta. – 2014. – vol. 123, P. 66.
8. Gryhorchak I. I., Ponedilok H. V. Impedance spectroscopy. – Lviv, 2011. (in Ukrainian).
9. Hjeim A-K., Lindbergh G. Experimental and theoretical analysis of LiMn2O4 cathodes for use in rechargeable lithium batteries by electrochemical impedance spectroscopy (EIS) // Electrochim. Acta. – 2002. – vol. 47, P. 1747.
10. Kern R., Sastrawan R., Ferbar J., Stangl R. Modeling and interpretation of electrical impedance spectra of dye solar cells operated under open-circuit conditions // Electrochim. Acta. – 2002. – vol. 47, P. 4213.
11. Kinnon W. R., Haering R. R. Physical Mechanisms of Intercalation, in: Modern Aspects of Electrochemistry. – New York, 1983.
12. Korovin N. V. Intercalation into cathode materials. Diffusion coefficient of Lithium // Elektrokimiya. – 1999. – vol. 33, P. 739. (in Russian).
13. Statistical theory of reaction-diffusion processes intercalation of ions in the "electrolyte-electrode". 1. Generalized transport equations Nernst-Planck type / Kostrobij P.P., Markovych B.M. et al. // ICMP– Lviv, 2014. Preprint-ICMP-14-03U.
14. Reaction-diffusion processes in systems "metal-gas" / Kostrobij P.P. Tokarchuk M.V. et al. – Lviv, 2009. (in Ukrainian).
15. Mandzyuk V. I., Nagima N. I., Lisovskyy R. P. Morphology and Electrochemical Properties of Thermal Modified Nanoporous Carbon as Electrode of Lithium Power Sources // J. of Nano- and Electronic Phys. – 2014. – vol. 6, No.1. (in Ukrainian).
16. Manthiram A. Lithium batteries, edited by Gholam-Abbas Nazri. – USA, 2009.
17. Electro-diffusion of ions in porous electrodes for capacitive extraction of renewable energy from salinity differences / Rica R. Ziano A.R. et al. // Electrochimica Acta. – 2013. – vol. 92, P. 304.
18. Umeda M., Dokko K. Electrochemical impedance study of Li-ion insertion into mesocarbon microbead single particle electrode (Part 1. Graphitized carbon) // Electrochim. – 2001, – vol. 47, P. 885.
19. Xie Y., Li J., Yuan C. Mathematical modeling of the electrochemical impedance spectroscopy in lithium ion battery cycling // Electrochimica. Acta. – 2014. – vol.127, P. 266.
20. Xia H., Lu Li, Ceder G. Li diffusion in thin films prepared by pulsed laser deposition // J. Power Sour., – 2006. – vol.159, P. 1422.
21. Zubarev D. N., Morozov V. G., Ropke G. Statistical Mechanics of Nonequilibrium Processes, vol.1. – Berlin, 1997.

Submitted on 04.11.14

Костробий П., д-р фіз.-мат. наук, Маркович Б., канд. фіз.-мат. наук
Токарчук Р., асист., каф. прикладної математики,
Інститут прикладної математики та фундаментальних наук, Національний університет "Львівська політехніка",
Черноморець Ю., асп., відділ теорії нерівноважних процесів, Інститут фізики конденсованих систем НАН України,
Токарчук М., д-р фіз.-мат. наук, каф. прикладної математики,
Інститут прикладної математики та фундаментальних наук, Національний університет "Львівська політехніка",
відділ теорії нерівноважних процесів, Інститут фізики конденсованих систем НАН України

СТАТИСТИЧНА ТЕОРІЯ ЕЛЕКТРОДИФУЗІЙНИХ ПРОЦЕСІВ ІНТЕРКАЛЯЦІЇ ІОНІВ В СИСТЕМІ "ЕЛЕКТРОЛІТ-ЕЛЕКТРОД"

Запропоновано статистичну теорію для класично-квантового опису електродифузійних процесів інтеркаляції в системі "електроліт-електрод". Використовуючи метод нерівноважного статистичного оператора, отримано узагальнені рівняння переносу типу Нернста-Планка для іонів та електронів в системі "електроліт-електрод". Ці рівняння враховують ефекти пам'яті в часі та просторову неоднорідність. Запропоновано одомірну спрощену модель інтеркаляції іонів в структуру електрода з врахуванням діелектричної поляризації.

Ключові слова: електроліт, електрод, інтеркаляція, нерівноважний статистичний оператор.

Костробий П., д-р физ.-мат. наук, Маркович Б., канд. физ.-мат. наук,
Токарчук Р., ассист., каф. прикладной математики,
Институт прикладной математики и фундаментальных наук, Национальный университет "Львовская политехника",
Черноморец Ю., асп., отдел теории неравновесных процессов, Институт физики конденсированных систем НАН Украины,
Токарчук М., д-р физ.-мат. наук, каф. прикладной математики, Институт прикладной математики и фундаментальных наук
Национальный университет "Львовская политехника", отдел теории неравновесных процессов,
Институт физики конденсированных систем НАН Украины

СТАТИСТИЧЕСКАЯ ТЕОРИЯ ЭЛЕКТРОДИФУЗИОННЫХ ПРОЦЕССОВ ИНТЕРКАЛЯЦИИ ИОНОВ В СИСТЕМЕ "ЭЛЕКТРОЛИТ-ЭЛЕКТРОД".

Предложено статистическую теорию для классическо-квантового описания электродифузионных процессов интеркаляции в системе "электролит-электрод". Используя метод неравновесного статистического оператора, получены обобщенные уравнения переноса типа Нернста-Планка для ионов и электронов в системе "электролит-электрод". Эти уравнения учитывают эффекты памяти во времени и пространственную неоднородность. Предложено одомерную упрощенную модель интеркаляции ионов в структуру электродов с учетом диелектрической поляризации.

Ключевые слова: электролит, электрод, интеркаляция, неравновесный статистический оператор.

Наукове видання



ВІСНИК

КИЇВСЬКОГО НАЦІОНАЛЬНОГО УНІВЕРСИТЕТУ ІМЕНІ ТАРАСА ШЕВЧЕНКА

РАДІОФІЗИКА ТА ЕЛЕКТРОНІКА

Випуск 1/2(21/22)

Друкується за авторською редакцією

Оригінал-макет виготовлено ВПЦ "Київський університет"

Автори опублікованих матеріалів несуть повну відповідальність за підбір, точність наведених фактів, цитат, економіко-статистичних даних, власних імен та інших відомостей. Редколегія залишає за собою право скорочувати та редагувати подані матеріали. Рукописи та дискети не повертаються.



Формат 60x84^{1/8}. Ум. друк. арк. 11,16. Наклад 300. Зам. № 214-7189.
Гарнітура Arial. Папір офсетний. Друк офсетний. Вид. № Рф1.
Підписано до друку 30.12.14

Видавець і виготовлювач
ВПЦ "Київський університет"

01601, Київ, б-р Т. Шевченка, 14, кімн. 43
☎ (38044) 239 3222; (38044) 239 3172; тел./факс (38044) 239 3128
e-mail: vpc@univ.kiev.ua
http: vpc.univ.kiev.ua

Свідоцтво суб'єкта видавничої справи ДК № 1103 від 31.10.02

